



This work is protected by copyright and other intellectual property rights and duplication or sale of all or part is not permitted, except that material may be duplicated by you for research, private study, criticism/review or educational purposes. Electronic or print copies are for your own personal, non-commercial use and shall not be passed to any other individual. No quotation may be published without proper acknowledgement. For any other use, or to quote extensively from the work, permission must be obtained from the copyright holder/s.

Synthetic and structural studies of high silica
MFI zeolites



Shelley Brace

Doctor of Philosophy

June 2017

Keele University

Abstract

A systematic series of high-silica fluoride MFI zeolites were efficiently synthesised using a variety of shape and size structure directing agents. The effects of these structure directing agents on the zeolite synthesised have been studied by the complementary use of X-ray diffraction and solid state NMR. These ^{14}N , ^{13}C and ^{29}Si NMR experiments yield information about the orientation of the structure directing agent within zeolite pores. They also identify covalently bonded fluoride in the form of pentacoordinated silicon whereby the first case of static and dynamic ordering of fluoride in the same zeolite is discovered by changing the structure directing agent.

A two-dimensional solid state NMR experiment has also been used to study ^{13}C isotopically labelled silicalite-1 synthesised using n-methyltributylammonium iodide. The double cross polarisation (DCP) experiment allows the distance to be determined between the structure directing agent and silicon framework for the first time in a zeolite system using NMR. This experiment has the potential to be replicated for silicalite-1 zeolites synthesised using alternate structure directing agents or for other zeolites systems.

To my mum;

Thank you.

Acknowledgements

The following PhD would simply not have been possible were it not for the kind and considerate contributions of the following people.

To Richard and Katherine;

For giving me so many years of support, guidance and insults.

To Dr Filip Wormald, Dr Daniel Dawson and the SS-NMR group at the University of St Andrews;

For attempting to teach me the ways of theoretical and practical solid state NMR.

To my parents and my family;

For the support, love and eternal questions of ‘What do you do?’ and ‘When are you going to get a real job?’ Additionally, for going over and beyond the parental obligation of putting a roof over my head until I reach eighteen.

To Dr John Staniforth, Professor Mark Ormerod and all the ever-changing members of CSMG;

For the opportunity to come to know you all, for teaching me about magic rocks, the presentations, the conferences, the dinners, for listening to my work, and the machines that don’t. And the friendships.

To Nigel;

For your unquestionable patience, support, love and miles driven!

To Phil, Dennis and all my dear Keele coffee friends;

Who helped to keep my belly full of coffee and my head full of memories.

Thank you.

Contents

Abstract	i
Acknowledgements	iii
Contents	iv
Record of Figures	vii
Record of Tables	xi
Glossary	xiii
1.0. Introduction	1
1.1. Zeolite Synthesis	3
1.1.1. <i>Silicon Source</i>	3
1.1.2. <i>Mineralising agent</i>	4
1.1.3. <i>Structure Directing Agent</i>	5
1.1.4. <i>Solvent System</i>	7
1.2. Methods of Synthesising MFI Zeolites	8
1.3. MFI Framework Structure	9
1.4. MFI Structural Formation	10
1.5. Characterisation Techniques	12
1.6. Aims of the Work	13
1.7. References	15
2.0. Methodology	21
2.1. Powder X-ray Diffraction (PXRD) Theory	21
2.1.1. <i>Methods of Extracting X-ray Diffraction Data</i>	24
2.2. NMR Theory	26
2.2.1. <i>Nuclear Spin</i>	26
2.2.2. <i>Zeeman Interaction</i>	27
2.2.2.1. <i>Boltzman Distribution and Population Density</i>	28
2.2.2.2. <i>Lamor Precession</i>	29
2.2.2.3. <i>Bulk Magnetisation</i>	30
2.2.2.4. <i>NMR Relaxation</i>	31
2.2.2.5. <i>NMR Interactions</i>	33
2.2.2.5.1. <i>Shielding</i>	33
2.2.2.5.2. <i>NMR Tensor Properties</i>	35
2.2.2.5.3. <i>Indirect Spin Coupling/ J-Couplings</i>	37
2.2.2.5.4. <i>Dipolar Coupling</i>	37
2.2.2.5.5. <i>Quadrupolar Coupling</i>	39
2.2.2.6. <i>Solid State NMR Techniques</i>	41
2.2.2.6.1. <i>Magic Angle Spinning</i>	42
2.2.2.6.2. <i>Cross Polarisation</i>	44
2.2.2.6.3. <i>High Power Decoupling</i>	45
2.2.2.6.4. <i>2D NMR Experiments</i>	46
2.3. Scanning Electron Microscopy Theory	46
2.4. Background to Instrumentation	47
2.4.1. <i>X-ray Diffraction</i>	47
2.4.2. <i>Solid State NMR</i>	48
2.4.2.1. <i>NMR Experimental Details and References</i>	48
2.4.2.1.1. <i>NMR Probe Specification</i>	49
2.4.2.1.2. <i>Variable Temperature NMR Experiments</i>	50
2.4.3. <i>Scanning Electron Microscopy</i>	50
2.5. References	51
3.0. Synthesis and Characterisation of Organic Structure Directing Agents	53

and Pure Silica Zeolites

3.1. Inorganic Pure Silica MFI Zeolites	54
3.1.1. Hydroxide Route Synthetic Methods	55
3.1.2. Fluoride Route Synthetic Methods	56
3.2. Successful Zeolite Structure Directing Agents	56
3.2.1. Synthesis of MFI using TPA ⁺ F ⁻	56
3.2.2. Synthesis of MFI using MTBA ⁺ F ⁻	59
3.2.3. Synthesis of MFI using ETBA ⁺ F ⁻	62
3.2.4. Synthesis of MFI using P(5)TBA ⁺ F ⁻	64
3.2.5. Synthesis of MFI using H(6)TBA ⁺ F ⁻	67
3.2.6. Synthesis of MFI using MTPA ⁺ F ⁻	70
3.2.7. Synthesis of MFI using ETPA ⁺ F ⁻	72
3.2.8. Synthesis of MFI using BTP(3)A ⁺ F ⁻	74
3.2.9. Synthesis of MFI using P5TP3A ⁺ F ⁻	77
3.2.10. Synthesis of MFI using H(6)TP(3)A ⁺ F ⁻	79
3.2.11. Synthesis of MFI using H(7)TP(3)A ⁺ F ⁻	81
3.2.12. Synthesis of MFI using TEP(3)A ⁺ F ⁻	84
3.2.13. Synthesis of MFI using TEIP(3)A ⁺ F ⁻	86
3.2.14. Synthesis of MFI using TEBA ⁺ F ⁻	88
3.2.15. Synthesis of MFI using TEP(5)A ⁺ F ⁻	90
3.2.16. Synthesis of MFI using TEH(6)A ⁺ F ⁻	92
3.2.17. Synthesis of MFI using TEH(7)A ⁺ F ⁻	95
3.2.18. Synthesis of MFI using TMH(6)A ⁺ F ⁻	97
3.2.19. Synthesis of MFI using DMDP(5)A ⁺ F ⁻	99
3.2.20. Synthesis of MFI using DEDBA ⁺ F ⁻	101
3.2.21. Synthesis of MFI using DMDIBA ⁺ F ⁻	104
3.2.22. Synthesis of MFI using DEDIBA ⁺ F ⁻	106
3.3. Unsuccessful MFI Structure Directing Agents	108
3.3.1. Synthesis of P(3)TBA ⁺ F ⁻	108
3.3.2. Synthesis of MFI using DP(3)DIP(3)A ⁺ F ⁻	110
3.4. Additional X-ray Diffraction Peak	111
3.5. References	113
4.0. Solid State NMR Study of MFI Zeolite Synthesised Using Varied Structure Directing Agents	114
<hr/>	
4.1. ¹³ C Solid State NMR	115
4.1.1. TPA F-Silicalite-1	115
4.1.2. N-alkyltripropylammonium Silicalite-1 Series	118
4.1.3. N-alkyltripropylammonium Silicalite-1 Summary	126
4.1.4. N-alkyltributylammonium Silicalite-1 Series	127
4.1.5. N-alkyltributylammonium Silicalite-1 Summary	131
4.1.6. N-alkyltriethylammonium Silicalite-1 Series	132
4.2. ¹⁴ N Solid State NMR	135
4.2.1. ¹⁴ N MAS NMR Results	137
4.2.2. ¹³ C and ¹⁴ N Solid State NMR Conclusions	148
4.3. References	150
5.0. The Effect of Structure Directing Agents on the Order of Fluoride in Pure Silica MFI Zeolites	152
<hr/>	
5.1. ²⁹ Si Solid State NMR Results	155
5.1.1. TPA F-silicalite-1	155
5.1.2. ²⁹ Si SS-NMR N-alkyltributylammonium Silicalite-1 Series	157
5.1.3. ²⁹ Si SS-NMR N-alkyltripropylammonium Silicalite-1 Series	167
5.2. ¹⁹ F Solid State NMR of Silicalite-1 Species	172
5.2.1. ¹⁹ F Solid State NMR Results	173

5.3. Conclusions	177
5.4. References	179
6.0. Determination of SDA to Framework Distance in Silicalite-1 by Solid State NMR	182
<hr/>	
6.1. Cross Polarisation Theory	183
6.1.1. <i>Cross Polarisation: The Experiment</i>	184
6.2. Synthesis	185
6.2.1. <i>¹³C labelled n-methyltriphenylsilane</i>	185
6.2.2. <i>Labelled ¹³C N-methyltributylammonium Iodide</i>	187
6.3. Double Cross Polarisation	189
6.3.1. <i>Double Cross Polarisation: Experimental Information</i>	190
6.3.2. <i>Double Cross Polarisation Experimental Set-up</i>	192
6.4. Rotational-Echo, Double Resonance (REDOR) Results	195
6.4.1. <i>REDOR Set-up</i>	197
6.4.2. <i>REDOR Results</i>	198
6.5. Conclusions	205
6.6. References	207
7.0. Conclusions	209
<hr/>	

Record of Figures

Figure 1.1	<i>Schematic diagram of MFI type zeolite framework structure</i>	2
Figure 1.2	<i>Schematic diagram of (left) pentacoordinated silicon unit [SiO₄/2F-] and (right) MFI zeolite framework with occluded n-methyltributylammonium SDA</i>	5
Figure 1.3	<i>Schematic representation of TPA silicalite-1 within the zeolite framework and the orientation of TPA within straight and sinusoidal channels (not to scale)</i>	6
Figure 1.4	<i>Schematic diagram of MFI zeolite structure</i>	9
Figure 1.5	<i>Schematic diagram of the 23 observed SBU's by Knight and Kinrade107 in TPA silicalite-1</i>	10
Figure 1.6	<i>Sigmoidal (S) shape curve of silicalite-1 zeolite growth</i>	11
Figure 1.7	<i>Burkett and Davis proposed mechanism for ZSM-5 formation using tetrapropylammonium SDA126</i>	12
Figure 2.1	<i>Schematic diagram of Bragg reflection from crystal planes with spacing dhkl</i>	21
Figure 2.2	<i>Laboratory photo of labelled laboratory Bruker D8 ADVANCE X-ray diffractometer</i>	23
Figure 2.3	<i>Schematic diagram showing Zeeman energy level splitting for spin 1/2 nucleus</i>	27
Figure 2.4	<i>diagram depicting the Larmor Precession of a spinning nucleus's orbit</i>	29
Figure 2.5	<i>Schematic diagram of net magnetisation aligned with applied magnetic field</i>	30
Figure 2.6	<i>Schematic diagram showing magnetisation being shifted into the xy plane after an applied pulse</i>	31
Figure 2.7	<i>Schematic diagram showing dipolar coupling between two dipole moments, I and S</i>	38
Figure 2.8	<i>Schematic diagram demonstrating the ϑ_R angle that is set to 54.74° for magic angle spinning</i>	43
Figure 3.1	<i>Schematic reaction diagrams of an alkyl halide with primary, secondary and tertiary amines to give quaternary ammonium iodide species, required as SDA's</i>	54
Figure 3.2	<i>Structure of TPA (tetrapropylammonium) cation SDA</i>	56
Figure 3.3	<i>XRD powder pattern of TPA/MFI on a Bruker Advance diffractometer with Cu Kα Source</i>	58
Figure 3.4	<i>Structure of MTB (methyltributylammonium) cations SDA</i>	59
Figure 3.5	<i>XRD powder pattern of MTBA/MFI on a Bruker Advance diffractometer with Cu Kα source</i>	62
Figure 3.6	<i>Structure of ETB (n-ethyl-triethylammonium) cation SDA</i>	62
Figure 3.7	<i>XRD powder pattern of ETBA/MFI on a Bruker Advance diffractometer with Cu Kα source</i>	64
Figure 3.8	<i>Structure of P5TBA (pentyltributylammonium) cation SDA</i>	64
Figure 3.9	<i>XRD powder pattern of P(5)TBA/MFI on a Bruker Advance diffractometer with Cu Kα source</i>	66
Figure 3.10	<i>Structure of H6TBA (n-hexyltributylammonium) cation SDA</i>	67
Figure 3.11	<i>XRD powder pattern of H(6)TBA/MFI on a Bruker Advance diffractometer with Cu Kα source</i>	70
Figure 3.12	<i>Structure of MTP3A (methyltripropylammonium) cation SDA</i>	70
Figure 3.13	<i>XRD powder pattern of MTP3A/MFI on a Bruker Advance diffractometer with Cu Kα source</i>	72
Figure 3.14	<i>Structure of ETP3A (ethyltripropylammonium) cation SDA</i>	72
Figure 3.15	<i>XRD powder pattern of ETP3A/MFI on a Bruker Advance diffractometer with Cu Kα source</i>	74
Figure 3.16	<i>Structure of BTP3A (N-butyltripropylammonium) cation SDA</i>	74
Figure 3.17	<i>XRD powder pattern of BTP(3)A/MFI on a Bruker Advance diffractometer with Cu Kα source</i>	76
Figure 3.18	<i>Structure of P5TP3A (Pentyltripropylammonium) cation SDA</i>	77
Figure 3.19	<i>XRD powder pattern of P(5)TP(3)A/MFI on a Bruker Advance diffractometer with Cu Kα source</i>	79
Figure 3.20	<i>Structure of H6TP3A (Hexyltripropylammonium) cation SDA</i>	79
Figure 3.21	<i>XRD powder pattern of H(6)TP(3)A/MFI on a Bruker Advance diffractometer with Cu Kα source</i>	81
Figure 3.22	<i>Structure of H(7)TP3A (Heptyltripropylammonium) cation</i>	81
Figure 3.23	<i>XRD powder pattern of H(7)TP(3)A/MFI on a Bruker Advance diffractometer with Cu</i>	83

	<i>Kα source</i>	
Figure 3.24	<i>Structure of TEP3A (triethyl-n-propylammonium) cation</i>	84
Figure 3.25	<i>XRD powder pattern of TEP(3)A/MFI on a Bruker Advance diffractometer with Cu Kα source</i>	85
Figure 3.26	<i>Structure of TEIP3A (triethyl-n-isopropylammonium) cation</i>	86
Figure 3.27	<i>XRD powder pattern of TEIP(3)A/MFI on a Bruker Advance diffractometer with Cu Kα source</i>	88
Figure 3.28	<i>Structure of TEBA (triethylbutylammonium) cation</i>	88
Figure 3.29	<i>XRD powder pattern of TEBA/MFI on a Bruker Advance diffractometer with Cu Kα source</i>	90
Figure 3.30	<i>Structure of TEP5A (triethylpentylammonium) cation SDA</i>	90
Figure 3.31	<i>XRD powder pattern of TEP5A/MFI on a Bruker Advance diffractometer with Cu Kα source</i>	92
Figure 3.32	<i>Structure of TEH6A (triethylhexylammonium) cation SDA</i>	92
Figure 3.33	<i>XRD powder pattern of TEH6A/MFI on a Bruker Advance diffractometer with Cu Kα source</i>	95
Figure 3.34	<i>Structure of TEH7A (triethyl-n-heptylammonium) cation SDA</i>	95
Figure 3.35	<i>XRD powder pattern of TEH(7)A/MFI on a Bruker Advance diffractometer with Cu Kα source</i>	97
Figure 3.36	<i>Structure of TMH(6)A (trimethyl-n-hexylammonium) cation</i>	97
Figure 3.37	<i>XRD powder pattern of TMH6A/MFI on a Bruker Advance diffractometer with Cu Kα source</i>	99
Figure 3.38	<i>Structure of DM DP(5)A (N,n-dimethyl-n,n-dipentylammonium) cation</i>	99
Figure 3.39	<i>XRD powder pattern of DM DP5A/MFI on a Bruker Advance diffractometer with Cu Kα source</i>	101
Figure 3.40	<i>Structure of DEDBA (diethyl-dibutylammonium) cation</i>	101
Figure 3.41	<i>XRD powder pattern of DEDBA/MFI on a Bruker Advance diffractometer with Cu Kα source</i>	103
Figure 3.42	<i>Structure of DM DIBA (Dimethyldiisobutylammonium) cation</i>	104
Figure 3.43	<i>XRD powder pattern of DM DIBA/MFI on a Bruker Advance diffractometer with Cu Kα source</i>	106
Figure 3.44	<i>Structure of DEDIBA (Diethyldiisobutylammonium) cation</i>	106
Figure 3.45	<i>XRD powder pattern of DEDIBA/MFI on a Bruker Advance diffractometer with Cu Kα source</i>	108
Figure 3.46	<i>Structure of P3TBA (N-propyltributylammonium) cation</i>	108
Figure 3.47	<i>Structure of DP DIPA (N,n-dipropyl-n,n-diisopropylammonium) cation</i>	110
Figure 4.1	<i>Schematic representation of TPA silicalite-1 within the zeolite framework and the orientation of TPA within straight and sinusoidal channels (not to scale)</i>	114
Figure 4.2	<i>$^{13}\text{C} \{^1\text{H}\}$ CP MAS NMR of silicalite-1 synthesised with tetrapropylammonium using the hydroxide route synthesis</i>	116
Figure 4.3	<i>$^{13}\text{C} \{^1\text{H}\}$ CP MAS NMR of silicalite-1 synthesised with tetrapropylammonium using the fluoride route synthesis</i>	117
Figure 4.4	<i>Structure of TPA (tetrapropylammonium) cation SDA</i>	117
Figure 4.5	<i>SEM Image of TPA silicalite-1 synthesised via the fluoride route. Rectangular shaped crystals of dimensions $\sim 30 \times 60 \mu\text{m}$ at x300 zoom</i>	118
Figure 4.6	<i>Structure of MTP3A (n-methyltripropylammonium) cation SDA</i>	118
Figure 4.7	<i>$^{13}\text{C} \{^1\text{H}\}$ CP MAS NMR of silicalite-1 synthesised with n-methyltripropylammonium using the fluoride route synthesis</i>	119
Figure 4.8	<i>Schematic representation of MTPA silicalite-1 within the zeolite framework and the orientation of MTPA within straight and sinusoidal channels (not to scale)</i>	120
Figure 4.9	<i>SEM Images of MTPA silicalite-1 synthesised using (left) hydroxide route producing spherical crystals</i>	120
Figure 4.10	<i>Structure of ETP3A (ethyltripropylammonium) cation SDA</i>	121
Figure 4.11	<i>$^{13}\text{C} \{^1\text{H}\}$ CP MAS NMR of silicalite-1 synthesised with n-ethyltripropylammonium using the fluoride route synthesis</i>	121
Figure 4.12	<i>$^{13}\text{C} \{^1\text{H}\}$ CP MAS NMR of silicalite-1 synthesised with the methyl to propyl series of n-alkyltripropylammonium from 2.5 – 15 ppm (intensity not to scale)</i>	122
Figure 4.13	<i>SEM Image of ETP silicalite-1 synthesised via the fluoride route. Coffin shaped crystals of dimensions</i>	122

Figure 4.14	Structure of BTP3A (<i>N</i> -butyltripropylammonium) cation SDA	123
Figure 4.15	^{13}C $\{^1\text{H}\}$ CP MAS NMR of silicalite-1 synthesised with <i>n</i> -butyltripropylammonium using the fluoride route synthesis	123
Figure 4.16	^{13}C $\{^1\text{H}\}$ CP MAS NMR of propyl to pentyl <i>n</i> -alkyltripropylammonium silicalite-1	124
Figure 4.17	Structure of P5TP3A (pentyltripropylammonium) cation SDA	124
Figure 4.18	^{13}C $\{^1\text{H}\}$ CP MAS NMR of silicalite-1 synthesised with <i>n</i> -pentyltripropylammonium using the fluoride route synthesis	125
Figure 4.19	SEM Image of P5TP3A silicalite-1 synthesised via the fluoride route. Spherical crystals of dimensions up to 10 μm	126
Figure 4.20	SEM Image of P5TP3A silicalite-1 synthesised via the hydroxide route. Spherical crystals of dimensions up to 10 μm	126
Figure 4.21	Structure of MTBA (<i>n</i> -methyltributylammonium cations) SDA	127
Figure 4.22	^{13}C $\{^1\text{H}\}$ CP MAS NMR of silicalite-1 synthesised with <i>n</i> -methyltributylammonium using the fluoride route synthesis	128
Figure 4.23	Schematic representation of MTBA silicalite-1 within the zeolite framework and the orientation of MTBA within straight and sinusoidal channels (not to scale)	129
Figure 4.24	Structure of ETB (<i>n</i> -ethyl-tripropylammonium) cation SDA	129
Figure 4.25	^{13}C $\{^1\text{H}\}$ CP MAS NMR of silicalite-1 synthesised with <i>n</i> -ethyltributylammonium using the fluoride route synthesis	129
Figure 4.26	Structure of P5TBA (pentyltributylammonium) cation SDA	130
Figure 4.27	^{13}C $\{^1\text{H}\}$ CP MAS NMR of silicalite-1 synthesised with <i>n</i> -pentyltributylammonium using the fluoride route synthesis	130
Figure 4.28	Schematic Diagram of <i>n</i> -alkyltriethylammonium cation series where the alkyl chain ranges from propyl to hexyl	132
Figure 4.29	^{13}C $\{^1\text{H}\}$ CP MAS NMR of silicalite-1 synthesised with <i>n</i> -alkyltriethylammonium silicalite-1 series	133
Figure 4.30	Comparison of ^{13}C $\{^1\text{H}\}$ NMR spectra for propyl to hexyl <i>n</i> -alkyltriethylammonium silicalite-1 from 11-18 ppm	134
Figure 4.31	Schematic diagram of the first and second order quadrupolar effects on the Zeeman interaction of a spin = 1 nuclei	136
Figure 4.32	^{14}N MAS NMR spectrum of TPA silicalite-1 and SOLA fitting profile ($\nu\text{MAS} = 2$ kHz)	138
Figure 4.33	^{14}N MAS NMR spectrum of MTPA silicalite-1 and SOLA fitting profile ($\nu\text{MAS} = 2$ kHz)	139
Figure 4.34	^{14}N MAS NMR spectrum of ETPA silicalite-1 and SOLA fitting profile ($\nu\text{MAS} = 2$ kHz)	140
Figure 4.35	Schematic diagram of increasing alkyl chain <i>n</i> -alkyltripropylammonium silicalite-1 series	141
Figure 4.36	^{14}N MAS NMR spectrum of BTPA silicalite-1 and SOLA fitting profile ($\nu\text{MAS} = 2$ kHz)	142
Figure 4.37	^{14}N MAS NMR spectrum of P5TP3A silicalite-1 and SOLA fitting profile ($\nu\text{MAS} = 2$ kHz)	143
Figure 4.38	Graph representing the asymmetry (η) parameters obtained for the <i>n</i> -alkyltripropylammonium silicalite-1 series	144
Figure 4.39	Graph representing the anisotropy (CQ) parameters obtained for the <i>n</i> -alkyltripropylammonium silicalite-1 series	144
Figure 4.40	^{14}N MAS NMR spectrum of MTBA silicalite-1 and SOLA fitting profile ($\nu\text{MAS} = 2$ kHz)	145
Figure 4.41	^{14}N MAS NMR spectrum of ETBA silicalite-1 and SOLA fitting profile ($\nu\text{MAS} = 2$ kHz)	146
Figure 4.42	^{14}N MAS NMR spectrum of P5TBA silicalite-1 and SOLA fitting profile ($\nu\text{MAS} = 2$ kHz)	147
Figure 5.1	Schematic diagram displaying pentacoordinated silicon species	153
Figure 5.2	Schematic diagram displaying pentacoordinated silicon species whereby the additional fluoride is covalently bonded to one si-9 site at any time	154
Figure 5.3	Spectrum (black) and deconvolution (blue) of ^1H $\{^{29}\text{Si}\}$ CP MAS NMR spectrum of [TPA]-F-MFI	155
Figure 5.4	^1H $\{^{29}\text{Si}\}$ CP MAS SS-NMR spectra of TPA F-MFI at 6 kHz rotation speed with a 7 ms contact time and 3 s recycle delay	156
Figure 5.5	Schematic diagram of structures of varied alkyl <i>n</i> -alkyltributylammonium cations in the tributylammonium silicalite-1 series	157
Figure 5.6	Spectrum (black) and deconvolution (blue) of ^1H $\{^{29}\text{Si}\}$ CP MAS NMR spectrum of [MTBA] F-MFI	158
Figure 5.7	X-ray diffraction pattern of ETBA F-MFI from 5 to 50 $2\theta^\circ$ for identification of monoclinic peaks	159
Figure 5.8	^1H $\{^{29}\text{Si}\}$ CP MAS SS-NMR spectra of MTB F-MFI at room temperature at 6 kHz	161

	<i>rotation, with a 7 ms contact time and 3 s recycle delay</i>	
Figure 5.9	$^1\text{H}\{^{29}\text{Si}\}$ CP MAS SS-NMR spectra of MTB F-MFI at 50 °C, 6 kHz rotation speed, a 7 ms contact time and 3 s recycle delay	162
Figure 5.10	$^1\text{H}\{^{29}\text{Si}\}$ CP MAS SS-NMR spectra of MTB F-MFI at – 40 °C, 6 kHz rotation speed, a 7 ms contact time and 3 s recycle delay	162
Figure 5.11	MestReNova deconvolution of $^1\text{H}\{^{29}\text{Si}\}$ CP MAS NMR spectrum of ETB F-MFI	163
Figure 5.12	$^1\text{H}\{^{29}\text{Si}\}$ CP MAS SS-NMR spectra of MTB F-MFI at room temperature, 6 kHz rotation speed, a 7 ms contact time and 3 s recycle delay	164
Figure 5.13	$^1\text{H}\{^{29}\text{Si}\}$ CP MAS SS-NMR spectra of ETB F-MFI at –10 °C, 6 kHz rotation speed, a 7 ms contact time and 3 s recycle delay	165
Figure 5.14	$^1\text{H}\{^{29}\text{Si}\}$ CP MAS SS-NMR spectra of P5TBA F-MFI at room temperature, 6 kHz rotation speed, a 7 ms contact time and 3 s recycle delay	165
Figure 5.15	2D structures of varied length n-alkyltripropylammonium cations	167
Figure 5.16	MestReNova deconvolution of $^1\text{H}\{^{29}\text{Si}\}$ CP MAS NMR spectrum of MTP F-MFI	168
Figure 5.17	$^1\text{H}\{^{29}\text{Si}\}$ CP MAS SS-NMR spectra of MTP F-MFI at room temperature, 6 kHz rotation speed, a 7 ms contact time and 3 s recycle delay	169
Figure 5.18	$^1\text{H}\{^{29}\text{Si}\}$ CP MAS SS-NMR spectra of MTPA F-MFI at – 40 °C, 6 kHz rotation speed, a 7 ms contact time and 3 s recycle delay	169
Figure 5.19	$^1\text{H}\{^{29}\text{Si}\}$ CP MAS SS-NMR spectra of ETPA F-MFI at room temperature, 6 kHz rotation speed, a 7 ms contact time and 3 s recycle delay	170
Figure 5.20	$^1\text{H}\{^{29}\text{Si}\}$ CP MAS SS-NMR spectra of BTPA F-MFI at room temperature, 6 kHz rotation speed, a 7 ms contact time and 3 s recycle delay	170
Figure 5.21	$^1\text{H}\{^{29}\text{Si}\}$ CP MAS SS-NMR spectra of P5TP3A F-MFI at – 40 °C, 6 kHz rotation speed, a 7 ms contact time and 3 s recycle delay	171
Figure 5.22	^{19}F MAS NMR of MTBA F-MFI at 30 kHz rotation speed and 280 K (spinning sidebands are asterisked*)	173
Figure 5.23	^{19}F MAS NMR of ETBA F-MFI at 30 kHz rotation speed - and 280 K (spinning sidebands are asterisked*)	174
Figure 2.24	^{19}F MAS NMR of MTPA F-MFI at 30 kHz rotation speed and 280 K (spinning sidebands are asterisked*)	175
Figure 2.25	^{19}F MAS NMR of ETPA F-MFI at 30 kHz rotation speed and 280 K (spinning sidebands are asterisked*)	176
Figure 5.26	^{19}F MAS NMR of BTPA F-MFI at 30 kHz rotation speed and 280 K (spinning sidebands are asterisked*)	176
Figure 6.1	Schematic diagram displaying pentacoordinated silicon species whereby the additional fluoride is covalently attached to one silicon-9 site at any one time	182
Figure 6.2	Structure of reference samples used for A. ^{13}C N-methyltriphenylsilane(MTPS) and B. ^{13}C (99 %), ^{15}N (99%) Glycine	185
Figure 6.3	Reaction scheme for the synthesis of labelled ^{13}C n-methyltriphenylsilane: Initial ^{13}C n-methyl lithium synthesis at 0 °C in Hexanes/ N_2 and secondary step for product synthesis under reflux/ N_2	186
Figure 6.4	Labelled molecular structure of MTPS for NMR assignment	187
Figure 6.5	Comparative spectra of ^{13}C NMR spectra for A. labelled ^{13}C MTBA and B. non-Labelled MTBA	188
Figure 6.6	XRD powder pattern of ^{13}C labelled MTBA/MFI on a Bruker Advance diffractometer with Cu Ka source	189
Figure 6.7	$^1\text{H} - ^{13}\text{C}$ Solid state MAS CP experiment on reference glycine for double CP experiment set-up	192
Figure 6.8	$^1\text{H} - ^{15}\text{N}$ Solid state MAS CP experiment on reference glycine for double CP experiment set-up	192
Figure 6.9	$^1\text{H} - ^{15}\text{N} - ^{13}\text{C}$ Solid state NMR double CP experiment on reference glycine	193
Figure 6.10	$^1\text{H} - ^{13}\text{C}$ Solid state MAS CP experiment on MTPS for double CP experiment set-up	193
Figure 6.11	$^1\text{H} - ^{29}\text{Si}$ Solid state MAS CP experiment on reference MTPS for double CP experiment set-up	194
Figure 6.12	$^{13}\text{C} - ^1\text{H} - ^{29}\text{Si}$ –Solid state double CP MAS NMR experiment on reference MTPS	194
Figure 6.13	$^1\text{H} - ^{13}\text{C}$ Solid state MAS CP experiment on ^{13}C MTBA/MFI for REDOR experiment	197
Figure 6.14	$^1\text{H} - ^{29}\text{Si}$ Solid state MAS CP experiment on ^{13}C MTBA/MFI for REDOR experiment	198
Figure 6.15	Regions of 1D spectrum from 2D REDOR experiment for most silicon environments with exception of the low intensity pentacoordinated peak 10 at -144 ppm	199
Figure 6.16	Schematic diagram of silicalite-1 zeolite and silicon assignments	201

Figure 6.17	<i>REDOR curves (blue data) of dephasing observed in regions exhibiting maximum dephasing with Solver Statistics parabolic approximation curve (black line) fitted up to 0.025 $\Delta S/SO$ for regions 4, 5 8 and 3</i>	202
Figure 6.18	<i>Schematic Diagram of a MTBA SDA in zeolite Silicalite-1</i>	203
Figure 6.19	<i>REDOR curves (blue data) of dephasing observed in regions exhibiting medium dephasing with Solver Statistics parabolic approximation curve (black line) fitted up to 0.025 $\Delta S/SO$ for regions 6, 1 and 7</i>	203
Figure 6.20	<i>REDOR curves (blue data) of dephasing observed in regions exhibiting maximum dephasing with Solver Statistics parabolic approximation curve (black line) fitted up to 0.025 $\Delta S'/SO$ for regions 2, 9 and 10.</i>	204

Record of Tables

Table 2.1	<i>Table displaying respective symmetry parameters for the seven crystal systems in increasing symmetry</i>	24
Table 2.2	<i>Table of the seven crystal systems d-spacings equations</i>	25
Table 2.3	<i>Table of seven crystal systems equations to calculate volume of unit cell</i>	25
Table 2.4	<i>Table of solution state NMR internal interactions isotropic averages</i>	35
Table 2.5	<i>Table describing the uses and examples of different types of Indirect Spin coupling parameters</i>	37
Table 2.6	<i>Experimental details for NMR spectra collected on a Bruker Avance III HD 400 MHz Spectrometer at Keele University, Staffordshire</i>	48
Table 2.7	<i>Experimental details for NMR spectra collected on a Bruker Avance III HD 400 MHz Spectrometer at University of St Andrews University, Fife</i>	48
Table 2.8	<i>Experimental details for NMR spectra collected on a Bruker Avance III HD 850 MHz Spectrometer at the Solid State NMR Facility at Warwick University.</i>	49
Table 3.1	<i>Table of synthetic methods for hydroxide route syntheses of MFI zeolite</i>	55
Table 3.2	<i>Table of synthetic methods for fluoride route syntheses of MFI zeolite</i>	56
Table 3.3	<i>Hydroxide route table of conditions for the synthesis of MFI using TPA</i>	57
Table 3.4	<i>Fluoride route table of conditions for the synthesis of MFI using TPA</i>	58
Table 3.5	<i>Hydroxide route table of conditions for the synthesis of MFI using MTBA</i>	60
Table 3.6	<i>Fluoride route table of conditions for the synthesis of MFI using MTBA</i>	61
Table 3.7	<i>Fluoride route table of conditions for the synthesis of MFI using ETBA</i>	63
Table 3.8	<i>Hydroxide route table of conditions for MFI zeolites synthesised using P(5)TBA</i>	65
Table 3.9	<i>Fluoride route table of conditions for MFI zeolites synthesised using P(5)TBA</i>	66
Table 3.10	<i>Hydroxide route table of conditions for the synthesis of MFI synthesised using H(6)TBA</i>	68
Table 3.11	<i>Fluoride route table of conditions for the synthesis of MFI synthesised using H(6)TBA</i>	68
Table 3.12	<i>Hydroxide route table of conditions for the synthesis of MFI using MTP(3)</i>	71
Table 3.13	<i>Fluoride route table of conditions for the synthesis of MFI using MTP(3)A</i>	71
Table 3.14	<i>Hydroxide Route table of conditions for the synthesis of MFI using ETP(3)A</i>	73
Table 3.15	<i>Fluoride route table of conditions for the synthesis of MFI using ETP(3)A</i>	73
Table 3.16	<i>Hydroxide route table of conditions for MFI synthesised using BTP(3)A</i>	75
Table 3.17	<i>Fluoride route table of conditions for MFI synthesised using BTP(3)</i>	76
Table 3.18	<i>Hydroxide route table of conditions for the synthesis of MFI using P(5)TP(3)A</i>	77
Table 3.19	<i>Fluoride route table of conditions for the synthesis of MFI using P(5)TP(3)</i>	78
Table 3.20	<i>Hydroxide route table of conditions for the synthesis of MFI using H(6)TP(3)A</i>	80
Table 3.21	<i>Fluoride route table of conditions for the synthesis of MFI synthesised using H(6)TP(3)A</i>	80
Table 3.22	<i>Hydroxide route table of conditions for the synthesis of MFI using H(7)TPA</i>	82
Table 3.23	<i>Fluoride route table of conditions for the synthesis of MFI using H(7)TPA</i>	83
Table 3.24	<i>Hydroxide route table of conditions for the synthesis of MFI using TEP(3)A</i>	84
Table 3.25	<i>Fluoride route table of conditions for the synthesis of MFI using TEP(3)A</i>	85

Table 3.26	<i>Hydroxide route table of conditions for the synthesis of MFI using TEIP(3)A</i>	86
Table 3.27	<i>Fluoride route table of conditions for the synthesis of MFI using TEIP(3)A</i>	87
Table 3.28	<i>Hydroxide route table of conditions for the synthesis of MFI using TEBA</i>	89
Table 3.29	<i>Fluoride route table of conditions for the synthesis of MFI using TEBA</i>	89
Table 3.30	<i>Hydroxide route table of conditions for the synthesis of MFI using TEP(5)A</i>	91
Table 3.31	<i>Fluoride route table of conditions for the synthesis of MFI using TEP(5)A</i>	91
Table 3.32	<i>Hydroxide route table of conditions for the synthesis of MFI using TEH(6)A</i>	93
Table 3.33	<i>Fluoride route table of conditions for the synthesis of MFI using TEH(6)A</i>	94
Table 3.34	<i>Hydroxide route table of conditions for the synthesis of MFI using TEH(7)A</i>	96
Table 3.35	<i>Fluoride route table of conditions for the synthesis of MFI using TEH(7)A</i>	96
Table 3.36	<i>Fluoride route table of conditions for the synthesis of MFI from TMH(6)A</i>	98
Table 3.37	<i>Hydroxide route table of conditions for the synthesis of MFI using DMDP(5)A</i>	100
Table 3.38	<i>Fluoride route table of conditions for the synthesis of MFI using DMDP(5)A</i>	100
Table 3.39	<i>Hydroxide route table of conditions for the synthesis of MFI using DEDBA</i>	102
Table 3.40	<i>Fluoride route table of conditions for the synthesis of MFI using DEDBA</i>	103
Table 3.41	<i>Hydroxide route table of conditions for the synthesis of MFI using DMDIBA</i>	104
Table 3.42	<i>Fluoride route table of conditions for the synthesis of MFI using DMDIBA</i>	105
Table 3.43	<i>Hydroxide route table of conditions for the synthesis of MFI using DEDIBA</i>	107
Table 3.44	<i>Fluoride route table of conditions for the synthesis of MFI using P(3)TBA</i>	109
Table 3.45	<i>Hydroxide route table of conditions for the synthesis of MFI using DP(3)DIP(3)A</i>	111
Table 3.46	<i>Fluoride route table of conditions for the synthesis of MFI using DPDIPA</i>	111
Table 4.1	<i>Table of chemical shift values for fluoride route TPA silicalite-1 sample using solid state NMR</i>	117
Table 4.2	<i>Table of chemical shift values for fluoride route MTP silicalite-1 sample using solid state NMR</i>	119
Table 4.3	<i>Table of chemical shift values for fluoride route ETP silicalite-1 sample using solid state NMR</i>	121
Table 4.4	<i>Table of chemical shift values for fluoride route BTP silicalite-1 sample using solid state NMR</i>	123
Table 4.5	<i>Table of chemical shift values for fluoride route P5TP3A silicalite-1 sample using solid state NMR</i>	125
Table 4.6	<i>Table showing progressive channel preference change upon ascending the n-alkyltripropylammonium silicalite-1 series</i>	126
Table 4.7	<i>Table of chemical shift values for fluoride route MTB silicalite-1 sample using solid state NMR</i>	128
Table 4.8	<i>Table of chemical shift values for fluoride route ETB silicalite-1 sample using solid state NMR</i>	130
Table 4.9	<i>Table of chemical shift values for fluoride route P5TBA silicalite-1 sample using solid state NMR</i>	131
Table 4.10	<i>Table showing change in channel preference upon ascending the n-alkyltributylammonium silicalite-1 series</i>	132
Table 4.11	<i>Table of ¹³C chemical shift assignments for the n-alkyltriethylammonium silicalite-1 series studied</i>	133
Table 4.12	<i>Table of ETPA and ETBA differences in parameters and determined structural qualities</i>	146
Table 5.1	<i>Table to summarise the changes observed in a monoclinic morphology of silicalite-1 as opposed to orthorhombic</i>	160
Table 5.2	<i>Table of experimental properties obtained from increasing alkyl chain length of n-alkyltributylammonium at varied temperatures</i>	166
Table 5.3	<i>Table of chemical shift resonances observed for silicalite-1 synthesised using varied structure directing agents</i>	172
Table 5.4	<i>Table of isotropic chemical shifts of silicalite-1 pentacoordinated fluoride</i>	177
Table 6.1	<i>Table of comparison of REDOR and DCP experimental requirements</i>	196
Table 6.2	<i>²⁹Si regions observed for known silicon peaks in ¹H-¹³C {²⁹Si} NMR spectrum</i>	200

Table 6.3	<i>Table comparing peak regions to reference framework silicon's and relative amount of dephasing observed</i>	200
Table 6.4	<i>Table of dipolar coupling constants and distances calculated for largest dephasing silicon peaks</i>	202
Table 6.5	<i>Table of dipolar coupling constants and distances calculated for medium dephased silicon peaks</i>	204

Glossary

TAA –	Tetralkylammonium
SDA –	Structure Directing Agent
NMR –	Nuclear Magnetic Resonance
PXRD –	Powder X-ray Diffraction
SS-NMR-	Solid State Nuclear Magnetic Resonance
TGA –	Thermogravimetric Analysis
SEM –	Scanning Electron Microscopy
ICP-OES -	Inductively Coupled Plasma Electron Spectroscopy
DLS -	Dynamic Light Scattering
IR -	Infrared Spectroscopy
AFM -	Atomic Force Microscopy
MOFs –	Metal Organic Framework
ZIFs –	Zeolite Imidazolate Frameworks
ICDD -	International Crystal Diffraction Database
REDOR-	Rotational Echo Double Resonance
DVT –	Direct Variable Temperature
CP -	Cross Polarisation
HPD -	High Power Decoupling
DCP -	Double Cross Polarisation
MAS -	Magic Angle Spinning
EDX-	Energy Dispersive X-ray
RF -	Radiofrequency
HPPD -	High Power Proton Decoupling
OSDA -	Organic Structure Directing Agent
TEA -	Tetraethylammonium
TMA -	Tetramethylammonium
CW -	Continuous Wave
EFG -	Electric Field Gradient
SSB -	Spinning Sideband Pattern

SOLA -	Solids Lineshape Analysis
SBU -	Secondary Building Unit
TPA -	Tetrapropylammonium
MTP -	N-methyltripropylammonium
ETP -	N-ethyltripropylammonium
BTPA -	N-butyltripropylammonium
P5TP3A -	N-pentyltripropylammonium
H6TPA -	N-hexyltripropylammonium
H7TPA -	N-heptyltripropylammonium
MTBA -	N-methyltributylammonium
ETBA -	N-ethyltributylammonium
P3TBA -	N-propyltributylammonium
TBA -	Tetrabutylammonium
P5TBA -	N-pentyltributylammonium
H6TBA -	N-hexyltributylammonium
TEP3A -	Triethyl-n-propylammonium
TEIP3A -	Triethyl-n-isopropylammonium
TEBA -	Triethyl-n-butylammonium
TEP5A -	Treiethyl-pentylammonium
TEH6A -	Triethyl-hexylammonium
TEH7A -	Triethyl-n-heptylammonium
TMH6A -	Trimethyl-n-hexylammonium
DMDP3A -	Dimethyldipropylammonium
DEDBA -	Diethyldibutylammonium
DEDIBA -	Diethyldiisobutylammonium
DP3DIP3A -	Dipropyldiisopropylammonium

1.0. Introduction

Zeolites are microporous crystalline framework structures made of inorganic materials and separated by distinct pores and channels. They can be synthesised in a laboratory as well as occurring naturally and were discovered in 1756 when Baron Axel Fredrik Cronstedt studied stilbite.¹ The Swedish mineralogist observed the loss of absorbed water upon heating stilbite, thereby coining the term zeolites from 'zeo' and 'lithos', boiling a stone.²

Almost 200 years later followed the first successful synthesis of a zeolite (despite a previous claim³). In 1948, Richard Barrer synthesised zeolite ZK-5 with KFI structure.⁴ He continued his work developing zeolite science^{5,6} whilst Robert Milton, of the Linde corporation concurrently started working on zeolite materials.^{7,8}

This pair, as well as numerous other contributors continued to develop a vast amount of new zeolite materials and have brought zeolite chemistry into an age whereby 231 zeolite framework types have been successfully established in the International Zeolite Association Structure Commission's Database of Zeolite Structures.⁹ The database associates each registered zeolite with a 3 letter code, representative of the framework type, where typical synthesised zeolite parameters are contained.

The zeolite structure consists of SiO_4 and $[\text{AlO}_4]^-$ tetrahedra connected by corner sharing of oxygen atoms to form large 3D structures.¹⁰ These 3D structures are able to accommodate water¹¹ or other ions¹² including sodium, potassium, calcium and magnesium^{13,14} within the framework pores and channels. This capability of zeolites is an asset and is responsible for the use of synthesised zeolites in many industrial applications.¹⁵

The nature of zeolites use in industry is predominantly twofold. The array of recurring pores and channels allow for their use as molecular sieves whereas acid forms of zeolites allow them to be used as catalysts. An example of the latter is the use of ZSM-5 zeolite as a additive in fluid

catalytic cracking (FCC) to make gasoline and hydro-cracking (HDC) to make middle distillates such as jet fuel.¹⁶

The discovery and eventual patenting of Zeolite ZSM-5 (Zeolite Socony Mobil five) (Figure 1.1) in 1972¹⁷ by Mobil Oil Company, provided perfect timing for the industrial requirement to eliminate the use of lead additives from gasoline therefore developing a method for extraction of octane from non-traditional sources.¹⁸

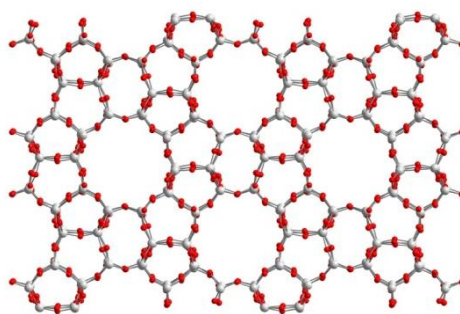


Figure 1.1 – Schematic diagram of MFI type zeolite framework structure

The discovery of the ZSM-5 zeolite opened the floodgates for the growth of zeolite and high-silica zeolite science. The synthesis of this new material required a combination of the following components at 125-175 °C for 5-9 days;



Where M = cation of n valence, W = aluminium or gallium, Y = silicon or germanium and $z = 0-40$

ZSM-5 has since become used in a variety of industrially important applications. The separation of xylenes in the petrochemical industry^{19,20,28,29} exemplifies its use as a molecular sieve whereas the ZSM-5 catalyst is also able to host the isomerisation of meta-xylene and para-xylene reaction within its pores and possesses a higher diffusion coefficient towards para-xylene, diffusing it out of the catalyst at a faster rate.²³

In addition to these important applications, zeolite ZSM-5 can also be used for the purification of gases,²⁴ catalysing epoxidation reactions,²⁵ the adsorption of non-polar hydrocarbons in water,²⁶ as shape selective catalysts,²⁷ in Langmuir-Blodgett films,²⁸ facilitating dehydrogenation of alcohol reactions²⁹ and in the absorption of alcohols.³⁰

Despite the importance and extensive research focus towards ZSM-5 chemistry, there still remain significant gaps within the knowledge of this particular zeolite, and zeolites in general. This lack of understanding occurs due to the complexity of the zeolites structural variations, as well as difficulties encompassed investigating the systems in situ to monitor nucleation, crystallisation and growth.³¹

The high silica analogue of ZSM-5 is silicalite-1. It maintains the MFI framework structure of ZSM-5 and replaces all aluminium content with silicon. Functionally, silicalite-1 preserves the molecular sieving properties, however replacement of +3 aluminium charge with +4 silicon, silicalite-1 loses the ion-exchange capabilities.³² Silicalite-1 can be synthesised efficiently,³³ at low temperatures (below 100 °C) and most importantly, is a highly ordered zeolite. It therefore provides a simpler structure in order to identify the effects of small changes in ZSM-5 and infer knowledge about zeolites in general.³⁴ For this reason it is one of the most widely hydrophobic zeolite materials investigated.³⁵

1.1. Zeolite Synthesis

The majority of zeolite syntheses require a silicon or aluminium source, mineralising agent, structure directing agent (SDA) and solvent.³⁶ These are discussed individually below, although it is important to note that there are many specific cases where zeolites have been successfully synthesised without these components.

1.1.1. Silicon Source

In order to form a zeolite framework structure, the appropriate silicon source is required. For example, silicon and aluminium sources are required for ZSM-5 synthesis but the replacement of

these elements by boron^{37,38}, titanium and other elements have been used to dope the structure and affect the product properties³⁹.

Only a silicon source is required for silicalite-1, the high-silica version of ZSM-5. The nature of the silicon source however has been proved to have an effect on the properties of the zeolite formed. The use of a fumed silica source SiO₂ (pyrogenic silica) can allow for the synthesis of larger crystals due to the slower rate of crystal growth. At this slow rate of crystal growth, larger crystals have time to form due to the low rate of nucleation. Comparatively, reaction mixtures using solution based silicon sources such as Ludox colloidal silica possess a larger number of nucleation sites and rapid growth leading to microcrystalline powders.⁴⁰

1.1.2. Mineralising agent

The traditional mineralising agent used in zeolite syntheses is a hydroxide based species with varying cations^{41,42} (e.g, sodium hydroxide). The role of the mineralising agent is multifunctional. The hydroxide ion is used to charge compensate the structure directing agent which leads to a large number of crystal defects.⁴³ This occurs from the creation of silanol nests^{44,43} within the structure, thereby limiting the long range crystalline order obtainable. A second role of the structure directing agent is to catalyse both the breaking and forming of Si-O-Si bonds^{45,46,47} (Si-O-Al bonds in ZSM-5), a process that the zeolite crystallisation rate is dependent upon.

Since 1978, the mineralising agent used in zeolite syntheses has tended towards the use of a fluoride based mineralising agent.⁴⁸ This new method by Flanigen and Patton involves the replacement of the traditional hydroxide species with fluoride ions, taking up all of its roles as a mineralising agent.⁴⁹ The use of the fluoride route reduces crystal defects⁵⁰ thereby increasing crystallinity,⁴³ increases crystal surface area⁵¹ therefore affecting catalytic properties of zeolites⁵¹ and has allowed the introduction of many new large pore zeolites.⁵² Additionally, the fluoride route synthesis affects the pH of the solution of reacting materials. The fluoride route changes the synthetic mixture from alkaline to a neutral pH and even a slightly acidic pH of 5 which effects the solubility of the silica source, eventually increasing the zeolite crystallisation rate.^{53,54}

A very interesting additional characteristic observed in silicalite-1^{55,56} and other high silica zeolites^{57,58}, synthesised using the fluoride route is the incorporation of the fluoride into the framework structure. This fluoride forms a covalent bond with a particular silicon⁴⁶ creating a pentacoordinated silicon unit $[\text{SiO}_{4/2}\text{F}]^-$.⁵⁹ This is demonstrated in Figure 1.2. and study of this interesting fluoride bond is developed further in Chapter 5.

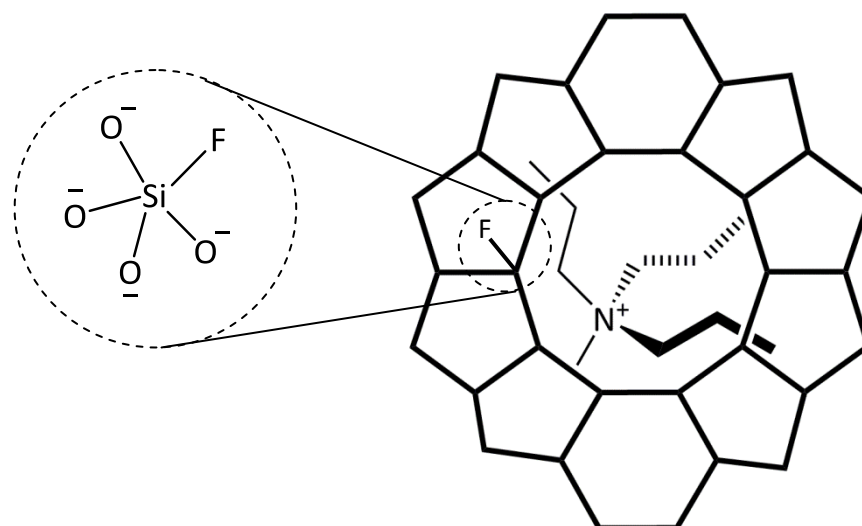


Figure 1.2 – Schematic diagram of (left) pentacoordinated silicon unit $[\text{SiO}_{4/2}\text{F}]^-$ and (right) MFI zeolite framework with occluded n-methyltributylammonium SDA

1.1.3. Structure Directing Agent

With the exception of SDA free syntheses,^{60,61,62} a structure directing agent is required for the synthesis of zeolite materials in order to direct the formation of the zeolite into a particular shape and size. Synthesis of the MFI framework typically uses an organic quaternary ammonium salt,^{63,64} although diamines and other organic molecules have also been successful.^{47,65,66} The cation species attracts silicon tetrahedra towards it during reaction, directing the framework structure around itself. For this reason, the structure directing agent has also been referred to as a template, or as having a templating effect. To add to the structural complexities of SDA use in zeolite syntheses, a whole variety of different structure directing agents have been able to synthesise the same zeolite material⁶⁶ whereas the same structure directing agents^{21,37} have also been able to synthesise many different zeolite materials,⁶⁷ under slightly different conditions.

In 1982, Price and co-workers⁶⁸ were able to structurally determine the position of the tetrapropylammonium cation within the zeolite pore in silicalite-1 using X-ray diffraction. This determination led to the conclusion that the tetrapropylammonium (TPA) cation sits in the zeolite pore with two propyl chains extended to each straight and sinusoidal channel,⁶⁹ as demonstrated (Figure 1.3).

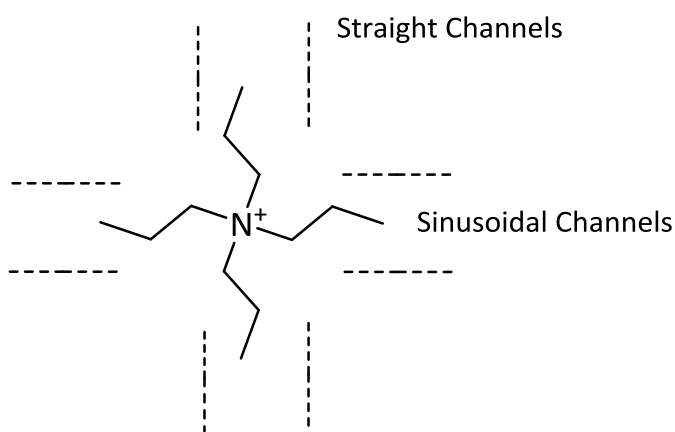


Figure 1.3 - Schematic representation of TPA silicalite-1 within the zeolite framework and the orientation of TPA within straight and sinusoidal channels (not to scale)

These observations led to the question of what properties are required in order to synthesise a particular zeolite, and at what point in-between does it become unfavourable to synthesise a particular zeolite, forming an alternate one instead.

In 1998, Zones and Nakagawa conducted a comparative study into the relationship between the SDA used in synthesis and the zeolite formed.⁷⁰ Their study focussed on four structure directing agents; tetraalkylammonium with alkyl chains varying from methyl to butyl. They found they could synthesise a variety of different zeolites, where a carbon to nitrogen (C:N) ratio of 9-13 yielded MFI zeolite. At the time, they deduced that upon increasing the C:N ratio, fewer zeolite products were obtainable. However, increasing the C:N ratio of an SDA also increases the hydrophobicity of the molecule^{71,72} such that it can be difficult to obtain zeolites using large SDA's without the subsequent addition of another cation.⁷³ Therein lies the introduction of the use of diamines in

zeolite syntheses.^{74,75} Increase of the SDA size used to tetrabutylammonium synthesises silicalite-2 zeolite which is the high silica analogue of ZSM-11 and structurally related to silicalite-1.⁷⁶

We now know that reaction temperature also plays a part in the synthesis of zeolites using large hydrophobic structure directing agents. Wu et al⁷⁷ managed to successfully synthesise ZSM-5 zeolites using the highly hydrophobic and sterically unfavourable CTBA (cetyltrimethylammonium bromide) SDA by increasing the temperature of reaction. These ZSM-5 samples were therefore able to be synthesised using an SDA with 19:1 C:N whereby each SDA molecule filled two pores in the straight channel thereby reducing the quantity of SDA required.

It is also known that larger SDA's require more reaction time to crystallise zeolites. This is due to the increase in hydrophobic character that weakens the interactions with the silicon dioxide forming network,⁷⁸ reducing the crystallisation rate. The use of an SDA that is too hydrophilic however does not lead to the essential interactions with silica during reaction,⁶⁶ meaning a medium hydrophobic SDA is preferential⁷⁹ to form the MFI framework structure.

1.1.4. Solvent System

In a typical hydrothermal zeolite synthesis, a large amount of water is usually required in order for silicon species to dissolve and form the required framework structure⁵³. The amount of water present however can slightly modify the SDAs role and allow very different pore architectures to be created using the same SDA.⁴³

Other solvents can also successfully synthesise zeolites. The solvothermal method⁸⁰ uses solvents such as ethylene glycol, diethylene, triethylene or tetraethylene⁸¹ whereby the change in solvent used is capable of changing the crystal shapes formed. The dry conversion method^{82,83} also allows for the synthesis of zeolites without using any solvent however it does involve the requirement of various humid environments.

1.2. Methods of Synthesising MFI Zeolites

Many different methods have been developed to crystallise zeolite materials but none as popular a choice as hydrothermal synthesis. The hydrothermal method^{97,98} involves the heating of a reaction mixture in a stainless steel autoclave where the high mobility of supercritical water (>373K)⁸⁶ and high pressure allow the reaction to occur. The autoclave can build up to a contained (autogeneous) high pressure and sustain applied high temperatures in order to allow crystal growth.⁸⁷

Despite the hydrothermal method enabling the possibility of high quality large crystals,⁸⁸ it also has negative aspects. The synthesis of materials cannot be seen to be monitored without the subsequent removing from reaction heat, quenching the reaction by opening the autoclave, and subsequently returning to reaction conditions. Clearly this disturbs the synthesis of the material inferring it is not effective for any comparative synthetic studies. It is possible to overcome these issues by in-situ x-ray synchrotron studies. These studies however require building special thin-walled autoclaves in order to be penetrated by the radiation.⁸⁹

The use of low-cost small polypropylene bottles and the dense-gel method^{34,103} on the other hand allows for the viewing of the sample in-situ without the need to open the vessel and quench the reaction.⁹¹ It also has the potential to allow for many samples to be placed under the same conditions and simply remove one at the required time which is significantly less disruptive. This has a huge advantage over systematic studies^{87,88} whereby the reaction has been quenched and an amount removed that is unlikely to include a uniform amount of reagents,⁹⁴ thereby affecting the remainder of the reaction mixture.³¹

This cheap and low temperature dense-gel method additionally allows observations of the biphasic mixture through the clear bottle. It allows identification of when sufficient solid product has increased in density and dropped to the bottom of the bottle.

The dense-gel method and hydrothermal method maintain overwhelming advantages over other available techniques. Sol-gel syntheses can successfully synthesise MFI zeolites⁹⁵ but require additional time in order to do so. The microwave method is a fast method of synthesising ZSM-5 materials^{47,81} but has not yet overcome the degradation of SDA's in the process.⁹⁶ The use of co-condensation methods allow MFI materials to be synthesised,⁹⁷ however are riddled with problems including the inability to calcine the product and excessive disorder in products formed.⁹⁸

1.3. MFI Framework Structure

The framework structure of MFI was first determined in 1981 by Olsen and co-workers.⁹⁹ At room temperature, MFI materials are orthorhombic and have a Pnma space group¹⁰⁰ however below room temperature they undergo a reversible phase change from orthorhombic to monoclinic.¹⁰¹

They have unit cell parameters of $a = 20.07 \text{ \AA}$, $b = 19.92 \text{ \AA}$ and $c = 13.42 \text{ \AA}$ ⁹⁹ and a 5-7 \AA ¹⁰² pore diameter making them a medium pore zeolite.

The MFI structure (Figure 1.4) consists of a series of pentasil units linked by mirror symmetry and is characterized by two perpendicular 10 member ring

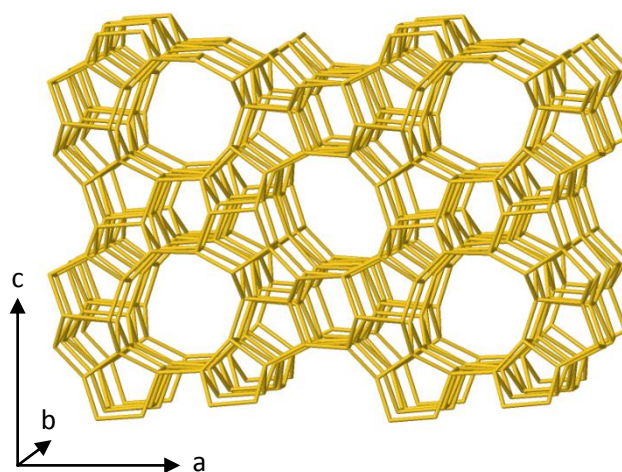


Figure 1.4 – Schematic diagram of MFI zeolite structure

channels;^{99,103} the straight channel parallel to the [010] and the sinusoidal channel parallel to [100].¹⁰⁴

The size and shape of the commonly used tetrapropylammonium cations for MFI syntheses are tightly fitted to the pore and channel size and shape¹⁰⁵ whereby the cation sits in the zeolite pore with the propyl chains facing the channel openings.¹⁰⁶ The use of different structure directing agents however can have a different orientation within the pore, dependant on the location of substituent's to facing and entering the difference size channel openings.⁵⁶ The sinusoidal channel

[100] has an elliptical pore opening size of 5.1 Å x 5.7 Å whereas the straight channel [010] has a large, circular pore opening of 5.4 Å x 5.6 Å.¹⁰⁷ The zeolite tends to form in the most sterically favourable manner⁵⁶ whereby more bulky substitutes tend to face the sinusoidal channel. This theory will be developed in Chapter 4 where the orientation of series of SDA's are identified using solid state NMR characterisation techniques.

Zeolite frameworks are made up of secondary building units (SBU's). The silicalite-1 framework structure is made up of the following 23 SBU's, established by Knight and co-workers from the use of ²⁹Si NMR¹⁰⁸ (Figure 1.5).

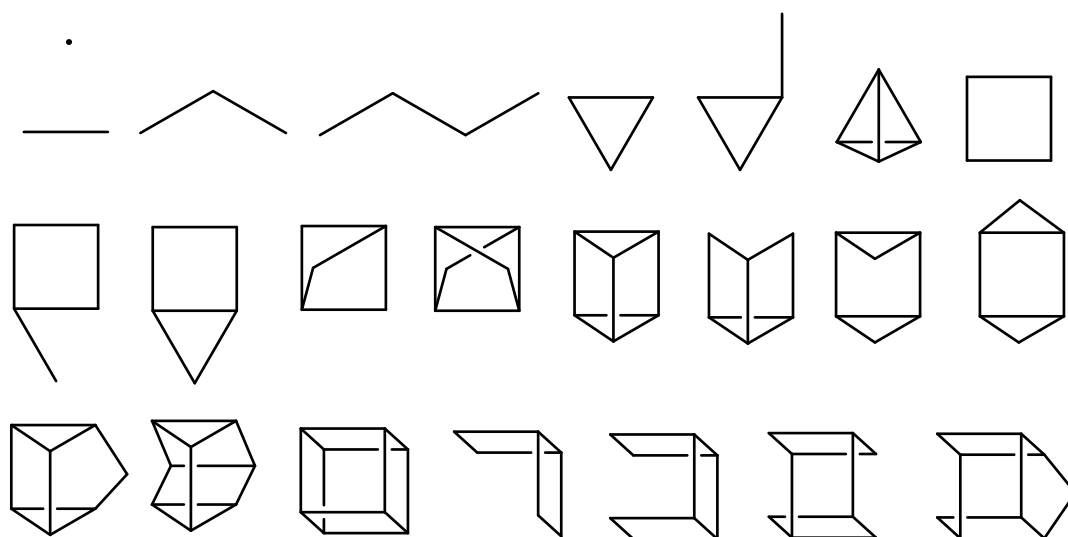


Figure 1.5 – Schematic diagram of the 23 observed SBU's by Knight and Kinrade¹⁰⁸ in TPA silicalite-1

1.4. MFI Structural Formation

Determining the mechanism of zeolite formation is a complex task that has seen an overwhelming number of studies throughout the last 30 years, yet still remains elusive.¹⁰⁹ Despite extensive attempts, there is no universal agreement of the mechanism of zeolite formation³¹ due to the complicated number of contributing factors affecting the nucleation and growth of zeolites¹¹⁰. For example, the presence or absence of mineralisers, chemical composition, temperature, time and even the degree of autoclave filling can all have an effect on the growth conditions of crystalline materials such as zeolites.⁵³

In addition to these factors is the ability of the zeolites to grow in different ways, depending on the synthetic conditions.¹¹¹ With a growing number of zeolites being established every year and increasing use in a variety of applications, the challenge of zeolite chemists is to deduce these mechanisms in order to custom-fit current structures as well as develop new ones.¹¹² Despite a lack of understanding of the specific mechanism and how varying factors affect it, some overarching features throughout the growth have been developed over the years.

These features include the general order of zeolite formation through a nucleation period and rapid crystallisation of the zeolite. This occurs due to eventual dissolving of sufficient silica in the solvent to reach the critical silica concentration (CAC) in order for forward reactions to win over equilibrium and initiate crystallisation.¹¹³ This has been demonstrated in typical sigmoidal shape curve obtained for crystallisation studies, as shown in Figure 1.6.¹¹⁴

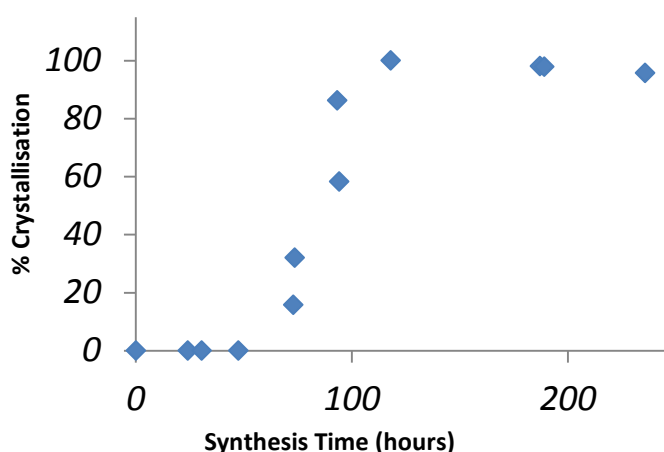


Figure 1.6 – Sigmoidal (S) shape curve of silicalite-1 zeolite growth

The introduction of clear solution zeolite syntheses has brought about the ability for small zeolite crystals to be synthesised using more efficient, lower temperature reactions than is traditionally found by using the hydrothermal method. These materials have been utilised in order to study information about zeolite nucleation and growth however nucleation studies of zeolite syntheses typically face many difficulties. These include extraction of species required at the desired time and finding methods to study the x-ray amorphous materials. The nucleation start point in zeolite synthesis has been the subject of a large debate since the controversial publications of Kirschhock and co-workers in the 90's,^{115,116,117} amongst others.^{112,118,119} They claimed the

existence of so-called room temperature silicate structures as a part of a nanoblock/nanoslab theory, based on previous literature.^{120,121} This work however lacked sufficient proof that these silicate species end up in the zeolite material as opposed to being spectator species and lacked silicon enriched materials¹⁰⁸ therefore was overwhelmingly disputed.^{122,123,124,125,126}

A general mechanism for the growth of ZSM-5 zeolite using TPA as an SDA can be found in the 1994 work by Burkett and Davis (Figure 1.7).¹²⁷

Burkett and Davis support previous work by Gies and Marler¹²⁸ within their mechanism of formation suggesting the interaction of non-covalent van der Waals or hydrophobic interactions occur between organic SDA's and silicate species in a organic-mediated zeolite synthesis.

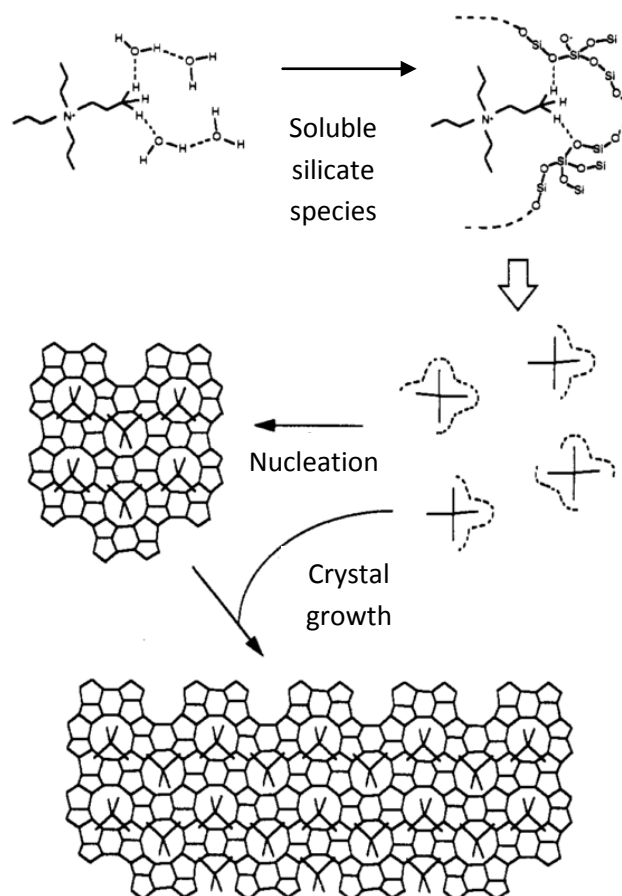


Figure 1.7 – Burkett and Davis proposed mechanism for ZSM-5 formation using tetrapropylammonium SDA¹²⁷

1.5. Characterisation Techniques

The characterisation of solid state materials such as zeolites primarily uses X-ray powder diffraction (PXRD). Not only can the fast, simple technique determine products, by-products and sample purity, it is also able to determine information such as unit cell parameters, volumes and framework types of crystalline materials by comparison to the International Centre for Diffraction Data (ICDD)¹²⁹ database of known materials.

XRD is a long-range order technique and requires a sample to be crystalline for determination of information. As such, during a zeolite nucleation and crystallisation, it is not able to determine any information about the structure while the sample remains X-ray amorphous or until sufficient long-range order has been established.

Due to these difficulties, zeolite scientists have sought complementary techniques to use with the XRD technique for a more rounded characterisation. Depending on the requirements of the particular sample being studied, the techniques used include, X-ray fluorescence¹³⁰, Infra-red Spectroscopy (IR)¹²³, Thermogravimetric Analysis (TGA)¹³¹, Single Crystal X-ray Diffraction⁸⁷, Solid state NMR (SS-NMR)¹³² and others¹³³.

The use of solid-state NMR as a complementary technique¹³⁴ to studying zeolites allows for a comprehensive study of the material on both long and short range order. It is able to be used as a probe for the organic components that x-ray diffraction cannot detect by simple NMR experiments and also allows the use of complex experiments to determine further information about bond distances in the inorganic-organic composite species. The difficulties observed in using single crystal XRD and the subsequent complementary use of solid-state NMR combined with XRD are discussed further in Chapter 5.

1.6. Aims of the Work

“Developing a molecular level description of high-silica zeolite nucleation and crystallisation is one of the most significant unresolved problems in zeolite science.”¹³⁵ In order to contribute to attempts of understanding more about zeolite structure and growth, the highly ordered silicalite-1 zeolite has been synthesised using the fluoride route and a variety of systematic structure directing agents. The determination of variable structure directing agent’s orientation within a highly ordered zeolite should contribute to the knowledge base about preferential orientations during crystal growth.

The complementary use of X-ray diffraction and solid state NMR has been used to study these materials in order to fulfil the following aims;

1. The successful synthesis of crystalline silicalite-1 materials using slight variants on the common SDA, tetrapropylammonium and confirmed by X-ray diffraction characterisation.
2. After confirmation of crystalline silicalite-1 materials, the use of solid state NMR techniques to probe the organic structure directing agent occluded within the zeolite framework. ^{13}C and ^{14}N solid state NMR experiments provide the opportunity to study the local structure and orientation of these organic molecules within the zeolite framework.
3. Study of the local structure of obtained inorganic framework materials to probe the nature of the $[\text{SiO}_{4/2}\text{F}]^-$ units from variable structure directing agents, by ^{29}Si and ^{19}F solid state NMR.
4. Determination of distance between the inorganic zeolite and occluded structure directing agent in labelled ^{13}C F-MTBA silicalite-1 by the use of a more complex, 2D NMR experiment.

1.7. References

- 1 A. Cronstedt, *Akad. Handl. Stock.*, 1756, **18**, 120.
- 2 T. M. Wortal, *Some Applications Of Zeolites Organic Chemistry*, Delft University Press, 1979.
- 3 H. St Claire Deville, *Comptes Rendus l'Académie des Sci.*, 1862, **54**, 324.
- 4 R. M. Barrer, *J. Chem. Soc.*, 1950, 1926.
- 5 R. Barrer, L. Hinds and E. White, *J. Am. Chem. Soc.*, 1953, 1466.
- 6 R. Aiello and R. M. Barrer, *J. Chem. Soc. A Inorganic, Phys. Theor.*, 1970, 1470.
- 7 U.S. Patent 2 822 243, 1959.
- 8 U.S. 3 008 803, 1961.
- 9 C. Baerlocher and L. B. McCusker, *Database Zeolite Struct.*
- 10 S. M. Woodley and R. Catlow, *Nat. Mater.*, 2008, **7**, 937–46.
- 11 S. Sircar, T. C. Golden and M. B. Rao, *Carbon N. Y.*, 1996, **34**, 1–12.
- 12 R. M. Barrer and W. M. Meier, *J. Chem. Soc.*, 1958, 299.
- 13 R. M. Barrer, *J. Chem. Soc.*, 1948, **2**, 127–132.
- 14 M. A. Jama and H. Yücel, *Sep. Sci. Technol.*, 1989, **24**, 1393–1416.
- 15 C. S. Cundy and P. Cox, *Chem. Rev.*, 2003, **103**, 663–701.
- 16 W. Vermeiren and J. P. Gilson, *Top. Catal.*, 2009, **52**, 1131–1161.
- 17 U.S. Patent 3 702 886, 1972.
- 18 T. F. Degan, G. K. Chitnis and P. H. Schipper, *Microporous Mesoporous Mater.*, 2000, **35–36**, 245.
- 19 G. Xomeritakis, Z. Lai and M. Tsapatsis, *Ind. Eng. Chem. Res.*, 2001, **40**, 544–552.
- 20 H. Sakai, T. Tomita and T. Takahashi, *Sep. Purif. Technol.*, 2001, **25**, 297–306.
- 21 J. Na, G. Liu, T. Zhou, G. Ding, S. Hu and L. Wang, *Catal. Letters*, 2013, **143**, 267–275.
- 22 X. J. Fan, F. Q. Zhong, G. Yu, J. G. Li and C. J. Sung, *J. Propuls. Power*, 2009, **25**, 1226–1232.
- 23 K. A. O. Santos, D. Neto, M. C. P. A. ; Moura, C. Ab and T. N. Dantas, 2011, **3**, 255–268.
- 24 J. Stelzer, M. Paulus, M. Hunger and J. Weitkamp, *Microporous Mesoporous Mater.*, 1998, **22**, 1–8.
- 25 T. Kim, B. Kwak and W. Ahn, *Mol. Sieves From Basic Res. To Ind. Appl.*, 2005, **158**, 1851–1858.
- 26 A. Basile and F. Gallucci, *Membranes for membrane reactors: preparation optimization and selection*, Wiley, 2011.
- 27 N. Kamiya, W. Iwama, T. Kudo, T. Nasuno, S. Fujiyama, K. Nishi and Y. Yokomori, *Acta Crystallogr. B.*, 2011, **67**, 508–15.
- 28 R. Xu, *From Zeolites to Porous MOF Materials - the 40th Anniversary of International*

- Zeolite Conference, 2 Vol Set, 1st Edition*, Elsevier, 1st Editio., 2007.
- 29 Y. Matsumura, *J. Catal.*, 1990, **122**, 352–361.
- 30 W. Zhu, J. M. van de Graaf, L. J. P. van den Broeke, F. Kapteijn and J. A. Moulijn, *Ind. Eng. Chem. Res.*, 1998, **37**, 1934–1942.
- 31 M. E. Davis and R. F. Lobo, *Chem. Mater.*, 1992, **4**, 756–768.
- 32 S. Wilson, B. M. Lok, C. A. Messina, T. R. Cannan and E. M. Flanigaen, *Intrazeolite Chem.*, 1982, **104**, 1146–1147.
- 33 C. A. Fyfe, R. J. Darton, H. Mowatt and Z. S. Lin, *Microporous Mesoporous Mater.*, 2011, **144**, 57–66.
- 34 E. Dib, A. Gimenez, T. Mineva and B. Alonso, *Dalt. Trans.*, 2015, **44**, 16680–16683.
- 35 K. Zhang, R. P. Lively, J. D. Noel, M. E. Dose, B. A. McCool, R. R. Chance and W. J. Koros, *Langmuir*, 2012, **28**, 8664–8673.
- 36 T. J. Daou, J. Dhainaut, A. Chappaz, N. Bats, B. Harbuzaru, H. Chaumeil, A. Defoin, L. Rouleau and J. Patarin, *Oil Gas Sci. Technol.*, 2014, **70**, 447–454.
- 37 G. S. Lee, Y. Nakagawa, S. Hwang, E. Davis, P. Wagner, L. Beck, S. I. Zones and M. E. Davis, *J. Am. Chem. Soc.*, 2002, **1**, 7024–7034.
- 38 H. Kessler, J. M. Chezeau, J. L. Guth, H. Strub and G. Coudurier, *Zeolites*, 1987, **7**, 360–366.
- 39 H. Zhang, Y. Liu, Z. Jiao, M. He and P. Wu, *Ind. Eng. Chem. Reserch*, 2009, **48**, 4334–4339.
- 40 Z. Lethbridge, J. Williams, R. Walton, K. Evans and C. Smith, *Microporous Mesoporous Mater.*, 2005, **79**, 339–352.
- 41 R. Aiello, F. Crea, E. Nigro, F. Testa, R. Mostowicz, a. Fonseca and J. B. Nagy, *Microporous Mesoporous Mater.*, 1999, **28**, 241–259.
- 42 L. Mafra, J. A. Vidal-Moya and T. Blasco, *Structural Characterization of Zeolites by Advanced Solid State NMR Spectroscopic Methods*, Elsevier Ltd, Burlington, 2012, vol. 77.
- 43 M. Camblor, L. Villaescusa and M. Diaz-Cabanas, *Top. Catal.*, 1999, **9**, 59–76.
- 44 J. M. Chezeau, L. Delmotte, J. L. Guth and Z. Gabelica, *Zeolites*, 1991, **11**, 598–606.
- 45 L. A. Villaescusa, W. Zhou, R. Morris, P. A. Barrett and D. Valencia, *J. Mater. Chem.*, 2004, 1982–1987.
- 46 C. A. Fyfe, D. H. Brouwer, A. R. Lewis and J. Chezeau, *J. Am. Chem. Soc.*, 2001, **123**, 6882–6891.
- 47 J. W. Jun, I. Ahmed, C.-U. Kim, K.-E. Jeong, S.-Y. Jeong and S. H. Jhung, *Catal. TODAY*, 2014, **232**, 108–113.
- 48 US PATENT 4073865, 1978.
- 49 S. I. Zones, R. J. Darton, R. Morris and S. Hwang, *J. Phys. Chem. B*, 2005, **109**, 652–61.
- 50 R. J. Darton, D. H. Brouwer, C. A. Fyfe, L. A. Villaescusa and R. E. Morris, *Chem. Mater.*, 2004, **16**, 600–603.

- 51 B. Louis and L. Kiwi-Minsker, *Microporous Mesoporous Mater.*, 2004, **74**, 171–178.
- 52 H. Jon, B. Lu, Y. Oumi, K. Itabashi and T. Sano, *Microporous Mesoporous Mater.*, 2006, **89**, 88–95.
- 53 R. M. Barrer, *Discuss. Faraday Soc.*, 1949, **5**, 326–337.
- 54 S. G. Fegan and B. M. Lowe, 1986, 785–799.
- 55 S. L. Brace, P. Wormald and R. J. Darton, *Phys. Chem. Chem. Phys.*, 2015, **17**, 11950–11953.
- 56 E. Dib, A. Gimenez, T. Mineva and B. Alonso, *Dalt. Trans.*, 2015, **44**, 16680–16683.
- 57 H. Koller, A. Wölker, L. A. Villaescusa, M. J. Díaz-Cabañas, S. Valencia and M. A. Camblor, *J. Am. Chem. Soc.*, 1999, **121**, 3368–3376.
- 58 M. P. Attfield, C. R. A. Catlow and A. A. Sokol, *Chem. Mater.*, 2001, **13**, 4708–4713.
- 59 H. Koller, A. Wolker, H. Eckert, C. Panz and P. Behrens, *Angew. Chemie - Int. Ed.*, 1997, **36**, 2823–2825.
- 60 W. Han, Y. Jia, N. Yao, W. Yang, M. He and G. Xiong, *J. Sol-Gel Sci. Technol.*, 2007, **43**, 205–211.
- 61 M. M. Mostafa, K. N. Rao, H. S. Harun, S. N. Basahel and I. S. A. El-Maksod, *Ceram. Int.*, 2013, **39**, 683–689.
- 62 M. Zhu, Z. Lu, I. Kumakiri, K. Tanaka, X. Chen and H. Kita, *J. Memb. Sci.*, 2012, **415–416**, 57–65.
- 63 R. McMullen and G. Jeffrey, *J. Chem. Phys.*, 1959, **31**, 1231.
- 64 R. M. Barrer and P. J. Denny, *J. Chem. Soc.*, 1961, 971–982.
- 65 A. Tuel, *Zeolites*, 1996, **16**, 108–117.
- 66 K. Tsuji and M. E. Davis, *Microporous Mater.*, 1997, **11**, 53–64.
- 67 S. I. Zones and A. W. Burton, *J. Mater. Chem.*, 2005, **15**, 4215–4223.
- 68 G. D. Price, J. J. Pluth, J. V. Smith, J. M. Bennett and R. L. Patton, *J. Am. Chem. Soc.*, 1982, **104**, 5971–5977.
- 69 C. Baerlocher and W. Meier, *Helv. Chim. Acta*, 1969, **52**, 1853.
- 70 S. I. Zones, Y. Nakagawa, G. S. Lee, C. Y. Chen and L. T. Yuen, *Microporous Mesoporous Mater.*, 1998, **21**, 199–211.
- 71 W. I. Babiaczyk, S. Bonella, L. Guidoni and G. Ciccotti, *J. Phys. Chem. B*, 2010, **114**, 15018–28.
- 72 W. M. Hendricks, A. T. Bell and C. J. Radke, *J. Phys. Chem.*, 1991, **95**, 9513–9518.
- 73 Y. Kubota, M. M. Helmkamp, S. I. Zones and M. E. Davis, *Microporous Mater.*, 1996, **6**, 213–229.
- 74 D. A. Woodcock, P. Lightfoot, L. A. Villaescusa, M.-J. Díaz-Cabañas, M. A. Camblor and D. Engberg, *Chem. Mater.*, 1999, **11**, 2508–2514.
- 75 M. Díaz-Cabañas and P. Barrett, *Chem. Commun.*, 1998, 1881–1882.

- 76 E. D. Burchart, H. Van Koningsveld and B. Van de Graaf, *Microporous Mater.*, 1997, **8**, 215–222.
- 77 D. Xu, J. Feng and S. Che, *Dalt. Trans*, 2014, **43**, 3612–3617.
- 78 J. D. Epping and B. F. Chmelka, *Curr. Opin. Colloid Interface Sci.*, 2006, **11**, 81–117.
- 79 Y. Kubota, M. M. Helmkamp, S. I. Zones and M. E. Davis, *Microporous Mater.*, 1996, **6**, 213–229.
- 80 M. L. Occelli and H. Robson, *Zeolite Synthesis*, American Chemical Society, 1989.
- 81 X. Chen, W. Yan, X. Cao, J. Yu and R. Xu, *Microporous Mesoporous Mater.*, 2009, **119**, 217–222.
- 82 S. Goergen, M. A. Saada, M. Soulard, L. Rouleau and J. Patarin, *J. Porous Mater.*, 2010, **17**, 635–641.
- 83 S. P. Naik, A. S. T. Chiang and R. W. Thompson, *J. Phys. Chem. B*, 2003, **107**, 7006–7014.
- 84 K. Iwakai, T. Tago, H. Konno, Y. Nakasaka and T. Masuda, *Microporous Mesoporous Mater.*, 2011, **141**, 167–174.
- 85 Y. Kubota, H. Maekawa, S. Miyata, T. Tatsumi and Y. Sugi, *Microporous Mesoporous Mater.*, 2007, **101**, 115–126.
- 86 A. K. Cheetham and P. Day, *Solid State Chemistry: Techniques, Volume 1*, Clarendon Press, 1987.
- 87 J. Kornatowski, *Zeolites*, 1988, **8**, 77–78.
- 88 T. Kadono, M. Tajima, T. Shiomura, N. Imawaka, S. Noda, T. Kubota and Y. Okamoto, *Microporous Mesoporous Mater.*, 2008, **115**, 454–460.
- 89 R. I. Walton and D. O’Hare, *Chem. Commun.*, 2000, 2283–2291.
- 90 C. A. Fyfe, Z. S. Lin, C. Tong and R. J. Darton, *Microporous Mesoporous Mater.*, 2012, **150**, 7–13.
- 91 S. D. Kinrade, C. T. G. Knight, D. L. Pole and R. T. Syvitski, *Inorg. Chem.*, 1998, **37**, 4278–4283.
- 92 C. D. Chang and A. T. Bell, *Catal. Letters*, 1991, **8**, 305–316.
- 93 S. A. Axon and J. Klinowski, *J. Chem. Soc., Faraday Trans.*, 1993, **89**, 4245–4248.
- 94 B. M. Weckhuysen, *Chem. Soc. Rev.*, 2010, **39**, 4557.
- 95 S. Kumar, R. L. Penn and M. Tsapatsis, *Microporous Mesoporous Mater.*, 2011, **144**, 74–81.
- 96 Y. Li and W. Yang, *J. Memb. Sci.*, 2008, **316**, 3–17.
- 97 K.-L. Wong, M. El Roz, L. Tosheva, J.-M. Goupil and S. Mintova, *Catal. Today*, 2013, **204**, 66–72.
- 98 G. Rios, G. Centi and N. Kanellopoulos, *Nanoporous materials for energy and the environment*, CRC Press, 2012.
- 99 D. Olsen, G. Kokotailo, S. Lawton and W. Meier, *J. Phys. Chem.*, 1981, **85**, 2238–2243.

- 100 B. F. Mentzen, *Mater. Res. Bull.*, 1992, **27**, 831–838.
- 101 D. G. Hay and H. Jaeger, *J. Chem. Soc. Chem. Commun.*, 1984, 1433.
- 102 S. P. Bates, W. J. M. van Well, R. A. van Santen and B. Smit, *J. Am. Chem. Soc.*, 1996, **118**, 6753–6759.
- 103 B. F. Mentzen, G. Bergeret, H. Emerich and H. Weber, *J. Phys. Chem. B*, 2006, **110**, 13741–52.
- 104 O. Geier, S. Vasenkov, E. Lehmann, J. Ka, U. Schemmert and R. A. Rakoczy, *J. Phys. Chem. B*, 2001, **42**, 10217–10222.
- 105 S. Senapati, J. Zimdars, J. Ren and H. Koller, *J. Mater. Chem. A*, 2014, **2**, 10470–10484.
- 106 H. Van Koningsveld, H. Van Bekkum and J. C. Jansen, *Acta Crystallogr. Sect. B*, 1987, **43**, 127–132.
- 107 P. Voogd, H. Van Bekkum, D. Shavit and H. W. Kouwenhoven, *J. Chem. Soc. Faraday Trans.*, 1991, **87**, 3575–3580.
- 108 C. T. G. Knight, S. D. Kinrade, C. E. A. Kirschhock, R. Ravishankar, F. Verspeurt, P. J. Grobet, P. A. Jacobs and J. A. Martens, *J. Phys. Chem. B*, 2002, **106**, 3329–3334.
- 109 V. Nikolakis, E. Kokkoli, M. Tirrell, M. Tsapatsis and D. G. Vlachos, *Chem. Mater.*, 2000, **12**, 845–853.
- 110 M. L. Occelli and H. Robson, *Zeolite Synthesis*, American Chemical Society, 1989.
- 111 N. Ren, B. Subotić, J. Bronić, Y. Tang, M. Dutour Sikirić, T. Mišić, V. Svetličić, S. Bosnar and T. Antonić Jelić, *Chem. Mater.*, 2012, **24**, 1726–1737.
- 112 S. Mintova, N. H. Olson, J. Senker and T. Bein, *Angew. Chemie Int. Ed.*, 2002, **41**, 2558–61.
- 113 J. D. Rimer, O. Trofymuk, R. F. Lobo, A. Navrotsky and D. G. Vlachos, *J. Phys. Chem. C*, 2008, **38**, 14754–14761.
- 114 R. Kumar, P. Mukherjee, R. Pandey, P. Rajmohan and A. Bhaumik, *Microporous Mesoporous Mater.*, 1998, **22**, 23–31.
- 115 C. E. A. Kirschhock, R. Ravishankar, F. Verspeurt, P. J. Grobet, P. A. Jacobs and J. A. Martens, *J. Phys. Chem. B*, 1999, **103**, 4965–4971.
- 116 C. E. A. Kirschhock, R. Ravishankar, F. Verspeurt, P. J. Grobet, P. A. Jacobs and J. A. Martens, *J. Phys. Chem. B*, 2002, **12**, 3333–3334.
- 117 C. E. A. Kirschhock, S. P. B. Kremer, P. J. Grobet, P. A. Jacobs and J. A. Martens, *J. Phys. Chem. B*, 2002, **106**, 4897–4900.
- 118 D. P. Petry, M. Haouas, S. C. C. Wong, A. Aerts, C. E. A. Kirschhock, J. a. Martens, S. J. Gaskell, M. W. Anderson and F. Taulelle, *J. Phys. Chem. C*, 2009, **113**, 20827–20836.
- 119 R. Ravishankar, C. E. A. Kirschhock, P. P. Knops-Gerrits, E. J. P. Feijen, P. J. Grobet, P. Vanoppen, F. C. De Schryver, G. Miehe, H. Fuess, B. J. Schoeman, P. Jacobs and J. Martens, *J. Phys. Chem. B*, 1999, **103**, 4960–4964.

- 120 B. J. Schoeman, *Zeolites*, 1997, **18**, 97–105.
- 121 P. de Moor, T. Beelen, R. van Santen, L. Beck and M. Davis, *J. Phys. Chem. B*, 2000, **104**, 7600–7611.
- 122 C. Knight, R. Syvitski and S. Kinrade, *Zeolites A Refin. Tool Des. Catal. Sites*, 1995, **97**, 483–488.
- 123 C. T. G. Knight, J. Wang and S. D. Kinrade, *Phys. Chem. Chem. Phys.*, 2006, **8**, 3099–103.
- 124 C. H. Cheng and D. F. Shantz, *J. Phys. Chem. B*, 2006, **110**, 313–318.
- 125 H. Ramanan, E. Kokkoli and M. Tsapatsis, *Angew. Chemie - Int. Ed.*, 2004, **43**, 4558–4561.
- 126 C. A. Fyfe, R. J. Darton, C. Schneider and F. Scheffler, *J. Phys. Chem. C*, 2008, **112**, 80–88.
- 127 S. L. Burkett and M. E. Davis, *Chem. Mater.*, 1995, **7**, 1453–1463.
- 128 H. Gies and B. Marler, *Zeolites*, 1992, **12**, 42–49.
- 129 International Center for Diffraction Data, *PDF-4+ 2016*, .
- 130 J. Klinowski, *Chem. Rev.*, 1991, **91**, 1459–1479.
- 131 J. B. Nagy, Z. Gabelica and E. G. Derouane, *Zeolites*, 1983, **3**, 43–49.
- 132 S. D. Kinrade, C. T. G. Knight, D. L. Pole and R. T. Syvitski, *Inorg. Chem.*, 1998, **37**, 4272–4277.
- 133 N. Ren, B. Subotic, J. Bronic, Y. Tang, M. D. Sikiric, T. Mis, V. Svetlic, S. Bosnar and T. A. Jelic, 2012.
- 134 R. Morris, *Kristallography*, 2007, **1**, 33–38.
- 135 L. Karwacki, M. H. F. Kox, D. a M. de Winter, M. R. Drury, J. D. Meeldijk, E. Stavitski, W. Schmidt, M. Mertens, P. Cubillas, N. John, A. Chan, N. Kahn, S. R. Bare, M. Anderson, J. Kornatowski and B. M. Weckhuysen, *Nat. Mater.*, 2009, **8**, 959–65.

2.0. Methodology

2.1. Powder X-ray Diffraction (PXRD) Theory

Powder X-ray diffraction (PXRD), more commonly referred to as XRD has become the most common method used to study inorganic materials due to its relatively quick¹ and easy determination of structural information. An XRD experiment is a non-invasive technique² that is conducted by creating a stream of electrons from a heated filament to bombard a metal target which is usually copper or molybdenum. Sufficiently high energy incident electrons are capable of ionising electrons in the 1s sub-shell of the metal which create short term vacancies. These are filled with 2s electrons dropping down a shell which in turn, emits an multiple X-rays of the metal energy.³ This energy can be used to calculate the X-ray wavelength as such:

$$\lambda = \frac{hc}{eV} \quad \text{Equation 2.1.}$$

Where, λ = X-ray wavelength (nm), h = Planck's constant, c = the speed of light, e = electron charge and V = excitation potential (kV)

X-rays are subsequently filtered so a single monochromatic X-ray beam is directed to the powdered sample (Figure 2.1) and interacts with electrons in the rotating sample.

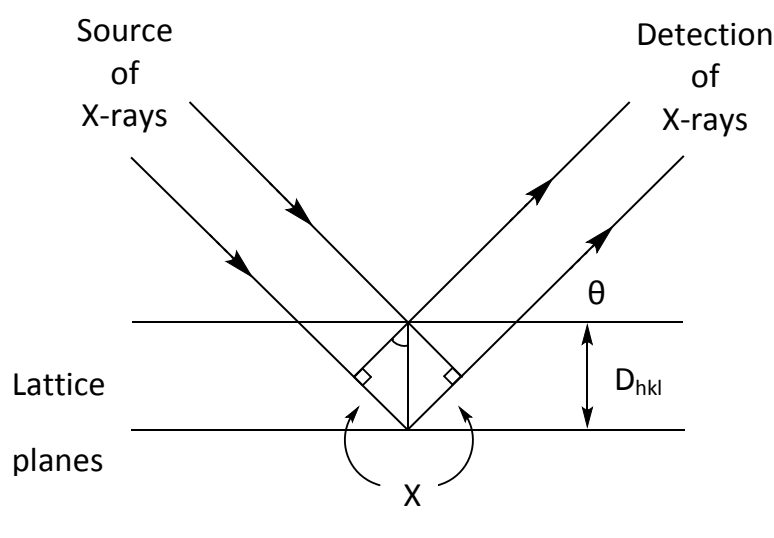


Figure 2.1 – Schematic diagram of Bragg reflection from crystal planes with spacing d_{hkl}

This interaction of X-rays and adjacent lattice planes in a rotating sample can be destructive or constructive. Only constructive interference allows for a peak in intensity which is any interference that adheres to Braggs Law (Equation 2.2.).

Bragg Equation
$$n\lambda = 2(d_{hkl}\sin\theta_{hkl})$$
 Equation 2.2.

Where λ = X-ray wavelength (nm), n = an integer, d_{hkl} = distance between planes of atoms (nm) and ϑ = half the angle between X-ray source beam and detector (°)

In an ideal X-ray diffraction sample, a powdered crystalline material should contain an infinite number of randomly ordered crystallites. These crystallites, of which some register for constructive interference, with their respective h, k and l indices, collectively make up a diffraction pattern. This diffraction pattern is called a fingerprint XRD pattern and can be compared to the International Centre for Diffraction Data (ICDD)⁴ database of reference diffraction patterns for the identification of known and unknown phases⁵ and impurities present. From this diffraction pattern, the lattice parameters, d-spacings, electronic properties, bond lengths and angles can all be determined.

A primary disadvantage to the use of X-ray diffraction is the long range crystal order required to study a sample;⁶ a feature that is not required when using solid-state NMR. Refinement techniques are additionally required in order to determine the quantity of phases present in a sample.⁷ The major disadvantage to using X-ray diffraction as a sole technique to study the chemical systems within this work however, centers on the inability of XRD to accurately detect short range order effects. Practically, this means that the local structure of $[\text{SiO}_{4/2}\text{F}]^-$ and Si-F distances are unable to be accurately determined. This topic will be discussed later in this work. As such, full structural determination of inorganic materials requires the collaboration of XRD with one or multiple other techniques, frequently techniques such as single crystal XRD, neutron diffraction,⁸ different types of vibrational spectroscopy⁹, electron microscopy¹⁰ and more recently,

solid state NMR.¹¹ The use of these techniques together allows the determination of information such as bond lengths within a unit cell that XRD alone is not capable of.

Some difficulty may also arise in full characterisation of certain types of materials that use similar precursors such as zeolites. Other sources of information may then be sought in this situation, for example referencing XRD powder patterns of zeolites to 'the collection of simulated XRD powder patterns for zeolites'.¹²

X-ray diffractometer equipment is used to take an X-ray diffraction pattern and comprises of 3 main components: An X-ray tube, sample holder with ground packed solid sample and X-ray detector, as shown in Figure 2.2.

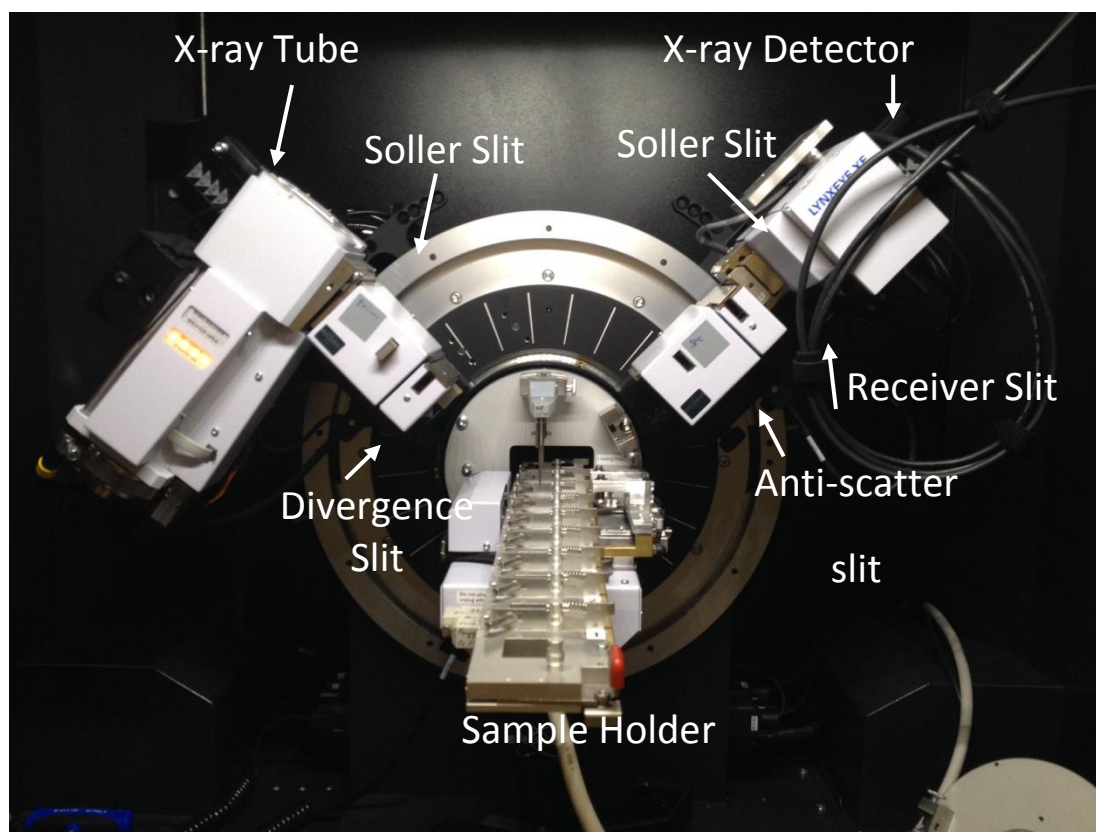


Figure 2.2 – Laboratory photo of labelled laboratory Bruker D8 ADVANCE X-ray diffractometer

2.1.1. Methods of Extracting X-ray Diffraction Data

X-ray diffraction characterises crystalline materials that match one of seven different types of crystal systems. These crystal systems define the make-up of the crystal and are dependent on the symmetry properties of the unit cell (Table 2.1).

Table 2.1 – Table displaying respective symmetry parameters for the seven crystal systems in increasing symmetry

Crystal system	Lattice parameters		Bravais lattices	Lattice symmetry
Triclinic	$a \neq b \neq c$	$\alpha \neq \beta \neq \gamma$	P	$\bar{1}$
Monoclinic	$a \neq b \neq c$	$\alpha = \gamma = 90^\circ, \beta \neq 90^\circ$	P, C	2/m
Orthorhombic	$a \neq b \neq c$	$\alpha \neq \beta \neq \gamma = 90^\circ$	P, C, I, F	mmm
Tetragonal	$a = b \neq c$	$\alpha \neq \beta \neq \gamma = 90^\circ$	P, I	4/mmm
Rhombohedral	$a = b = c$	$\alpha \neq \beta \neq \gamma \neq 90^\circ$	R	3m
Hexagonal	$a = b \neq c$	$\alpha \neq \beta = 90^\circ, \gamma = 120^\circ$	P	6/mmm
Cubic	$a = b = c$	$\alpha \neq \beta \neq \gamma = 90^\circ$	P, I, F	m3m

Where, P= primitive cell, C= side-centred cells, I= body-centred, F= face centred cells

These unit cells are made up of their corresponding lattice parameters which specifies the relationship of unit cell lengths and angles that make up the crystal.

The different Bravais lattices that apply to the seven crystal systems in Table 2.1 are defined as follows:

- Primitive (P)* – Lattice points on corners of the unit cell only
- Body-centred (I)* – Lattice points on corners of the unit cell plus in the centre of the unit cell
- Face-centred (F)* - Lattice points on corners of the unit cell plus in the centre of all faces
- Side-centred (C)* – Lattice points on corners of the unit cell plus in the centre of all side-only vertical faces

The distance between planes of crystals in a crystalline sample can be calculated dependant on crystal system.

Table 2.2 – Table of the seven crystal systems d-spacings equations

Crystal system	D-spacings Equation
Triclinic	$\frac{1}{d^2} = \frac{1}{V^2} (S_{11}h^2 + S_{22}k^2 + S_{33}l^2 + 2S_{12}hk + 2S_{23}kl + 2S_{13}hl)$ <p>Where, $S_{11} = b^2c^2\sin^2\alpha$, $S_{22} = a^2c^2\sin^2\beta$, $S_{33} = a^2b^2\sin^2\gamma$, $S_{12} = abc^2(\cos\alpha\cos\beta - \cos\gamma)$, $S_{23} = a^2bc(\cos\beta\cos\gamma - \cos\alpha)$ and $S_{13} = ab^2c(\cos\gamma\cos\alpha - \cos\beta)$</p>
Monoclinic	$\frac{1}{d^2} = \frac{1}{\sin^2\beta} \left(\frac{h^2}{a^2} + \frac{k^2\sin^2\beta}{b^2} + \frac{l^2}{c^2} - \frac{2hlc\cos\beta}{ac} \right)$
Orthorhombic	$\frac{1}{d^2} = \left(\frac{h^2}{a^2} + \frac{k^2}{b^2} + \frac{l^2}{c^2} \right)$
Tetragonal	$\frac{1}{d^2} = \frac{h^2 + k^2}{a^2} + \frac{l^2}{c^2}$
Rhombohedral	$\frac{1}{d^2} = \frac{(h^2 + k^2 + l^2)\sin^2\alpha + 2(hk + kl + hl)(\cos^2\alpha - \cos\alpha)}{a^2(1 - 3\cos^2\alpha + 2\cos^3\alpha)}$
Hexagonal	$\frac{1}{d^2} = \frac{4}{3} \left(\frac{h^2 + hk + k^2}{a^2} \right) + \frac{l^2}{c^2}$
Cubic	$\frac{1}{d^2} = \frac{h^2 + k^2 + l^2}{a^2}$

The unit cell volume of a material can also be calculated using Table 2.3, and if the crystal density is known, other useful information can be calculated as such as the mass per unit cell. This can be very useful for working out, for example the ratio of structure directing agents per unit cell of zeolite crystals.

Table 2.3 – Table of seven crystal systems equations to calculate volume of unit cell

Crystal system	Volume Equation
Triclinic	$V = abc\sqrt{1 - \cos^2\alpha - \cos^2\beta - \cos^2\gamma + 2\cos\alpha\cos\beta\cos\gamma}$
Monoclinic	$V = abc \sin\beta$
Orthorhombic	$V = abc$
Tetragonal	$V = a^2c$
Rhombohedral	$V = a^3\sqrt{1 - 3\cos^2\alpha + 2\cos^3\alpha}$
Hexagonal	$V = (\sqrt{3}a^2c)/2$
Cubic	$V = a^3$

The data derived from an X-ray diffraction pattern can also be refined using a least squares method. This can help with XRD issues such as peak overlapping and non-random distributions of crystallites.

2.2. NMR Theory

Nuclear magnetic resonance (NMR) spectroscopy is the study of the local order of nuclei in a magnetic field. A nucleus in a system will have an internal magnetic field called nuclear spin, and can also have an external magnetic field applied. The external magnetic field differs by being the field the nucleus is exposed to statically, such as during an NMR experiment.

An NMR spectrometer, with an external magnetic field uses a radiofrequency (RF) pulse to irradiate nuclei in a sample whereby the NMR spectrometer is used to study the response. This RF radiation is applied as an RF pulse, derived specifically for the study of NMR active nuclei, which are any nuclei with a spin of $\frac{1}{2}$ or $> \frac{1}{2}$.¹³

2.2.1. Nuclear Spin

Determination the net spin of a nucleus occurs via the balance of electrons and protons in the outer shells of a nucleus. An even amount of neutrons and protons gives a balanced nucleus where the spins are paired against each other and cancel out, leaving no overall nuclear spin observed and an NMR inactive nucleus, for example ^{12}C . When the total neutron and proton count gives an odd value, the overall nuclear spin is a half-integer, as such as $1/2$ ($^{13}\text{C}_6$), $3/2$ ($^{11}\text{B}_5$) and $5/2$ ($^{27}\text{Al}_{13}$). When both neutron and proton values are odd, the nuclear spin is an integer, as such as 1 for $^{14}\text{N}_7$. Out of these nuclear spin options, only nuclei with an overall spin number $\geq \frac{1}{2}$ are NMR active and have angular momentum (γ). The nuclear spin number is crucial because different spin nuclei have different qualities in NMR.

Spin $\frac{1}{2}$ nuclei provide the simplest route of spectral determination using NMR spectroscopy. The number of energy levels possible can be calculated by Equation 2.3:

$$\text{Energy Orientations} = 2I + 1 \quad \text{Equation 2.3.}$$

(Where I = overall nuclear spin for all non-isochronous nuclei)

2.2.2. Zeeman Interaction

The Zeeman interaction is the largest interaction facing spin $\frac{1}{2}$ nuclei. It governs the interaction between the associated magnetic moment (μ) of a nucleus with spin, in the external magnetic field.

The Zeeman Effect states that when nuclei are not exposed to a magnetic field, they have the same energy. This is demonstrated for a spin $\frac{1}{2}$ nuclei below (Figure 2.3):

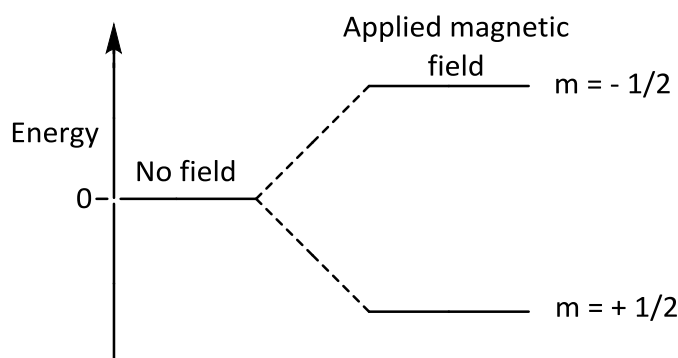


Figure 2.3 – Schematic diagram showing Zeeman energy level splitting for spin 1/2 nucleus

When a nucleus is exposed to an external magnetic field in an NMR experiment, the spins of the nuclei align either with or against the magnetic field and split into high and low energy states. These separated energy levels now have different magnetic quantum numbers (m), representative of the direction of angular momentum: $+1/2$ (α) for the nuclei aligned with the external magnetic field, and $-1/2$ (β) for nuclei aligned in opposition to the external magnetic field.

The total Zeeman energy of all nuclear spin species in a sample of given spin can be calculated as follows (Equation 2.4.).

$$\text{Zeeman Energy} \quad E_Z = \left(\frac{\gamma_j}{2\pi} \right) h m_j B_0 \quad \text{Equation 2.4.}$$

Where E_z = total Zeeman energy, γ_j = magnetogyric ratio of nucleus ($\text{rads}^{-1}\text{T}^{-1}$), h = Planck's constant, m_j = spin quantum number of nucleus and B_0 = applied magnetic field (T)

2.2.2.1. Boltzman Distribution and Population Density

The populations of nuclei in separate energy states are governed by thermodynamics and the Boltzman distribution (Equation 2.5.);

$$\frac{N_{Upper}}{N_{Lower}} = e^{\frac{-\Delta E}{kt}} \quad \text{Equation 2.5.}$$

Planck's equation

$$\Delta E = h\nu \quad \text{Equation 2.6.}$$

Where $N_{Upper/lower}$ = the number of nuclei in the upper and lower energy states, E = energy difference between spin states, k = Boltzman constant, t = temperature (K), h = Planck's constant and ν = frequency (s^{-1})

Due to the lower energy of the +1/2 (α) energy level where nuclei are aligned with the external magnetic field (B_0) at room temperature, there is a slightly higher nuclei population density present. It is these nuclei that can be excited into the upper -1/2 (β) energy state by a radiofrequency pulse.

These energy levels (Equation 2.7.) and the frequency of the radiation (Equation 2.8.) required to excite lower energy state nuclei can be calculated by the following equations:

$$\text{Energy level energy} \quad E = \frac{-\gamma I h B_0}{2\pi} \quad \text{Equation 2.7.}$$

$$\text{Transitional Energy} \quad \Delta E = \frac{\gamma h B_0}{2\pi} \quad \text{Equation 2.8.}$$

Where γ = magnetogyric ratio ($\text{rads}^{-1}\text{T}^{-1}$) I = overall nuclear spin, B_0 = external magnetic field (T) and h = Planck's constant

If enough target nuclei in the lower energy state are excited, the distribution of both energy levels may become equal and the spin cycle will be saturated. This requires a relaxation period before further excitation of nuclei commences.

2.2.2.2. Lamor Precession

The quantization of magnetic moments as $+\frac{1}{2}$ and $-\frac{1}{2}$ means nuclei can never fully align with the z plane of magnetisation. This ensures that there is always a part of the magnetic moment in the xy plane, as demonstrated below (Figure 2.4) and is the reason for Lamor precession.¹⁴

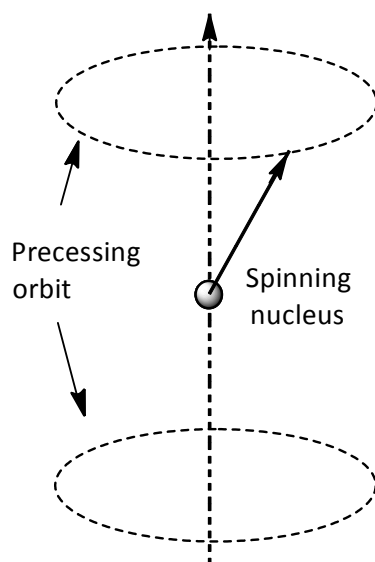


Figure 2.4 –Diagram depicting the Lamor Precession of a spinning nucleus's orbit

The spinning nucleus has intrinsic angular momentum and a magnetic moment. It generates a small magnetic field while precessing on its axis and as such can be said to be a vector, maintaining both magnitude and a direction in space.

The rate of this magnitude is referred to as Lamor Precession (Hz) (Equation 2.9.) and is proportional to its spin (Equation 2.10.).

Lamor Precession

$$\nu = \frac{\gamma B_0}{2\pi}$$

Equation 2.9.

$$\mu = \frac{\gamma I h}{2\pi} \quad \text{or} \quad \mu = \gamma \hbar$$

Equation 2.10.

Where μ = nuclear magnetic moment, γ = magnetogyric ratio ($\text{rad s}^{-1} \text{T}^{-1}$), I = nuclear spin quantum number, h = Planck's constant, ν = Larmor frequency (Hz) and B_0 = applied magnetic field (T)

2.2.2.3. Bulk Magnetisation

The nucleus discussed has a magnetic moment and its spin allows precession almost in line with the applied magnetisation. Practically however, the overall effect of all nuclei in a sample needs to be considered for the purpose of applying a radiofrequency pulse. When all opposing magnetic moments cancel out, a residual net nuclear magnetic moment remains from the larger population density of nuclei in the lower energy $+1/2$ (α) spin energy level. This overall magnetic moment is known as bulk magnetisation and aligns almost along the direction of the external magnetic field, B_0 (Figure 2.5)¹³.

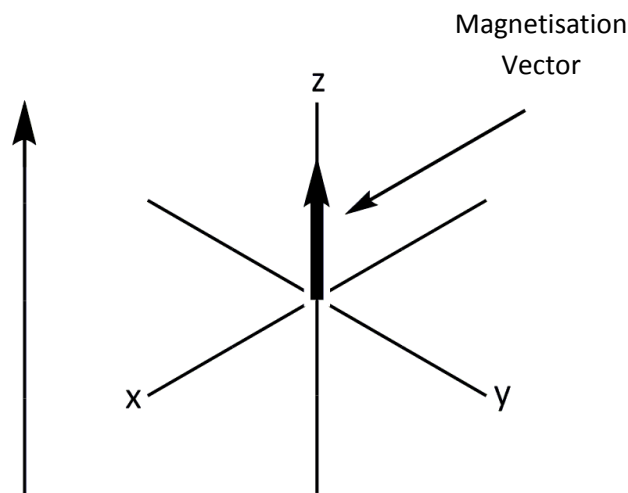


Figure 2.5 - Schematic diagram of net magnetisation aligned with applied magnetic field

This magnetisation vector that aligns with the magnetic field can be shifted by a radiofrequency pulse, for a certain amount of time (t_p), in the xy plane. This pulse generates an oscillating

magnetic field (B_1) at right angles to the applied magnetic field (B_0).¹⁵ The net magnetisation that is initially aligned with the applied magnetic field is tipped by the pulse to an angle (Θ) calculated using Equation 2.11., shown in Figure 2.6.

$$\Theta = \gamma B_1 t_p \quad \text{Equation 2.11.}$$

Where Θ = radiofrequency pulse angle, γ is the magnetogyric ratio ($\text{rads}^{-1}\text{T}^{-1}$), B_1 = oscillating magnetic field (Hz) and t_p = radiofrequency pulse time (s)

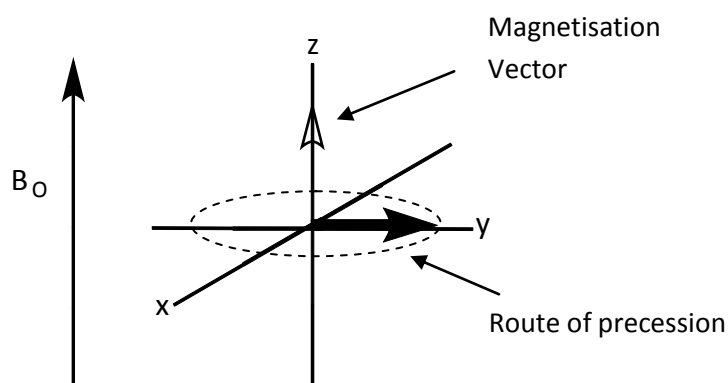


Figure 2.6 –Schematic diagram showing magnetisation being shifted into the xy plane after an applied pulse

After the radiofrequency pulse has been applied, the population densities return to their Boltzman distribution by a process called relaxation. Relaxation allows xy magnetisation to decay via free induction decay (FID) whereby all individual oscillations are detected by the NMR spectrometer.

2.2.2.4. NMR Relaxation

The relaxation of nuclear magnetisation is required to return to the z plane equilibrium state with the applied magnetic field before a subsequent radiofrequency pulse can be applied. This is essential as detection occurs in the xy plane, collecting a specified number of FID scans. The

relaxation period and the type of relaxation required are affected by the particular interactions relevant to the nuclear spins, such as shielding, dipolar coupling and quadrupolar coupling.

The following are common types of relaxation:

T1 Spin-lattice relaxation (longitudinal relaxation): This relaxation process concerns the relaxation back to the z plane along with the applied magnetic field (Figure 2.5) and the re-establishment of initial Gaussian population distributions. This relaxation time can be calculated for a homogeneous solid sample as follows:

$$M_z(t) - M_0 = (M_z(0) - M_0) \exp\left(\frac{-t}{T_1}\right) \quad \text{Equation 2.12.}$$

Where, $M_z(0)$ = magnetisation in the z plane, M = nuclear spin magnetisation vector, T_1 is the decay constant for the recovery to the z plane of the nuclear spin magnetisation (s)

A large spin-lattice relaxation time may increase the overall NMR data collection time drastically making the experiment less viable.

T2 Spin-spin relaxation (transverse relaxation): Upon application of a 90° radiofrequency pulse to a sample, nuclear spins become temporarily aligned in the new applied direction. After a time (T_2) the nuclear spins decay due to either inhomogeneities in the field or spin interactions that do not transfer energy to the lattice (T_1 relaxation). The extent of this decay and T_2 relaxation is referred to as dephasing delay and can be calculated from spectral peaks widths (Equation 2.13.):

$$T_2 \sim \frac{1}{\Delta\nu_{1/2}} \quad \text{Equation 2.13.}$$

Where $\nu_{1/2}$ = peak line width at half height

2.2.2.5. NMR Interactions

In addition to the external magnetic field placed upon nuclei (E_{RF}) and the Zeeman interaction (E_Z), a range of internal interactions can also contribute to the field experienced by a nucleus. These additional contributions are shielding (E_S), indirect spin couplings (E_J), dipolar couplings (E_D) and quadrupolar couplings (E_Q).

$$E_{NMR} = E_Z + E_{RF} + E_{CS} + E_J + E_D + E_Q \quad \text{Equation 2.14.}$$

These interactions are expressed above in the general Hamiltonian (Equation 2.14.), which demonstrates the total sum of terms of energy contributions on a nucleus under a magnetic field and will be tackled individually.

2.2.2.5.1. Shielding (E_{CS})

Shielding in NMR refers to the creation of a second magnetic field around the nucleus, induced when nuclei are placed under an applied magnetic field to precess in opposition to the applied magnetic field. It occurs in any atom possessing more than one electron shell and can be calculated as follows (Equation 2.15.):

$$\text{Chemical Shielding} \quad E_{CS} = \gamma \hat{I} \cdot \sigma \cdot B_0 \quad \text{Equation 2.15.}$$

Where E_{CS} = chemical shift interaction, γ is gyromagnetic ratio ($\text{rad s}^{-1}\text{T}^{-1}$), σ is shielding tensor (Hz) and B_0 = applied magnetic field (T)

Due to this shielding, the applied magnetic field is not exactly equal to that felt at the nucleus so the effective nuclear magnetic strength is used instead (Equation 2.16.):

$$\text{Effective Nucleus Strength} \quad B_{eff} = B_0 (1 - \sigma) \quad \text{Equation 2.16.}$$

Where B_0 = applied magnetic field (T) and σ = total shielding contributions (ppm)

This calculated difference between the applied field strength and experienced field strength at the nucleus is displayed as chemical shift, differentiating between nuclei of different magnetic equivalence and is the reason for the NMR spectra we can interpret.

Shielding and chemical shift are affected by the following three components: Diamagnetic contributions (σ_d), paramagnetic contributions (σ_p) and neighbouring group anisotropy (σ_n), shown in Equation 2.17.

Chemical Shielding
$$\sigma = \sigma_d + \sigma_n + \sigma_p$$
 Equation 2.17.

Diamagnetic Shielding (σ_d): When electrons are placed in a magnetic field, they circulate the s-orbital creating a self-instigated induced field. This diamagnetic shielding means that in addition to the attractive forces between the positive nucleus and negative electrons, there is an additional repulsion between electrons in the induced magnetic field. Therefore, increasing electrons reduces the electrostatic force and increases the atomic size. This diamagnetic contribution to shielding is distance dependant so the core electrons have the majority effect on diamagnetic shielding of the nucleus, giving rise to a relatively constant diamagnetic shielding for all individual atoms (Equation 2.18). It also means that nuclei that are surrounded by more electrons are shielded from the magnet more than nuclei that are surrounded by fewer electrons.

Diamagnetic Shielding
$$D_S = \frac{1}{R_i^3}$$
 Equation 2.18.

Where D = Diamagnetic shielding (ppm) and r_i = the distance of the i^{th} electron in the nucleus

Paramagnetic Shielding (σ_p): A distortion of electron distribution in p-orbital energy level states by the external magnetic field creates paramagnetic shielding. Excited electronic states may exist in the ground electronic state with remnant paramagnetic properties that causes relatively large deshielding effects of nearby nuclei. Practically, this means that these nuclei will be more affected

by the external magnetic field and this will be demonstrated in the nuclei's respective chemical shift. This paramagnetic effect is the principle shielding effect of all nuclei heavier than ^1H and is governed by TIP (Temperature Independent Paramagnetism).

Neighbouring group anisotropy (σ_n): This contribution to shielding is significantly more important for ^1H NMR experiments than any heavier element NMR experiment. This is due to the size of the neighbouring group effects being no larger than a few ppm affecting only ^1H NMR's small chemical shift range.

Diamagnetic movements of electrons in s-orbital (as discussed in Diamagnetic Shielding (σ_d)) creates a self-instigated magnetic field. This means that the occurrence of any double bonds, neighbouring electron withdrawing or donating groups or lone pairs will have an effect on neighbouring nuclei and subsequently affect the nuclear chemical shift observed.

2.2.2.5.2. NMR Tensor Properties

Solution state NMR allows molecules a random tumbling motion which reduces internal interactions to their isotropic averages as such (Table 2.4):

Table 2.4 - Table of solution state NMR internal interactions isotropic averages

Internal Interaction	Tensor	Isotropic Average
Chemical Shielding	E_{CS}	σ_{ISO}
Indirect Coupling	E_J	J_{ISO}
Dipolar Coupling	E_D	0
Quadrupolar Coupling	E_Q	0

In solid state NMR, there is no anisotropic molecular tumbling and internal interactions are orientation dependant meaning they can be regarded as tensors. A shielding tensor can be thought of as being the effect that shielding electrons have on their nucleus from the external magnetic field (Equation 2.19.).

$$B_s = -\sigma B_0 \quad \text{Equation 2.19.}$$

Where B_s = effective magnetic field at the nucleus (T), σ = shielding tensor and B_0 = applied magnetic field (T)

This tensor can be adapted into a matrix with a diagonal σ principal axis frame (PAF) (Equation 2.20.):

$$\sigma = \begin{pmatrix} \sigma_{xx} & \sigma_{xy} & \sigma_{xz} \\ \sigma_{yx} & \sigma_{yy} & \sigma_{yz} \\ \sigma_{zx} & \sigma_{zy} & \sigma_{zz} \end{pmatrix} \quad \text{Equation 2.20.}$$

Symmetrical properties can be eliminated in the full shielding tensor leaving the principal components only (Equation 2.21.).

$$\text{Principal Components} \quad \sigma = \sigma_{xx} \sigma_{yy} \sigma_{zz} \quad \text{Equation 2.21.}$$

The isotropic average of molecules in solution state NMR reduces the principal components to an isotropic shielding average as shown (Equation 2.22.):

$$\text{Isotropic shielding:} \quad \sigma_{iso} = \frac{1}{3} (\sigma_{XX} + \sigma_{YY} + \sigma_{ZZ}) \quad \text{Equation 2.22.}$$

High resolution solid state NMR experiments also reduce orientation dependant components to the isotropic average by spinning at the magic angle. In solid state NMR however another two components are considered. These are the anisotropy (Equation 2.23.) and asymmetry (Equation 2.24.) parameters that contribute to chemical shift anisotropy and can be calculated as follows:

$$\text{Anisotropy} \quad \Delta\sigma_{ani} = \sigma_{zz} - \frac{1}{2} (\sigma_{XX} + \sigma_{YY}) \quad \text{Equation 2.23.}$$

Asymmetry

$$j = \frac{3(\sigma_{XX} - \sigma_{YY})}{2\Delta\sigma}$$

Equation 2.24.

2.2.2.5.3. Indirect spin couplings/ J-Couplings (E_j)

Indirect couplings are a through-bond interaction between two nuclear spins, sometimes referred to as Scalar coupling. They give information about the molecular orientation and atomic connectivity which can be a very useful tool in solution NMR. In a solution NMR spectrum, this coupling can provide three important parameters, summarised in Table 2.5.

Table 2.5 - Table describing the uses and examples of different types of Indirect Spin coupling parameters

Useful Parameters from Indirect Spin-Coupling	Example	Use
Sign of Coupling	<i>+, -</i>	Defined on whether the energy is higher or lower than the other nuclei when the spins match or oppose
Coupling Strength	<i>Weak, Strong</i>	Strength of coupling indicates the distance of coupling or strength of magnetic moment on attached nuclei
Coupling Multiplicity	<i>Doublet, Double, Doublet</i>	Identification of the amount of (non-equivalent) nuclei coupled to the nucleus of interest

This type of coupling is less of a consideration in solid-state NMR due to it being considered the smallest interaction in magnitude¹⁶ for most light nuclei that are studied. Although typically discussed as a through-bond interaction, it can interestingly be used to prove the existence of bonding through-space in nuclei that are in very close proximity in zeolites.^{17,18} The determination of useful structural information from J coupling is determined in the Chapter 6.

2.2.2.5.4. Dipolar Coupling (E_D)

Dipolar coupling is based on the through space interaction between two nuclei acting as small magnets. Each nucleus's magnetic field overlaps with the other, giving rise to a shift in the energy of nuclear spin levels.

Due to the rapid tumbling motion of molecules in solution state NMR, the isotropic component reduces to zero meaning this interaction can play no part on resonance frequencies, but does play a key role in relaxation times. Correspondingly it is not a concern to remove, but also means no useful information can be yielded from it, such as is the case for solid-state NMR.

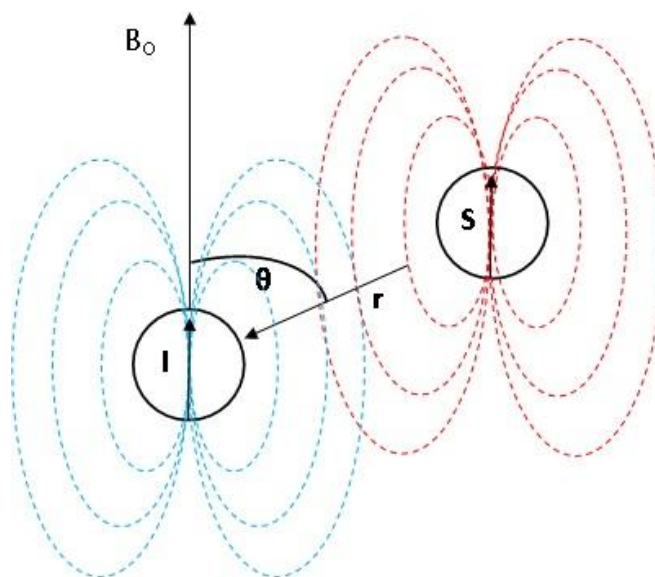


Figure 2.7 – Schematic diagram showing dipolar coupling between two dipole moments, I and S

In solid state NMR, there is no rapid tumbling of molecules or removal of dipolar coupling, leading to major line broadening in the NMR spectra. The strength of the dipolar interaction, similarly to diamagnetic shielding, is related to distance between dipoles in question (Equation 2.25.).

$$\text{Dipolar Energy} \quad E_D = r^{-3} \quad \text{Equation 2.25.}$$

The energy of this dipolar coupling can be calculated based on molecular orientation if the distance between the two dipole moments is known, in the following first order calculation (Equation 2.26.).

$$\text{Dipolar Energy} \quad E_D = \left(\frac{\mu_I \mu_S}{r^3} \right) - \left(\frac{3(\mu_I \hat{r})(\mu_S \hat{r})}{r^5} \right) \frac{\mu_0}{4\pi} \quad \text{Equation 2.26.}$$

Where $\mu_{I/S}$ = magnetic moments of dipoles I and S ($N m T^{-1}$), r = distance between two dipoles (m), μ_0 = Permeability constant and \hat{r} = vector between magnetic dipoles

The dipolar coupling constant (Equation 2.27.) can also be calculated from the dipolar energy (Equation 2.28) as shown:

$$E_D = -D_{IS} m_I m_S (3\cos^2\theta - 1)h \quad \text{Equation 2.27.}$$

Where dipolar distance can also be calculated as follows:

$$D_{IS} = \frac{\gamma_I \gamma_S \hbar \mu_0}{8 \pi^2 r_{IS}^3} \quad \text{Equation 2.28.}$$

Where D = dipolar coupling constant between I and S , $\gamma_{I/S}$ = magnetogyric ratios of dipoles I and S ($\text{rad s}^{-1} \text{T}^{-1}$), r = distance between two dipoles (m), μ_0 = Permeability constant and \hbar = reduced Planck's constant

Dipolar coupling can be exploited for distance determination^{19,20} in a variety of different chemical multi-spin²¹ systems including zeolites²² in solid state NMR via experiments such as REDOR.^{23,24}

This theory is developed in Chapter 6.

2.2.2.5.5. Quadrupolar Coupling (E_Q)

Quadrupolar coupling occurs as an additional internal interaction in quadrupolar nuclei only, which are any nuclei with a spin number over $\frac{1}{2}$. The quadrupolar interaction is a coupling between the nuclear electric quadrupole moment (eQ) and electric field gradient (EFG) and can be positive or negative dependant on the charge distribution of a nucleus. This means that in addition to the collection of all local magnetic field interactions already experienced, quadrupolar nuclei also interact with electric field gradients at the nucleus.

EFG is a tensor property making quadrupolar coupling a tensor and implying the same rules to the internal interaction as tensors in chemical shielding (2.2.2.5.2 NMR Tensor Properties). Therefore, the isotropic average reduces to zero as shown (Equation 2.29.):

$$E_Q = \frac{1}{3}(Q_{XX} + Q_{YY} + Q_{ZZ}) \quad \text{Equation 2.29.}$$

In solution state NMR, resonance frequencies remain unaffected by quadrupolar nuclei due to the zero quadrupolar isotropic average. However, quadrupolar nuclei retain their negative effect on line broadening and relaxation times making some nuclei with large quadrupolar moments very difficult to study by solution state NMR.

Solid state NMR however can benefit from the utilisation of quadrupolar nuclei and quadrupolar moments. They can be determined and manipulated to give important information about the sample that would not be possible in solution state NMR. Namely these pieces of information are anisotropy (χ) and asymmetry (η) and can be calculated as follows:

$$\text{Quadrupolar Coupling Constant} \quad \chi (C_Q) = \frac{e^2 Q q_{ZZ}}{h} \quad \text{Equation 2.30.}$$

$$\text{Quadrupolar Asymmetry Parameter} \quad \eta = \frac{q_{YY} - q_{XX}}{q_{ZZ}} \quad \text{Equation 2.31.}$$

Where $X = \text{quadrupolar coupling constant}$, $n = (0 \leq n \leq 1)$, $eQ = \text{nuclear quadrupole moment (em}^2)$, $eq_{ZZ} = \text{the largest principal component of the EFG in a } q_{ZZ} \geq q_{YY} \geq q_{XX}$ and $h = \text{Planck's constant}$

The asymmetry parameter calculated above determines the amount of symmetry in the charge density of a nucleus. For example, a non-symmetrical charge density whereby the charge region is compressed or extended over the nuclei will lead to the contribution of an asymmetry parameter to the quadrupolar coupling constant.

When almost spherical or spherical charge densities exist in a nucleus, the quadrupolar asymmetry parameter will be small and as such the total quadrupolar effects will be small. This may lead to a small or unidentifiable effect on the NMR spectra in terms of line broadening and relaxation times and therefore be of minimal inconvenience or utilisation. Larger asymmetries correspondingly have a much larger effect and are discussed herein.

Most quadrupolar nuclei have a spin number that follows the pattern of $1/2, 3/2, 5/2$. In these spin number nuclei, the central transition refers to a transition between the $-1/2$ to $1/2$. In this transition only, the quadrupole effects can be equal, meaning the quadrupole transition frequency equals zero and is orientation independent. For this reason, the central transition peak observed on a solid state NMR spectrum has a significantly larger intensity than any following satellite transitions. These following satellite transitions are orientation based (Equation 2.32.) resulting in intensity being spread over a significantly wider frequency range compared to the central transitions.

Energy of first order quadrupole energy:

$$E_Q = \left(\frac{3m_I^2 - I(I+1)}{8I(2I-1)\hbar} \right) ((3\cos^2\theta) + \eta\cos 2\theta \sin^2\theta) \chi \quad \text{Equation 2.32.}$$

Where E_Q = quadrupolar energy, θ = the angle between asymmetry axis and applied magnetic field, h = reduced Planck's constant, I = spin number, m_I = the spin component quantum number and X = asymmetry parameter

These first order quadrupolar contributions are complicated further when quadrupolar nuclei asymmetry is large and second order contributions are required. These additional contributions that are required to be taken into account are the zero, second and fourth order contributions that also contribute to the broadening of the spectral peaks.

2.2.2.6. Solid State NMR Techniques

The use and development of solid state NMR over the last few decades has allowed the technique to be brought up to speed with its solution state counterpart and has additionally brought about the possibility of new information about materials that solution state NMR is not capable of; for example determination of complex protein structures.²⁵ This has been made possible due to the ability of solid state NMR to selectively exploit or eliminate certain internal magnetic field

interactions mentioned in the previous Hamiltonian (Equation 2.14.), namely dipolar coupling (E_D) and quadrupolar coupling (E_Q).

Unlike solution state NMR's fast random tumbling of molecules, solid state NMR is anisotropic, meaning that a vast array of randomly directed molecules will exist with respect to the external magnetic field. As such, all molecular nuclei will be observed in the NMR spectrum leading to a broad peak. The solid state NMR developments over the last few decades has allowed for the removal of these additional interactions in order to gain similar sharp spectral peaks to that observed in solution state NMR. The reintroduction of selective information is possible via the development of the following solid state NMR techniques that are often combined: Magic Angle Spinning (MAS), Cross Polarisation (CP), High Power Decoupling (HPD) and other optional 2D experiments. These are discussed individually as follows.

2.2.2.6.1. Magic Angle Spinning

The internal interactions, described in Chapter 2.2.2.5 , all have an orientation dependent component as shown:

$$\frac{1}{2}(3\cos^2\theta - 1) \quad \text{Equation 2.33.}$$

Where ϑ = the angle between the internuclear vector and applied magnetic field B_0 (°)

It has long been discovered however that the rotation of the sample at 54.74° , the magic angle²⁶ allows for the averaging of Equation 2.33. that somewhat mimics the tumbling motion of molecules in solution state NMR and reduces the line broadening of anisotropic dipolar interactions.

In a powdered sample, all orientations must be taken into account for θ , where the sample is rotated at an angle of θ_R (Figure 2.8) which will change with time as the sample is rotated. The derivations of the magic angle can be summarised as follows (Equation 2.34.):

$$\left(\frac{1}{2}(3\cos^2\theta - 1) = \frac{1}{2}(3\cos^2\theta_R - 1) \frac{1}{2}(3\cos^2\beta - 1) \right) \text{ Equation 2.34.}$$

Where ϑ = angle between the applied magnetic field and determined molecular interaction ($^\circ$), θ = distance between the axis of rotation and determined molecular interaction ($^\circ$) and ϑ_R = fixed experimental angle ($^\circ$)

If the angle of θ_R is set to 54.7356° , the value of $(3\cos^2\theta_R - 1)$ becomes equal to zero. This in turn averages the entire orientation dependant calculation of $(3\cos^2\theta)$ to zero on the condition that the spin is sufficiently fast to average θ in comparison with interaction anisotropy. To reduce most broadening effects, the spin rate must be vastly greater than the interaction line widths. In practice, a minimal increase in spin rate can be sufficient to reduce shielding interactions however a drastically higher rate is required in order to attempt to reduce or entirely remove proton dipolar couplings but it can be impossible to average out some quadrupolar effects.¹⁶

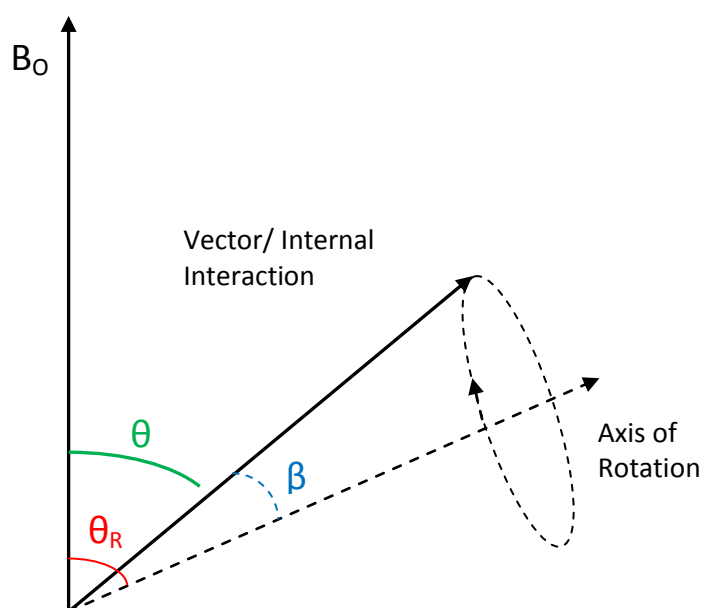


Figure 2.8 – Schematic diagram demonstrating the θ_R angle that is set to 54.74° for magic angle spinning

Due to these features, the selective reintroduction of chemical shift anisotropy and determination of respective information is possible by varying spin speeds. It is possible to select a spin speed that is fast enough to reduce line broadening but slow enough to include spinning sidebands at spin rate distances outwards from the central peak of isotropic resonance.²⁷ These spinning sidebands can be used to determine key information about anisotropic interactions²⁸ as such as ¹⁴N quadrupolar chemical shift anisotropy and asymmetry parameters via the use of additional software like Bruker SOLA²⁹ or DmFit³⁰ (developed in Chapter 4).

In a relatively quiet NMR spectrum, spinning sidebands may be of minimal inconvenience however in a more cluttered NMR spectrum, spinning sidebands may overlap spectral peaks. Due to the occurrence of these sidebands at a distance equal to the spin rate, they can simply be spun out to a convenient location on the NMR spectrum where minimal to no peak overlap occurs.

2.2.2.6.2. Cross Polarisation

Direct excitation for single pulse sequences can be performed in solid state NMR for highly abundant nuclei. For any other nuclei, the following problems occur. Significantly bad signal to noise ratio due to the low abundance of NMR active nuclei. Correspondingly, longer experimental times in order to gain appropriate resolution spectra. Also, very long spin-lattice relaxation times are experienced ranging from many seconds for ¹³C and ¹⁵N to many minutes for ²⁹Si.¹⁶

The application of a cross polarisation pulse sequence reduces the above problems by magnetisation transfer from highly abundant NMR-active nuclei to the dilute spin. The cross polarisation experiment benefits from reduced recycle delays to the length of the abundant nuclei, increasing spectral resolution available in a given time.

The occurrence and efficiency of cross polarisation is dependent on 3 features. These are the matching of Hartmann-Hahn³¹ conditions, the distance between the dipolar coupling nuclei that are experiencing the polarisation transfer and the mobility of the molecules in the solid state, whereby more increased molecular mobility leads to longer relaxation times. These features and

more are further developed in Chapter 6 whereby cross polarisation is a key feature in the distance determination experiments conducted.

2.2.2.6.3. High Power Decoupling

The process of decoupling allows removal of splitting patterns observed in an NMR spectrum. In solution state NMR, splitting patterns can often be very useful in helping to identify different peaks for molecular assignment so decoupling is typically undesired for the large majority of nuclei studied. In solid state NMR however, coupling significantly contributes to line-widths of peaks and reduces spectral resolution. NMR experiments with a large proton contribution suffer from considerable proton coupling and line broadening. This may be overcome by the latter of the two types of decoupling:

High power homonuclear decoupling: identifying the same isotope in the NMR spectrum that is being excited by radiofrequency pulses.

High power heteronuclear decoupling: identifying a different isotope in the NMR spectrum than is being excited by radiofrequency pulses. This type of decoupling is one of the easiest techniques used to remove or reduce heteronuclear couplings between nuclei at normal magnetic fields (up to 400 MHz)³². Examples of decoupling experiments used in this work and processes involved are as follows:

Continuous wave (CW)³³ decoupling can be added to an MAS NMR experiment whereby a high power is asserted continuously upon the ^1H or ^{19}F nuclei resonance whilst the other nuclei's spectrum is collected. There are realistic dangers to damaging equipment from the application of high power in continuous wave, of a long amount of time. The risks of damaging amplifiers or high power being converted into heat that the probe cannot take will lead to arcing of the probe. In order to avoid these problems, a combination of limiting decoupling power and applying a maximum radiofrequency duty cycle are imposed.

The duty cycle imposed is a proportional amount of time compared to the experiment time that a proportional amount of power is applied to the sample. For CW decoupling a 10 – 20 % duty cycle limit is imposed and can be calculated:

$$\text{Duty – cycle} = \frac{\text{total RF on–time}}{\text{total repetition time}} \quad \text{Equation 2.35.}$$

SPINAL-64³⁴ high-power decoupling is a family of 64 small phase incremental sequences.³⁵ It involves slow phase changes of 1-2 ms and phase steps of $\pi/2$ and has been proved as a very useful tool against the high MAS speed experiments of rigid solids.^{36 37} The use of SPINAL-64 high power decoupling over more traditional choices allows for a more efficient decoupling program that yields specific advantages in triple resonance experiments such as REDOR,²³ developed further in chapter 6.

2.2.2.6.4. 2D NMR Experiments

Similar to solution state NMR, solid state NMR can also perform two dimensional (2D) spectroscopy with the same nuclei (homonuclear) or different nuclei (heteronuclear). In these experiments, a transfer of magnetisation is measured between either the bonds or through space interactions, dependant on the type of experiment, allowing the user more characterisation capabilities when 1D NMR is not sufficient.³⁸ Certain 2D NMR experiments have been used in this thesis and the theory will be developed in chapter 6.

2.3. Scanning Electron Microscopy Theory

The morphology of crystals can be studied by Scanning Electron Microscopy (SEM) imaging. This technique allows for the study of the crystal surface, whereby crystal shapes and dimensions may not only be viewed and measured, but can also be photographed.

Crystal morphologies can have a large effect on the practical applications of a compound. For example, MFI (ZSM-5) samples synthesised under slightly different conditions may lead to entirely different crystal morphology, crystal dimensions and particle sizes. These different chemical

properties can have a large effect on the practical applications of materials in terms of their reactive properties, and uses. The collaborative study of these materials by SEM can therefore be advantageous because SEM is able to distinguish between samples that are the same material however, have different crystal structure and reactive properties that other common techniques, such as X-ray diffraction are not capable of.

Scanning Electron Microscopy has various advantages over simple optical light. It can provide a magnification power of up to 300,000 times, which is significantly more than the 1-500 times magnification permitted by optical light. SEM is capable of studying with very good depth of field. This can be very important and useful when studying crystal morphologies because it gives an almost 3D view useful when viewing or studying shapes. They are even capable of looking past the surface of the object, contributing to the 3D-like imaging; a quality that is not common to all spectroscopic methods.

An SEM works by a low energy (up to 50 eV)¹ electron beam projecting down a channel of lenses onto the surface of a sample. The scanning motion provides a signal to the secondary electron detector which is used to create an image. The useful combination of SEM with Energy Dispersive X-rays (EDX) can allow for the identification of minor phases and elements that may be overwhelmed in XRD and not observed.

2.4. Background to Instrumentation

2.4.1. X-ray Diffraction

Equipment and Sample Preparation: X-ray diffraction powder patterns were collected on a Bruker D8 advance with Cu α radiation of 1.5406 Å at 40 kV tube voltage and 40mA tube current. Samples were ground into a fine powder and pressed into a Bruker PMMA sample holder.

Technical Experimental Details: Initial X-ray diffraction experiments were run from 5 – 60 2θ ° range with a 0.07 ° slit size and 4 second step time.

Analytical Software: These powder patterns were referenced to published diffraction files registered in the ICDD-PDF-4 Powder Diffraction Database⁴. Characterisation of experimental powder patterns was conducted by comparison to reference files of products, starting materials and impurities.

2.4.2. Solid State NMR

2.4.2.1. NMR Experimental Details and References

Various NMR spectrometers have been used for the solid state NMR experiments conducted here and are outlined below:

Table 2.6 – Experimental details for NMR spectra collected on a Bruker Avance III HD 400 MHz Spectrometer at Keele University, Staffordshire

Experiment Type	Experimental Details
¹ H	Collected using 2.5 mm rotors at 400.13 MHz for ¹ H. Experiments were conducted using a recycle delay of 3 s and a 6 kHz spinning rate.
²⁹ Si{ ¹ H} CP MAS	Collected using 2.5 mm rotors at 79.47 MHz for ²⁹ Si and 400.13 MHz for ¹ H. Experiments were conducted using a 3 ms contact time, a linear ramp on the ¹ H contact pulse (30% slope), SPINAL-64 ³⁹ ¹ H decoupling, q 3 s recycle delay and a 6 kHz spinning rate.
Reference Sample	²⁹ Si chemical shifts were referenced to TMS using the cubic octamer Q8M8 - Si ₈ O ₁₂ [OSi(CH ₃) ₃] as an external secondary standard.
¹³ C{ ¹ H} CP MAS	Collected using a 2.5 mm rotor at 100.59 MHz for ¹³ C and 400.13 MHz for ¹ H. Experiments were conducted using a 3 ms contact time, a linear ramp on the ¹ H contact pulse (30% slope), SPINAL-64 ¹ H decoupling, recycle delay of 3 s and a 6 kHz spinning rate.
Reference Sample	¹³ C chemical shifts were referenced to TMS using adamantane as an external secondary standard.

Table 2.7 - Experimental details for NMR spectra collected on a Bruker Avance III HD 400 MHz Spectrometer at University of St Andrews University, Fife

Experiment Type	Experimental Details
¹³ C{ ¹ H} CP MAS	Collected using a 1.9 mm rotor at 100.60 MHz for ¹³ C and 400.12 for ¹ H. Experiments were conducted using a 5 s recycle delay, 4 ms contact time, SPINAL-64 ¹ H decoupling and 10 kHz spinning rate.
Reference Sample	¹³ C chemical shifts were referenced to TMS with Alanine as a secondary reference
²⁹ Si MAS	Collected using a 1.9 mm rotor at 79.49 MHz for ²⁹ Si. Experiments were conducted using a recycle delay of 120 s, a 2 ms contact time and 10 kHz spinning rate.
Reference Sample	²⁹ Si chemical shifts referenced to TMS with Q8M8 - Si ₈ O ₁₂ [OSi(CH ₃) ₃] as a

	secondary reference
¹⁹ F MAS	Collected using a 1.9 mm rotor at 376.49 MHz for ¹⁹ F. Experiments were conducted at 280 K using a spin echo, recycle delay of 20 s and a 30 kHz spinning rate.
Reference Sample	¹⁹ F chemical shifts were referenced to a replacement sample of C ₆ F ₆ ($\delta F = -166.4$ ppm with respect to the signal for CFCl ₃).
¹⁴ N MAS	Collected using a 1.9 mm rotor at 28.92 MHz for ¹⁴ N. Experiments were conducted using a 1 ms contact time, recycle delay of 5 s and 10 kHz spinning speed.
Reference Sample	¹⁴ N chemical shifts were referenced to NH ₄ Cl

Table 2.8 - Experimental details for NMR spectra collected on a Bruker Avance III HD 850 MHz Spectrometer at the Solid State NMR Facility at Warwick University.

Experiment Type	Experimental Details
14N MAS	Collected using a 7 mm rotor at 61.42 MHz for ¹⁴ N. Experiments were conducted using a 1 ms contact time, recycle delay of 0.5 s and 2 kHz spinning speed.
Reference Sample	¹⁴ N chemical shifts were referenced using NH ₄ Cl

2.4.2.1.1. NMR and Probe Specification

Keele University

NMR: Bruker AVANCE III HD 400 MHz 35 kHz DVT standard-bore triple channel ¹H/X/Y
CP MAS SS-NMR

Probe: 2.5 mm triple resonance TriGamma ¹H/X/Y MAS probe

University of St Andrews

NMR: Bruker AVANCE III 400 MHz 40 kHz DVT wide-bore four-channel ¹H/F/X/Y CP MAS
SS-NMR

Probe: 4.0 mm dual channel ¹H/X MAS probe

University of Warwick Central Facility

NMR: Bruker AVANCE III 850 MHz kHz DVT wide-bore four-channel 7.0 mm ¹H/F/X/Y CP
MAS SS-NMR

Probe: 7.0 mm low gamma CP MAS probe

2.4.2.1.2. Variable Temperature NMR Experiments

Variable temperature ^{13}C $\{^1\text{H}\}$ CP MAS experiments were conducted on a Bruker Avance III 400 MHz spectrometer capable of a -50 to +80 °C temperature range of the air flow.

Heating experiments were conducted by the Bruker in built direct variable temperature (DVT) control system which heats airflow and then regulates it in order to match the specified temperature for the sample.

Low temperature experiments were conducted by adapting the air flow line to include a large 5-loop coil followed by a desiccator (anhydrous calcium sulphate). This coil was submersed into a 25 litre nitrogen dewar to reduce the temperature of the air flow. The temperature was then controlled by a combination of the Bruker DVT thermometer and airflow regulators to meet the specified temperature requirement. Due to ratio of the size of the nitrogen dewar and loss of nitrogen for a four-day experiment, the dewar was monitored and accordingly refilled roughly every 8 hours.

2.4.3. Scanning Electron Microscopy

Equipment and Sample Preparation: Scanning electron microscopy imaging was conducted on a Hitachi Tabletop Electron Microscope TM3000. Samples were prepared by being loaded onto 15 mm Hitachi stubs that are screwed into the piece of equipment in a fixed location. Disposable 12 mm carbon covered adhesive tabs were used to affix the sample to the stubs. Any sample that was not securely stuck to the adhesive was removed prior to being placed in the equipment for air evacuation.

Technical Experimental Details: Samples were studied by SEM analysis using voltages of 5 kV or 15 kV with microscope magnification capabilities of up to 30,000 times.

2.5. References

- 1 A. K. Cheetham and P. Day, *Solid State Chemistry: Techniques, Volume 1*, Clarendon Press, 1987.
- 2 R. I. Walton, R. I. Smith and D. O'Hare, *Microporous Mesoporous Mater.*, 2001, **48**, 79–88.
- 3 C. Suryanarayana and M. G. Norton, *X-Ray diffraction : a practical approach*, 1998.
- 4 International Center for Diffraction Data, *PDF-4+ 2016*, .
- 5 B. Fultz and J. M. Howe, *Transmission Electron Microscopy and Diffractometry of Materials (Third Edition)*, 2007.
- 6 R. Ryoo, J. M. Kim, C. H. Ko and C. H. Shin, *J. Phys. Chem*, 1996, **3654**, 17718–17721.
- 7 P. A. Jacobs and J. A. Martens, *Synthesis of high-silica aluminosilicate zeolites*, Elsevier, 1987.
- 8 S. Schorr, *Sol. Energy Mater. Sol. Cells*, 2011, **95**, 1482–1488.
- 9 V. Escribano, E. Lopez, M. Panizza, C. Resini, J. Amores and G. Busca, *Solid State Sci.*, 2003, **5**, 1369–1376.
- 10 A. B. Morgan and J. W. Gilman, *J. Appl. Polym. Sci.*, 2003, **87**, 1329–1338.
- 11 R. Morris, *Kristallography*, 2007, **1**, 33–38.
- 12 M. M. J. Treacy, 2001.
- 13 J. Keeler, *SpringerReference*, 2002, 211.
- 14 J. Edwards, in *Process NMR*, Danbury, Connecticut, 2008.
- 15 D. Williams and I. Fleming, *Spectroscopic Methods in Organic Chemistry: 5th Edition*, London: McGraw-Hill Publishing Co, 5th edn., 1995.
- 16 D. Apperley, R. Harris and P. Hodgkinson, *Solid-state NMR: basic principles & practice*, Momentum Press, 2012.
- 17 R. M. Shayib, N. C. George, R. Seshadri, A. W. Burton, S. I. Zones and B. F. Chmelka, *J. Am. Chem. Soc.*, 2011, **133**, 18728–18741.
- 18 D. Wisser, S. I. Bruckner, F. M. Wisser, G. Althoff-Ospelt, J. Getzschmann, S. Kaskel and E. Brunner, *Solid State Nucl. Magn. Reson.*, 2015, **66**, 33–39.
- 19 T. Gullion, in *Modern Magnetic Resonance*, Springer Netherlands, Dordrecht, 2008, pp. 713–718.
- 20 J. E. Roberts, G. S. Harbison, M. G. Munowitz, J. Herzfeld and R. G. Griffin, *J. Am. Chem. Soc.*, 1987, **109**, 4163–4169.
- 21 J. Schaefer, *J. Magn. Reson.*, 1999, **137**, 272–275.
- 22 C. A. Fyfe, D. H. Brouwer, A. R. Lewis and J. Chezeau, *J. Am. Chem. Soc.*, 2001, **123**, 6882–6891.
- 23 T. Gullion and J. Schaefer, *J. Magn. Reson.*, 1989, **81**, 196–200.

- 24 M. Bertmer and H. Eckert, *Solid State Nucl. Magn. Reson.*, 1999, **15**, 139–152.
- 25 H. Müller, M. Etzkorn and H. Heise, 2013, pp. 121–156.
- 26 E. R. Andrew, A. Bradbury and R. G. Eades, *Nature*, 1958, **182**, 1659–1659.
- 27 M. A. Caporini, C. J. Turner, A. Bielecki and R. G. Griffin, *J. Magn. Reson.*, 2009, **200**, 233–238.
- 28 A. Bax, N. M. Szeverenyi and G. E. Maciel, *J. Magn. Reson.*, 1983, **51**, 400–408.
- 29 SOLA Topspin 3.2, Bruker, 2016.
- 30 D. Massiot, DmFit, 2011.
- 31 S. Hartmann and H. E., *Phys. Rev.*, 1962, **128**, 2042.
- 32 M. J. Duer, *Introduction to solid-state NMR spectroscopy*, Blackwell, 2004.
- 33 A. Bloom and J. Shoolery, *Phys. Rev.*, 1955, **97**, 1261–1265.
- 34 T. Bräuniger, P. Wormald and P. Hodgkinson, *Curr. Dev. Solid State NMR Spectrosc.*, 2002, **133**, 1549–1554.
- 35 B. M. Fung, A. K. Khitrin and K. Ermolaev, *J. Magn. Reson.*, 2000, **142**, 97–101.
- 36 E. F. Baxter, T. D. Bennett, C. Mellot-Draznieks, C. Gervais, F. Blanc and A. K. Cheetham, *Phys. Chem. Chem. Phys.*, 2015, **17**, 25191–25196.
- 37 S. L. Brace, P. Wormald and R. J. Darton, *Phys. Chem. Chem. Phys.*, 2015, **17**, 11950–11953.
- 38 N. C. Nielsen, L. A. Strassø and A. B. Nielsen, in *Solid-State NMR*, ed. J. Chan, Springer Berlin Heidelberg, 2011, pp. 1–45.
- 39 T. Bräuniger, P. Wormald and P. Hodgkinson, *Curr. Dev. Solid State NMR Spectrosc.*, 2002, **133**, 1549–1554.

3.0. Synthesis and Characterisation of Organic Structure Directing Agents and Pure Silica Zeolites

The successful synthesis of high silica zeolites has previously been obtained using various structure directing agents¹ and mineralising agents at low efficient temperatures (100 °C).² As discussed in Chapter 1 (Introduction), the increasing development of zeolite chemistry and the ZSM-5 (MFI) material since its discovery in 1972³ has laid the way for a plethora of research about ZSM-5 allowing for successful determination of the structure and properties. Despite the wealth of knowledge and studies surrounding this chemical system, the nucleation and growth mechanisms, as well as the effects of adapting synthetic methods or reaction conditions are still very poorly understood.^{4,5} A lot can be gained from the determination of information about this chemical system, and the high silica analogue; silicalite-1.

The nature of the structure directing agent required for a silicalite-1 zeolite syntheses are typically quaternary ammonium cations.⁶ Despite the relatively simple synthetic procedure, tetrapropylammonium iodide⁷ remains the dominant structure directing agent of choice for many studies of the silicalite-1 system, despite the existence of a more efficient structure directing agent, n-methyltributylammonium iodide (MTBA).⁸

With the exception of tetrapropylammonium cations, the quaternary ammonium cations required for structure directing agents are not sufficiently common materials to be available to purchase and must be synthesised for use. These quaternary ammonium species must be charge balanced for silicalite-1 syntheses, so quaternary ammonium halides have been used in this work. These quaternary ammonium halides were synthesised via an amine alkylation by S_N2 substitution reaction which involved the reaction of an alkyl halide with either a primary, secondary or tertiary amine, as shown in Figure 3.1:

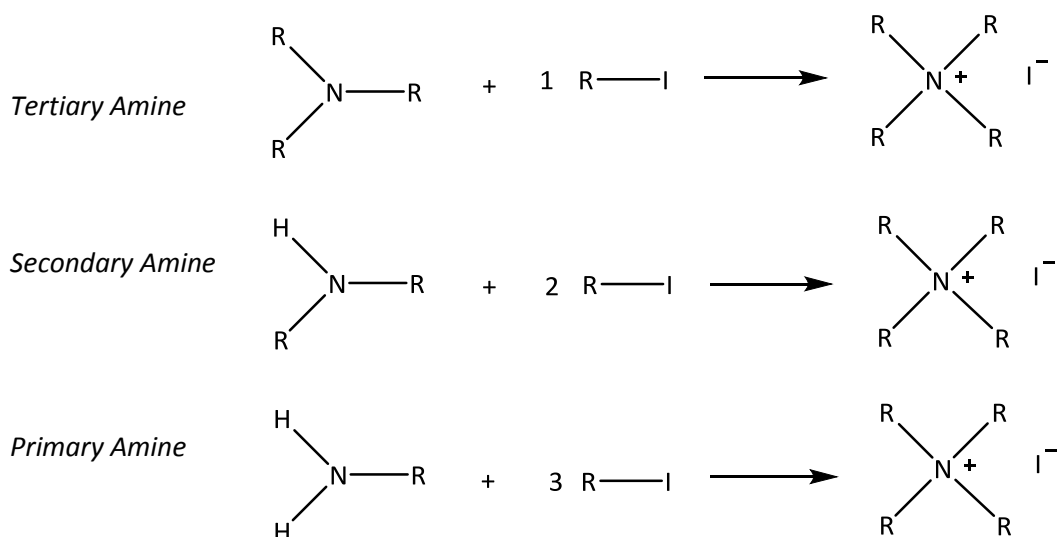


Figure 3.1 - Schematic reaction diagrams of an alkyl halide with primary, secondary and tertiary amines to give quaternary ammonium iodide species, required as SDA's

There have been reports of a difference in activity in zeolite synthesis from different quaternary ammonium halides.⁹ Despite this work reporting an increasing crystallisation time as you descend the halides, all SDA's were synthesised in the iodide form due to the availability of alkyl iodides and the ease in which they synthesise the quaternary ammonium SDA's required.

On the occasion that there was more than one method of synthesising the required quaternary ammonium iodide, the simplest synthetic route was chosen for maximum yield retrieval and ease. This was always the substitution using the smallest alkyl iodide with the largest alkyl amine. The substitution reaction occurred via a reflux reaction in methanol for increasing times dependant on the length of the alkyl halide.

In this work, the high-silica zeolite silicalite-1, (MFI framework) has been synthesised using a variety of different quaternary alkyl structure directing agents and mineralising agents for the purpose of identifying the characteristic differences in the zeolites formed.

3.1. Inorganic Pure Silica MFI Zeolites

Over recent years, a lot of focus has been given to finding new structure directing agents for zeolite syntheses as it has been established that altering the structure directing agent alkyl chain

length can affect the zeolite formed and the size of the channels and pores.¹⁰ In accordance with the findings of Zones and Nakagawa¹¹ the SDA C:N of 9-13:1 is used as a basis on which to begin. The initial works herein therefore use tetrapropylammonium iodide, the common SDA used to synthesise MFI zeolite¹² and n-methyltributylammonium iodide,⁸ another more efficient and recently discovered SDA for synthesising MFI zeolites.

Synthetic attempts of making pure silica MFI using the hydroxide route and a variety of SDAs has been attempted using the following reaction methods and vessels: Hydrothermal synthesis in 23 ml and 46 ml autoclaves and the dense-gel methods in 8 ml polypropylene bottles, 30 ml PFE bottles and 5.66 ml glass vials.

3.1.1. Hydroxide Route Synthetic Methods

Reaction methods used in this work follow synthetic methods retrieved from previously successful syntheses of MFI zeolites. Fyfe et al¹³ investigated different synthetic methods and reagent types for the effective and efficient synthesis of MFI zeolite. The methods used are summarised as in Table 3.1:

Table 3.1 - Table of synthetic methods for hydroxide route syntheses of MFI zeolite

Reaction Type/Vessel	Reaction Details
<u>1</u> <i>Dense-gel synthesis in 8 ml polypropylene bottle</i>	Method adapted from 'Sample B' in Fyfe et al ¹³ whereby sodium hydroxide was added as mineralising agent to reduce reaction time
<u>2</u> <i>Hydrothermal synthesis in 23 ml autoclave</i>	Synthetic method adapted from 'Sample K' in Fyfe et al ¹³ to include more water
<u>3</u> <i>Hydrothermal synthesis in 46 ml autoclave</i>	Synthetic method scaled up from 'Sample K' in Fyfe et al ¹³ and adapted from <u>2</u> , to include more water
<u>4</u> <i>Dense-gel synthesis in 30 ml polypropylene bottle</i>	Synthetic method replicated <u>1</u> , to investigate whether dehydration would occur in a different bottle type
<u>5</u> <i>Dense-gel synthesis in 5.66 ml glass vial</i>	Synthetic method scaled down from <u>1</u> , to investigate whether dehydration would occur in a different vessel type

On occasion, the reaction methods and molar compositions from Fyfe et al¹³ have been altered from the initial syntheses, dependant on the particular requirements or difficulties discovered. Examples of this include changing the reaction vessel type, vessel size, temperature of reaction

and length of oven time. This also included the addition of more distilled water to some larger structure directing agents such as TEHA, that crystallise MFI zeolite slower for the purpose of reducing the long term slow dehydration experienced.

3.1.2. Fluoride Route Synthetic Methods

Fluoride route syntheses used in this work also follow the comparative study of Fyfe et al¹³ and are summarised in Table 3.2.

Table 3.2 - Table of synthetic methods for fluoride route syntheses of MFI zeolite

Reaction Type/Vessel	Reaction Details
1 <i>Dense-gel synthesis in 8 ml polypropylene bottle</i>	Synthetic method from Sample N in Fyfe et al ¹³
2 <i>Hydrothermal synthesis in 23 ml autoclave</i>	Scaled down adaptation from Sample K in Fyfe et al ¹³ with increased water content
3 <i>Hydrothermal synthesis in 46 ml autoclave</i>	Adaptation from Sample K in Fyfe et al ¹³ with increased water content
4 <i>Dense-gel synthesis in 30 ml polypropylene bottle</i>	Scaled down adaptation from Sample K in Fyfe et al ¹³ with increased water content

These reaction methods, were also taken and adapted from initial MFI zeolite syntheses published by Fyfe et al.¹³ Similarly the samples were exposed to a variety of vessel types and sizes to attempt to reduce dehydration experienced in polypropylene bottles.

3.2. Successful Zeolite Structure Directing Agents

3.2.1. Synthesis of MFI using TPA⁺I⁻ - Tetrapropylammonium Iodide

SDA Synthesis: The structure directing agent TPA⁺I⁻ (Figure 3.2) is readily available for purchasing from Sigma-Aldrich and as such, did not require synthesising. It was characterised for purity before use as follows: ¹H NMR (300 MHz, CDCl₃, ppm) δ 3.42 (8H, m, N-CH₂-), 1.65 (8H, m, CH₂-CH₃), 1.15 (12H, s, (CH₂-CH₃)); ¹³C NMR (300MHz, CDCl₃,

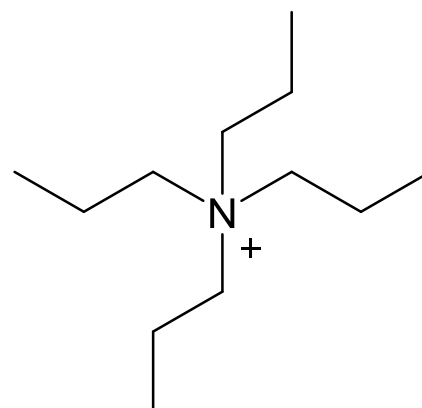


Figure 3.2 - Structure of TPA (tetrapropylammonium) cation SDA

ppm) δ 61.10 (N-CH₂-CH₂), 16.20 (N-CH₂-CH₂), 11.10 (CH₂-CH₃). The successful characterisation of TPA allowed for the next stage of synthesis of the MFI type zeolite.

Zeolite Synthesis: Zeolite MFI was synthesised using tetrapropylammonium iodide in a variety of different synthetic methods and reaction vessels.

Table 3.3 and Table 3.4 contain the details of all reactions attempted using the hydroxide and fluoride route respectively.

Table 3.3 - Hydroxide route table of conditions for the synthesis of MFI using TPA

Synthetic Method	Ludox 30% (g)	TP(3)A SDA (g)	H ₂ O (ml)	NaOH (ml)	Synthesis Time (days)	MFI Successful
<i>Exp 1.a. Hydroxide route hydrothermal crystallisation curve synthesis in 8 ml polypropylene bottle</i>						
<i>100 °C oven</i>						
Molar Composition	1.0 SiO ₂ : 0.14 TP(3)A: 26.03 H ₂ O: 0.13 NaOH					
Amount Used	3.0	0.66	3.0	2.0	Variable	Y
<i>Exp 1.b. Hydroxide route hydrothermal synthesis in 8 ml polypropylene bottle</i>						
<i>100 °C oven</i>						
Molar Composition	1.0 SiO ₂ : 0.15 TP(3)A: 18.60 H ₂ O: 0.13 NaOH					
Amount used	3.0	0.66	1.0	2.0	Variable	Y
<i>Exp 1.c. Hydroxide route dense-gel synthesis in 30 ml PFE bottle</i>						
<i>100 °C oven</i>						
Molar Composition	1.0 SiO ₂ : 0.14 TP(3)A: 18.20 H ₂ O: 0.13 NaOH					
Amount Used	3.0	0.65	1.0	2.0	5	Y
<i>Exp 1.d. Hydroxide route dense-gel synthesis in 5.66 ml screw top glass vial</i>						
<i>100 °C oven</i>						
Molar Composition	1.0 SiO ₂ : 0.17 TP(3)A: 0.16 NaOH: 29.82 H ₂ O					
Amount Used	2.0	0.43	2.0	1.33	5	Y

An example hydroxide route synthesis of MFI for crystallisation curves (*Exp 1.a*) using tetrapropylammonium iodide was prepared as follows: 0.66 g TPAI and 3.0 ml of distilled water were measured into an 8 ml narrow-mouth polypropylene bottle. 2.0 ml of 1M sodium hydroxide and 3.0 g of 30% Ludox LS were added to the bottle and the bottle mouth wrapped with PTFE tape before the lid was sealed. The bottle was mixed on a vortex mixer to before being placed in a 100 °C oven for the specified time.

Table 3.4 - Fluoride route table of conditions for the synthesis of MFI using TPA

Synthetic Method	Ludox 40% (g)	TP(3)A SDA (g)	H₂O (ml)	NH₄F (g)	Synthesis Time (days)	MFI Successful
<i>Exp.2.a. Fluoride route dense-gel crystallisation curve synthesis 8 ml polypropylene bottle 100 °C oven</i>						
Molar Composition	1 SiO ₂ : 0.09 TP(3)A: 8.34 H ₂ O: 0.68 NH ₄ F					
Amount Used	3.0	0.58	1.2	1.5	Variable	Y
<i>Exp.2.b. Fluoride route synthesis in 30 ml PFE bottle 100 °C oven</i>						
Molar Composition	1 SiO ₂ : 0.05 TP(3)A: 11.69 H ₂ O: 0.74 NH ₄ F					
Amount Used	1.65	0.47	5.79	0.75	Variable	Y
Synthetic Method	SiO₂ (g)	TP(3)A SDA (g)	H₂O (ml)	NH₄F (g)	Synthesis Time (days)	MFI Successful
<i>Exp.2.c. Fluoride route hydrothermal synthesis in 46 ml autoclave 180 °C oven</i>						
Molar Composition	1.0 SiO ₂ : 0.14 TP(3)A: 20.0 H ₂ O:1.0 NH ₄ F					
Amount Used	1.0	0.75	6.0	0.63	5	Y

Work-up: After removing the polypropylene bottle from the oven and allowing the content to cool to room temperature and pressure, the product was washed (30 ml distilled water) and centrifuged (3500 rpm, 15 minutes) three times yielding a white solid. The sample was then dried (60 °C, overnight) and confirmed as zeolite MFI by comparison of the XRD diffraction pattern obtained (Figure 3.3), to that published by IZA.¹⁴

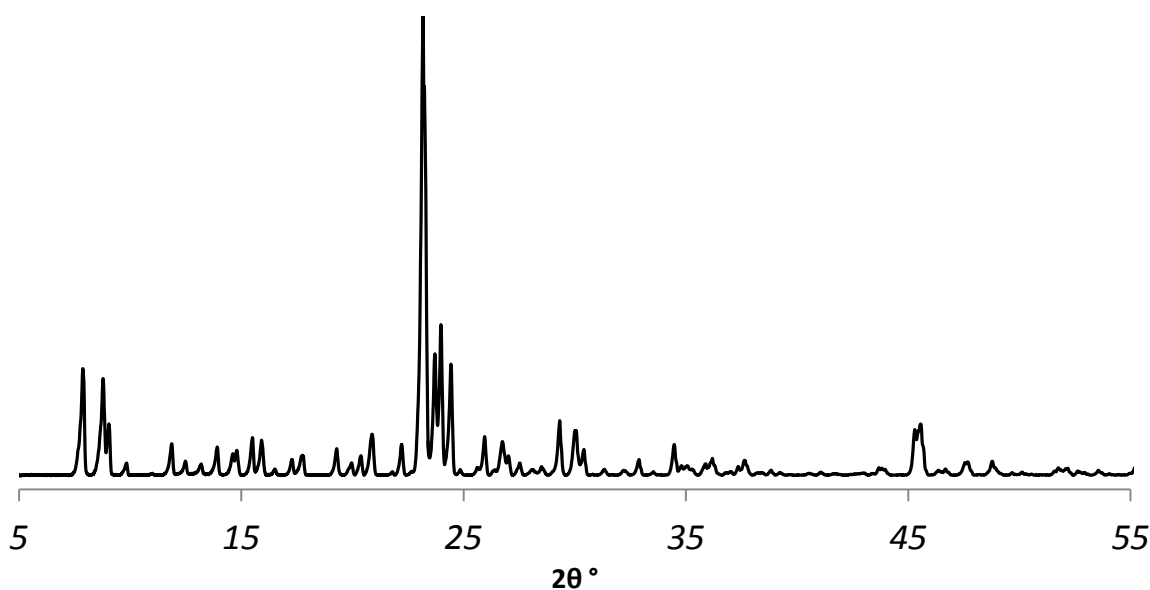


Figure 3.3 - XRD powder pattern of TPA/MFI on a Bruker Advance diffractometer with Cu K α source

3.2.2. Synthesis of MFI using MTBA⁺I⁻ - N-methyltributylammonium Iodide

SDA Synthesis: N-methyltributylammonium

Iodide (Figure 3.4) was synthesised by refluxing an excess of 1-iodomethane (11.4 g, 80.32 mmol) with tributylamine (6.61 g, 35.68 mmol) in 100 ml methanol for 24 hours. After reflux, the methanol was removed under reduced pressure and the

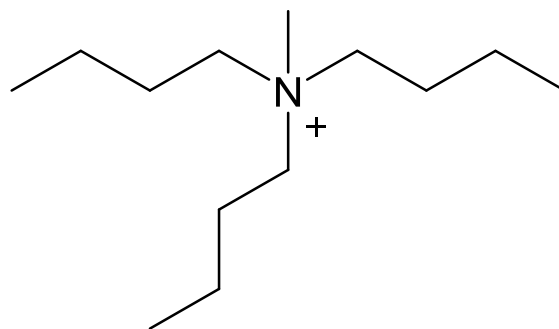


Figure 3.4 - Structure of MTB (methyltributylammonium) cations SDA

product was recrystallised from a mixture of ethyl acetate and a minimum amount of ethanol to remove any soluble impurities. White crystals were obtained (9.8853 g, 84.50 %) and characterised as follows: ¹H NMR (300 MHz, CDCl₃, ppm) δ 3.45 (6H, m, N-CH₂), 3.32 (3H, s, N-CH₃), 1.40 (6H, m, CH₂-CH₂-CH₂), 1.45 (6H, m, CH₂-CH₂-CH₃), 1.05 (9H, s, CH₂-CH₃); ¹³C NMR (300MHz, CDCl₃, ppm) δ 61.77 (N-CH₂-CH₂), 49.27 (N-CH₃), 24.45 (N-CH₂-CH₂), 19.67 (CH₂-CH₂-CH₃), 13.85 (CH₂-CH₂-CH₃).

Zeolite Synthesis: Zeolite MFI was synthesised using n-methyltributylammonium iodide in a variety of different synthetic methods and reaction vessels. Table 3.5 and Table 3.6 contain the details of all reaction methods attempted using the hydroxide and fluoride route respectively.

Table 3.5 - Hydroxide route table of conditions for the synthesis of MFI using MTBA

Synthetic Method	Ludox 30% (g)	MTBA SDA (g)	H ₂ O (ml)	NaOH (ml)	Synthesis Time (days)	MFI Successful
<i>Exp.3.a. Hydroxide route dense-gel crystallisation curve synthesis in 8 ml polypropylene bottles 100 °C oven</i>						
Molar Composition	1.0 SiO ₂ : 0.14 MTBA: 26.50 H ₂ O: 0.13 NaOH					
Amount Used	3	0.66 g	3	2	Variable	Y
<i>Exp.3.b. Hydroxide route dense-gel synthesis in 8 ml polypropylene bottle 100 °C oven</i>						
Molar Composition	1.0 SiO ₂ : 0.16 MTBA: 18.60 H ₂ O: 0.13 NaOH					
Standard Synthesis	3.0	0.78	1	2	10	Y
+ 1 ml H ₂ O	3.0	0.78	2	2	10	Y
+ 2 ml H ₂ O	3.0	0.78	3	2	10	Y
+ 3 ml H ₂ O	3.0	0.78	4	2	10	Y
<i>Exp.3.c. Hydroxide route dense-gel synthesis in 5.66 ml glass vial 100 °C oven</i>						
Molar Composition	1.0 SiO ₂ : 0.17 MTB: 0.16 NaOH: 29.82 H ₂ O					
Amount Used	2.0	0.52	2.0	1.33	5	Y

An example hydroxide route synthesis (*Exp.3.b.*) of MFI using n-methyltributylammonium iodide as was prepared as follows: 0.52 g of MTBAI and 2.0 ml of distilled water were added to a an 8 ml narrow-mouth polypropylene bottle with 1.33 ml of 1M sodium hydroxide and 2.0 g of 30% Ludox LS. The contents were mixed on a vortex mixer and subsequently placed in a 100 °C oven for 5 days.

Table 3.6 - Fluoride route table of conditions for the synthesis of MFI using MTBA

Synthetic Method	Ludox LS 40 % (g)	MTBA SDA (g)	H₂O (ml)	NH₄F (g)	Synthesis Time (days)	MFI Successful
<i>Exp.4.a. Fluoride route dense-gel crystallisation curve synthesis in 8 ml polypropylene bottles 100 °C oven</i>						
Molar Composition	1.0 SiO ₂ : 0.08 MTBA: 8.34 H ₂ O: 2.0 NH ₄ F					
Amount Used	3.0	0.50	1.2	1.5	Variable	Y
Synthetic Method	SiO₂ (g)	MTBA SDA (g)	H₂O (ml)	NH₄F (g)	Synthesis Time (days)	MFI Successful
<i>Exp.4.b. Fluoride route hydrothermal synthesis in 46 ml autoclave 180 °C oven</i>						
Molar Composition	1.0 SiO ₂ : 0.08 MTBA: 20.02 H ₂ O: 1.0 NH ₄ F					
23 ml Autoclave	1.0	0.43	6.0	0.62	6	Y
23 ml autoclave	1.0	0.43	6.0	0.62	10	Y
46 ml autoclave	2.0	0.83	12.0	1.23	7	Y
Synthetic Method	SiO₂ (g)	MTBA SDA (g)	H₂O (ml)	(NH₄)HF₂ (g)	Synthesis Time (days)	MFI Successful
<i>Exp.4.c. Fluoride route hydrothermal synthesis in 46 ml autoclave 100 °C oven</i>						
Molar Composition	1.0 SiO ₂ : 0.08 MTBA: 20.0 H ₂ O: 1.00 (NH ₄)HF ₂					
Amount Used	1.0	0.43	6.0	0.95	21	N
	2.0	0.83	12.0	1.23	7	Y

Work-up: After removing the glass vial from the oven and allowing the content to cool to room temperature and pressure, the product was washed (30 ml distilled water) and centrifuged (3500 rpm, 15 minutes) three times yielding a white solid. The sample was later dried (60 °C, overnight) and confirmed as zeolite MFI by comparison of the XRD diffraction pattern obtained (Figure 3.5), to that published by the International Zeolite Association.¹⁴

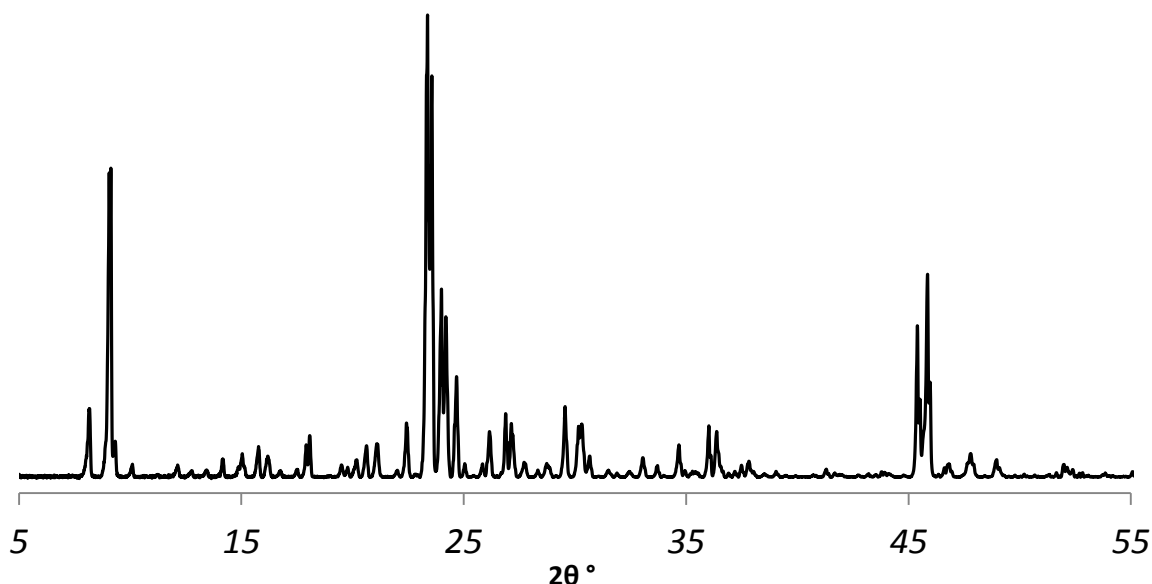


Figure 3.5 - XRD powder pattern of MTBA/MFI on a Bruker Advance diffractometer with Cu K α source

3.2.3. Synthesis of MFI using ETBA+I⁻ - N-ethyltributylammonium Iodide

SDA Synthesis: n-ethyl-tributylammonium iodide (Figure 3.6) was synthesised by refluxing 1-iodoethane (3.85 g, 24.88 mmol) and tributylamine (3.88 g, 24.88 mmol) in 100 ml methanol for 48 hours.

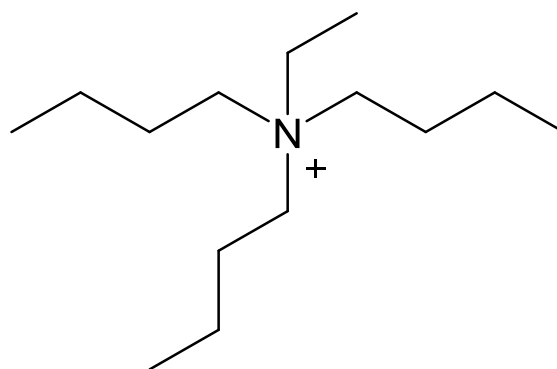


Figure 3.6 - Structure of ETB (n-ethyl-triethylammonium) cation SDA

After reflux, the methanol was removed under reduced pressure and the product

was recrystallised from a mixture of ethyl acetate and a minimum amount of ethanol to remove any soluble impurities. White crystals were obtained (6.05 g, 39.23 %) and characterised as follows: ¹H NMR (300 MHz, CDCl₃, ppm) δ 3.51 (2H, m, N-CH₂-CH₃), 3.32 (6H, m, N-CH₂-CH₂), 1.68 (N-CH₂-CH₂), 1.45 (6H, m, N-CH₂-CH₂-CH₂), 1.40 (3H, m, N-CH₂-CH₃), 1.10 (9H, m, CH₂-CH₂-CH₃); ¹³C NMR (300MHz, CDCl₃, ppm) δ 58.46 (N-CH₂-CH₂), 54.85 (N-CH₂-CH₃), 24.16 (N-CH₂-CH₂), 19.72 (CH₂-CH₂-CH₃), 13.68 (CH₂-CH₂-CH₃), 8.47 (N-CH₂-CH₃).

Zeolite Synthesis: Zeolite MFI was synthesised using n-ethyltributylammonium iodide in a variety of different synthetic methods and reaction vessels. Table 3.7 contains the details of all reaction

methods attempted using the fluoride route.

Table 3.7 - Fluoride route table of conditions for the synthesis of MFI using ETBA

Synthetic Method	SiO ₂ (g)	ETBA (g)	H ₂ O (ml)	NH ₄ F (g)	Synthesis Time (days)	MFI Successful
<i>Exp 5. a. Fluoride route hydrothermal synthesis in 46 ml autoclave 180 °C oven</i>						
Molar Composition	1.0 SiO ₂ : 0.08 ETBA: 20.02 H ₂ O: 1.0 NH ₄ F					
Amount Used	1.0	0.45	6.0	0.62	5	Y
	2.0	0.91	12.0	1.23	5	Y
	2.0	0.91	12.0	1.23	7	Y
<i>Exp 5. b. Fluoride route dense-gel synthesis with autoclave recipe in 8 ml plastic bottle 100 °C oven</i>						
Molar Composition	1.0 SiO ₂ : 0.08 ETBA: 20.0 H ₂ O: 1.62 NH ₄ F					
Amount Used	1.0	0.46	6.0	1.0	5	N (D)
	1.0	0.46	6.0	1.0	25	Y

An example hydrothermal fluoride route synthesis (Exp 5. a.) of MFI using N-ethyltributylammonium iodide as an SDA was prepared as follows: 0.46 g of ETBA and 1.0 g ammonium fluoride were added to a 23 ml Teflon lined stainless steel autoclave liner. 6.0 ml of distilled water and 2.0 g of silicon dioxide were added to the mixture and stirred thoroughly to form a thick gel before being the autoclave was sealed and placed in a 180 °C oven for 5 days.

Work-up: After removing the autoclave from the oven and allowing the content to cool to room temperature and pressure. The product was washed (30 ml distilled water) and centrifuged (3500 rpm, 15 minutes) three times yielding a white solid. The sample was later dried (60 °C, overnight) and confirmed as zeolite MFI by comparison of the XRD diffraction pattern obtained (Figure 3.7), to that published by International Zeolite Association.¹⁴

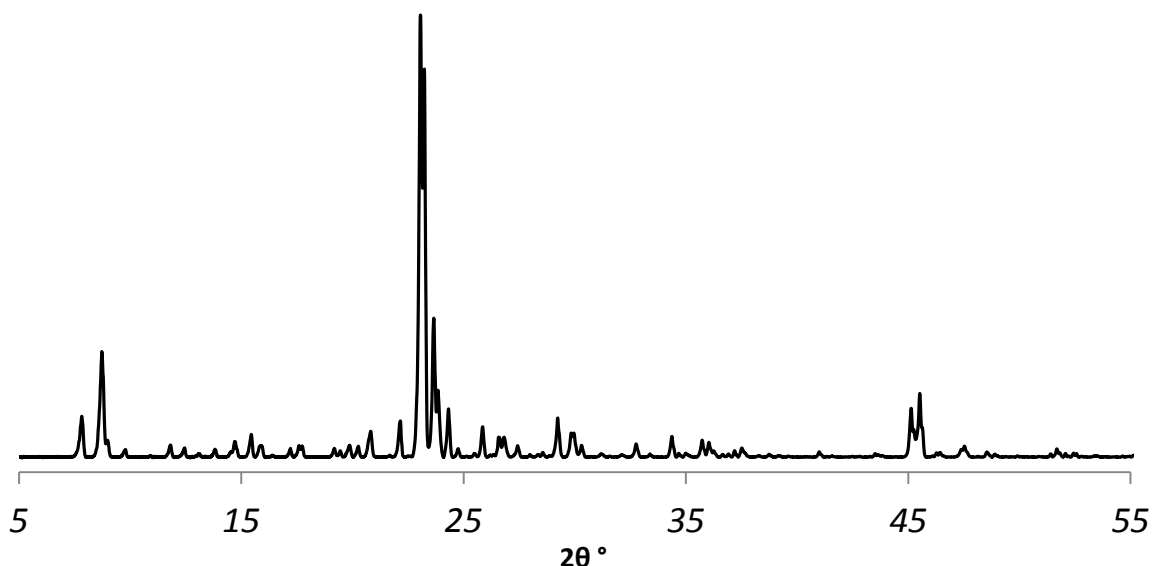


Figure 3.7 - XRD powder pattern of ETBA/MFI on a Bruker Advance diffractometer with Cu K α source

3.2.4. Synthesis of MFI using P(5)TBA⁺I⁻ - N-pentyltributylammonium Iodide

SDA Synthesis: The SDA N-pentyltributylammonium iodide (Figure 3.8) was synthesised by refluxing tributylamine (6.22 g, 33.58 mmol) and 1-iodopentane (6.65 g, 33.58 mmol) in 100 ml methanol for 5 days. The methanol was removed under reduced pressure and the product was recrystallised with a mixture of ethyl acetate and a minimum

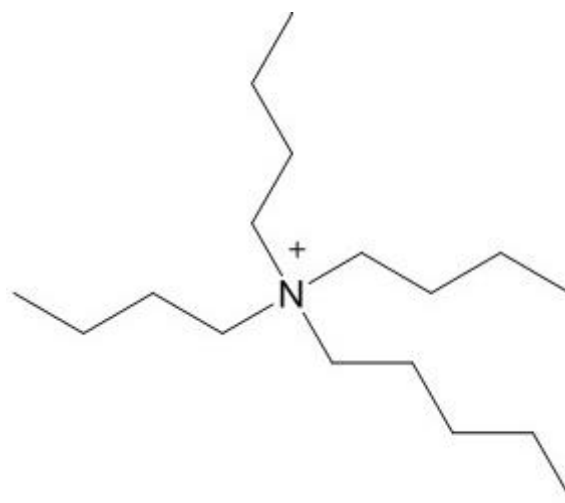


Figure 3.8 - Structure of P5TBA (pentyltributylammonium) cation SDA

amount of ethanol to remove any soluble impurities. White crystals were obtained (5.62 g, 43.66 %) and characterised as follows: ¹H NMR (300 MHz, CDCl₃, ppm) δ 3.29 (6H, m, N-CH₂-CH₂)₃, 3.25 (2H, m, N-CH₂-CH₂), 1.59 (6H, m, N-CH₂-CH₂)₃, 1.58 (2H, w, N-CH₂-CH₂), 1.36 (6H, m, CH₂-CH₂-CH₃)₃, 1.30 (2H, m, CH₂-CH₂-CH₃), 1.27 (2H, w, CH₂-CH₂-CH₃), 0.90 (6H, s, CH₂-CH₃)₃, 0.81 (3H, m, CH₂-CH₃); ¹³C NMR (300MHz, CDCl₃, ppm) δ 59.23 (N-CH₂), 59.07 (N-CH₂)₃, 28.31 (N-CH₂-CH₂), 24.25 (N-CH₂-CH₂)₃, 22.20 (CH₂-CH₂-CH₃), 22.05 (CH₂-CH₂-CH₃), 19.73 (CH₂-CH₂-CH₃)₃, 13.80 (CH₂-CH₃), 13.71 (CH₂-CH₃)₃.

Zeolite Synthesis: Zeolite MFI was synthesised using N-pentyltributylammonium iodide in a variety of different synthetic methods and reaction vessels. Table 3.8 and Table 3.9 contain the details of all reaction methods attempted using the hydroxide and fluoride route respectively.

Table 3.8 - Hydroxide route table of conditions for MFI zeolites synthesised using P(5)TBA

Synthetic Method	Ludox 30% (g)	P(5)TBA SDA (g)	H ₂ O (ml)	NaOH (ml)	Synthesis Time (days)	MFI Successful
Exp 6.a. Hydroxide route dense-gel method for crystallisation curves in 8 ml polypropylene bottle						
100 °C oven						
Molar Composition	1.0 SiO ₂ : 0.14 P(5)TBA: 18.20 H ₂ O: 0.13 NaOH					
Amount Used	3.0	0.77	1.0	2.0	7	Y

An example hydroxide route dense-gel synthesis (Exp 6.a.) of MFI using n-pentyltributylammonium iodide as was prepared as follows: 0.77 g P(5)TBAI was added to an 8 ml narrow-mouth polypropylene bottle with 1.0 ml of distilled water. 2.0 ml of 1M sodium hydroxide and 3.0 g of 30 % Ludox LS was added to the bottle of reactants and the bottle mouth wrapped with PTFE tape before the lid was sealed as tightly as possible. The bottle was placed on a vortex mixer to mix the reagents before being placed in a 100 °C oven for the specified time.

Table 3.9 - Fluoride route table of conditions for MFI zeolites synthesised using P(5)TBA

Synthetic Method	SiO ₂ (g)	P(5)TBA SDA (g)	H ₂ O (ml)	NH ₄ F (g)	Synthesis Time (days)	MFI Successful
<i>Exp 7. a. Hydroxide route hydrothermal synthesis in an 46 ml autoclave 100 °C oven</i>						
Molar Composition	1.0 SiO ₂ : 0.08 P(5)TBA: 20.02 H ₂ O: 1.0 NH ₄ F					
Amount Used	1.0	0.51	6.0	0.62	7	N
	2.0	1.02	12.0	1.23	7	Y
<i>Exp 7. b. Fluoride route hydrothermal synthesis in 23 ml autoclave 180 °C oven</i>						
Molar Composition	1.0 SiO ₂ : 0.08 P(5)TBA: 20.0 H ₂ O: 1.0 NH ₄ F					
Amount Used	1.0	0.46	6.0	1.0	5	N (D)
Synthetic Method	SiO ₂ (g)	P(5)TBA SDA (g)	H ₂ O (ml)	(NH ₄)HF ₂ (g)	Synthesis Time (days)	MFI Successful
<i>Exp 7. c. Fluoride route hydrothermal synthesis in 23 ml autoclave 100 ° oven</i>						
Molar Composition	1.0 SiO ₂ : 0.08 P(5)TBA: 20.0 H ₂ O: 1.00 NH ₄ HF					
Amount Used	1.0	0.51	6.0	0.95	21	N

Work-up: After removing the polypropylene bottle from the oven and allowing the content to cool to room temperature and pressure, the product was washed (30 ml distilled water) and centrifuged (3500 rpm, 15 minutes) three times yielding a white solid. The sample was later dried (60 °C, overnight) and confirmed as zeolite MFI by comparison of the XRD diffraction pattern obtained (Figure 3.9), to that published by International Zeolite Association.¹⁴

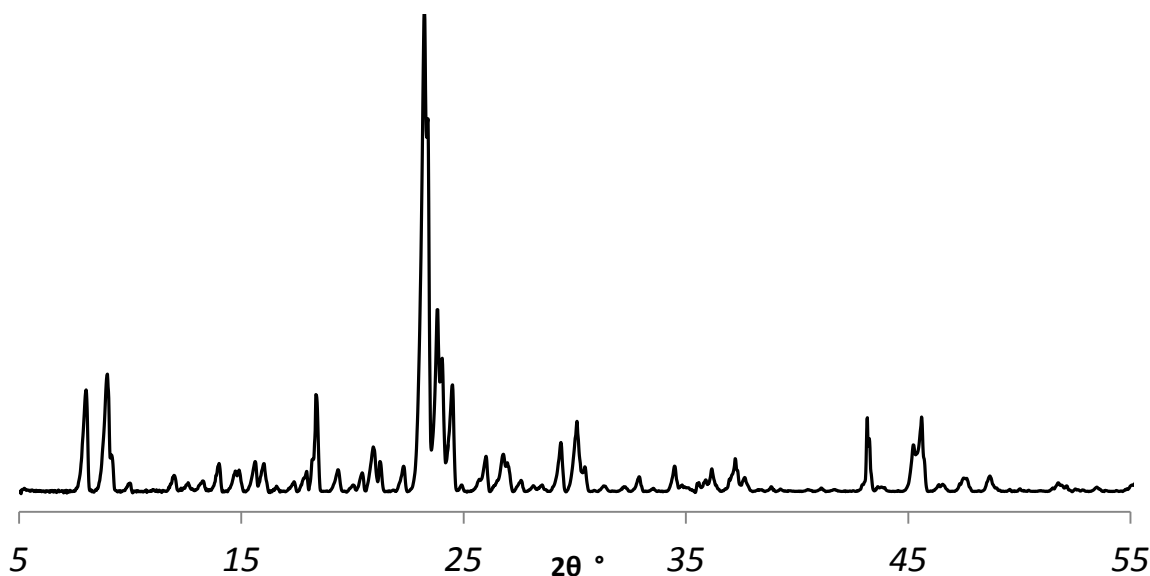


Figure 3.9 - XRD powder pattern of P(5)TBA/MFI on a Bruker Advance diffractometer with Cu K α source

3.2.5. Synthesis of MFI using H(6)TBAI - N-hexyltribuylammonium Iodide

SDA Synthesis: The SDA n-hexyltribuylammonium iodide (Figure 3.10) was synthesised by refluxing tributylamine (12 g, 647.4 mmol) and 1-iodohexane (13.73 g, 647.4 mmol) in 100 ml methanol for 5 days.

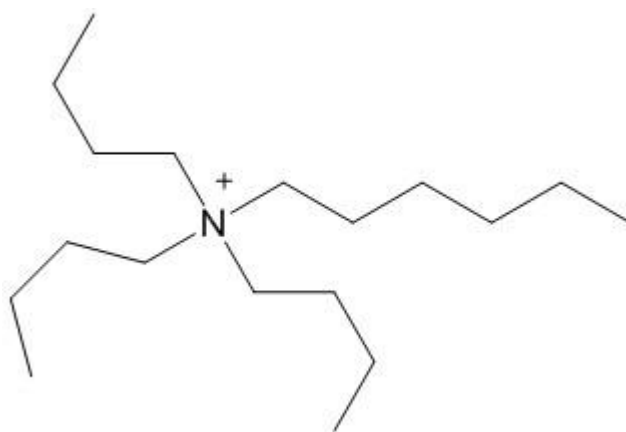


Figure 3.10 - Structure of H6TBA (n-hexyltribuylammonium) cation SDA

After reflux, the methanol was removed under reduced pressure

and the product was recrystallised using a mixture of ethyl acetate and a minimum amount of ethanol to remove any soluble impurities. White crystals were obtained (14.34 g, 57.18 %) and characterised as follows: ^1H NMR (300 MHz, CDCl_3 , ppm) δ 3.56 (6H, t, N- $\text{CH}_2\text{-CH}_2\text{-CH}_2\text{-CH}_3$), 3.32 (2H, t, N- $\text{CH}_2\text{-CH}_2\text{-CH}_2\text{-CH}_2$), 1.72 (2H, m(5), N- $\text{CH}_2\text{-CH}_2\text{-CH}_2\text{-CH}_2$), 1.67 (6H, m(5), N- $\text{CH}_2\text{-CH}_2\text{-CH}_2\text{-CH}_3$), 1.46 (6H, m(6), N- $\text{CH}_2\text{-CH}_2\text{-CH}_2\text{-CH}_3$), 1.36 (2H, m(5), N- $\text{CH}_2\text{-CH}_2\text{-CH}_2\text{-CH}_2$), 1.33 (2H, m(5), N- $\text{CH}_2\text{-CH}_2\text{-CH}_2\text{-CH}_2$), 1.31 (2H, m(6), $\text{CH}_2\text{-CH}_2\text{-CH}_2\text{-CH}_2\text{-CH}_3$), 1.00 (9H, t, N- $\text{CH}_2\text{-CH}_2\text{-CH}_2\text{-CH}_3$), 0.88 (3H, t, $\text{CH}_2\text{-CH}_2\text{-CH}_2\text{-CH}_2\text{-CH}_3$); ^{13}C NMR (300MHz, CDCl_3 , ppm) δ 59.35 (N- $\text{CH}_2\text{-CH}_2\text{-CH}_2\text{-CH}_2$), 59.20 (N- $\text{CH}_2\text{-CH}_2\text{-CH}_2\text{-CH}_3$), 32.21 ($\text{CH}_2\text{-CH}_2\text{-CH}_2\text{-CH}_2\text{-CH}_3$), 26.07 (N- $\text{CH}_2\text{-CH}_2\text{-CH}_2\text{-CH}_2$), 24.32 (N- $\text{CH}_2\text{-CH}_2\text{-CH}_2\text{-CH}_3$), 22.44 (N- $\text{CH}_2\text{-CH}_2\text{-CH}_2\text{-CH}_2$), 22.37 ($\text{CH}_2\text{-CH}_2\text{-CH}_2\text{-CH}_2\text{-CH}_3$), 19.80 (N- $\text{CH}_2\text{-CH}_2\text{-CH}_2\text{-CH}_3$), 14.00 ($\text{CH}_2\text{-CH}_2\text{-CH}_2\text{-CH}_2\text{-CH}_3$), 13.68 (N- $\text{CH}_2\text{-CH}_2\text{-CH}_2\text{-CH}_3$).

Zeolite Synthesis: Zeolite MFI was synthesised using n-hexyltribuylammonium iodide in a variety of different synthetic methods and reaction vessels. Table 3.10 and Table 3.11 contain the details of all reactions attempted using the hydroxide and fluoride route respectively.

Table 3.10 - Hydroxide route table of conditions for the synthesis of MFI synthesised using H(6)TBA

Synthetic Method	Ludox 30% (g)	H(6)TBA SDA (g)	H ₂ O (ml)	NaOH (ml)	Synthesis Time (days)	MFI Successful
<i>Exp. 8.a. Hydroxide route dense-gel crystallisation curve synthesis in 8 ml polypropylene bottles</i>						
100 °C oven						
Molar Composition	1.0 SiO ₂ : 0.16 H(6)TBA: 0.13 NaOH: 18.60 H ₂ O					
Amount Used	3.0	0.95	1.0	2.0	Variable	Y
	3.0	0.79	1.0	2.0	Variable	N
<i>Exp.8.b. Hydroxide route dense-gel synthesis in 8 ml polypropylene bottle</i>						
100 °C oven						
Molar Composition	1.0 SiO ₂ : 0.16 H(6)TBA: 18.60 H ₂ O: 0.13 NaOH					
Amount Used	3.0	0.95	1.0	2.0	10	N
+2 ml	3.0	0.95	3.0	2.0	10	N
<i>Exp.8.c. Hydroxide route hydrothermal synthesis in 46 ml autoclave</i>						
100 °C oven						
Molar Composition	1.0 SiO ₂ : 0.14 H(6)TBA: 18.60 H ₂ O: 0.13 NaOH					
Amount Used	3.0	0.82	1.0	2.0	14	N
<i>Exp.8.d. Hydroxide route hydrothermal synthesis in 46 ml autoclave</i>						
180 °C oven						
Molar Composition	1.0 SiO ₂ : 0.14 H(6)TBA: 18.60 H ₂ O: 0.13 NaOH					
Amount Used	3.0	0.82	1.0	2.0	7	Y

An example hydroxide route synthesis for crystallisation curves (*Exp.8.b.*) of MFI using n-hexyltributylammonium iodide as was prepared as follows: 0.95 g H(6)TBAI was added to an 8 ml narrow-mouth polypropylene bottle with 1.0 ml of distilled water. 2.0 ml of 1M sodium hydroxide and 3.0 g of 30 % Ludox LS were added to the bottle of reactants and the bottle mouth wrapped with PTFE tape before the lid was sealed as tightly as possible. The bottle was mixed on a vortex mixer before the bottle placed in a 100 °C oven for the specified time.

Table 3.11 - Fluoride route table of conditions for the synthesis of MFI synthesised using H(6)TBA

Synthetic Method	Ludox 40% (g)	H(6)TBA SDA (g)	H₂O (ml)	NH₄F (ml)	Synthesis Time (days)	MFI Successful
<i>Exp.9.a. Fluoride route dense-gel synthesis in 8 ml polypropylene bottles 100 °C oven</i>						
Molar Composition	1.0 SiO ₂ : 0.15 H(6)TBA: 8.34 H ₂ O: 2.03 NH ₄ F					
Amount Used	3.0	1.16	1.2	1.5	10	N
Molar Composition	1.0 SiO ₂ : 0.08 H(6)TBA: 8.34 H ₂ O: 2.00 NH ₄ F					
Amount Used	3.0	0.64	1.2	1.5	10	Peaks forming
Synthetic Method	SiO₂ (g)	H(6)TBA SDA (g)	H₂O (ml)	NH₄F (g)	Synthesis Time (days)	MFI Successful
<i>Exp.9.b. Fluoride route dense-gel synthesis in 8 ml polypropylene bottle 100 ° oven</i>						
Molar Composition	1.0 SiO ₂ : 0.08 H(6)TBA: 20.0 H ₂ O: 1.0 NH ₄ F					
Amount Used	1.0	0.53	6.0	0.62	15	Y
	1.0	0.95	6.0	0.62	10	N
Synthetic Method	SiO₂ (g)	H(6)TBA SDA (g)	H₂O (ml)	(NH₄)HF₂ (g)	Synthesis Time (days)	MFI Successful
<i>Exp.9.c. Fluoride route hydrothermal synthesis in 23 ml autoclave 100 °C oven</i>						
Molar Composition	1.0 SiO ₂ : 0.08 H(6)TBA: 20.0 H ₂ O: 1.00 (NH ₄)HF ₂					
Amount Used	1.0	0.52	6.0	0.95	21	N
	1.0	0.80	6.0	0.95	35	N
<i>Exp.9.d. Fluoride route hydrothermal autoclave synthesis in 46 ml autoclave 180 °C oven</i>						
Molar Composition	1.0 SiO ₂ : 0.08 H(6)TBA: 20.0 H ₂ O: 1.0 (NH ₄)HF ₂					
Amount Used	1.0	0.53	6.0	0.62	6	N

Work-up: After removing the polypropylene bottle from the oven and allowing the content to cool to room temperature and pressure, the product was washed (30 ml distilled water) and centrifuged (3500 rpm, 15 minutes) three times yielding a white solid. The sample was later dried (60 °C, overnight) and confirmed as zeolite MFI by comparison of the XRD diffraction pattern obtained (Figure 3.11), to that published by IZA International Zeolite Association.¹⁴

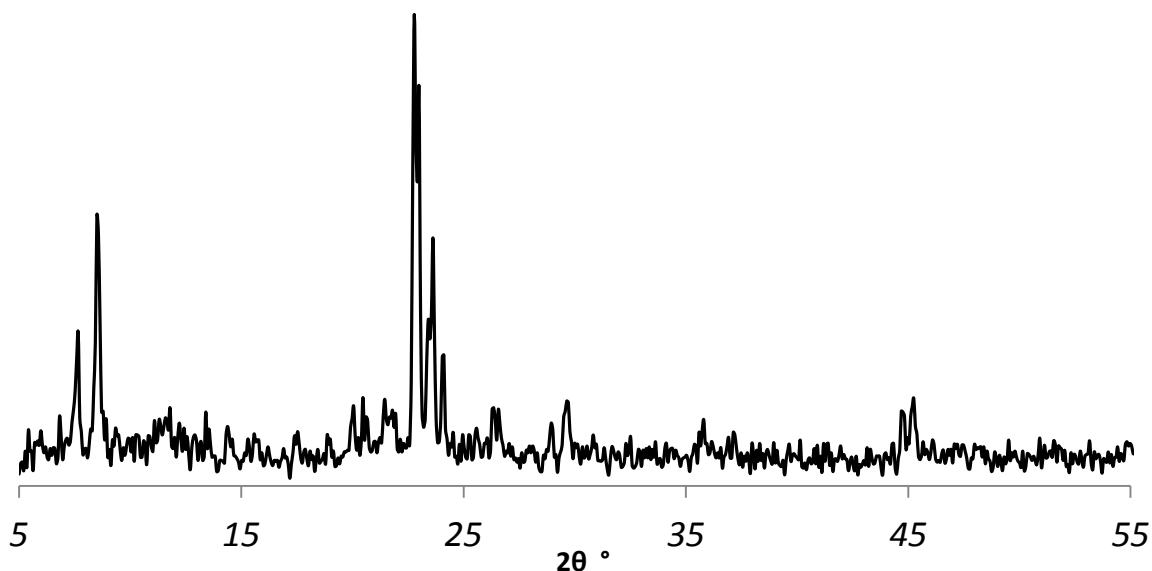


Figure 3.11 - XRD powder pattern of H(6)TBA/MFI on a Bruker Advance diffractometer with Cu K α source

3.2.6. Synthesis of MFI using MTPA⁺I⁻ - N-methyltripropylammonium Iodide

SDA Synthesis: The SDA n-methyl-tripropylammonium iodide (Figure 3.12) was synthesised by refluxing an excess of 1-iodomethane (18.24 g, 128.5 mmol) with tripropylamine (10.54 g, 73.58 mmol) in 100 ml methanol for 24 hours. After reflux, the methanol was removed under reduced pressure and the product was recrystallised with a mixture of ethyl acetate and a minimum amount of ethanol to remove any soluble impurities.

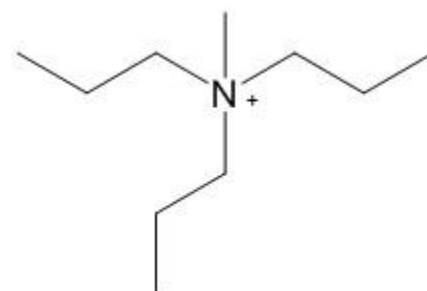


Figure 3.12 - Structure of MTP3A (methyltri-propylammonium) cation SDA

White crystals were obtained (18.86 g, 89.86 %) and characterised as follows: ^1H NMR (300 MHz, CDCl_3 , ppm) δ 3.35 (6H, t, N- CH_2 - CH_2), 3.20 (3H, s, N- CH_3), 1.72 (6H, m, CH_2 - CH_2 - CH_3), 0.97 (9H, t, CH_2 - CH_3); ^{13}C NMR (300MHz, CDCl_3 , ppm) δ 63.61 (N- CH_2 - CH_2), 49.33 (N- CH_3), 16.16 (CH_2 - CH_2 - CH_3), 10.80 (CH_2 - CH_3).

Zeolite Synthesis: Zeolite MFI was synthesised using n-methyltri-propylammonium iodide in a variety of different synthetic methods and reaction vessels. Table 3.12 and Table 3.13 contain the details of all reactions attempted using the hydroxide and fluoride route respectively.

Table 3.12 - Hydroxide route table of conditions for the synthesis of MFI using MTP(3)

Synthetic Method	Ludox 30% (g)	MTP(3) SDA (g)	H ₂ O (ml)	NaOH (ml)	Synthesis Time (days)	MFI Successful
<i>Exp 10. a. Hydroxide route dense-gel crystallisation curves synthesis in 8 ml polypropylene bottles</i>						
<i>100 °C oven</i>						
Molar Composition	1.0 SiO ₂ : 0.13 MTP(3): 18.20 H ₂ O: 0.13 NaOH					
Amount Used	3.0	0.56	1.0	2.0	Variable	Y
<i>Exp 10. b. Hydroxide route hydrothermal synthesis in 46 ml autoclave</i>						
<i>180 °C oven</i>						
Molar Composition	1.0 SiO ₂ : 0.13 MTP(3): 18.20 H ₂ O: 0.13 NaOH					
Amount Used	3.0	0.56	1.0	2.0	9	Y

An example fluoride route synthesis of MFI using n-methyltriethylammonium iodide as an SDA was prepared as follows: 0.36 g of MTP(3)A and 0.62 g ammonium fluoride were added to a 8 ml narrow-mouth polypropylene bottle. 6.0 ml of distilled water and 1.0 g of silicon dioxide was added to the mixture and stirred thoroughly to form a thick gel. The bottle was then mixed on a vortex mixer to ensure the reagents were homogeneously mixed before being placed in a 100 °C oven for 15 days.

Table 3.13 - Fluoride route table of conditions for the synthesis of MFI using MTP(3)A

Synthetic Method	Ludox 40% (g)	MTP(3)A SDA (g)	H ₂ O (ml)	NH ₄ F (g)	Synthesis Time (days)	MFI Successful
<i>Exp 11. a. Fluoride route dense-gel crystallisation curve synthesis in 8 ml polypropylene bottles</i>						
<i>100 °C oven</i>						
Molar Composition	1.0 SiO ₂ : 0.09 MTP(3): 8.34 H ₂ O: 0.68 NH ₄ F					
Amount Used	3.0	0.56	1.2	1.5	Variable	Y
	3.0	0.82	1.2	1.5	Variable	Y
Synthetic Method	SiO ₂ (g)	MTP(3)A SDA (g)	H ₂ O (ml)	NH ₄ F (g)	Synthesis Time (days)	MFI Successful
<i>Exp 11. a. Fluoride route dense-gel standard synthesis in 8 ml polypropylene bottles</i>						
<i>100 °C oven</i>						
Molar Composition	1.0 SiO ₂ : 0.08 MTP(3)A: 20.0 H ₂ O: 1.0 NH ₄ F					
Amount Used	1.0	0.36	6.0	0.62	15	Y

Work-up: After removing the plastic bottle from the oven and allowing the content to cool to room temperature, the product was washed (30 ml distilled water) and centrifuged (3500 rpm, 15 minutes) three times yielding a white solid. The sample was later dried (60 °C, overnight) and

confirmed as zeolite MFI by comparison of the XRD diffraction pattern obtained (Figure 3.13) to that published by International Zeolite Association.¹⁴

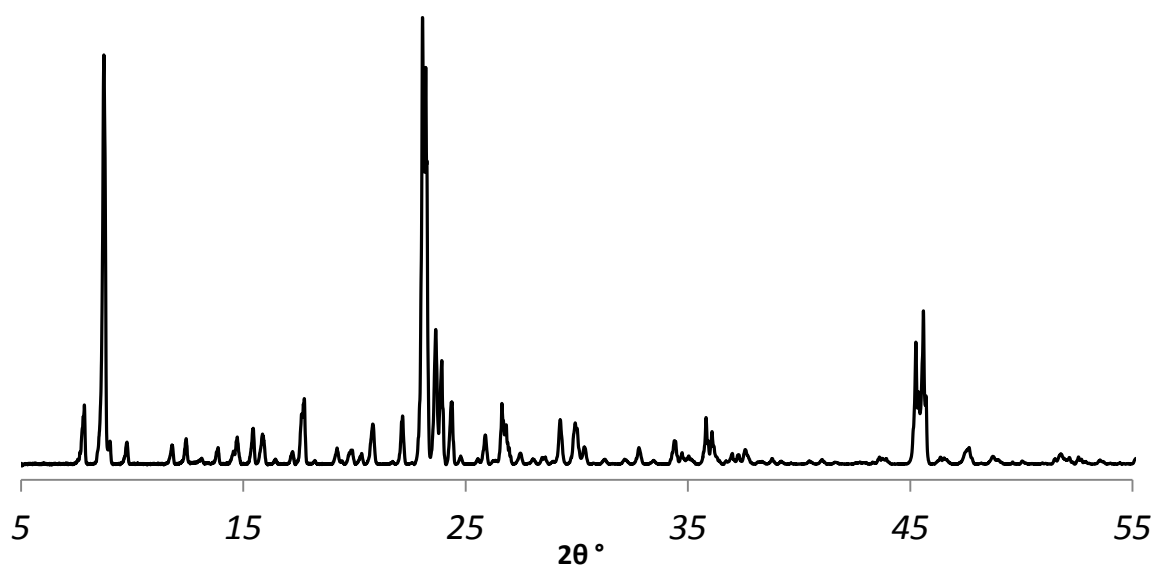


Figure 3.13 - XRD powder pattern of MTP3A/MFI on a Bruker Advance diffractometer with Cu Kα source

3.2.7. Synthesis of MFI using ETPA+I⁻ - N-ethyltripropylammonium Iodide

SDA Synthesis: The SDA N-ethyl-tripropylammonium iodide (Figure 3.14) was synthesised by refluxing 1-iodoethane (8.20 g, 52.56 mmol) and tripropylamine (7.53 g, 52.56 mmol) in 100 ml methanol for 48 hours. After reflux, the methanol was removed under reduced pressure and the product was recrystallised with a mixture of ethyl acetate and a minimum amount of ethanol to remove any

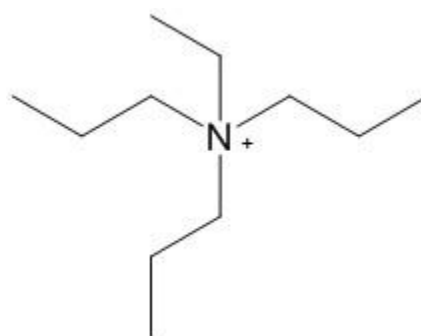


Figure 3.14 - Structure of ETP3A (ethyltripropylammonium) cation SDA

soluble impurities. White crystals were obtained (9.29 g, 57.51 %) and characterised as follows: ¹H NMR (300 MHz, CDCl₃, ppm) δ 3.42 (2H, m, N-CH₂-CH₃), 3.21 (6H, m, N-CH₂-CH₂), 1.66 (6H, m, CH₂-CH₂-CH₃), 1.27 (3H, m, CH₂-CH₃), 0.94 (9H, s, CH₂-CH₃); ¹³C NMR (300MHz, CDCl₃, ppm) δ 60.19 (N-CH₂-CH₂), 54.91 (N-CH₂-CH₃), 15.95 (CH₂-CH₂-CH₃), 10.91 (CH₂-CH₃), 8.46 (N-CH₂-CH₃).

Zeolite Synthesis; Zeolite MFI was synthesised using N-ethyltripropylammonium iodide in a variety of different synthetic methods and reaction vessels. Table 3.14 and Table 3.15 contain

the details of all reactions attempted using the hydroxide and fluoride route, respectively.

Table 3.14 - Hydroxide Route table of conditions for the synthesis of MFI using ETP(3)A

Synthetic Method	Ludox 30% (g)	ETP(3) SDA (g)	H ₂ O (ml)	NaOH (ml)	Synthesis Time (days)	MFI Successful
<i>Exp.12.a. Hydroxide route dense-gel crystallisation curve synthesis in 8 ml polypropylene bottle 100 °C oven</i>						
Molar Composition	1.0 SiO ₂ : 0.13 ETP(3): 18.20 H ₂ O: 0.13 NaOH					
Amount Used	3.0	0.60	1.0	2.0	Variable	Y
<i>Exp.12.b. Hydroxide route hydrothermal synthesis in 46 ml autoclave 240 °C oven</i>						
Molar Composition	1.0 SiO ₂ : 0.13 ETP(3): 18.20 H ₂ O: 0.13 NaOH					
Amount Used	3.0	0.60	1.0	2.0	8	N

An example dense-gel hydroxide route synthesis (Exp.12.a.) of MFI using N-ethyltripropylammonium iodide as an SDA was prepared as follows: 0.60 g of ETP(3)AI and 2.0 ml (1M) sodium hydroxide were added to an 8 ml narrow-mouth polypropylene bottle. 1.0 ml of distilled water and 3.0 g of 30 % Ludox LS was added to the mixture and stirred thoroughly to form a thick homogenous gel. The bottle was sealed and placed in a 100 °C oven for the specified time.

Table 3.15 - Fluoride route table of conditions for the synthesis of MFI using ETP(3)A

Synthetic Method	Ludox 30% (g)	ETP(3) SDA (g)	H ₂ O (ml)	NH ₄ F (g)	Synthesis Time (days)	MFI Successful
<i>Exp.13 a. Fluoride dense-gel crystallisation curves synthesis in 8ml polypropylene bottles 100 °C oven</i>						
Molar Composition	1.0 SiO ₂ : 0.09 ETP(3): 8.34 H ₂ O: 0.68 NH ₄ F					
Amount Used	3.0	0.56	1.2	1.5	Variable	Y
<i>Exp.13. b. Fluoride route hydrothermal synthesis in 23 ml autoclave 100 °C oven</i>						
Molar Composition	1.0 SiO ₂ : 0.08 ETP(3)A: 20.0 H ₂ O: 1.54 NH ₄ F					
Amount Used	1.0	0.65	6.0	0.62	37	N

Work-up: After removing the polypropylene bottle from the oven and allowing the content to cool to room temperature and pressure, the product was washed (30 ml distilled water) and centrifuged (3500 rpm, 15 minutes) three times yielding a white solid. The sample was later dried

(60 °C, overnight) and confirmed as zeolite MFI by comparison of the XRD diffraction pattern obtained (Figure 3.15), to that published by International Zeolite Association.¹⁴

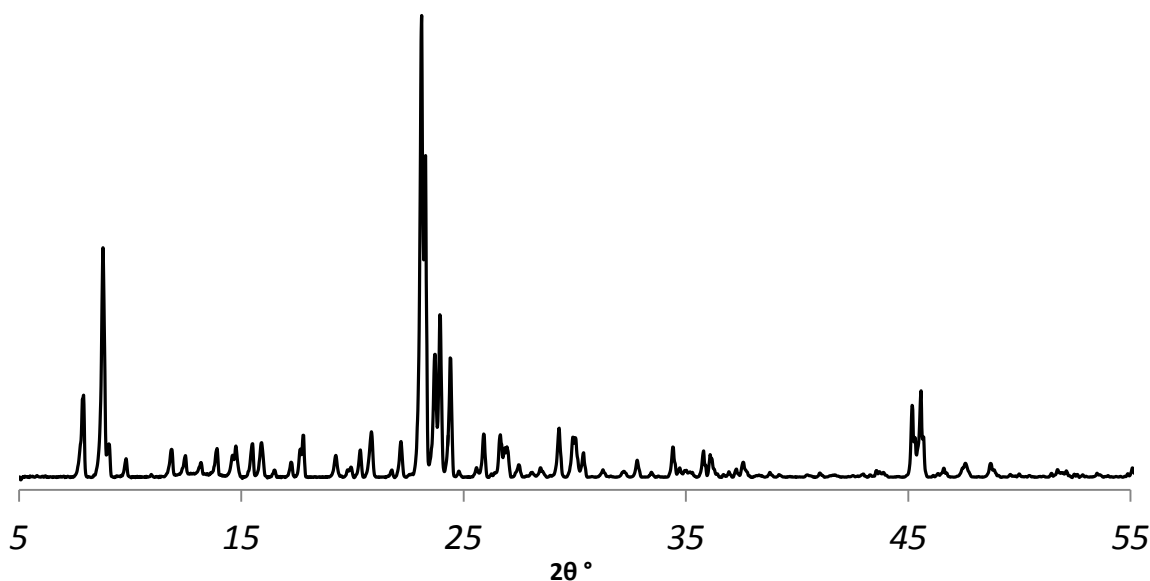


Figure 3.15 - XRD powder pattern of ETP3A/MFI on a Bruker Advance diffractometer with Cu K α source

3.2.8. Synthesis of MFI using BTP(3)A⁺I⁻ – N-butyltripropylammonium Iodide

SDA Synthesis: The SDA n-butyltripropylammonium iodide (Figure 3.16) was synthesised by refluxing iodobutane (9.69 g, 52.56 mmol) and tripropylamine (7.53 g, 52.56 mmol) in 50 ml methanol for 4 days. After reflux, the methanol was removed under reduced pressure

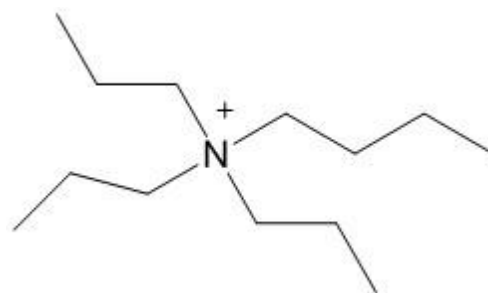


Figure 3.16 - Structure of BTP3A (N-butyltripropylammonium) cation SDA

and the product was recrystallised using ethyl acetate and a minimum amount of ethanol to remove any soluble impurities. White crystals were obtained (11.59 g, 67.45 %) and characterised as follows: ¹H NMR (300 MHz, CDCl₃, ppm) δ 3.36 (2H, t, CH₂-CH₂-CH₂), 3.31 (6H, t, N-CH₂-CH₂-CH₃), 1.75 (6H, m(6), N-CH₂-CH₂-CH₃), 1.66 (2H, m(5), N-CH₂-CH₂-CH₂), 1.43 (2H, m(6), CH₂-CH₂-CH₂-CH₃), 1.07 (6H, t, N-CH₂-CH₂-CH₃), 0.97 (2H, t, CH₂-CH₂-CH₂-CH₃). ¹³C NMR (300MHz, CDCl₃, ppm) δ 60.86 (N-CH₂-CH₂-CH₂), 59.27 (N-CH₂-CH₂-CH₃), 24.30 (N-CH₂-CH₂-CH₂), 19.78 (N-CH₂-CH₂-CH₂), 16.13 (N-CH₂-CH₂-CH₃), 13.77 (CH₂-CH₂-CH₂-CH₃), 10.97 (N-CH₂-CH₂-CH₃).

Zeolite Synthesis: Zeolite MFI was synthesised using n-butyltripropylammonium iodide in a variety of different synthetic methods and reaction vessels. Table 3.16 and Table 3.17 contain the details of all reactions attempted using the hydroxide and fluoride route respectively.

Table 3.16 - Hydroxide route table of conditions for MFI synthesised using BTP(3)A

Synthetic Method	Ludox 30% (g)	BTP(3)A SDA (g)	H ₂ O (ml)	NaOH (ml)	Synthesis Time (days)	MFI Successful
<i>Exp.14.a. Hydroxide route dense-gel method for crystallisation curves in 8 ml polypropylene bottle</i>						
<i>100 °C oven</i>						
Molar Composition	1.0 SiO ₂ : 0.06 BTP(3)A: 11.16 H ₂ O: 0.06 NaOH					
Amount Used	3.0	0.64	1.0	2.0	Variable	Y
Molar Composition	1.0 SiO ₂ : 0.06 BTP(3)A: 18.60 H ₂ O: 0.06 NaOH					
Amount Used	3.0	0.64	3.0	2.0	Variable	Y

An example fluoride route crystallisation curve synthesis of MFI using n-butyltripropylammonium iodide as an SDA was prepared as follows: 0.60 g of BTP(3)AI and 1.50 g ammonium fluoride were added to a 8 ml narrow-mouth polypropylene bottle. 6 ml of distilled water and 3.0 g of 30 % Ludox LS were added to the mixture and stirred thoroughly to form a thick gel. The bottle was mixed on the vortex mixer for 5 seconds before being placed in a 100 °C oven for the specified synthesis time.

Table 3.17 - Fluoride route table of conditions for MFI synthesised using BTP(3)

Synthetic Method	Ludox 40% (g)	BTP(3)A SDA (g)	H ₂ O (ml)	NH ₄ F (g)	Synthesis Time (days)	MFI Successful
<i>Exp 15.a. Fluoride route hydrothermal crystallisation curves synthesis in 8 ml polypropylene bottles</i>						
<i>100 °C oven</i>						
Molar Composition	1.0 SiO ₂ : 0.09 BTP(3)A: 8.34 H ₂ O: 0.68 NH ₄ F					
Amount Used	3.0	0.60	1.2	1.5	Variable	Y
Molar Composition	1.0 SiO ₂ : 0.12 BTP(3)A: 17.22 H ₂ O: 2.7 NH ₄ F					
Amount Used	2.25	0.60	3.3	1.5	Variable	Y
Synthetic Method	SiO ₂ (g)	BTP(3)A SDA (g)	H ₂ O (ml)	NH ₄ F (g)	Synthesis Time (days)	MFI Successful
<i>Exp.15. b. Fluoride route hydrothermal synthesis in 46 ml autoclave</i>						
<i>180 °C oven</i>						
Molar Composition	1.0 SiO ₂ : 0.08 BTP(3)A: 20.0 H ₂ O: 1.0 NH ₄ F					
Amount Used	2.0	0.87	12.0	1.23	6	Peaks forming
SDA dissolved first	2.0	0.87	12.0	0.68	6	Y
<i>Exp.15.c. Fluoride route hydrothermal synthesis in 8 ml polypropylene bottles</i>						
<i>100 °C oven</i>						
Molar Composition	1.0 SiO ₂ : 0.08 BTP(3)A: 20.0 H ₂ O: 1.0 NH ₄ F					
Amount Used	1.0	0.43	6.0	0.62	15	Y

Work-up: After removing the plastic bottle from the oven and allowing the content to cool to room temperature and pressure, the product was washed (30 ml distilled water) and centrifuged (3500 rpm, 15 minutes) three times yielding a white solid. The sample was later dried (60 °C, overnight) and confirmed as zeolite MFI by comparison of the XRD diffraction pattern obtained (Figure 3.17) to that published by International Zeolite Association.¹⁴

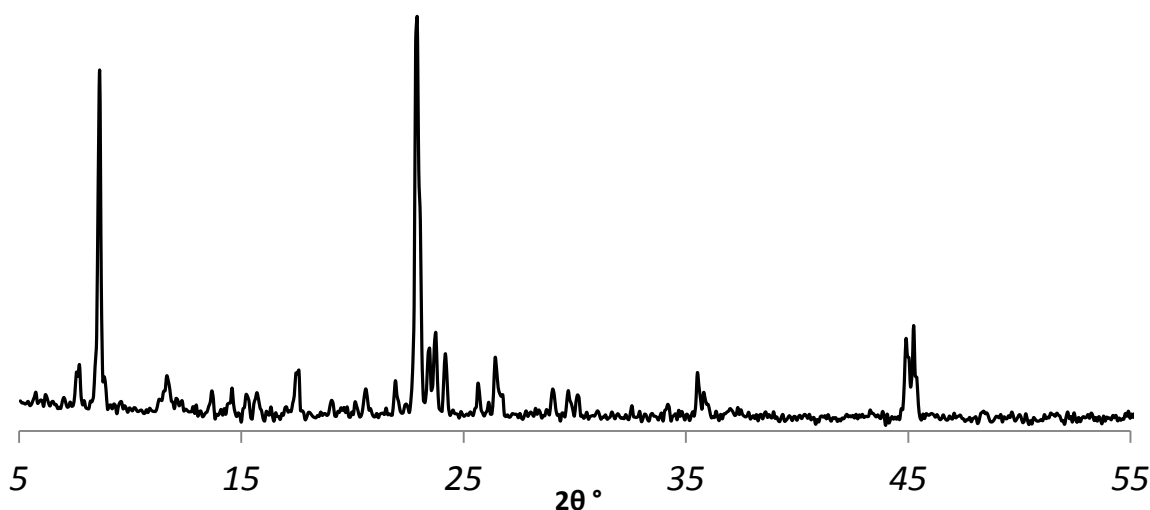


Figure 3.17 - XRD powder pattern of BTP(3)A/MFI on a Bruker Advance diffractometer with Cu Kα source

3.2.9. Synthesis of MFI using P5TP3A+I⁻ - N-pentyltripropylammonium Iodide

SDA Synthesis: The SDA n-pentyl-tripropylammonium iodide (Figure 3.18) was synthesised by refluxing iodopentane (9.10 g, 45.98 mmol) and tripropylamine (6.58 g, 45.98 mmol) in 100 ml methanol for 4 days. After reflux, the methanol was removed under

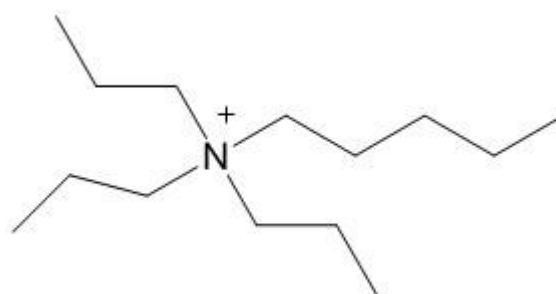


Figure 3.18 - Structure of P5TP3A (Pentyltripropylammonium) cation SDA

reduced pressure and the product was recrystallised with a mixture of ethyl acetate and a minimum amount of ethanol to remove any soluble impurities. White crystals (3.46 g, 21.77 %) were obtained and characterised as follows: ¹H NMR (300 MHz, CDCl₃, ppm) δ 3.28 (6H, t, N-CH₂-CH₂-CH₃), 3.25 (2H, t, N-CH₂-CH₂-CH₂), 1.68 (6H, m(6), N-CH₂-CH₂-CH₃), 1.62 (2H, m(5), N-CH₂-CH₂-CH₃), 1.30 (2H, m(5), N-CH₂-CH₂-CH₂), 1.28 (2H, m(6), CH₂-CH₂-CH₂-CH₃), 0.96 (9H, t, N-CH₂-CH₂-CH₃), 0.81 (3H, t, CH₂-CH₂-CH₂-CH₃).

¹³C NMR (300MHz, CDCl₃, ppm) δ 60.08 (N-CH₂-CH₂-CH₃), 59.46 (N-CH₂-CH₂-CH₂), 22.29 (N-CH₂-CH₂-CH₂-CH₂), 22.10 (N-CH₂-CH₂-CH₂), 16.10 (CH₂-CH₂-CH₂-CH₃), 13.90 (N-CH₂-CH₂-CH₃), 11.28 (CH₂-CH₂-CH₂-CH₃), 10.95 (N-CH₂-CH₂-CH₃).

Zeolite Synthesis: Zeolite MFI was synthesised using n-pentyltripropylammonium iodide in a variety of different synthetic methods and reaction vessels. Table 3.18 and Table 3.19 contain the details of all reactions attempted using the hydroxide and fluoride route, respectively.

Table 3.18 - Hydroxide route table of conditions for the synthesis of MFI using P(5)TP(3)

Synthetic Method	Ludox 30% (g)	P(5)TP(3)A SDA (g)	H ₂ O (ml)	NaOH (ml)	Synthesis Time (days)	MFI Successful
<i>Exp 16. a. Hydroxide route dense-gel synthesis in 8 ml polypropylene bottle 100 °C oven</i>						
Molar Composition	1.0 SiO ₂ ; 0.16 P(5)P(3)A: 26.0 H ₂ O: 0.13 NaOH					
Amount Used	3.0	0.81	3.0	2.0	12	Y
<i>Exp 16. b. Hydroxide route dense-gel crystallisation curves synthesis in 8 ml polypropylene bottle 100 °C oven</i>						
Molar Composition	1.0 SiO ₂ ; 0.11 P(5)TP(3)A: 18.60 H ₂ O: 0.13 NaOH					
Amount Used	3.0	0.55	1.0	2.0	Variable	Y

An example fluoride route dense-gel synthesis (*Exp.17b.*) of MFI using n-pentyltripropylammonium iodide as an SDA was prepared as follows: 0.47 g of P(5)TP(3)AI and 0.62 g ammonium fluoride were added to a 23 ml Teflon lined stainless steel autoclave liner. 6.0 ml of distilled water and 1.0 g of silicon dioxide were added to the mixture and stirred thoroughly to form a thick gel before the autoclave was sealed and placed in a 100 °C oven for 25 days.

Table 3.19 - Fluoride route table of conditions for the synthesis of MFI using P(5)TP(3)

Synthetic Method	Ludox 40% (g)	P(5)TP(3)A SDA (g)	H₂O (ml)	NH₄F (g)	Synthesis Time (days)	MFI Successful
<i>Exp.17.a. Fluoride route dense-gel synthesis in 8 ml polypropylene bottle 100 °C oven</i>						
Molar Composition	1.0 SiO ₂ : 0.08 P(5)TP(3)A: 8.34 H ₂ O: 2.0 NH ₄ F					
Amount Used	3.0	0.55	1.2	1.5	7	Y
Synthetic Method	SiO₂ (g)	P(5)TP(3)A SDA (g)	H₂O (ml)	NH₄F (g)	Synthesis Time (days)	MFI Successful
<i>Exp.17.b. Fluoride route hydrothermal synthesis in 23 ml autoclave 100 °C oven</i>						
Molar Composition	1.0 SiO ₂ : 0.08 P(5)TP(3)A: 20.0 H ₂ O: 1.0 NH ₄ F					
Amount Used	1.0	0.47	6.0	0.62	25	Peaks forming
	1.0	0.81	4.0	0.62	12	N (D)

Work-up: After removing the autoclave from the oven and allowing the content to cool to room temperature and pressure, the product was washed (30 ml distilled water) and centrifuged (3500 rpm, 15 minutes) three times yielding a white solid. The sample was later dried (60 °C, overnight) and confirmed as zeolite MFI by comparison of the XRD diffraction pattern obtained (Figure 3.19), to that published by International Zeolite Association.¹⁴

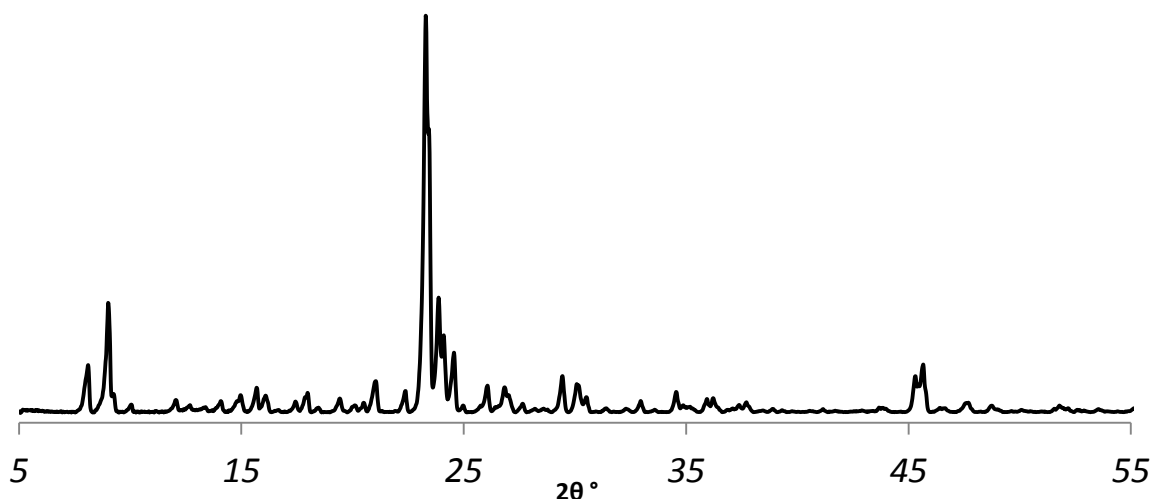


Figure 3.19 - XRD powder pattern of P(5)TP(3)A/MFI on a Bruker Advance diffractometer with Cu K α source

3.2.10. Synthesis of MFI using H(6)TP(3)A – N-hexyltripropylammonium Iodide

SDA Synthesis: The SDA n-hexyltripropylammonium iodide (Figure 3.20) was synthesised by refluxing tripropylamine (7.19 g, 33.88 mmol) and 1-iodohexane (4.85 g, 33.88

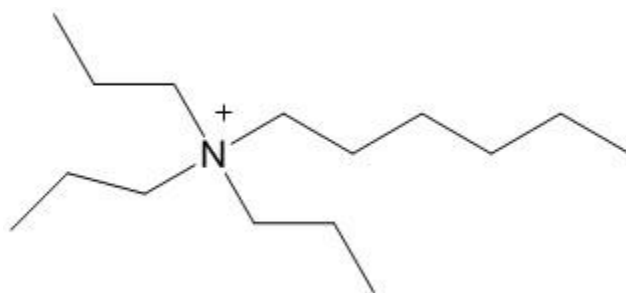


Figure 3.20 - Structure of H6TP3A (Hexyltripropylammonium) cation SDA

mmol) in 100ml methanol for 6 days.

The methanol was removed under reduced pressure and the product was recrystallised with a mixture of ethyl acetate and a minimum amount of ethanol to remove any soluble impurities. White crystals (1.27 g, 10.54 %) were obtained and characterised as follows: ^1H NMR (300 MHz, CDCl_3 , ppm) δ 3.37 (2H, t, N-CH $_2$ -CH $_2$ -CH $_2$), 3.33 (6H, t, N-CH $_2$ -CH $_2$ -CH $_3$), 1.79 (6H, m(6), N-CH $_2$ -CH $_2$ -CH $_3$), 1.72 (2H, m(5), N-CH $_2$ -CH $_2$ -CH $_2$), 1.40 (2H, t, N-CH $_2$ -CH $_2$ -CH $_2$), 1.36 (2H, t, CH $_2$ -CH $_2$ -CH $_2$ -CH $_2$), 1.31 (2H, t, CH $_2$ -CH $_2$ -CH $_2$ -CH $_3$), 1.07 (9H, t, N-CH $_2$ -CH $_2$ -CH $_3$), 0.90 (3H, t, CH $_2$ -CH $_2$ -CH $_2$ -CH $_3$).

^{13}C NMR (300MHz, CDCl_3 , ppm) δ 60.94 (N-CH $_2$ -CH $_2$ -CH $_3$), 59.52 (N-CH $_2$ -CH $_2$ -CH $_2$), 31.25 (CH $_2$ -CH $_2$ -CH $_2$ -CH $_3$), 26.10 (N-CH $_2$ -CH $_2$ -CH $_2$), 22.45 (N-CH $_2$ -CH $_2$ -CH $_2$), 22.41 (CH $_2$ -CH $_2$ -CH $_2$ -CH $_3$), 16.15 (N-CH $_2$ -CH $_2$ -CH $_3$), 13.92 (N-CH $_2$ -CH $_2$ -CH $_3$), 10.97 (CH $_2$ -CH $_2$ -CH $_2$ -CH $_3$).

Zeolite Synthesis: Zeolite MFI was synthesised using n-hexyltripropylammonium iodide in a variety of different synthetic methods and reaction vessels. Table 3.20 and Table 3.21 contain the details of all reactions attempted using the hydroxide and fluoride route respectively.

Table 3.20 - Hydroxide route table of conditions for the synthesis of MFI using H(6)TP(3)A

Synthetic Method	Ludox 30% (g)	H(6)TP(3)A SDA (g)	H ₂ O (ml)	NaOH (ml)	Synthesis Time (days)	MFI Successful
<i>Exp.18.a. Hydroxide route dense-gel synthesis in 8 ml polypropylene bottle 100 °C oven</i>						
Molar Composition	1.0 SiO ₂ : 0.13 H(6)TP(3)A: 26.0 H ₂ O: 0.13 NaOH					
Amount Used	3.0	0.71	3.0	2.0	9	Y
	3.0	0.71	1.0	2.0	9	Y

An example hydroxide route synthesis (*Exp.18.a.*) of MFI using n-hexyltripropylammonium iodide as an SDA was prepared as follows: 0.71 g of H(6)TP(3)AI and 2.0 ml (1 M) sodium hydroxide were added to a 8 ml narrow-mouth polypropylene bottle. 1.0 ml of distilled water and 3.0 g of 30 % Ludox LS were added to the mixture and stirred thoroughly to form a thick gel. The bottle was then mixed on the vortex mixer for 5 seconds before being placed in a 100 °C oven for the specified synthesis time.

Table 3.21 - Fluoride route table of conditions for the synthesis of MFI synthesised using H(6)TP(3)A

Synthetic Method	Ludox 40% (g)	H(6)TP(3)A SDA (g)	H ₂ O (ml)	NH ₄ F (g)	Synthesis Time (days)	MFI Successful
<i>Exp 19. a. Fluoride route dense-gel synthesis in 8 ml polypropylene bottle 100 °C oven</i>						
Molar Composition	1.0 SiO ₂ : 0.15 H(6)TP(3)A: 8.34 H ₂ O: 0.68 NH ₄ F					
Amount Used	2.52	0.87	1.0	1.04	9	1/2
Synthetic Method	SiO ₂ (g)	H(6)TP(3)A SDA (g)	H ₂ O (ml)	NH ₄ F (g)	Synthesis Time (days)	MFI Successful
<i>Exp 19. b. Fluoride route hydrothermal synthesis in 23 ml autoclave 100 °C oven</i>						
Molar Composition	1.0 SiO ₂ : 0.14 H(6)TP(3)A: 20.0 H ₂ O: 1.0 NH ₄ F					
Amount Used	1.0	0.85	6.0	0.62	9	N

Work-up: After removing the polypropylene bottle from the oven and allowing the content to cool to room temperature and pressure, the product was washed (30 ml distilled water) and centrifuged (3500 rpm, 15 minutes) three times yielding a white solid. The sample was later dried

(60 °C, overnight) and confirmed as zeolite MFI by comparison of the XRD diffraction pattern obtained (Figure 3.21) to that published by International Zeolite Association.¹⁴

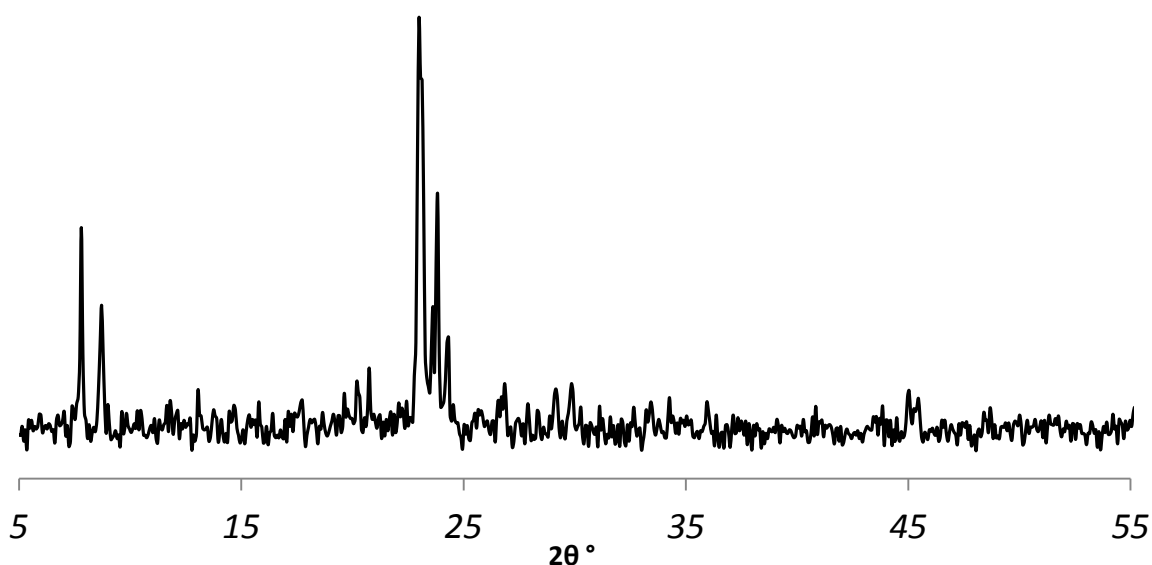


Figure 3.21 - XRD powder pattern of H(6)TP(3)A/MFI on a Bruker Advance diffractometer with Cu K α source

3.2.11. Synthesis of MFI using H(7)TP3A⁺I⁻ - N-heptyltripropylammonium Iodide

SDA Synthesis: The SDA n-heptyltripropylammonium iodide (Figure 3.22) was synthesised by refluxing iodoheptane (4.85 g, 33.88 mmol) and tripropylamine

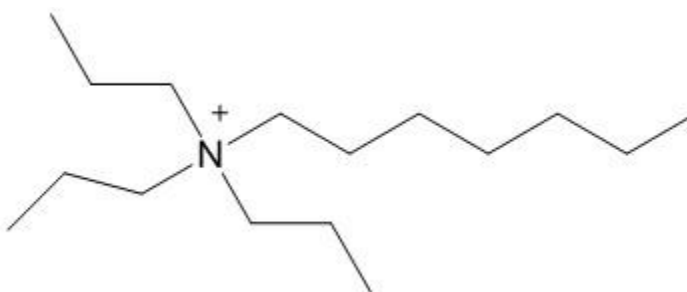


Figure 3.22 - Structure of H(7)TP3A (Heptyltripropylammonium) cation

(7.19 g, 33.88 mmol) in 50 ml methanol for 7 days. After reflux, the methanol was removed under reduced pressure and the product was recrystallised with a mixture of ethyl acetate and a minimum amount of ethanol to remove any soluble impurities.

White crystals were obtained (1.27 g, 10.56 %) and characterised as follows: ^1H NMR (300 MHz, CDCl_3 , ppm) δ 3.34 (6H, t, N- $\underline{\text{CH}_2}$ - CH_2 - CH_3), 3.31 (2H, t, N- $\underline{\text{CH}_2}$ - CH_2 - CH_2), 1.75 (6H, m(6), N- CH_2 - $\underline{\text{CH}_2}$ - CH_3), 1.67 (2H, m(5), N- CH_2 - $\underline{\text{CH}_2}$ - CH_2), 1.37 (2H, m(5), N- CH_2 - CH_2 - $\underline{\text{CH}_2}$), 1.35 (2H, m(5), $\underline{\text{CH}_2}$ - CH_2 - CH_3), 1.26 (2H, m(5), CH_2 - $\underline{\text{CH}_2}$ - CH_2 - CH_3), 1.24 (2H, m(6), CH_2 - CH_2 - $\underline{\text{CH}_2}$ - CH_3), 1.05 (9H, t, N- CH_2 - CH_2 - $\underline{\text{CH}_3}$), 0.86 (3H, t, CH_2 - $\underline{\text{CH}_2}$ - CH_2 - CH_3); ^{13}C NMR (300MHz, CDCl_3 , ppm) δ 60.88 (N- $\underline{\text{CH}_2}$ - CH_2 - CH_2), 59.47 (N- $\underline{\text{CH}_2}$ - CH_2 - CH_3), 31.58 (CH_2 - CH_2 - $\underline{\text{CH}_2}$ - CH_3), 28.84 ($\underline{\text{CH}_2}$ - CH_2 - CH_2 - CH_3), 26.40 (N- CH_2 - $\underline{\text{CH}_2}$ - CH_2), 22.47 (N- CH_2 - $\underline{\text{CH}_2}$ - $\underline{\text{CH}_2}$), 22.43 84 (CH_2 - $\underline{\text{CH}_2}$ - CH_2 - CH_3), 16.15 (N- CH_2 - $\underline{\text{CH}_2}$ - CH_3), 14.04 (CH_2 - CH_2 - $\underline{\text{CH}_3}$), 10.99 (N- CH_2 - CH_2 - $\underline{\text{CH}_3}$).

Zeolite Synthesis: Zeolite MFI was synthesised using n-heptyltripropylammonium iodide in a variety of different synthetic methods and reaction vessels. Table 3.22 and Table 3.23 contain the details of all reactions attempted using the hydroxide and fluoride route respectively.

Table 3.22 - Hydroxide route table of conditions for the synthesis of MFI using H(7)TPA

Synthetic Method	Ludox 30% (g)	H(7)TP(3)A SDA (g)	H ₂ O (ml)	NaOH 1M (ml)	Synthesis Time (days)	MFI Successful
<i>Exp.20.a. Hydroxide route dense-gel crystallisation curve synthesis in 30 ml PFE bottle 100 °oven</i>						
Molar Composition	1.0 SiO ₂ : 0.15 H(7)TP(3)A: 18.60 H ₂ O: 0.13 NaOH					
Amount Used	3.0	0.82	1.0	2.0	Variable	Y
<i>Exp.20.b. Hydroxide route normal synthesis 8 ml polypropylene bottle 100 °C oven</i>						
Molar Composition	1.0 SiO ₂ : 0.13 H(7)TP(3)A: 18.60 H ₂ O: 0.13 NaOH					
Amount Used	3.0	0.53	1.0	2.0	17	Y
	3.0	0.53	1.0	2.0	20	Y

An example fluoride route dense-gel synthesis (*Exp.21.b.*) of MFI using n-heptyltripropylammonium iodide as an SDA was prepared as follows: 0.66 g of H(7)TP(3)AI and 1.50 g ammonium fluoride were added to a 8 ml narrow-mouth polypropylene bottle. 1.5 ml of distilled water and 3.0 g of 40 % Ludox LS were added to the mixture and stirred thoroughly to form a thick gel. The bottle was then mixed on the vortex mixer for 5 seconds before subsequently being placed in a 100 °C oven for the 14 days.

Table 3.23 - Fluoride route table of conditions for the synthesis of MFI using H(7)TPA

Synthetic Method	SiO ₂ (g)	H(7)TP(3)A SDA (g)	H ₂ O (ml)	NH ₄ F (g)	Synthesis Time (days)	MFI Successful
<i>Ex. 21.a. Fluoride route hydrothermal synthesis in 23 ml autoclave 100 °C oven</i>						
Molar Composition	1.0 SiO ₂ : 0.18 H(7)TP(3)A: 20.0 H ₂ O: 1.0 NH ₄ F					
Amount Used	1.0	1.08	6.0	0.62	14	N
Synthetic Method	Ludox 40% (g)	H(7)TP(3)A SDA (g)	H ₂ O (ml)	NH ₄ F (g)	Synthesis Time (days)	MFI Successful
<i>Exp.21.b. Fluoride route dense-gel synthesis 8 ml polypropylene bottle 100 °C oven</i>						
Molar Composition	1.0 SiO ₂ : 0.09 H(7)TP(3)A: 8.34 H ₂ O: 0.68 NH ₄ F					
Amount Used	3.0	0.66	1.2	1.5	10	N
	3.0	0.66	1.2	1.5	14	Peaks forming

Work-up: After removing the polypropylene bottle from the oven and allowing the content to cool to room temperature and pressure, the product was washed (30 ml distilled water) and centrifuged (3500 rpm, 15 minutes) three times yielding a white solid. The sample was later dried (60 °C, overnight) and confirmed as zeolite MFI by comparison of the XRD diffraction pattern obtained (Figure 3.23) to that published by International Zeolite Association.¹⁴

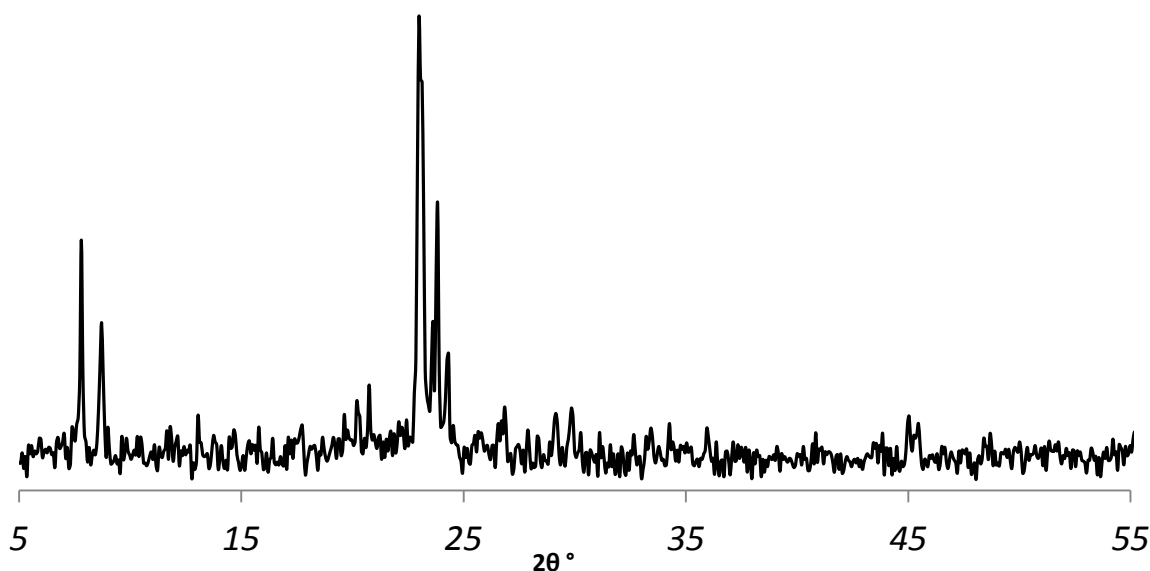


Figure 3.23 - XRD powder pattern of H(7)TP(3)A/MFI on a Bruker Advance diffractometer with Cu K α source

3.2.12. Synthesis of MFI using TEPAI(3) – Triethyl-N-propylammonium Iodide

SDA Synthesis: Triethyl-N-propylammonium iodide (Figure 3.24) was synthesised by refluxing an equimolar mixture of 1-iodopropane (8.40 g, 49.41 mmol), triethylamine HCl (5 g, 49.41 mmol) and sodium carbonate (5.24 g, 49.44 mmol) in 100 ml methanol for 72 hours. After reflux, the sodium carbonate was removed via a cold filtration before the

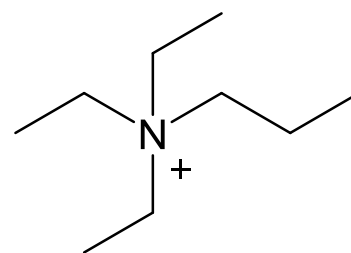


Figure 3.24 - Structure of TEP3A (triethyl-n-propylammonium) cation

solvent was removed under reduced pressure producing a crude product. The product was then recrystallised using a mixture of ethyl acetate and a minimum amount of ethanol to remove any soluble impurities. White crystals were obtained (12.44g, 92.96%) and characterised as follows: ^1H NMR (300 MHz, CDCl_3 , ppm) δ 3.40 (6H, s, N- $\text{CH}_2\text{-CH}_3$), 3.20 (2H, w, N- $\text{CH}_2\text{-CH}_2$), 1.72 (2H, w, $\text{CH}_2\text{-CH}_3$), 1.35 (9H, s, $\text{CH}_2\text{-CH}_3$), 1.00 (3H, m, $\text{CH}_2\text{-CH}_3$); ^{13}C NMR (300MHz, CDCl_3 , ppm) δ 59.3 (N- $\text{CH}_2\text{-CH}_3$), 53.8 (N- $\text{CH}_2\text{-CH}_2$), 15.83 ($\text{CH}_2\text{-CH}_2\text{-CH}_3$), 10.98 (N- $\text{CH}_2\text{-CH}_3$), 8.33 ($\text{CH}_2\text{-CH}_3$).

Zeolite Synthesis: Zeolite MFI was synthesised using triethyl-N-propylammonium iodide in a variety of different synthetic methods and reaction vessels. Table 3.24 and Table 3.25 contain the details of all reactions attempted using the hydroxide and fluoride route respectively.

Table 3.24 - Hydroxide route table of conditions for the synthesis of MFI using TEP(3)A

Synthetic Method	Ludox 30% (g)	TEP(3)A SDA (g)	H ₂ O (ml)	NaOH (ml)	Synthesis Time (days)	MFI Successful
<i>Exp 22. a. Hydroxide route dense-gel crystallisation curve synthesis in 8 ml polypropylene bottle 100 °C oven</i>						
Molar Composition	1.0 SiO ₂ : 0.16 TEP(3)A: 18.70 H ₂ O: 0.13 NaOH					
Amount Used	3.0	0.65	1	2	Variable	Y
Molar Composition	1.00 SiO ₂ : 0.14 TEP(3)A: 26.15 H ₂ O: 0.13 NaOH					
Amount Used	3.00	0.56	3	2	Variable	N
<i>Exp.22.b. Fluoride route dense-gel synthesis in 5.66 ml glass vial 100°C oven</i>						
Molar Composition	1.0 SiO ₂ : 0.18 TEP(3)A: 29.82 H ₂ O: 0.16 NaOH					
Amount Used	2	0.41	2	1.33	7	Y

An example hydroxide route synthesis (*Exp.22.b.*) of MFI using triethyl-N-propylammonium iodide as was prepared as follows: 0.41 g of TEP(3)AI and 2.0 ml of distilled water were mixed and

added to 1.33 ml of 1M sodium hydroxide and 2.0 g of 30 % Ludox LS. This homogenous gel was transferred to a narrow 5.66 ml glass vial and subsequently placed in a 100 °C oven for 7 days.

Table 3.25 - Fluoride route table of conditions for the synthesis of MFI using TEP(3)A

Synthetic Method	SiO ₂ (g)	TEP(3)A SDA (g)	H ₂ O (ml)	NH ₄ F (g)	Synthesis Time (days)	MFI Successful
<i>Exp 23.a. Fluoride route dense-gel synthesis in 8 ml polypropylene bottle 100 °C oven</i>						
Molar Composition	1.0 SiO ₂ : 0.12 TEP(3)A: 6.67 H ₂ O: 2.43 NH ₄ F					
Amount Used	1.0	0.51	2.0	1.5	11	N
Molar Composition	1.0 SiO ₂ : 0.12 TEP(3)A: 11.0 H ₂ O: 2.43 NH ₄ F					
Amount Used	1.0	0.51	3.3	1.5	11	N

Work-up: After removing the glass vial from the oven and allowing the content to cool to room temperature and pressure, the product was washed (30 ml distilled water) and centrifuged (3500 rpm, 15 minutes) three times yielding a white solid. The sample was later dried (60 °C, overnight) and confirmed as zeolite MFI by comparison of the XRD diffraction pattern obtained (Figure 3.25) to that published by International Zeolite Association.¹⁴

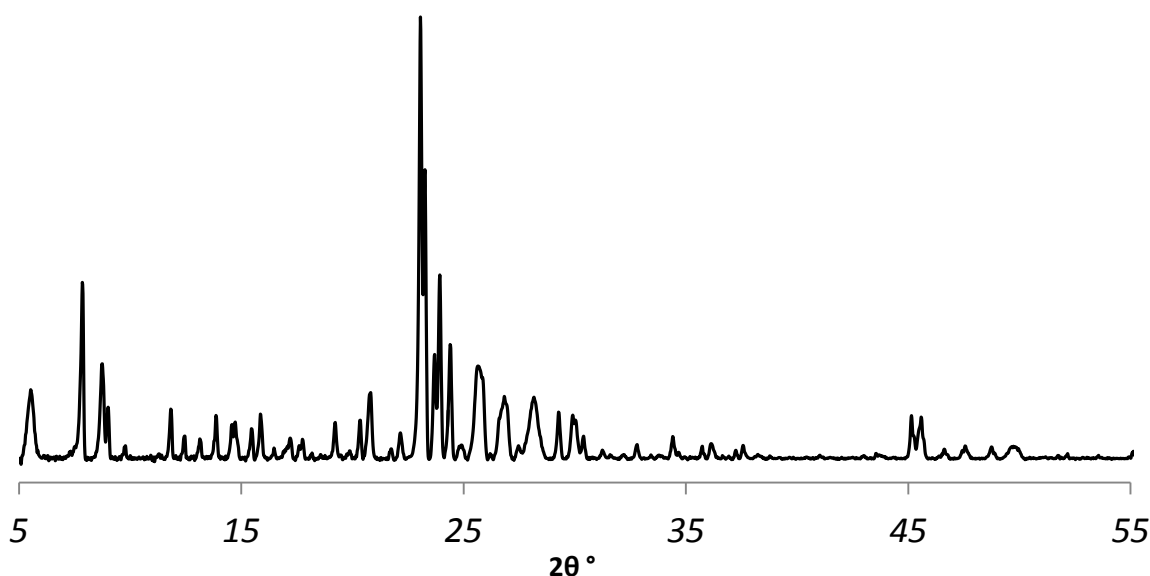


Figure 3.25 – XRD powder pattern of TEP(3)A/MFI on a Bruker Advance diffractometer with Cu K α source

An additional peak can be observed on the above XRD spectrum at ~5.4 2 θ that is not a part of the MFI diffraction fingerprint. This peak has been observed in multiple XRD diffraction patterns and as such will be discussed collectively in Chapter 3.4 Additional X-ray Diffraction Peak.

3.2.13. Synthesis of MFI using TEIP(3)A⁺I⁻ - Triethyl-N-isopropylammonium Iodide

SDA Synthesis: The SDA triethyl-N-isopropylammonium iodide (Figure 3.26) was synthesised by refluxing triethylamine (2.18 g, 21.52 mmol) and 2-iodopropane (10.77 g, 21.52 mmol) in 100 ml methanol for 3 days. After reflux, the methanol was removed under reduced pressure and the product was recrystallised using a mixture of ethyl acetate and a minimum amount of

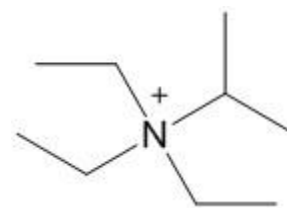


Figure 3.26 - Structure of TEIP3A (triethyl-n-isopropylammonium) cation

ethanol to remove any soluble impurities. White crystals were obtained (2.93 g, 50.23 %) and characterised as follows: ¹H NMR (300 MHz, CDCl₃, ppm) δ 3.39 (1H, m(7), N-CH-(CH₃)₂), 3.14 (6H, q, N-CH₂-CH₃), 1.39 (9H, t, N-CH₂-CH₃), 1.34 (6H, t, N-CH-(CH₃)₂); ¹³C NMR (300MHz, CDCl₃, ppm): δ 63.67 (N-CH-(CH₃)₂), 46.67 (N-CH₂-CH₃), 17.58 (N-CH-(CH₃)₂), 9.95 (N-CH-(CH₃)₂), 8.89 (N-CH₂-CH₃).

Zeolite Synthesis: Zeolite MFI was synthesised using triethyl-N-isopropylammonium iodide in a variety of different synthetic methods and reaction vessels. Table 3.26 and Table 3.27 and contain the details of all reactions attempted using the hydroxide and fluoride route respectively.

Table 3.26 - Hydroxide route table of conditions for the synthesis of MFI using TEIP(3)A

Synthetic Method	Ludox 30% (g)	TEIP(3)A SDA (g)	H ₂ O (ml)	NaOH 1M (ml)	Synthesis Time (days)	MFI Successful
<i>Exp. 24.a. Hydroxide route dense-gel synthesis in 8 ml polypropylene bottle 100 °C oven</i>						
Molar Composition	1.0 SiO ₂ : 0.13 TEIP(3)A : 25.42 H ₂ O: 0.16 NaOH					
Amount Used	3.0	0.54	3.0	2.0	12	N
<i>Exp.24.b. Hydroxide route dense-gel crystallisation curves synthesis in 8 ml polypropylene bottle 100 °C oven</i>						
Molar Composition	1.0 SiO ₂ : 0.13 TEIP(3)A: 18.20 H ₂ O: 0.16 NaOH					
Amount Used	3.0	0.54	1.0	2.0	Variable	N

An example fluoride route synthesis (*Exp. 25. d.*) of MFI using triethyl-N-isopropylammonium iodide as an SDA was prepared as follows: 0.51 g of TEIP(3)AI and 1.50 g ammonium fluoride were added to a 30 ml narrow-mouth PFE bottle. 1.5 ml of distilled water and 1.0 g of silicon

dioxide were added to the mixture and stirred thoroughly to form a thick gel. The bottle was then mixed on the vortex mixer for 5 seconds before subsequently being placed in a 100 °C oven for 11 days.

Table 3.27 - Fluoride route table of conditions for the synthesis of MFI using TEIP(3)A

Synthetic Method	Ludox 40% (g)	TEIP(3)A SDA (g)	H₂O (ml)	NH₄F (ml)	Synthesis Time (days)	MFI Successful
<i>Exp. 25. a. Fluoride route dense-gel synthesis in 8 ml polypropylene bottle 100 °C oven</i>						
Molar Composition	1.0 SiO ₂ : 0.15 TEIP(3)A: 8.33 H ₂ O: 2.0 (NH ₄)HF ₂					
Amount Used	3.0	0.79	1.2	2.30	12	N (D)
Synthetic Method	SiO₂ (g)	TEIP(3)A SDA (g)	H₂O (ml)	NH₄F (g)	Synthesis Time (days)	MFI Successful
<i>Exp. 25.b. Fluoride route hydrothermal synthesis in 23 ml autoclave 100 °C oven</i>						
Molar Composition	1.0 SiO ₂ : 0.08 TEIP(3)A: 20.0 H ₂ O: 1.54 H ₂ O					
Amount Used	1.0	0.65	6.0	0.62	37	N
<i>Exp. 25. c. Fluoride route dense-gel synthesis in 30 ml PFE bottle 100 °C oven</i>						
Molar Composition	1.0 SiO ₂ : 0.12 TEIP(3): 11.0 H ₂ O: 2.43 NH ₄ F					
Amount Used	1.0	0.51	2.0	1.5	11	Y
Synthetic Method	SiO₂ (g)	TEIP(3)A SDA (g)	H₂O (ml)	(NH₄)HF₂ (g)	Synthesis Time (days)	MFI Successful
<i>Exp. 25. d. Fluoride route dense-gel synthesis in 30 ml PFE bottle 100 °C oven</i>						
Molar Composition	1.0 SiO ₂ : 0.14 TEIP(3)A: 20.0 H ₂ O: 1.12 (NH ₄)HF ₂					
Amount Used	1.0	0.65	6.0	0.95	12	N

Work-up: After removing the PFE bottle from the oven and allowing the content to cool to room temperature and pressure, the content was washed (30 ml distilled water) and centrifuged (3500 rpm, 15 minutes) three times yielding a white solid. The sample was later dried (60 °C, overnight) and confirmed as zeolite MFI by comparison of the XRD diffraction pattern obtained (Figure 3.27), to that published by International Zeolite Association.¹⁴

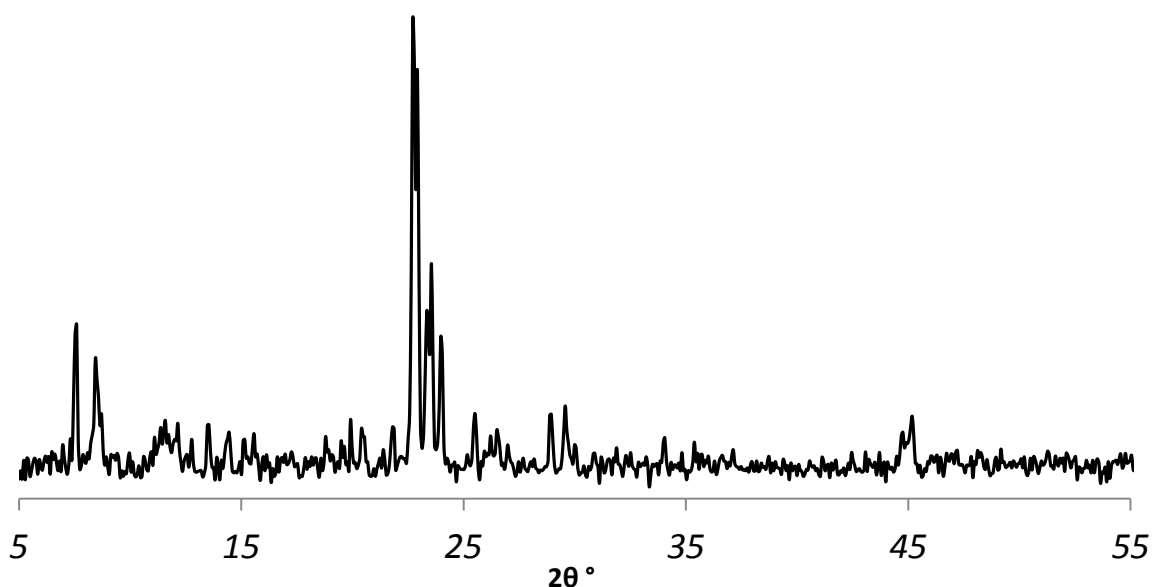


Figure 3.27 - XRD powder pattern of TEIP(3)A/MFI on a Bruker Advance diffractometer with Cu K α source

3.2.14. Synthesis of MFI using TEBAI – Triethyl-N-butylammonium Iodide

SDA Synthesis: The SDA triethyl-N-butylammonium iodide (Figure 3.28) was successfully synthesised by refluxing 1-iodobutane (18.18 g, 98.8 mmol) and triethylamine (5.00

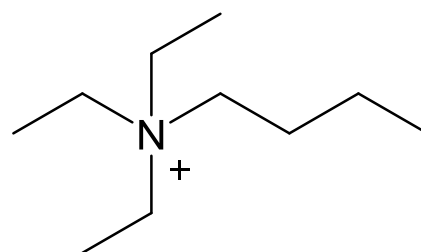


Figure 3.28 - Structure of TEBA (triethylbutylammonium) cation

g, 49.4 mmol) in 100ml methanol for 4 days. After reflux, the methanol was removed under reduced pressure and

the product was recrystallised with a mixture of hot ethyl acetate and a minimum amount of ethanol to remove any soluble impurities. White crystals were obtained (12.3 g, 79.50 %) and characterised as follows: ^1H NMR (300 MHz, CDCl_3 , ppm) δ 3.25 (6H, s, $\text{N-CH}_2\text{-CH}_2$), 3.09 (2H, m, $\text{N-CH}_2\text{-CH}_2$), 1.48 (2H, m, $\text{CH}_2\text{-CH}_2\text{-CH}_2$), 1.24 (2H, m, $\text{CH}_2\text{-CH}_2\text{-CH}_3$), 1.17 (9H, s, $\text{CH}_2\text{-CH}_3$), 0.79 (3H, s, $\text{CH}_2\text{-CH}_3$); ^{13}C NMR (300MHz, CDCl_3 , ppm) δ 57.46 ($\text{N-CH}_2\text{-CH}_3$), 53.71 ($\text{N-CH}_2\text{-CH}_2$), 24.06 ($\text{CH}_2\text{-CH}_2\text{-CH}_3$), 19.77 ($\text{N-CH}_2\text{-CH}_3$), 13.80 ($\text{CH}_2\text{-CH}_3$), 8.35 ($\text{CH}_2\text{-CH}_3$).

Zeolite Synthesis: Zeolite MFI was synthesised using triethyl-N-butylammonium iodide in a variety of different synthetic methods and reaction vessels. Table 3.28 and Table 3.29 contain the details of all reactions attempted using the hydroxide and fluoride route, respectively.

Table 3.28 - Hydroxide route table of conditions for the synthesis of MFI using TEBA

Synthetic Method	Ludox 30% (g)	TEBA SDA (g)	H₂O (ml)	NaOH (ml)	Synthesis Time (days)	MFI Successful
<i>Exp. 26. a. Hydroxide route dense-gel synthesis in 8 ml polypropylene bottle 100 °C oven</i>						
Molar Composition	1.0 SiO ₂ : 0.14 TEBA: 33.4 H ₂ O: 0.13 NaOH					
Amount Used	3.0	0.68	2	2	17	Y
<i>Exp. 26.b. Hydroxide route dense-gel crystallisation curves synthesis in 8 ml polypropylene bottle 100 °C oven</i>						
Molar Composition	1.0 SiO ₂ : 0.13 TEBA: 26.0 H ₂ O: 0.13 NaOH					
Amount Used	3.0	0.59	3.0	2.0	Variable	Y
<i>Exp. 26. c. Hydroxide route hydrothermal synthesis in 46 ml autoclave 100 °C oven</i>						
Molar Composition	1.0 SiO ₂ : 0.16 TEBA: 18.60 H ₂ O: 0.13 NaOH					
Amount Used	3.0	0.68	1.0	2.0	17	Y
<i>Exp 26. d. Hydroxide route dense-gel synthesis in 30 ml PFE bottle 100° C oven</i>						
Molar Composition	1.0 SiO ₂ : 0.16 TEBA: 18.60 H ₂ O: 0.13 NaOH					
Amount Used	3.0	0.68	1.0	2.0	7	N

An example hydroxide hydrothermal synthesis (*Exp. 26. c.*) of MFI using triethyl-N-butylammonium iodide as an SDA was prepared as follows: 0.68 g of TEBAI and 2.0 ml (1 M) sodium hydroxide were added to a 46 ml Teflon lined stainless steel autoclave liner. 1.0 ml of distilled water and 1.0 g of silicon dioxide were added to the mixture and stirred thoroughly to form a thick gel before the autoclave was placed in a 100 °C oven for 17 days.

Table 3.29 - Fluoride route table of conditions for the synthesis of MFI using TEBA

Synthetic Method	Ludox 40% (g)	TEBA SDA (g)	H₂O (ml)	NH₄F (g)	Synthesis Time (days)	MFI Successful
<i>Exp.27. a. Fluoride route dense-gel crystallisation curves synthesis in 8 ml polypropylene bottle 100 °C oven</i>						
Molar Composition	1.0 SiO ₂ : 0.08 TEBA: 8.34 H ₂ O: 0.68 NH ₄ F					
Amount Used	3.0	0.54	1.2	1.5	Variable	N
Synthetic Method	SiO₂ (g)	TEBA (g)	H₂O (ml)	NH₄F (g)	Synthesis Time (days)	MFI Successful
<i>Exp.27.b. Fluoride route dense-gel synthesis in 30 ml PFE bottle 100 °C oven</i>						
Molar Composition	1.0 SiO ₂ : 0.08 TEBA: 20.0 H ₂ O: 1.0 NH ₄ F					
Amount Used	1.0	0.38	6.0	0.62	15	N

Work-up: After removing the autoclave from the oven and allowing the content to cool to room temperature and pressure, the product was washed (30 ml distilled water) and centrifuged (3500 rpm, 15 minutes) three times yielding a white solid. The sample was later dried (60 °C, overnight) and confirmed as zeolite MFI by comparison of the XRD diffraction pattern obtained (Figure 3.29), to that published by International Zeolite Association.¹⁴

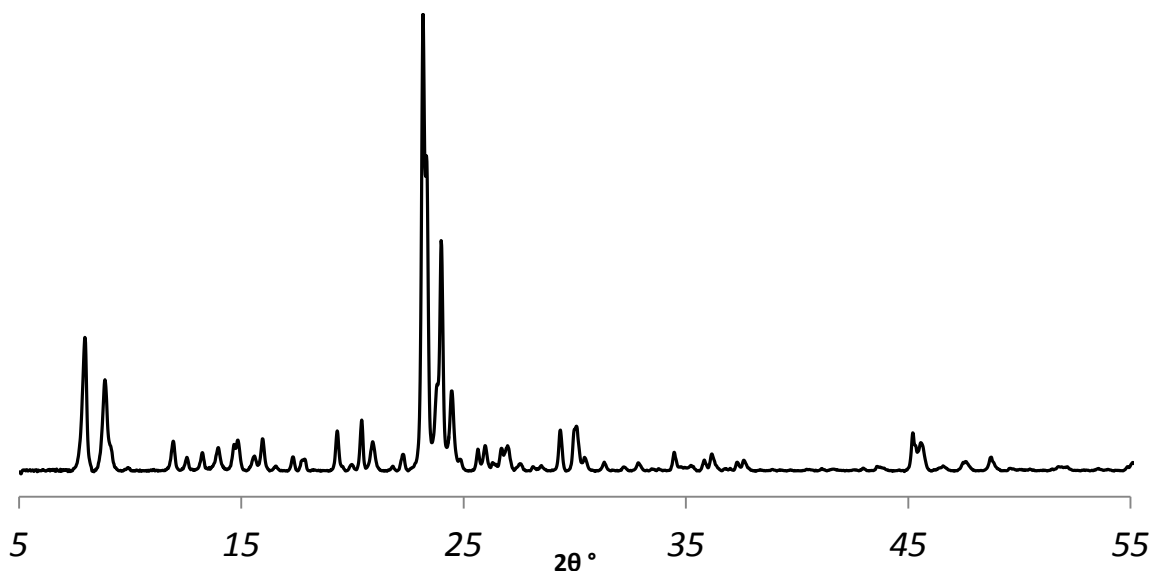


Figure 3.29 - XRD powder pattern of TEBA/MFI on a Bruker Advance diffractometer with Cu K α source

3.2.15. Synthesis of MFI using TEP(5)A – Triethyl-N-pentylammonium Iodide

SDA Synthesis: The SDA triethyl-N-pentylammonium iodide (Figure 3.30) was synthesised by refluxing an equimolar mixture of 1-iodopentane (21.31 g, 107.6 mmol), triethylamine (10.89 g, 107.6 mmol) in 100 ml methanol for 5 days.

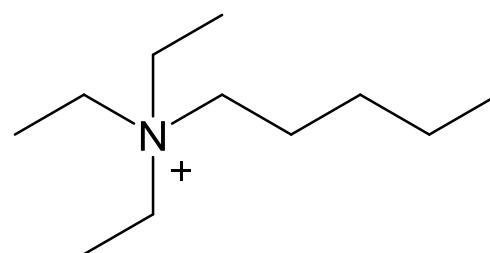


Figure 3.30 - Structure of TEP5A (triethyl-N-pentylammonium) cation SDA

The methanol was removed under reduced pressure and the product was recrystallised using a mixture of ethyl acetate and a minimum amount of ethanol to remove any soluble impurities. White crystals were obtained (11.52 g, 77.99 %) and characterised as follows: ¹H NMR (300 MHz, CDCl₃, ppm) δ 3.48 (6H, q, N-CH₂-CH₃), 3.28 (2H, q, N-CH₂-CH₂), 1.72 (2H, m, N-CH₂-CH₂), 1.39 (9H, t, N-CH₂-CH₃), 1.39 (2H, m, CH₂-CH₂-CH₃), 1.39 (9H, m, CH₂-CH₂-CH₃), 0.92 (3H, t, CH₂-CH₂-CH₃);

¹³C NMR (300MHz, CDCl₃, ppm) δ 57.53 (N-CH₂-CH₃), 53.75 (N-CH₂-CH₂), 28.44 (N-CH₂-CH₂), 22.30 (CH₂-CH₂-CH₃), 21.92 (CH₂-CH₂-CH₃), 12.91 (CH₂-CH₂-CH₃), 8.32 (N-CH₂-CH₃).

Zeolite Synthesis: Zeolite MFI was synthesised using triethyl-N-penylammonium iodide in a variety of different synthetic methods and reaction vessels. Table 3.30 and Table 3.31 contain the details of all reactions attempted using the hydroxide and fluoride route, respectively.

Table 3.30 - Hydroxide route table of conditions for the synthesis of MFI using TEP(5)A

Synthetic Method	Ludox 30% (g)	TEP(5)A SDA (g)	H ₂ O (ml)	NaOH (ml)	Synthesis Time (days)	MFI Successful
<i>Exp.28.a. Hydroxide route dense-gel crystallisation curves synthesis in 8 ml polypropylene bottle 100 °C oven</i>						
Molar Composition	1.00 SiO ₂ : 0.16 TEP(5)A: 0.13 NaOH: 18.69 H ₂ O					
Amount Used	3.00	0.65	1.0	2.0	Variable	N
<i>Exp.28.b. Hydroxide route hydrothermal synthesis in 46 ml autoclave 100 °C oven</i>						
Molar Composition	1.0 SiO ₂ : 0.16 TEP(5)A: 0.13 NaOH: 18.20 H ₂ O					
Amount Used	3.0	0.72	1.0	2.0	32	Y
<i>Exp.28.c. Hydroxide route dense-gel synthesis in 30 ml PFE bottle 100 °C oven</i>						
Molar Composition	1.0 SiO ₂ : 0.16 TEP(5)A: 0.13 NaOH: 18.20 H ₂ O					
Amount Used	3.0	0.72	1.0	2.0	33	Y

An example hydroxide route synthesis (*Exp.29.a.*) of MFI using triethyl-N-pentylammonium iodide as an SDA was prepared as follows: 0.72 g of TEP(5)Al and 2.0 ml (1 M) sodium hydroxide were added to a 30 ml narrow-mouth PFE bottle. 1.0 ml of distilled water and 3.0 g of 30 % Ludox LS were added to the mixture and stirred thoroughly to form a thick gel before the bottle was placed in a 100 °C oven for 33 days.

Table 3.31 - Fluoride route table of conditions for the synthesis of MFI using TEP(5)A

Synthetic Method	SiO ₂ (g)	TEP(5)A SDA (g)	H ₂ O (ml)	NH ₄ F (ml)	Synthesis Time (days)	MFI Successful
<i>Exp.29.a. Fluoride route dense-gel method in 8 ml polypropylene bottle 100 °oven</i>						
Molar Composition	1.0 SiO ₂ : 0.12 TEP(5)A: 6.67 H ₂ O: 2.43 NH ₄ F					
Amount Used	1.0	0.56	2.0	1.5	11	N

Work-up: After removing the bottle from the oven and allowing the content to cool to room temperature and pressure, the product was washed (30 ml distilled water) and centrifuged (3500

rpm, 15 minutes) three times yielding a white solid. The sample was later dried (60 °C, overnight) and confirmed as zeolite MFI by comparison of the XRD diffraction pattern obtained (Figure 3.31), to that published by International Zeolite Association.¹⁴

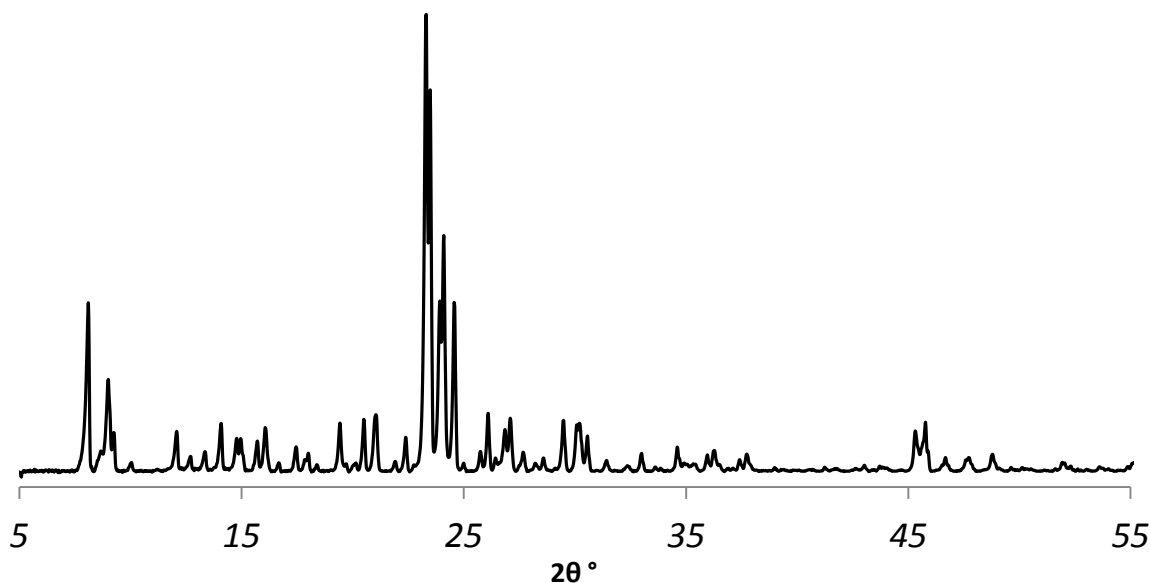


Figure 3.31 - XRD powder pattern of TEP5A/MFI on a Bruker Advance diffractometer with Cu K α source

3.2.16. Synthesis of MFI using TEH(6)A⁺I⁻ - Triethyl-N-hexylammonium Iodide

SDA Synthesis: The SDA triethyl-N-hexylammonium iodide (Figure 3.32) was synthesised by refluxing 1-iodohexane (12.56 g, 59.25 mmol) and triethylamine (3.60 g, 35.56 mmol) in 100 ml methanol for 120 hours.

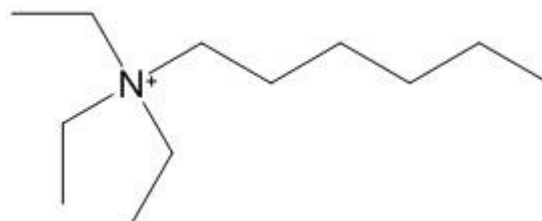


Figure 3.32 - Structure of TEH6A (triethyl-N-hexylammonium) cation SDA

After reflux, the methanol was removed under reduced pressure and the product was recrystallised using a mixture of ethyl acetate and a minimum amount of ethanol to remove any soluble impurities. White crystals were obtained (16.98 g, 91.73 %) and characterised as follows: ¹H NMR (300 MHz, CDCl₃, ppm) δ 3.34 (2H, m, N-CH₂-CH₂), 3.23 (6H, m, N-CH₂-CH₃), 3.11 (2H, m, CH₂-CH₂-CH₂), 2.50 (2H, m, CH₂-CH₂-CH₂), 1.55 (9H, s, CH₂-CH₃), 1.30 (2H, m, CH₂-CH₂-CH₂), 1.15

(2H, m, CH₂-CH₂-CH₃), 0.86 (3H, s, CH₂-CH₃); ¹³C NMR (300MHz, CDCl₃, ppm) δ 57.64 (N-CH₂-CH₂), 53.70 (N-CH₂-CH₃), 31.20 (N-CH₂-CH₂), 26.08 (N-CH₂-CH₂-CH₂), 22.43 (CH₂-CH₂-CH₃), 22.10 (CH₂-CH₂-CH₃), 13.89 (CH₂-CH₂-CH₃), 8.30 (N-CH₂-CH₃).

Zeolite Synthesis: Zeolite MFI was synthesised using triethyl-N-hexylammonium iodide in a variety of different synthetic methods and reaction vessels. Table 3.32 and Table 3.33 contain the details of all reactions attempted using the hydroxide and fluoride route, respectively.

Table 3.32 - Hydroxide route table of conditions for the synthesis of MFI using TEH(6)A

Synthetic Method	Ludox 30% (g)	TEH(6)A SDA (g)	H ₂ O (ml)	NaOH (1 M) (ml)	Synthesis Time (days)	MFI Successful
<i>Exp.30.a. Hydroxide route dense-gel synthesis in 8 ml polypropylene bottle 100 °C oven</i>						
Molar Composition	1.0 SiO ₂ : 0.16 TEH(6)A: 26 H ₂ O: 0.13 NaOH					
Amount Used	1.5	0.37	1.5	1	10	N
+ 0.5 ml H ₂ O	1.5	0.37	2	1	20	N
+1 ml	1.5	0.37	2.5	1	21	Initial Peaks Forming
+1.5 ml	1.5	0.37	3	1	22	N
+ 2 ml	1.5	0.37	3.5	1	10	N
+2.5 ml	1.5	0.37	4	1	23	Y
+ 3 ml	1.5	0.37	4.5	1	7	N
+3.5 ml	1.5	0.37	5	1	10	N
+3.5 ml	1.5	0.37	5	1	24	N
+ 4 ml	1.5	0.37	5.5	1	10	N
- 2 ml	3.0	0.65	1.0	2.0	32	Y
<i>Exp.30.b. Hydroxide route dense-gel crystallisation curves synthesis in 8 ml polypropylene bottles 100 °C oven</i>						
Molar Composition	1.0 SiO ₂ : 0.14 TEH(6)A: 26.03 H ₂ O: 0.13 NaOH					
Amount Used	3.0	0.66	3.0	2.0	Variable	Y
½	1.5	0.37	1.5	1	Variable	N (D)
<i>Exp.30.c. Hydroxide route dense-gel synthesis in 30 ml PFE bottle 100 °C oven</i>						
Molar Composition	1.0 SiO ₂ : 18.60 H ₂ O: 0.16 TEH(6)A: 0.13 NaOH					
Amount Used	3.0	0.74	1.0	2	10	N
	3.0	0.74	1.0	2	14	N

An example hydroxide route synthesis (*Exp.30.b.*) of MFI using triethyl-N-hexylammonium iodide as an SDA was prepared as follows: 0.66 g of TEH(6)AI and 2.0 ml 1 M sodium hydroxide were added to a narrow-mouth polypropylene bottle. 3.0 ml of distilled water and 3.0 g of Ludox LS were added to the mixture and stirred thoroughly to form a thick gel. The bottle was then placed

on a vortex mixer for 5 seconds before being placed in a 100 °C oven for the specified time.

Table 3.33 - Fluoride route table of conditions for the synthesis of MFI using TEH(6)A

Synthetic Method	Ludox (40 %) (g)	TEH(6)A SDA (g)	H₂O (ml)	NH₄F (ml)	Synthesis Time (days)	MFI Successful
<i>Exp.30.a. Fluoride route dense-gel method for crystallisation curves in 8 ml polypropylene bottles</i>						
<i>100 °C oven</i>						
Molar Composition	1.0 SiO ₂ : 0.09 TEH(6)A: 8.34 H ₂ O: 0.68 NH ₄ F					
Amount Used	3.0	0.58	1.2	1.5	Variable	N
Synthetic Method	SiO₂ (g)	TEH(6)A SDA (g)	H₂O (ml)	NH₄F (ml)	Synthesis Time (days)	MFI Successful
<i>Exp.30.b. Fluoride Route dense-gel synthesis in 8 ml polypropylene bottles</i>						
<i>100 °C oven</i>						
Molar Composition	1.0 SiO ₂ : 0.12 TEH(6)A: 6.67 H ₂ O: 2.43 NH ₄ F					
Amount Used	1.0	0.59	2.0	1.5	11	N
Molar Composition	1.0 SiO ₂ : 0.12 TEH(6)A: 11.0 H ₂ O: 2.43 NH ₄ F					
Increased H ₂ O	1.0	0.59	3.3	1.5	11	N
<i>Exp.31.c. Fluoride route hydrothermal synthesis in 23 ml autoclave</i>						
<i>100 °C oven</i>						
Molar Composition	1 SiO ₂ : 0.06 TEH(6)A: 11.72 H ₂ O: 0.74 NH ₄ F					
Amount Used	1.64	0.47	5.74	0.75	22	1/2

Work-up: After removing the bottle from the oven and allowing the content to cool to room temperature and pressure, the product was washed (30 ml distilled water) and centrifuged (3500 rpm, 15 minutes) three times yielding a white solid. The sample was later dried (60 °C, overnight) and confirmed as zeolite MFI by comparison of the XRD diffraction pattern obtained (Figure 3.33), to that published by International Zeolite Association.¹⁴

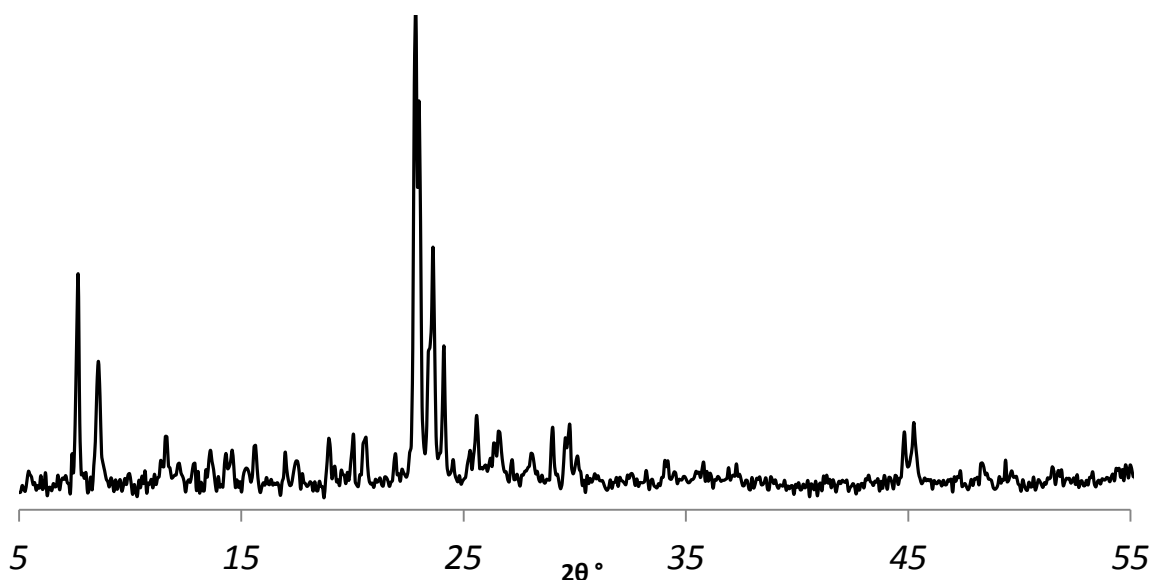


Figure 3.33 - XRD powder pattern of TEH6A/MFI on a Bruker Advance diffractometer with Cu K α source

An additional peak can be observed on the above XRD spectrum at ~ 5.4 $2\theta^\circ$ that is not a part of the MFI diffraction fingerprint. This peak has been observed in multiple XRD diffraction patterns and as such will be discussed collectively in Chapter 3.4 Additional X-ray Diffraction Peak.

3.2.17. Synthesis of MFI using TEH(7)A⁺I⁻ - Triethyl-N-heptylammonium Iodide

SDA Synthesis: The SDA triethyl-heptylammonium iodide (Figure 3.34) was synthesised by refluxing an equimolar mixture of triethylamine (3.36 g, 35.87 mmol) and 1-

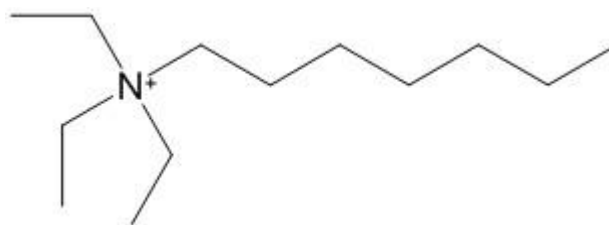


Figure 3.34 - Structure of TEH7A (triethyl-n-heptylammonium) cation SDA

iodoheptane (8.11 g, 35.87 mmol) in 50 ml methanol for 7 days. After reflux, the methanol was removed under reduced pressure and the product was recrystallised using a mixture of ethyl acetate and a minimum amount of ethanol to remove any soluble impurities. White crystals were obtained (7.69 g, 83.08 %) and characterised as follows: ^1H NMR (300 MHz, CDCl_3 , ppm) δ 3.34 (6H, q, N- CH_2 - CH_3), 3.23 (2H, q, N- CH_2 - CH_2), 1.66 (2H, m, N- CH_2 - CH_2), 1.40 (2H, m, N- CH_2 - CH_2 - CH_2), δ 1.3 (9H, t, N- CH_2 - CH_3), 1.32 (2H, m, CH_2 - CH_2 - CH_2 - CH_3), 1.26 (2H, m, CH_2 - CH_2 - CH_3), 1.23 (2H, m, CH_2 - CH_2 - CH_3), 0.83 (3H, t, CH_2 - CH_2 - CH_3); ^{13}C NMR (300MHz, CDCl_3 , ppm) δ 57.72 (N- CH_2 -

CH₂), 53.76 (N-CH₂-CH₃), 31.47 (N-CH₂-CH₂), 28.83 (N-CH₂-CH₂-CH₂), 26.42 (CH₂-CH₂-CH₂-CH₃), 22.47 (CH₂-CH₂-CH₃), 22.12 (CH₂-CH₂-CH₃), 14.04 (CH₂-CH₂-CH₃), 8.31 (N-CH₂-CH₃).

Zeolite Synthesis: Zeolite MFI was synthesised using triethyl-N-heptylammonium iodide in a variety of different synthetic methods and reaction vessels. Table 3.34 and Table 3.35 contains the details of all reactions attempted using the hydroxide and fluoride route, respectively.

Table 3.34 - Hydroxide route table of conditions for the synthesis of MFI using TEH(7)A

Synthetic Method	Ludox 30% (g)	TEH(7)A SDA (g)	H ₂ O (ml)	NaOH 1M (ml)	Synthesis Time (days)	MFI Successful
<i>Exp.32.a. Hydroxide route dense-gel crystallisation curves synthesis in 8 ml polypropylene bottle 100 °C oven</i>						
Molar Composition	1.0 SiO ₂ : 0.17 TEH(7)A: 18.60 H ₂ O: 0.14 NaOH					
Amount Used	3.0	0.82	1.0	2.0	7	Y

An example hydroxide route synthesis (*Exp.32.a.*) of MFI using triethyl-N-heptylammonium iodide as an SDA was prepared as follows: 0.82 g of TEH(7)Al and 2.0 ml (1 M) sodium hydroxide were added to a 8 ml narrow-mouth polypropylene bottle. 1.0 ml of distilled water and 3.0 g of 30 % Ludox LS were added to the mixture and stirred thoroughly to form a thick gel. The bottle was then mixed on the vortex mixer for 5 seconds before being placed in a 100 °C oven for the 7 days.

Table 3.35 - Fluoride route table of conditions for the synthesis of MFI using TEH(7)A

Synthetic Method	Ludox LS 40 % (g)	TEH(7)A SDA (g)	H ₂ O (ml)	NH ₄ F (ml)	Synthesis Time (days)	MFI Successful
<i>Exp.33.a. Fluoride route dense-gel synthesis in 8 ml polypropylene bottle 100 °C oven</i>						
Molar Composition	1.0 SiO ₂ : 0.08 TEH(7)A: 8.34 H ₂ O: 2.02 NH ₄ F					
Amount Used	3.0	0.52	1.2	1.5	7	N
Synthetic Method	SiO ₂ (g)	TEH(7)A SDA (g)	H ₂ O (ml)	NH ₄ F (ml)	Synthesis Time (days)	MFI Successful
<i>Exp.33.b. Fluoride Route dense-gel synthesis in 8 ml polypropylene bottle 100 °C oven</i>						
Molar Composition	1.0 SiO ₂ : 0.14 TEH(7)A: 20.0 H ₂ O: 1.00 NH ₄ F					
Amount Used	1.0	0.78	6.0	0.62	14	N

Work-up: After removing the bottle from the oven and allowing the content to cool to room temperature and pressure, the product was washed (30 ml distilled water) and centrifuged (3500 rpm, 15 minutes) three times yielding a white solid. The sample was later dried (60 °C, overnight) and confirmed as zeolite MFI by comparison of the XRD diffraction pattern obtained (Figure 3.35), to that published by International Zeolite Association.¹⁴

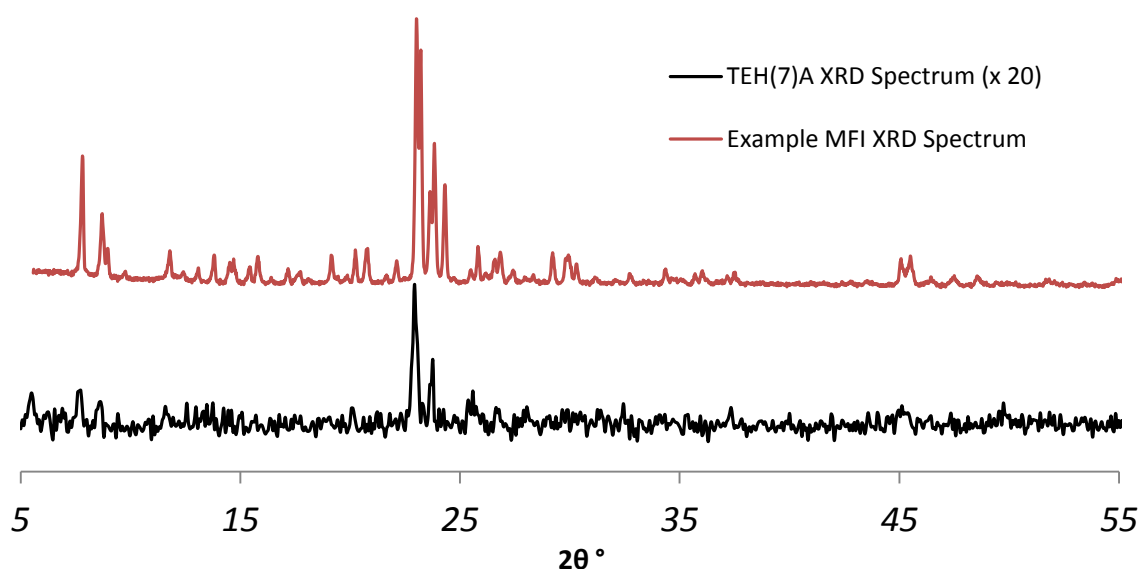


Figure 3.35 - XRD powder pattern of TEH(7)A/MFI on a Bruker Advance diffractometer with Cu K α source

An additional peak can be observed on the above XRD spectrum at $\sim 5.42 \theta^\circ$ that is not a part of the MFI diffraction fingerprint. This peak has been observed in multiple XRD diffraction patterns and as such will be discussed collectively in Chapter 3.4 Additional X-ray Diffraction Peak.

3.2.18. Synthesis of MFI using TMH(6)A⁺I⁻ - Trimethyl-N-hexylammonium Iodide

SDA Synthesis: The SDA trimethyl-hexylammonium iodide (Figure 3.36) was synthesised by refluxing hexylamine (3.83 g, 37.8

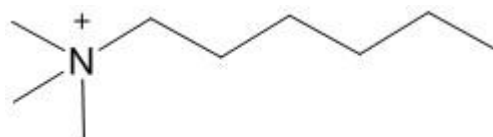


Figure 3.36 - Structure of TMH(6)A (trimethyl-n-hexylammonium) cation

mmol) and iodomethane (16.12 g, 113.5 mmol) in

100 ml methanol for 48 hours. After reflux, the methanol was removed under reduced pressure and the product was recrystallised with a mixture of ethyl acetate and a minimum amount of ethanol to remove any soluble impurities. White crystals were obtained (1.00 g, 9.47 %), and

characterised as follows: ^1H NMR (300 MHz, CDCl_3 , ppm) δ 3.62 (2H, t, N-CH_2), 3.44 (9H, s, N-CH_3), 1.76 (2H, m(5), $\text{N-CH}_2\text{-CH}_2$), 1.38 (2H, m(5), $\text{N-CH}_2\text{-CH}_2\text{-CH}_2$), 1.35 (2H, m(5), $\text{CH}_2\text{-CH}_2\text{-CH}_3$), 1.32 (2H, m(6), $\text{CH}_2\text{-CH}_3$), 0.88 (3H, t, $\text{CH}_2\text{-CH}_3$); ^{13}C NMR (300MHz, CDCl_3 , ppm) δ 67.18 (N-CH_2), 53.81 (N-CH_3), 31.27 ($\text{N-CH}_2\text{-CH}_2$), 25.70 ($\text{N-CH}_2\text{-CH}_2\text{-CH}_2$), 23.19 ($\text{CH}_2\text{-CH}_2\text{-CH}_3$), 22.41 ($\text{CH}_2\text{-CH}_2\text{-CH}_3$), 13.95 ($\text{CH}_2\text{-CH}_3$).

Zeolite Synthesis: Zeolite MFI was synthesised using triethyl-N-heptylammonium iodide in a variety of different synthetic methods and reaction vessels. Table 3.36 contains the details of all reactions attempted using the fluoride route.

Table 3.36 - Fluoride route table of conditions for the synthesis of MFI from TMH(6)A

Synthetic Method	Ludox 40 % (g)	TMH(6)A SDA (g)	H_2O (ml)	NH_4F (ml)	Synthesis Time (days)	MFI Successful
<i>Exp. 34.a. Fluoride route dense-gel synthesis in 8 ml polypropylene bottle</i>						
100 °C oven						
Molar Composition	1.0 SiO_2 : 0.08 TMHA: 8.34 H_2O : 2.0 NH_4F					
Amount Used	3.0	0.44	1.2	1.5	7	Y

An example fluoride route synthesis (*Exp. 34.a.*) of MFI using trimethyl-N-hexylammonium iodide as an SDA was prepared as follows: 0.44 g of TMH(6)A and 1.50 g ammonium fluoride were added to an 8 ml narrow-mouth polypropylene bottle. 1.5 ml of distilled water and 3.0 g of 40 % Ludox LS was added to the mixture and stirred thoroughly to form a thick gel. The bottle was then mixed on the vortex mixer for 5 seconds before being placed in a 100 °C oven for the 7 days.

Work-up: After removing the polypropylene bottle from the oven and allowing the content to cool to room temperature and pressure, the product was washed (30 ml distilled water) and centrifuged (3500 rpm, 15 minutes) three times yielding a white solid. The sample was later dried (60 °C, overnight) and confirmed as zeolite MFI by comparison of the XRD diffraction pattern obtained (Figure 3.37) to that published by International Zeolite Association.¹⁴

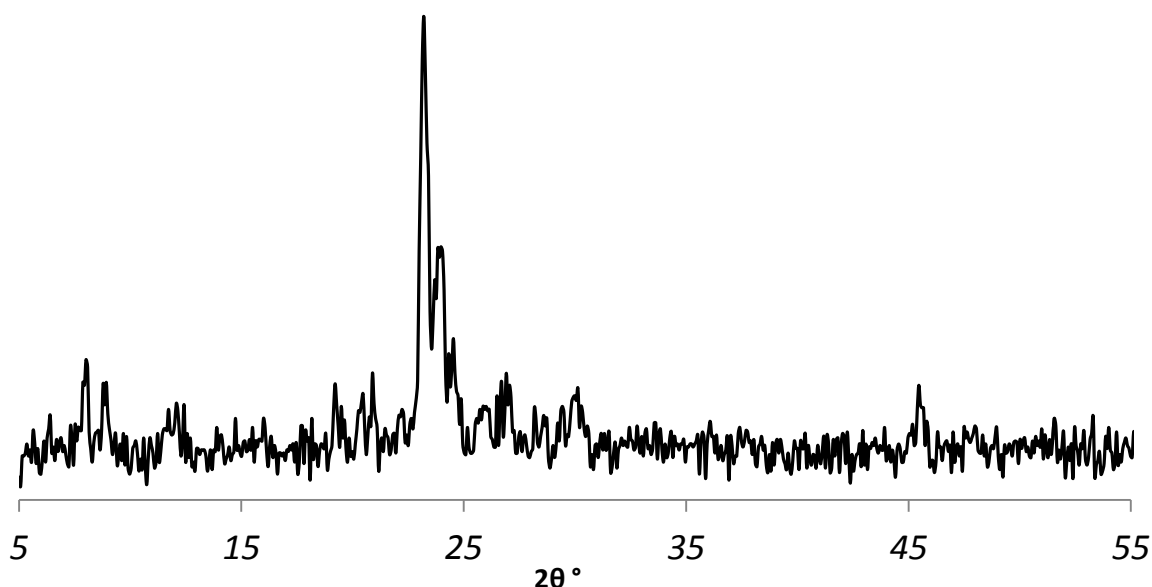


Figure 3.37 - XRD powder pattern of TMH6A/MFI on a Bruker Advance diffractometer with Cu K α source

3.2.19. Synthesis of MFI using DMDP(5)A⁺I⁻ - N,N-dimethyl-N,N-dipentylammonium Iodide

SDA Synthesis: The SDA N,N-dimethyl-N,N-dipentylammonium iodide (Figure 3.38) was synthesised by refluxing a mixture

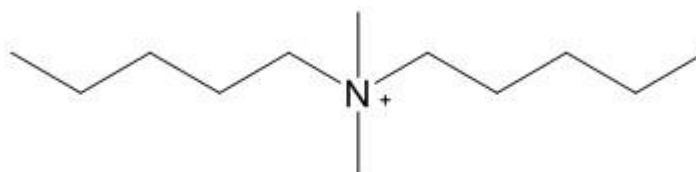


Figure 3.38 - Structure of DMDP(5)A (N,N-dimethyl-N,N-dipentylammonium) cation

of dimethylamine HCl (2.91 g, 35.67 mmol), sodium carbonate (3.78 g, 35.67 mmol) and iodopentane (7.95 g, 40.15 mmol) in 100 ml ethanol for 7 days. After reflux, the sodium carbonate was removed via a cold filtration and then the methanol removed under reduced pressure. The crude product was recrystallised using a mixture of ethyl acetate and a minimum amount of ethanol to remove any soluble impurities. White crystals were obtained (3.02 g, 28.09 %) and characterised as follows: ^1H NMR (300 MHz, CDCl_3 , ppm) δ 3.43 (4H, t, N- CH_2 - CH_2), 3.39 (6H, s, N- CH_3), 1.75 (4H, m, N- CH_2 - CH_2), 1.43 (4H, m, CH_2 - CH_2 - CH_2), 1.40 (4H, m, CH_2 - CH_2 - CH_3), 0.94 (6H, t, CH_2 - CH_3); ^{13}C NMR (300MHz, CDCl_3 , ppm): δ 64.25 (N- CH_2 - CH_2), 51.41 (N- CH_3), 28.16 (N- CH_2 - CH_2), 22.49 (CH_2 - CH_2 - CH_3), 22.27 (CH_2 - CH_2 - CH_3), 13.81 (CH_2 - CH_2 - CH_3).

Zeolite Synthesis: Zeolite MFI was synthesised using N,N-dimethyl-N,N-dipentylammonium iodide in a variety of different synthetic methods and reaction vessels. Table 3.37 and Table 3.38 and

contain the details of all reactions attempted using the hydroxide and fluoride route, respectively.

Table 3.37 - Hydroxide route table of conditions for the synthesis of MFI using DMDP(5)A

Synthetic Method	Ludox 30% (g)	DMDP(5) SDA (g)	H ₂ O (ml)	NaOH (ml)	Synthesis Time (days)	MFI Successful
<i>Exp. 35.a. Hydroxide dense-gel synthesis in 8 ml polypropylene bottle 100 °C oven</i>						
Molar Composition	1.0 SiO ₂ : 0.16 DMDP(5)A: 18.60 H ₂ O: 0.13 NaOH					
Amount Used	3.0	0.74	1.0	2.0	10 days	Y
+ 1 ml H ₂ O	3.0	0.74	2.0	2.0	10 days	Y
+ 2 ml H ₂ O	3.0	0.74	3.0	2.0	10 days	Y

An example fluoride route synthesis (*Exp.36.a*) of MFI using N,N-dimethyl-N,N-dipentylammonium iodide as an SDA was prepared as follows: 0.97 g of DMDP(5)AI and 1.64 g ammonium fluoride were added to a 30 ml PFE bottle. 7.47 ml of distilled water and 3.15 g of silicon dioxide were added to the mixture and stirred thoroughly to form a thick gel. The bottle was then mixed on the vortex mixer for 5 seconds before being placed in a 100 °C oven for 16 days.

Table 3.38 - Fluoride route table of conditions for the synthesis of MFI using DMDP(5)A

Synthetic Method	SiO ₂ (g)	DMDP(5) SDA (g)	H ₂ O (ml)	NH ₄ F (g)	Synthesis Time (days)	MFI Successful
<i>Exp.36.a. Fluoride route dense-gel synthesis in 30 ml PFE bottle 100 °C oven</i>						
Molar Composition	1.0 SiO ₂ : 0.06 DMDP(5)A: 7.90 H ₂ O: 0.84 NH ₄ F					
Amount Used	3.15	0.97	7.47	1.64	16	½

Work-up: After removing the bottle from the oven and allowing the content to cool to room temperature and pressure, the product was washed (30 ml distilled water) and centrifuged (3500 rpm, 15 minutes) three times yielding a white solid. The sample was later dried (60 °C, overnight) and confirmed as zeolite MFI by comparison of the XRD diffraction pattern obtained (Figure 3.39) to that published by International Zeolite Association.¹⁴

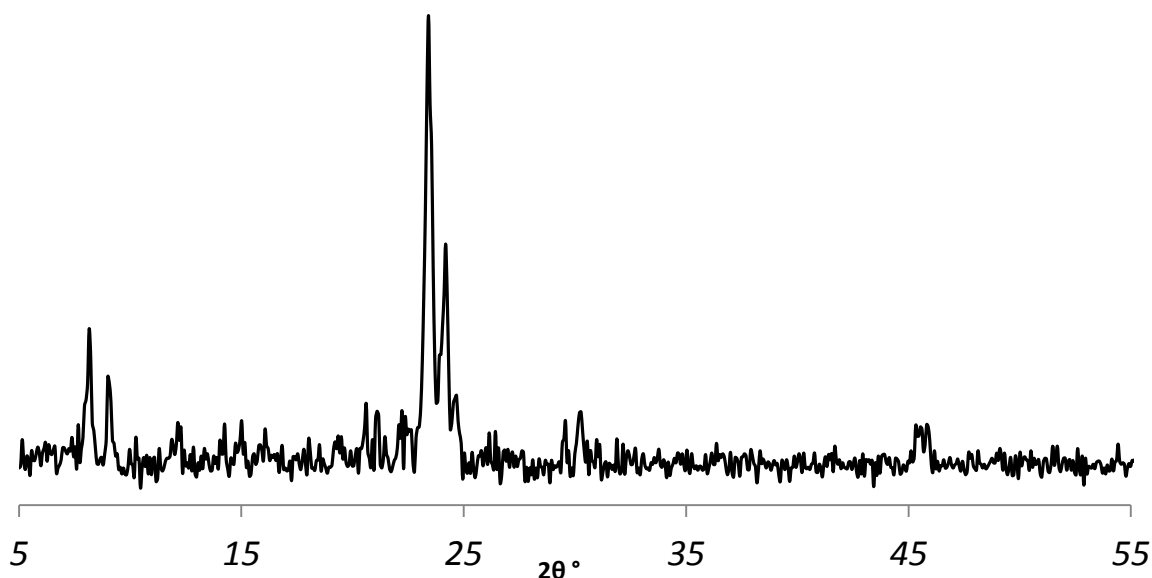


Figure 3.39 - XRD powder pattern of DMDP5A/MFI on a Bruker Advance diffractometer with Cu K α source

3.2.20. Synthesis of MFI using DEDBA+I⁻ - N,N-diethyl-N,N-dibutylammonium Iodide

SDA Synthesis: The SDA N,N-diethyl-N,N-dibutylammonium iodide (Figure 3.40) was synthesised by refluxing a 2:1:1 mixture of 1-iodobutane (33.58 g, 182.48 mmol), diethylamine HCl (10 g, 91.24 mmol) and

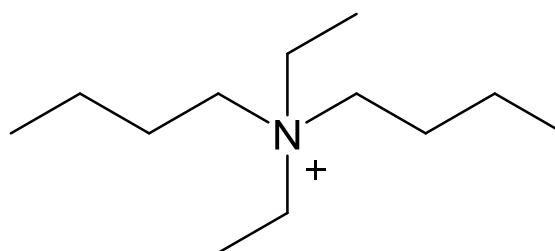


Figure 3.40 - Structure of DEDBA (diethyl-dibutylammonium) cation

sodium carbonate (9.67 g, 91.24 mmol) in 100 ml methanol for 4 days. The methanol was removed under reduced pressure and the product was recrystallised from a mixture of ethyl acetate and a minimum amount of ethanol mixture to remove any soluble impurities. White crystals were obtained (18.60 g, 65.09 %) and characterised as follows; ¹H NMR (300 MHz, CDCl₃, ppm) δ 3.45 (4H, q, N-CH₂-CH₃), 3.30 (4H, t, N-CH₂-CH₂), 1.75 (4H, m(5), CH₂-CH₂-CH₂), 1.45 (4H, m(6), CH₂-CH₂-CH₃), 1.37 (6H, t, N-CH₂-CH₃), 0.95 (6H, t, CH₂-CH₂-CH₃); ¹³C NMR (300MHz, CDCl₃, ppm) δ 58.06 (N-CH₂-CH₂), 54.20 (N-CH₂-CH₃), 24.10 (CH₂-CH₂-CH₂), 19.70 (CH₂-CH₂-CH₃), 13.80 (CH₂-CH₃), 8.40 (N-CH₂-CH₃).

Zeolite Synthesis: Zeolite MFI was synthesised using N,N-diethyl-N,N-dibutylammonium iodide in a variety of different synthetic methods and reaction vessels. Table 3.39 and Table 3.40 contain the details of all reactions attempted using the hydroxide and fluoride route respectively.

Table 3.39 - Hydroxide route table of conditions for the synthesis of MFI using DEDBA

Synthetic Method	Ludox 30 % (g)	DEDBA SDA (g)	H ₂ O (ml)	NaOH (ml)	Synthesis Time (days)	MFI Successful
<i>Exp. 37.a. Hydroxide route dense-gel synthesis in 8 ml polypropylene bottle 100°C oven</i>						
Molar Composition	1.0 SiO ₂ : 0.16 DEDBA: 18.60 H ₂ O: 0.13 NaOH					
Amount Used	3.0	0.74	1.0	2.0	10	Y
+ 1 ml H ₂ O	3.0	0.74	2.0	2.0	10	Y
+ 2 ml H ₂ O	3.0	0.74	3.0	2.0	10	Y
+ 3 ml H ₂ O	3.0	0.74	4.0	2.0	10	Y
+ 4 ml H ₂ O	3.0	0.74	5.0	2.0	10	Y
<i>Exp.37.b. Hydroxide route dense-gel crystallisation curves synthesis in 8 ml polypropylene bottle 100 °C oven</i>						
Molar Composition	1.0 SiO ₂ : 0.13 DEDBA: 18.60H ₂ O: 0.13 NaOH					
Amount Used	3.0	0.62	1.0	2.0	Variable	Y
Molar Composition	1.0 SiO ₂ : 0.13 DEDBA: 26.50 H ₂ O: 0.13 NaOH					
Amount Used	3.0	0.62	3.0	2.0	Variable	Y
<i>Exp.37.c. Hydroxide route dense-gel synthesis in 5.66 ml glass vial synthesis 100 °C oven</i>						
Molar Composition	1.0 SiO ₂ : 0.17 DEDBA: 0.16 NaOH: 29.82 H ₂ O					
Amount Used	3.0	0.52	2.0	1.33	7	N

An example fluoride route synthesis (*Exp.37.b.*) of MFI using N,N-diethyl-N,N-dibutylammonium iodide as an SDA was prepared as follows: 0.59 g of DEDBAI and 1.50 g ammonium fluoride were added to an 8 ml narrow-mouth polypropylene bottle. 1.5 ml of distilled water and 3.0 g of 40 % Ludox LS were added to the mixture and stirred thoroughly to form a thick gel. The bottle was then mixed on the vortex mixer for 5 seconds before being placed in a 100 °C oven for the specified synthesis time.

Table 3.40 - Fluoride route table of conditions for the synthesis of MFI using DEDBA

Synthetic Method	Ludox 30 % (g)	DEDBA SDA (g)	H₂O (ml)	NH₄F (g)	Synthesis Time (days)	MFI Successful
<i>Exp.38.a. Fluoride route dense-gel synthesis in 8 ml polypropylene bottle 100 °C oven</i>						
Molar Composition	1 SiO ₂ : 0.05 DEDBA: 11.69 H ₂ O: 0.74 NH ₄ F					
Amount Used	1.65	0.47	5.79	0.75	Variable	Y
Synthetic Method	Ludox 40 % (g)	DEDBA SDA (g)	H₂O (ml)	NH₄F (g)	Synthesis Time (days)	MFI Successful
<i>Exp.38.b. Fluoride Route dense-gel crystallisation curves synthesis in 8 ml polypropylene bottle 100 °C oven</i>						
Molar Composition	1.0 SiO ₂ : 0.09 DEDBA: 8.34 H ₂ O: 0.68 NH ₄ F					
Amount Used	3.0	0.59	1.2	1.5	Variable	Y
Synthetic Method	SiO₂ (g)	DEDBA SDA (g)	H₂O (ml)	NH₄F (g)	Synthesis Time (days)	MFI Successful
<i>Exp.38.c. Fluoride route hydrothermal synthesis in 46 ml autoclave 180 °C oven</i>						
Molar Composition	1.0 SiO ₂ : 0.08 DEDBA: 20.0 H ₂ O: 1.0 NH ₄ F					
Amount Used	2.0	0.84	12.0	1.23	6	N

Work-up: After removing the polypropylene bottle from the oven and allowing the content to cool to room temperature and pressure, the product was washed (30 ml distilled water) and centrifuged (3500 rpm, 15 minutes) three times yielding a white solid. The sample was later dried (60 °C, overnight) and confirmed as zeolite MFI by comparison of the XRD diffraction pattern obtained (Figure 3.41) to that published by International Zeolite Association.¹⁴

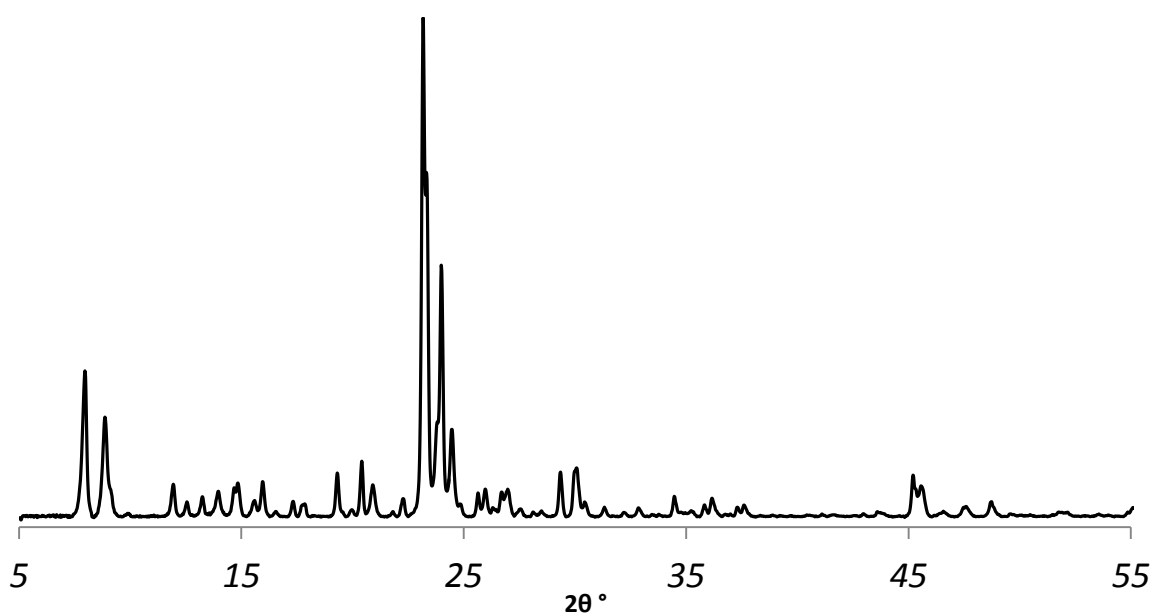


Figure 3.41 - XRD powder pattern of DEDBA/MFI on a Bruker Advance diffractometer with Cu K α source

3.2.21. Synthesis of MFI using DMDIBA⁺I⁻ - N,N-dimethyl-N,N-diisobutylammonium Chloride

SDA Synthesis: The SDA N,N-dimethyl-N,N-diisobutylammonium chloride (Figure 3.42) was synthesised by refluxing a 2:1:1 mixture of 2-chlorobutane (6.98 g, 75.45 mmol), dimethylamine HCl (3.08 g, 37.72 mmol), and sodium carbonate (4.00 g,

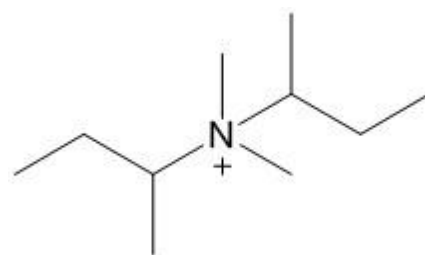


Figure 3.42 - Structure of DMDIBA (N,N-dimethyl-N,N-diisobutylammonium) cation

37.72 mmol) in 100 ml methanol for 4 days. After reflux, the sodium carbonate was removed via a cold filtration before the solvent was removed under reduced pressure producing a crude product. The product was then recrystallised using a mixture of ethyl acetate and a minimum amount of ethanol to remove any soluble impurities. White crystals were obtained (0.54 g, 7.45 %) however the NMR results were not obtained. This low yield may have been due to the bulkiness of the 2-chlorobutane being added, or due to the difficulties in adding two of these substituents to the amine. Despite the failed NMR, the next stage of MFI zeolite synthesis was attempted and yielded successful formation of MFI zeolite.

Zeolite Synthesis: Zeolite MFI was synthesised using N,N-dimethyl-N,N-diisobutylammonium iodide in a variety of different synthetic methods and reaction vessels. Table 3.41 and Table 3.42 and contain the details of all reactions attempted using the hydroxide and fluoride route, respectively.

Table 3.41 - Hydroxide route table of conditions for the synthesis of MFI using DMDIBA

Synthetic Method	Ludox 30% (g)	DMDIBA SDA (g)	H ₂ O (ml)	NaOH (ml)	Synthesis Time (days)	MFI Successful
<i>Exp.39.a. Hydroxide route dense-gel synthesis in 30 ml PFE bottle 100 °C oven</i>						
Molar Composition Amount Used	1.0 SiO ₂ : 1.00	0.11 DMDIBA: 0.16	10.71 H ₂ O: 0.33	0.13 NaOH: 0.66	18	Y
Molar Composition Amount Used	1.0 SiO ₂ : 3.0	0.13 DMDIBA: 0.57	26.0 H ₂ O: 1.0	0.13 NaOH: 2.0	14	Peaks forming

An example hydroxide route synthesis (*Exp.39.a.*) of MFI using N-N-dimethyl-N-N-diisobutylammonium iodide as an SDA was prepared as follows: 0.16 g of DMDIBA and 0.66 ml (1 M) sodium hydroxide were added to a 30 ml PFE bottle. 0.33 ml of distilled water and 1.0 g of 30 % Ludox LS were added to the mixture and mixed on a vortex mixer for 5 seconds before being placed in a 100 °C oven for 18 days.

Table 3.42 - Fluoride route table of conditions for the synthesis of MFI using DMDIBA

Synthetic Method	Ludox 40% (g)	DMDIBA SDA (g)	H₂O (ml)	NH₄F (g)	Synthesis Time (days)	MFI Successful
<i>Exp.40.a. Fluoride route dense-gel synthesis in 30 ml PFE bottle 100 °C oven</i>						
Molar Composition	1.0 SiO ₂ : 0.08 DMDIBA: 8.34 H ₂ O: 0.68 NH ₄ F					
Amount Used	3.0	0.46	1.2	1.5	14	N
Synthetic Method	SiO₂ (g)	DMDIBA SDA (g)	H₂O (ml)	NH₄F (g)	Synthesis Time (days)	MFI Successful
<i>Exp.41.a. Fluoride route dense-gel synthesis in 8 ml polypropylene bottle 100 °C oven</i>						
Molar Composition	1.0 SiO ₂ : 0.08 DMDIBA: 20.0 H ₂ O: 1.0 NH ₄ F					
Amount Used	1.0	0.38	6.0	0.62	15	N

Work-up: After removing the bottle from the oven and allowing the content to cool to room temperature and pressure, the product was washed (30 ml distilled water) and centrifuged (3500 rpm, 15 minutes) three times yielding a white solid. The sample was later dried (60 °C, overnight) and confirmed as zeolite MFI by comparison of the XRD diffraction pattern obtained (Figure 3.43), to that published by International Zeolite Association.¹⁴

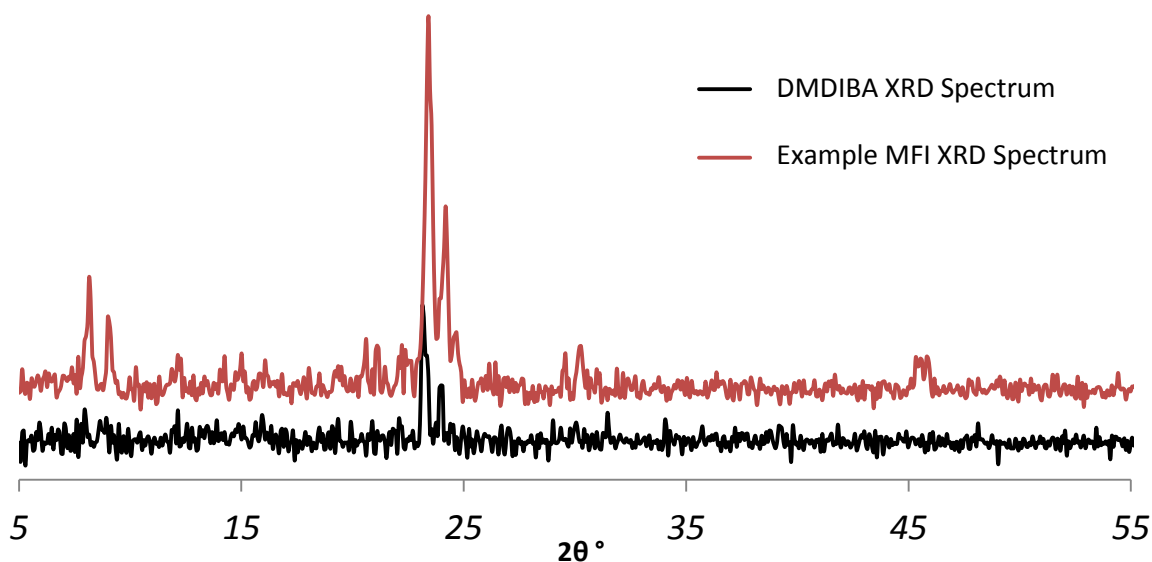


Figure 3.43 - XRD powder pattern of DMDIBA/MFI on a Bruker Advance diffractometer with Cu K α source

3.2.22. Synthesis of MFI using DEDIBA+I⁻ (N,N-diethyl-N,N-diisobutylammonium Chloride)

SDA Synthesis: The SDA N,N-diethyl-N,N-diisobutylammonium chloride (Figure 3.44) was synthesised by refluxing a 2:1:1 mixture of 2-chlorobutane (6.98 g, 75.44 mmol), diethylamine HCl (4.13 g, 37.72 mmol) and sodium carbonate (4.00 g, 37.72 mmol) in 100 ml methanol for 4 days. After reflux, the sodium carbonate was removed via

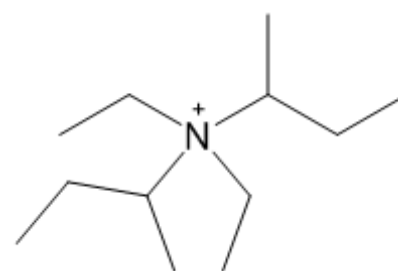


Figure 3.44 - Structure of DEDIBA (N,N-diethyl-N,N-diisobutylammonium) cation

a cold filtration before the solvent was removed under reduced pressure. The product was recrystallised with a mixture of ethyl acetate and a minimum amount of ethanol to remove any soluble impurities whereby white crystals were obtained (0.34 g, 3.20 %) and characterised as follows: ^1H NMR (300 MHz, CDCl_3 , ppm) δ 3.58 (2H, q, N-CH), 3.52 (4H, q, N-CH₂), 2.22 (4H, m(5), N-CH-CH₂), 1.78 (6H, d, N-CH-CH₃), 1.45 (6H, t, N-CH₂-CH₃), 1.19 (6H, t, CH-CH₂-CH₃). ^{13}C NMR (300MHz, CDCl_3 , ppm) δ 66.11 (N-CH), 60.03 (N-CH₂), 24.32 (N-CH-CH₂), 23.30 (N-CH-CH₃), 8.74 (CH-CH₂-CH₃), 8.34 (N-CH₂-CH₃).

Zeolite Synthesis: Zeolite MFI was synthesised using N,N-diethyl-N,N-diisobutylammonium iodide in a variety of different synthetic methods and reaction vessels. Table 3.43 contains the details of

all reactions attempted using the hydroxide route.

Table 3.43 - Hydroxide route table of conditions for the synthesis of MFI using DEDIBA

Synthetic Method	Ludox 30% (g)	DEDIBA SDA (g)	H ₂ O (ml)	NaOH (ml)	Synthesis Time (days)	MFI Successful
Exp.41.a. Hydroxide route dense-gel synthesis in 8 ml polypropylene bottle						
100 °C oven						
Molar Composition	1.0 SiO ₂ : 0.22 DEDIBA: 18.60 H ₂ O: 0.13 NaOH					
Amount Used	3	0.74	1	2	10	N
+ 1 ml H ₂ O	3	0.74	2	2	10	N (D)
+ 2 ml	3	0.74	3	2	10	N (D)
+ 4 ml	3	0.74	5	2	10	N
+ 1 ml	3	0.74	2	2	10	N
+ 2 ml	3	0.74	3	2	10	N
+ 2 ml	3	0.74	3	2	13	N
+ 2 ml	3	0.74	3	2	15	N
+ 2 ml	3	0.74	3	2	20	N
+ 3 ml	3	0.78	4	2	7	Y
Exp.41.b. Hydroxide route dense-gel crystallisation curves synthesis in 8 ml polypropylene bottle						
100 °C oven						
Molar Composition	1.0 SiO ₂ : 0.14 DEDIBA: 26.50 H ₂ O: 0.13 NaOH					
Amount Used	3 g	0.65 g	3 ml	2 ml	Variable	N
Exp.41.c. Hydroxide route dense-gel synthesis in 5.66 ml glass vial						
100 °C oven						
Molar Composition	1.0 SiO ₂ : 0.14 DEDIB : 26.36 H ₂ O : 0.14 NaOH					
Amount Used	1.98 g	0.43 g	2 ml	1.33 ml	7 days	N

An example hydroxide route synthesis (*Exp.41.a.*) of MFI using N,N-diethyl-N,N-diisobutylammonium iodide as an SDA was prepared as follows: 0.78 g of DEDIBA and 2.0 ml (1 M) sodium hydroxide were added to a 8 ml polypropylene bottle. 4.0 ml of distilled water and 3.0 g of 30 % Ludox LS were added to the mixture and mixed on a vortex mixer for 5 seconds to form a thick gel. The plastic bottle was sealed and placed in a 100 °C oven for 7 days.

Work-up: After removing the bottle from the oven and allowing the content to cool to room temperature and pressure, the product was washed (30 ml distilled water) and centrifuged (3500 rpm, 15 minutes) three times yielding a white solid. The sample was later dried (60 °C, overnight) and confirmed as zeolite MFI by comparison of the XRD diffraction pattern obtained (Figure 3.45), to that published by International Zeolite Association¹⁴.

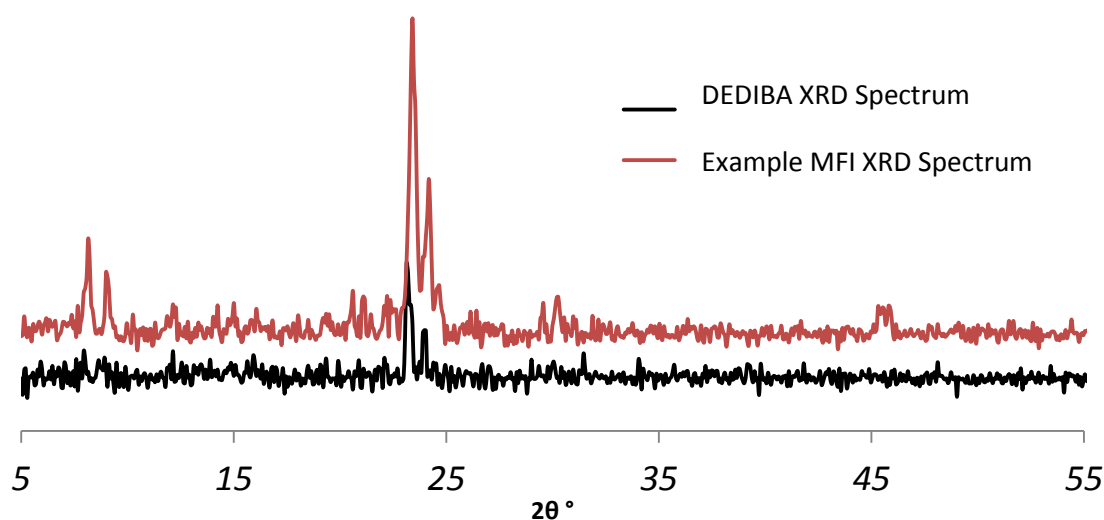


Figure 3.45 - XRD powder pattern of DEDIBA/MFI on a Bruker Advance diffractometer with Cu K α source

Silicalite-1 synthesised using N,N-diethyl-N,N-diisobutylammonium iodide can be synthesised under the above conditions (*Exp.41.a.*) but lacks long range order. It has therefore been overlaid with an example X-ray diffraction pattern of another successful silicalite-1 (MFI) sample to demonstrate the peaks forming correctly for MFI the framework.

3.3. Unsuccessful MFI Structure Directing Agents

The following structure directing agents did not successfully synthesise silicalite-1 or any zeolite despite an excessive amount of attempts and being characteristically similar to structure directing agents that do successfully synthesis Silicalte-1 with MFI and MEL frameworks.

3.3.1. Synthesis of P(3)TBAI - N-propyltributylammonium Iodide

SDA Synthesis: The SDA n-propyl-tributylammonium iodide (Figure 3.46) was synthesised by refluxing iodopropane (5.71 g, 33.6mmol) and tributylamine (6.22 g, 33.6mmol) in 100 ml methanol for 3 days.

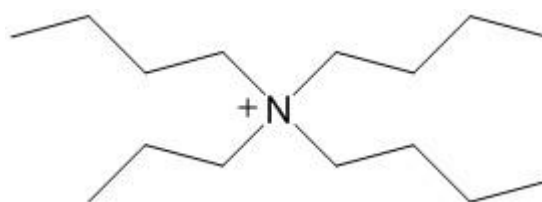


Figure 3.46 - Structure of P3TBA (N-propyltributylammonium) cation

The methanol was removed under reduced pressure and the product was recrystallised with a mixture of ethyl acetate and a minimum amount of ethanol to remove any soluble impurities.

White crystals were obtained (3.06 g, 25.64 %) and characterised as follows: ^1H NMR (300 MHz, CDCl_3 , ppm) δ 3.35 (6H, m, $\text{N-CH}_2\text{-CH}_2$), δ 3.30 (2H, w, $\text{N-CH}_2\text{-CH}_2$), δ 1.77 (2H, w, $\text{N-CH}_2\text{-CH}_2$), δ 1.67 (6H, m, $\text{N-CH}_2\text{-CH}_2$), δ 1.44 (6H, m, $\text{CH}_2\text{-CH}_2\text{-CH}_3$), δ 1.04 (3H, m, $\text{CH}_2\text{-CH}_2\text{-CH}_3$), δ 0.98 (9H, s, $\text{CH}_2\text{-CH}_3$); ^{13}C NMR (300MHz, CDCl_3 , ppm) δ 60.81 ($\text{N-CH}_2\text{-CH}_2\text{-CH}_3$), δ 59.20 ($\text{N-CH}_2\text{-CH}_2\text{-CH}_2$), δ 24.30 ($\text{N-CH}_2\text{-CH}_2\text{-CH}_2$), δ 19.78 ($\text{N-CH}_2\text{-CH}_2\text{-CH}_2$), δ 16.13, ($\text{N-CH}_2\text{-CH}_2\text{-CH}_3$), δ 13.78, ($\text{N-CH}_2\text{-CH}_2\text{-CH}_2$), δ 10.96 ($\text{N-CH}_2\text{-CH}_2\text{-CH}_2\text{-CH}_3$).

Zeolite Synthesis: Zeolite MFI was synthesised using N-propyltributylammonium iodide in a variety of different synthetic methods and reaction vessels. Figure 3.45 contains the details of all reactions attempted using the fluoride route.

An example fluoride route synthesis (*Exp.42.b.*) of MFI using N,N-dipropyl-N,N-diisopropylammonium iodide as an SDA was prepared as follows: 0.46 g of P(3)TBA and 0.95 g ammonium hydrogen fluoride were added to a 46 ml Teflon lined stainless steel autoclave liner. 6.0 ml of distilled water and 1.0 g of silicon dioxide were added to the mixture and stirred thoroughly to form a thick gel before the autoclave was placed in a 100 °C oven for 21 days.

Table 3.44 - Fluoride route table of conditions for the synthesis of MFI using P(3)TBA

Synthetic Method	SiO_2 (g)	P(3)TBA SDA (g)	H_2O (ml)	NH_4F (g)	Synthesis Time (days)	MFI Successful
<i>Exp 42.a. Fluoride route hydrothermal synthesis in 46 ml autoclave 180 °C oven</i>						
Molar Composition	1.0 SiO_2 : 0.08 P(3)TBA: 20.02 H_2O : 1.0 NH_4F					
Amount Used	1.0	0.47	6.0	0.62	5	N
	1.0	0.47	6.0	0.62	25	N
	2.0	0.95	12.0	1.23	4	N
	2.0	0.95	12.0	1.23	7	N
Synthetic Method	SiO_2 (g)	P(3)TBA SDA (g)	H_2O (ml)	$(\text{NH}_4)\text{HF}_2$ (g)	Synthesis Time (days)	MFI Successful
<i>Exp.42.b. Fluoride route hydrothermal synthesis in 46 ml autoclave 100 °C oven</i>						
Molar Composition	1.0 SiO_2 : 0.08 P(3)TBA: 20.02 H_2O : 1.00 $(\text{NH}_4)\text{HF}_2$					
Amount Used	1.0	0.47	6.0	0.95	21	N

Work-up: After removing the autoclave from the oven and allowing the content to cool to room temperature and pressure, the product was washed (30 ml distilled water) and centrifuged (3500

rpm, 15 minutes) three times yielding a white solid. The sample was later dried (60 °C, overnight) and studied by XRD crystallography however yielded XRD amorphous material.

3.3.2. Synthesis of MFI using DP(3)DIP(3)A⁺I⁻ - N,N-dipropyl-N,N-diisopropylammonium Iodide

SDA Synthesis: The SDA N,N-dipropyl-N,N-diisopropylammonium iodide (Figure 3.47) was synthesised by refluxing dipropylamine (3.69 g, 36.47 mmol) and 2-iodopropane (12.40 g, 72.93 mmol) in 100ml methanol for 3 days. The methanol was removed under reduced pressure and the product was recrystallised using a mixture of ethyl acetate and a minimum amount of ethanol to remove any soluble impurities. White crystals were obtained (6.55 g, 20.79 mmol) and characterised as follows:

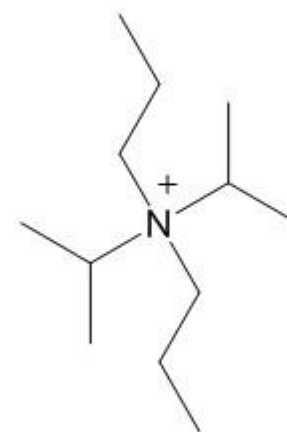


Figure 3.47 - Structure of DPDIPA (N,N-dipropyl-N,N-diisopropylammonium) cation

¹H NMR (300 MHz, CDCl₃, ppm) δ 3.72 (2H, q, N-CH-(CH₃)₂), 2.97 (4H, t, N-CH₂-CH₂), 1.97 (4H, m(6), N-CH₂-CH₂), 1.45 (12H, d, N-CH-(CH₃)₂), 0.97 (6H, t, CH₂-CH₃); ¹³C NMR (300MHz, CDCl₃, ppm) δ 55.42 (N-CH-(CH₃)₂), 52.21 (N-CH₂-CH₂), 18.27 (N-CH-(CH₃)₂), 17.08 (CH₂-CH₂-CH₃), 11.51 (CH₂-CH₂-CH₃).

Zeolite Synthesis: Zeolite MFI was synthesised using N,N-dipropyl-N,N-diisopropylammonium iodide in a variety of different synthetic methods and reaction vessels. Table 3.45 and Table 3.46 and contain the details of all unsuccessful reaction attempts using the hydroxide and fluoride route, respectively.

Table 3.45 - Hydroxide route table of conditions for the synthesis of MFI using DP(3)DIP(3)A

Synthetic Method	Ludox 30% (g)	DMDIBA SDA (g)	H ₂ O (ml)	NaOH (ml)	Synthesis Time (days)	MFI Successful
<i>Exp.43.a. Hydroxide route dense-gel synthesis in 8 ml polypropylene bottle 100 °C oven</i>						
Molar Composition	1.0 SiO ₂ : 0.13 DP(3)DIP(3)A: 0.18.60 H ₂ O: 0.13 NaOH					
Amount Used	3.0	0.63	1.0	2.0	10	N
	3.0	0.63	1.0	2.0	14	N

Table 3.46 - Fluoride route table of conditions for the synthesis of MFI using DPDIPA

Synthetic Method	Ludox LS 30% (g)	DP(3)DIP(3) SDA (g)	H ₂ O (ml)	NH ₄ F (g)	Synthesis Time (days)	MFI Successful
<i>Exp.44.a. Fluoride route autoclave hydrothermal method 100 °oven</i>						
Molar Composition	1.0 SiO ₂ : 0.18 DP(3)DIP(3)A: 20.0 H ₂ O: 1.0 NH ₄ F					
Amount Used	1.0	0.91	6.0	0.62	14	N

3.4. Additional X-ray Diffraction Peak

An additional peak at 5.2 2 θ° has been observed in X-ray diffraction patterns of MFI synthesised using the following structure directing agents: triethyl-n-propylammonium iodide, some triethyl-N-hexylammonium iodide samples and triethyl-N-heptylammonium iodide.

When powder patterns were researched in the 'The Collection of Simulated XRD Powder Patterns for Zeolites', two possible substances were found that may be assigned to this peak: Perlielite (LTL framework) and VPI-5 (VFI framework). Perlielite with LTL framework was dismissed as an option because it has no silicon only based related materials. Additionally, it has a peak at ~22.5 2 θ° that should also be observed if this species was present and is not observed in the XRD powder pattern.

The VFI framework however, has a silicon based related material called MCM-9.¹⁵ The peak observed at ~5.4 2 θ° corresponds to the first peak on the MCM-9 spectra¹⁶ however this is the only strong peak and MCM-9, as a large mesoporous structure does not have good crystallinity and long-range order. Any other peaks in the MCM-9 spectra present are very small by comparison. Some can be identified and some appear to be missing. It is possible some are overlapped by much stronger silicalite-1 (MFI framework) peaks and it is also possible that due to the

lack of long-range order, some crystal faces have not fully formed and as such the peaks are missing. Additionally this zeolite is synthesised with quaternary ammonium cations^{16,18} and can be synthesised using n-alkyltrimethylammonium SDA's.¹⁷ It is thought that the zeolites synthesised within this chapter are high silica MFI with MCM-9 intergrowths due to the small nature of the triethylammonium which closely resembles the alkyltrimethylammonium cations used in the literature.

3.5. References

- 1 A. Rojas, L. Gomez-Hortigueela and M. A. Camblor, *J. Am. Chem. Soc.*, 2012, **134**, 3845–3856.
- 2 C. A. Fyfe, R. J. Darton, H. Mowatt and Z. S. Lin, *Microporous Mesoporous Mater.*, 2011, **144**, 57–66.
- 3 U.S., 1972.
- 4 C. S. Cundy and P. Cox, *Chem. Rev.*, 2003, **103**, 663–701.
- 5 P. A. Barrett, M. A. Camblor, A. Corma, R. H. Jones and L. A. Villaescusa, *J. Phys. Chem. B*, 1998, **102**, 4147–4155.
- 6 J. Cejka, H. Bekkum, A. Corma and F. Schueth, *Introduction to Zeolite Molecular Sieves*, 2007.
- 7 P. Jacobs and J. Martens, *Stud. Surf. Sci. Catal.*, 1987, **33**, 47–111.
- 8 C. A. Fyfe, Z. S. Lin, C. Tong and R. J. Darton, *Microporous Mesoporous Mater.*, 2012, **150**, 7–13.
- 9 A. Çulfaz, U. Gündüz and H. Orbey, *Cryst. Res. Technol.*, 1993, **28**, 29–38.
- 10 J. Na, G. Liu, T. Zhou, G. Ding, S. Hu and L. Wang, *Catal. Letters*, 2013, **143**, 267–275.
- 11 S. I. Zones, Y. Nakagawa, G. S. Lee, C. Y. Chen and L. T. Yuen, *Microporous Mesoporous Mater.*, 1998, **21**, 199–211.
- 12 S. L. Burkett and M. E. Davis, *J. Phys. Chem.*, 1994, **98**, 4647–4653.
- 13 C. A. Fyfe, R. J. Darton, H. Mowatt and Z. S. Lin, *Microporous Mesoporous Mater.*, 2011, **144**, 57–66.
- 14 C. Baerlocher and L. B. McCusker, *Database Zeolite Struct.*
- 15 E. G. Derouane, L. Maistriau, Z. Gabelica, A. Tuel, J. B. Nagy and R. Von Ballmoos, *Appl. Catal.*, 1989, **51**, L13–L20.
- 16 M. E. Davis, P. E. Hathaway and C. Montes, *Zeolites*, 1989, **9**, 436–439.
- 17 C. C. Costa, D. M. A. Melo, M. A. F. Melo, M. E. Mendoza, J. C. Nascimento, J. M. Andrade and J. M. F. Barros, *J. Porous Mater.*, 2014, **21**, 1069–1077.
- 18 M. E. Davis, C. Montes, P. E. Hathaway, J. P. Arhancet, D. L. Hasha and J. M. Garces, *J. Am. Chem. Soc.*, 1989, **111**, 3919–3924.

4.0. Solid State NMR Study of MFI Zeolite Synthesised Using Varied Structure Directing Agents

Carbon (^{13}C) and nitrogen (^{14}N) solid state NMR experiments have been used to explore the effects of altering structure directing agent size and shape in the synthesis of silicalite-1. Previous studies exist on ZSM-5¹ and the high-silica version, silicalite-1^{2,3} using hydroxide route syntheses and more recently studying the fluoride route synthesis.⁴ The majority of these studies have focused on the use of tetrapropylammonium (TPA) as a structure directing agent (SDA)⁵, leaving a wealth of undiscovered knowledge that could contribute to the chemistry of zeolites.

The structure of the ZSM-5 framework has been established since 1981⁶ and in 1987 the location of the structure directing agent was defined within the zeolite pore, with propyl chains not fully extended but pointing towards the straight [010] and sinusoidal channels [100].⁵ This is demonstrated in Figure 4.1;

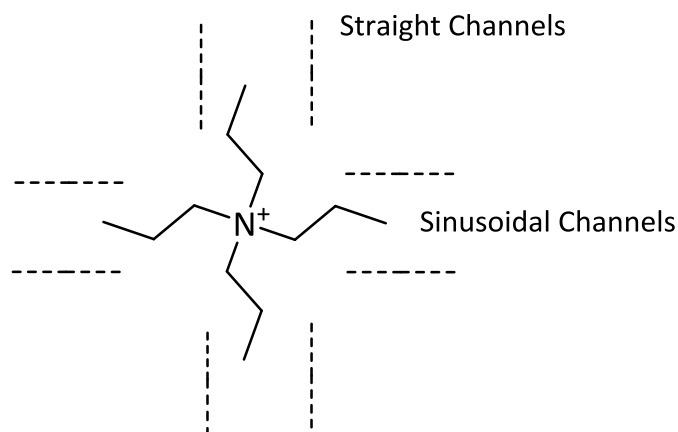


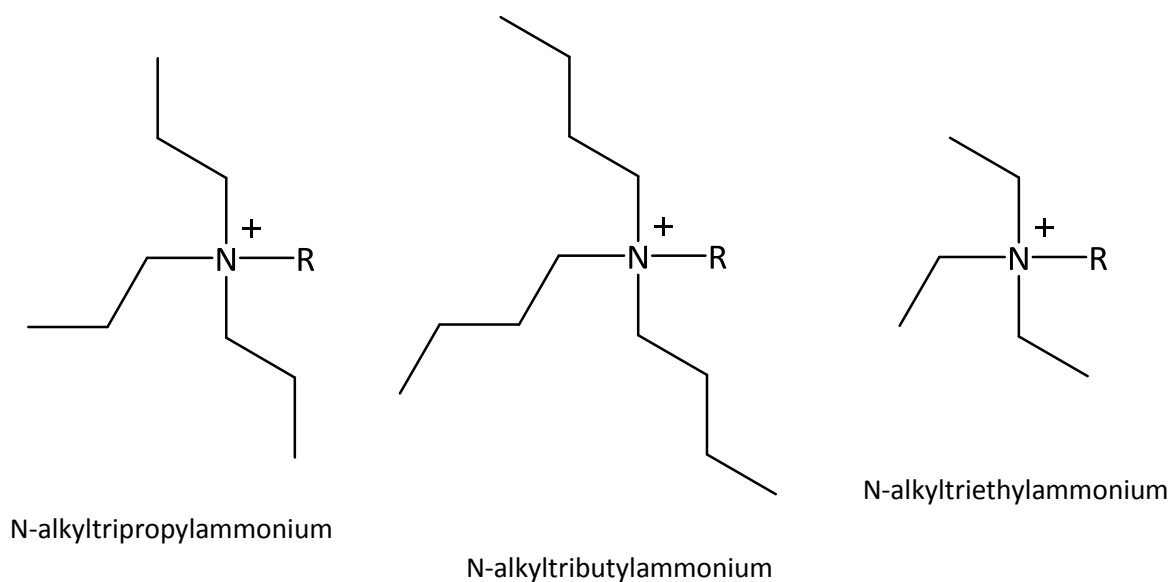
Figure 4.1 - Schematic representation of TPA silicalite-1 within the zeolite framework and the orientation of TPA within straight and sinusoidal channels (not to scale)

More recently, further structural information has been determined about the zeolite structure including the inclusion of the fluoride mineralising agent into the structure,⁷ differences in silicalite-1 channel opening sizes (straight = 5.4 Å x 5.6 Å, sinusoidal = 5.1 Å x 5.7 Å)⁸ and the effects of varying alkyl chain length of TPA SDA in silicalite-1.⁹

The use of a systematic study of SDA's on the simple efficient zeolite silicalite-1,¹⁰ could help to identify why some structure directing agents produce more crystalline zeolites and what synthetic qualities are responsible, as well as the effects of different structure directing agents on silicalite-1's crystal shape and size that are key aspects to their absorption properties.

4.1. ¹³C Solid State NMR

Carbon solid state NMR studies ¹³C {¹H} have been used to determine the local effects and orientation of the following series of structure directing agents synthesised in Chapter 3 in silicalite-1 zeolite;



4.1.1. TPA F-Silicalite-1

The synthesis of Silicalite-1 using tetrapropylammonium (TPA) as an organic SDA is commonly observed in the literature.^{4,11,12} Initial spectra obtained of TPA silicalite-1 using the hydroxide route synthesis returned a low resolution spectrum (Figure 4.2), with large peak linewidths and minimal peak splitting observed at the terminal (C_γ) carbon at ~10 ppm.

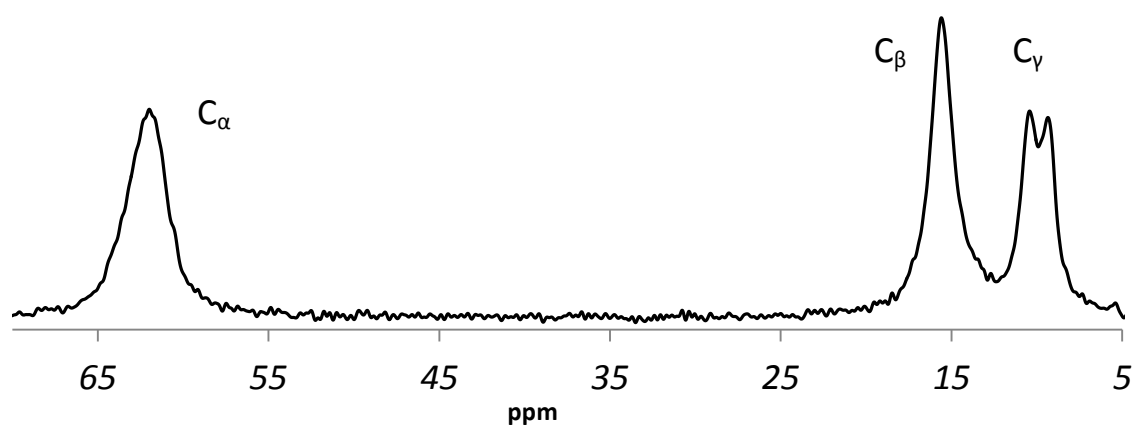


Figure 4.2 – $^1\text{H}\{^{13}\text{C}\}$ CP MAS NMR of silicalite-1 synthesised with tetrapropylammonium using the hydroxide route synthesis

The silicalite-1 TPA terminal C_γ peak has been observed splitting in MFI and other zeolites since the early 1980s in MFI^{2,13,14,15} and other zeolites¹⁶ where the reasons for its occurrence have been the subject of a literature debate. Initial works by Nagy and co-workers¹⁵ and Boxhoorn and co-workers¹⁷ considered many options but deduced the splitting is due to TPA ion interactions with the straight and sinusoidal channels of different chemical environments. Nagy and co-workers¹⁸ later deemed this splitting due to steric contact between the methyl groups of two adjacent TPA molecules whereas Burkett and Davis¹⁹ deemed it due to a difference in van der Waal interactions between the methyls and framework species of the straight and sinusoidal channels.^{2,16} This latter view would indicate that there are two individual resonances; one from the two propyl C_γ interactions with the straight channel, and the other from the two propyl C_γ interactions with the sinusoidal channel.

In more recent years the development of synthetic procedures and solid state NMR capabilities have continued to provide higher resolution spectra whereby in 1998 Gougeon and co-workers⁴ successfully elucidated 8 peaks in the silicalite-1 TPA system by using fluoride as a replacement mineralising agent. Use of the fluoride route allows for almost defect-free zeolites to be produced allowing very good spectral resolution to be obtained. As such, 8 carbons peaks can be distinguished from Figure 4.3 and characterised as follows (Table 4.1).

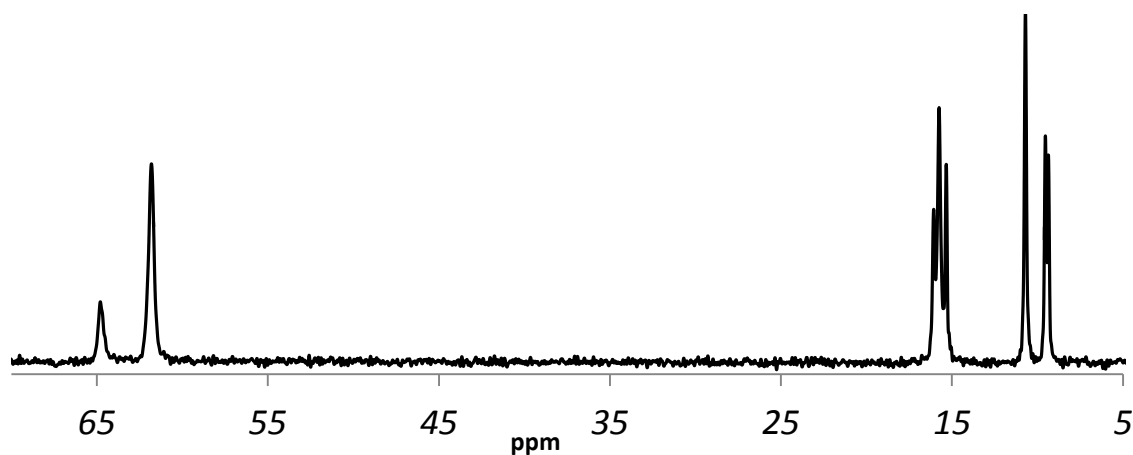


Figure 4.3 - $^1\text{H} \{^{13}\text{C}\}$ CP MAS NMR of silicalite-1 synthesised with tetrapropylammonium using the fluoride route synthesis

Table 4.1 - Table of chemical shift values for fluoride route TPA silicalite-1 sample using solid state NMR

TPA Alkyl Assignment (δ)	C1 (α) / ppm	C2(β) / ppm	C3 (γ) / ppm
$^1\text{H} \{^{13}\text{C}\}$ CP MAS SS NMR	64.80 / 61.82	16.07 / 15.75 15.33	10.70 – straight 9.53/ 9.36 - sinusoidal

The significant chemical resolution enhancement elucidates 8 carbon resonances for the 3 carbons (α , β , γ) in TPA silicalite-1 (Figure 4.4). The C_γ split peaks are individually assigned as per previous assignments by Abraham and co-workers (ZSM-5),²⁰ and Dib and co-workers (silicalite-1)⁹ to the straight and sinusoidal channels.

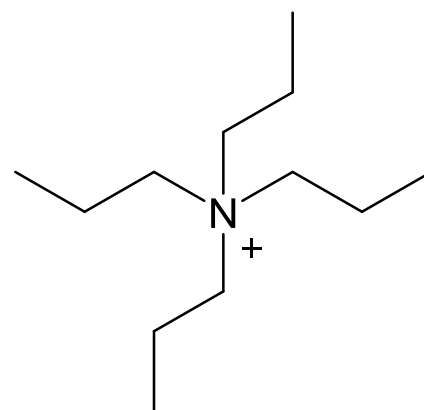


Figure 4.4 - Structure of TPA (tetrapropylammonium) cation SDA

The NMR spectrum obtained displays the same peak splitting as previously observed whereby a carbon peak area ratio of 1:1 is observed, indicating two propyl arms are extended in, or towards the straight channel, and two the sinusoidal channel.

Despite being previously observed on multiple occasions^{9,12,13}, the splitting of TPA silicalite-1 C_α is difficult to justify. It cannot arise due to residual dipolar coupling to the ^{14}N as the C_α values (determined later in this chapter) are not of sufficient size²¹ and the strength of the applied magnetic field has no effect on them.²² They also do not arise due to the location of the fluoride

within the zeolite pore as the fluoride has now been determined²³ to sit within the $[4^15^26^2]$ cage covalently bonded to silicon, therefore they are not sufficiently close. Remaining options involve different chemical shift peaks due to molecular motion within the SDA and therefore different interactions with the zeolite framework.

The zeolite framework is sensitive to lots of contributing factors during crystallisation. These include the reagent composition, crystallisation time and temperature amongst others and all of these can have an effect on the crystal size and shape produced.²⁴ The study of TPA silicalite-1 zeolite synthesised using the fluoride route produces rectangular crystals of 30 x 60 μm dimensions by SEM Imaging (Figure 4.5).

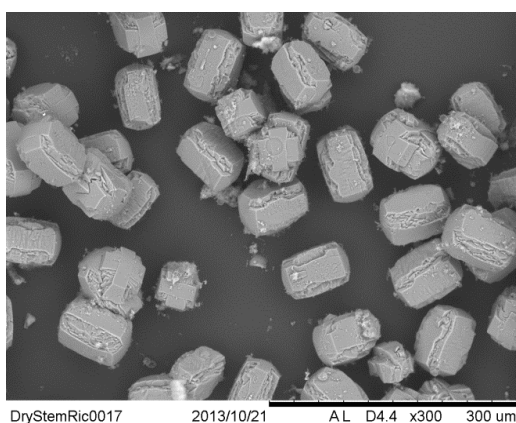


Figure 4.5 - SEM Image of TPA silicalite-1 synthesised via the fluoride route. Rectangular shaped crystals of dimensions ~ 30 x 60 μm at 300 x zoom

4.1.2. N-alkyltriethylammonium Silicalite-1 Series

In order to discover more about this system, the n-alkyltriethylammonium silicalite-1 series was studied by ^{13}C solid state NMR altering the alkyl chain length from methyl to pentyl.

4.1.2.1. MTPA F-Silicalite-1

The smallest alkyl chain in the successful synthesis of n-alkyltriethylammonium silicalite-1 series is n-methyltriethylammonium, shown right (Figure 4.6).

This zeolite rapidly crystallises within 2 days at 100 $^{\circ}\text{C}$

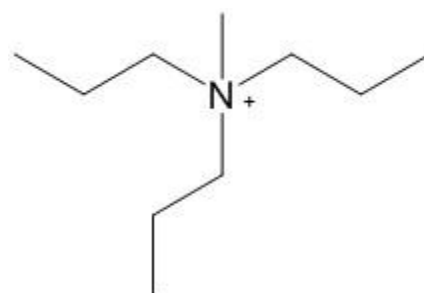


Figure 4.6 - Structure of MTP3A (n-methyltriethylammonium) cation SDA

using the described dense-gel synthetic method in Chapter 3.

The spectral resolution obtained for MTPA F silicalite-1 also displays significant enhancements over previous samples synthesised using the hydroxide route. The $^{13}\text{C}\{^1\text{H}\}$ CP MAS NMR spectrum is shown below (Figure 4.7) and assigned as follows (Table 4.2):

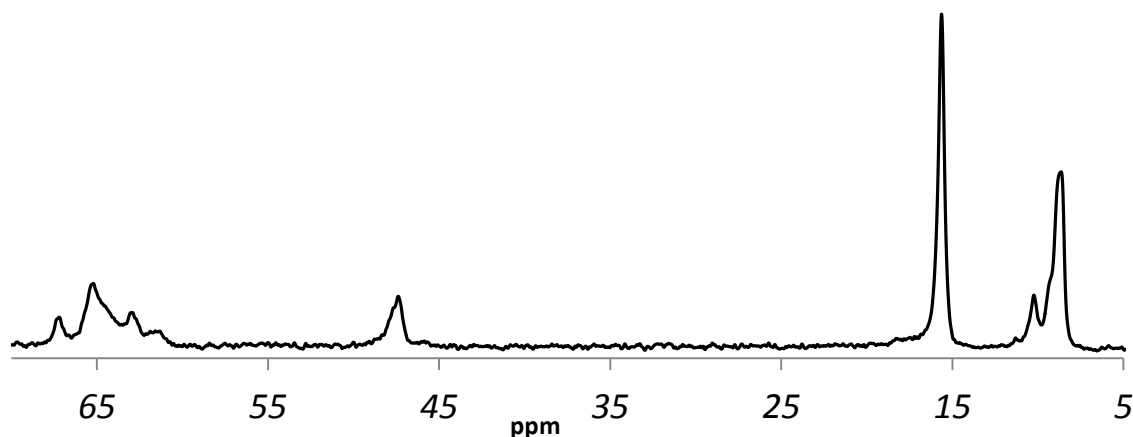


Figure 4.7 – $^{13}\text{C}\{^1\text{H}\}$ CP MAS NMR of silicalite-1 synthesised with n-methyltripropylammonium using the fluoride route synthesis

Table 4.2 - Table of chemical shift values for fluoride route MTP silicalite-1 sample using solid state NMR

MTP(3)A Assignment (δ)	N-methyl / ppm	Tripropyl / ppm		
		C2 (α)	C3 (β)	C4 (γ)
$^1\text{H}\{^{13}\text{C}\}$ CP MAS	47.40	67.22 / 65.22	15.64	10.24
SS NMR	47.71	62.93 / 61.61		9.31 / 8.61

A minimum of 10 carbon peaks can be deciphered from the $^{13}\text{C}\{^1\text{H}\}$ spectrum above (Figure 4.7) for the MTPA structure directing agent in silicalite-1.

The method used to study the channel location of various alkyl chains within these series of SDA silicalite-1 samples is a method previously used by Dib and co-workers²⁵. The method involved identification of a carbon resonance (e.g, C_β) that is split into two chemical resonances for carbons directed towards the straight and sinusoidal channels. For the tetrapropylammonium silicalite-1, the peak areas observed should exist in a 2:2 ratio for the two propyl chains in each straight and sinusoidal environment. However, when one propyl chain is replaced with another alkyl chain, methyl in this sample, the ratio changes to a 1:2 ratio of propyl chains in the straight

and sinusoidal channel indicating the methyl chain location in the straight channel, as shown in Figure 4.8;

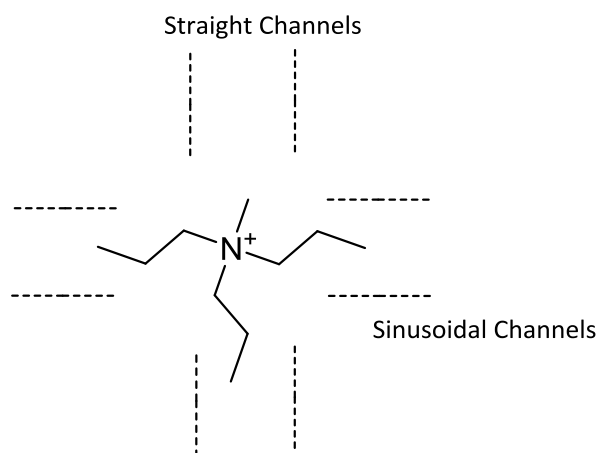


Figure 4.8 - Schematic representation of MTPA silicalite-1 within the zeolite framework and the orientation of MTPA within straight and sinusoidal channels (not to scale)

Interestingly, the replacement of fluoride as a mineralising agent²⁶ not only adds a new covalent bond to the system, reduces crystal defects²⁷ and crystallisation time but it also has a dramatic effect on the crystal shape and size obtained.²⁸ This is demonstrated in Figure 4.9 whereby the hydroxide route synthesis yields ~ 5 μm diameter spherical crystals and the fluoride yields the classical coffin shape crystals (25 μm x 80 μm) dimensions;

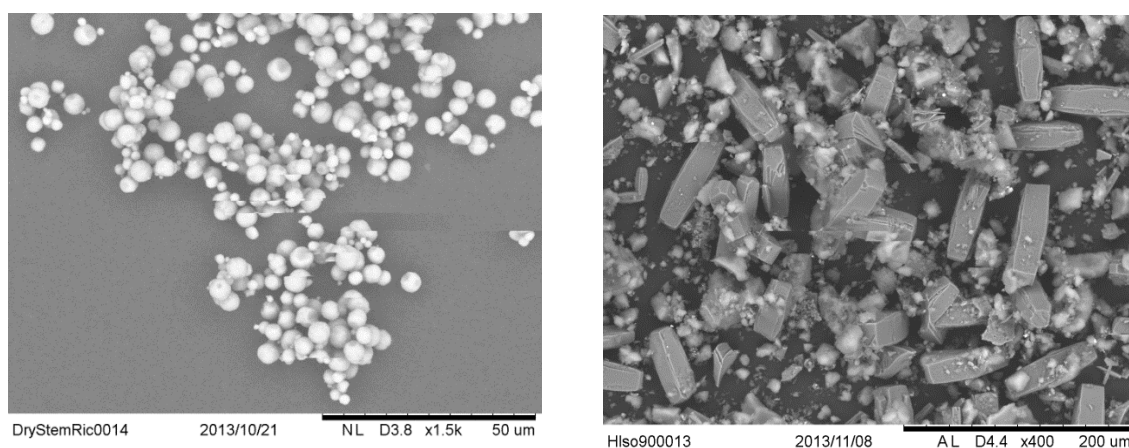


Figure 4.9 – SEM Images of MTPA silicalite-1 synthesised using (left) hydroxide route producing spherical crystals ~5 μm and (right) fluoride route producing coffin shape crystals of 25 x 80 μm size

4.1.2.2. ETPA Silicalite-1

Upon increasing the alkyl chain length from methyl to n-ethyltripropylammonium (Figure 4.10) silicalite-1, a minimum of 10 carbon peaks can be identified. The spectrum is shown below in Figure 4.11 and characterised in Table 4.3:

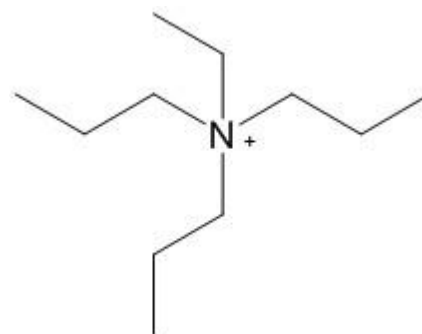


Figure 4.10 - Structure of ETP3A (ethyltripropylammonium) cation SDA

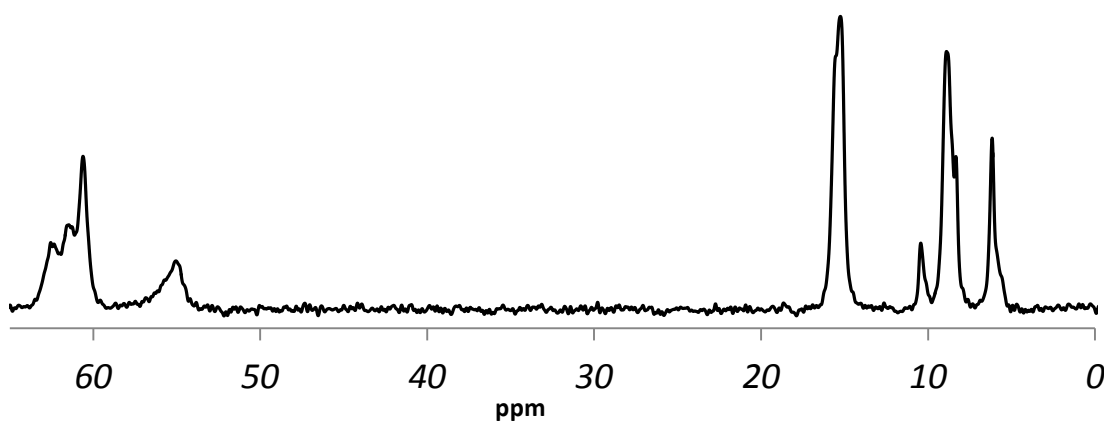


Figure 4.11 – $^{13}\text{C}\{^1\text{H}\}$ CP MAS NMR of silicalite-1 synthesised with n-ethyltripropylammonium using the fluoride route synthesis

Table 4.3 – Table of chemical shift values for fluoride route ETP silicalite-1 sample using solid state NMR

ETPA Assignment (δ)	N-ethyl / ppm		Tripropyl / ppm		
	C1 (α)	C2 (β)	C3 (α)	C4 (β)	C5 (γ)
$^1\text{H}\{^{13}\text{C}\}$ CP MAS SS NMR	55.06	6.18	62.56 / 61.47 60.62	15.56 15.28	10.44 / 8.90 8.34

A splitting pattern emerges for the propyl chain that allows comparison to previously observed spectra of TPA and MTP silicalite-1 (Figure 4.12);

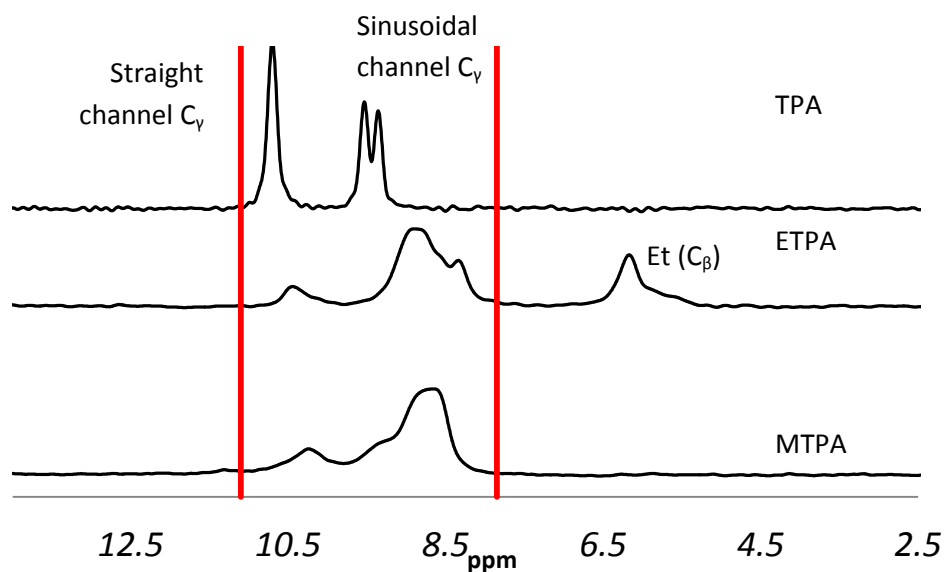


Figure 4.12 - $^{13}\text{C}\{^1\text{H}\}$ CP MAS NMR of silicalite-1 synthesised with the methyl to propyl series of n-alkyltripropylammonium from 2.5 – 15 ppm (intensity not to scale)

As indicated within the red region of Figure 4.12, a decrease in the straight channel carbon resonance for ETPA propyl C_γ is observed. This peak reduction represents the replacement of a straight channel propyl chain with both methyl and ethyl respectively, as has been as previously observed by Dib ad co-workers.⁹

The increase in structure directing agent size to n-ethyltripropylammonium silicalite-1 appears to effect the crystals formed whereby the shape and size of the crystals more closely resemble crystals synthesised using TPA (Figure 4.13).

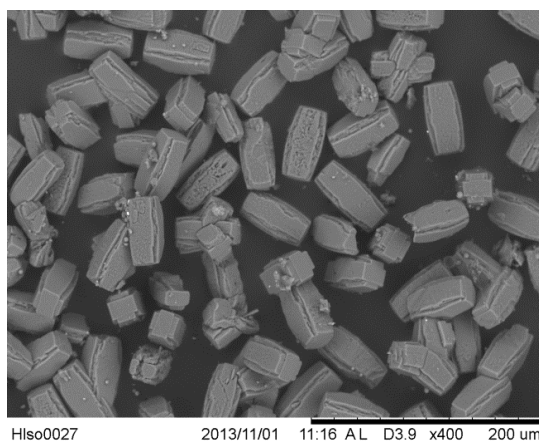


Figure 4.13 - SEM Image of ETP silicalite-1 synthesised via the fluoride route. Coffin shaped crystals of dimensions $\sim 40 \times 90 \mu\text{m}$ at 400 x zoom

4.1.2.3. BTPA Silicalite-1

Upon increasing the alkyl chain length to n-butyltriethylammonium as silicalite-1 SDA (Figure 4.14), a minimum of 10 carbon resonances can also be deciphered from the NMR spectrum shown (Figure 4.15) and characterised (Table 4.4):

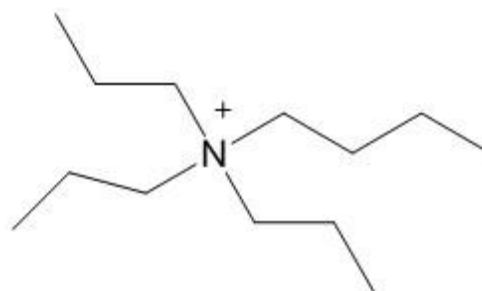


Figure 4.14 - Structure of BTP3A (N-butyltriethylammonium) cation SDA

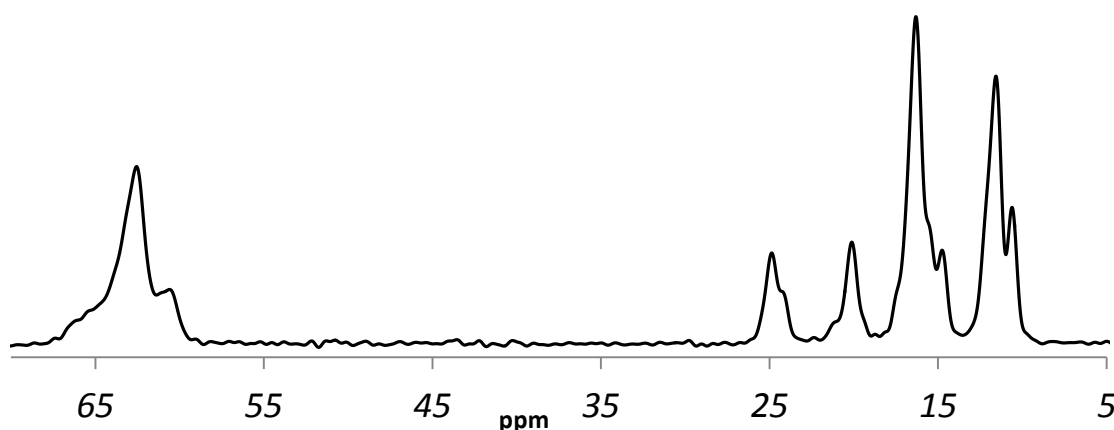


Figure 4.15 - $^{13}\text{C} \{^1\text{H}\}$ CP MAS NMR of silicalite-1 synthesised with n-butyltriethylammonium using the fluoride route synthesis

Table 4.4 - Table of chemical shift values for fluoride route BTP silicalite-1 sample using solid state NMR

BTPA Assignment (δ)	N-butyl / ppm				Tripropyl / ppm		
	C4 (α)	C5 (β)	C6 (γ)	C7 (δ)	C1 (α)	C2 (β)	C3 (γ)
$^1\text{H} \{^{13}\text{C}\}$ CP MAS	60.60	24.87	20.12	14.76	62.56	16.31	11.57
SS NMR		24.24			64.76		10.61

In BTPA silicalite-1 we observe the opposite effect to methyl and ethyl in the n-alkyltriethylammonium species. A reduction in propyl C_γ peak area is observed in the sinusoidal channel, as opposed to the straight channel. This reduction of the sinusoidal channel propyl occurs due to the replacement of the butyl extended into the sinusoidal channel which has also previously been observed⁹ (Figure 4.16).

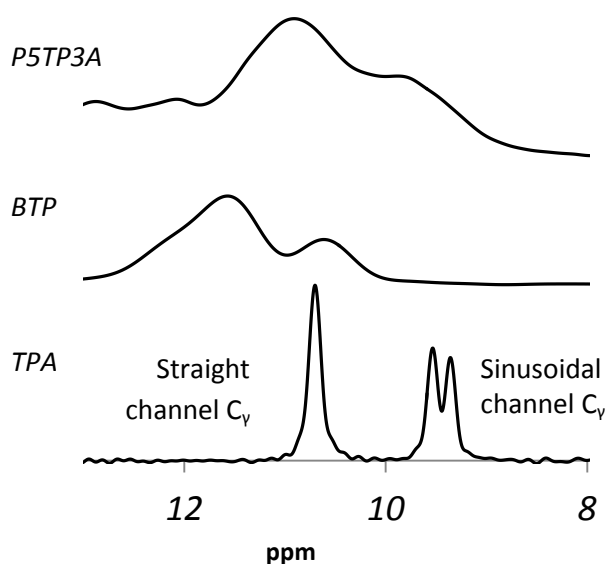


Figure 4.16 - $^{13}\text{C} \{^1\text{H}\}$ CP MAS NMR of propyl to pentyl n-alkyltripropylammonium silicalite-1 (intensity not to scale)

4.1.2.4. P5TP3A Silicalite-1

Upon increasing the alkyl chain length in the n-alkyltripropylammonium silicalite-1 series, the trend of reduced propyl C_γ peak area in the sinusoidal channel continues. A preference for the n-pentyltripropylammonium cation (Figure 4.17) to sit in the silicalite-1 pore with the pentyl chain directing into the sinusoidal channel is observed.

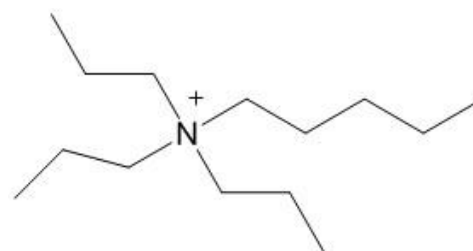


Figure 4.17 - Structure of P5TP3A (pentyltripropylammonium) cation SDA

The full spectrum (Figure 4.18) and assignment (Table 4.5) are shown below and depict many peaks starting to show signs of splitting. Despite this peak splitting observed, a reduction in resolution is observed in silicalite-1 synthesised using larger structure directing agents.

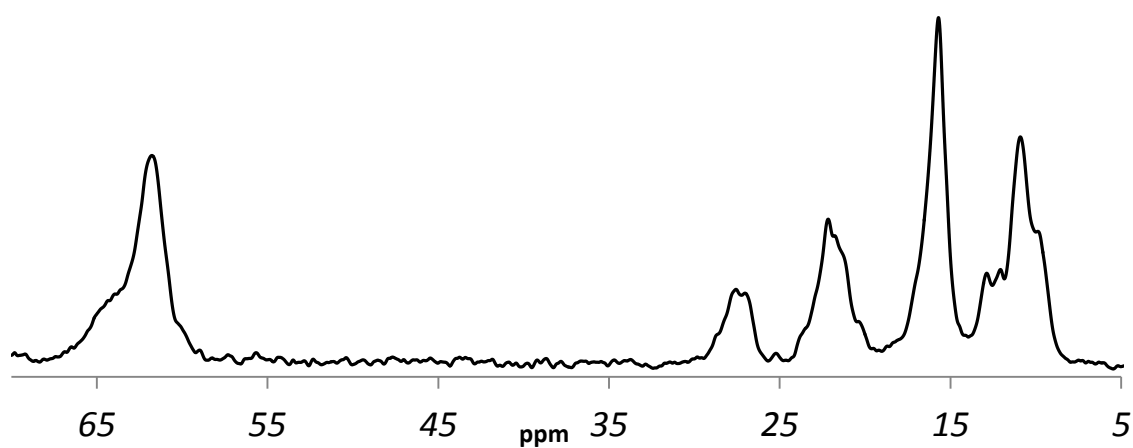


Figure 4.18 - $^{13}\text{C} \{^1\text{H}\}$ CP MAS NMR of silicalite-1 synthesised with n-pentyltripropylammonium using the fluoride route synthesis

Table 4.5 - Table of chemical shift values for fluoride route P5TP3A silicalite-1 sample using solid state NMR

P5TP3A Assignment (δ)	N-pentyl / ppm					Tripropyl / ppm		
	C4 (α)	C5 (β)	C6 (γ)	C7 (δ)	C8 (ϵ)	C1 (α)	C2 (β)	C (γ)
$^1\text{H} \{^{13}\text{C}\}$ CP	63.98	27.56	22.17	16.78	12.90	61.78	15.27	10.92
MAS SS NMR		26.99	21.73		12.09			9.85

It is interesting to note that when using the hydroxide route synthesis, the increase of methyl to pentyl in the n-alkyltripropylammonium silicalite-1 series has no effect on the crystal shapes observed but leads to a progressive increase in crystal size from 5 μm using MTPA up to 10 μm using P5TP3A silicalite-1 (Figure 4.19).

The fluoride route synthesis however, slowly morphs in crystal shape during the increase from methyl to pentyl in n-alkyltripropylammonium silicalite-1. The observed change morphs from $\sim 25 \times 80 \mu\text{m}$ flat-faced rectangular crystals to smaller (up to 10 μm) tabular twinned crystal shapes.

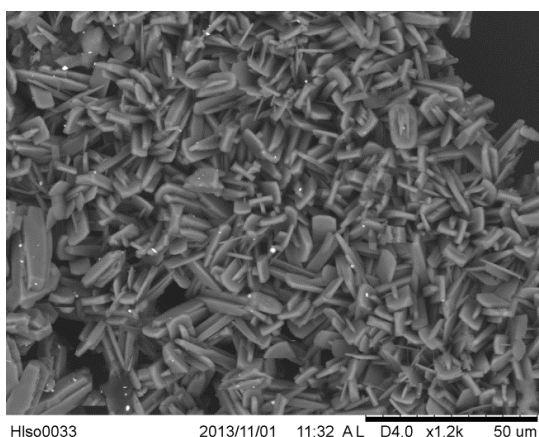


Figure 4.20 - SEM Image of P5TP3A silicalite-1 synthesised via the fluoride route. Twinned tabular crystals

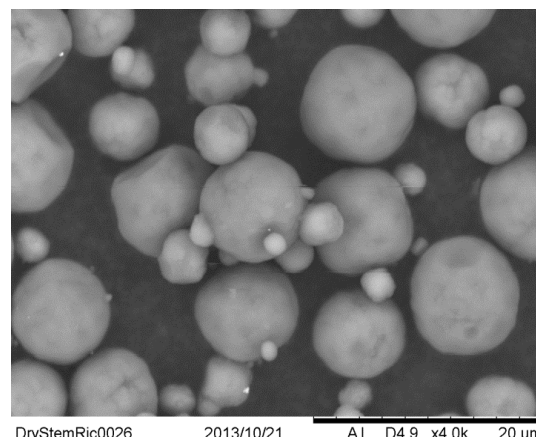


Figure 4.19 - SEM Image of P5TP3A silicalite-1 synthesised via the hydroxide route. Spherical crystals of dimensions up to 10 µm

4.1.3. N-alkyltripropylammonium Silicalite-1 Summary

Increasing the length of the alkyl chain in n-alkyltripropylammonium silicalite-1 has the effect of changing channel preference of the n-alkyl substituent from the straight to sinusoidal channel at propyl (Table 4.6):

Table 4.6 – Table showing progressive channel preference change upon ascending the n-alkyltripropylammonium silicalite-1 series

Silicalite-1 SDA	N-alkyl channel preference
MTPA	Straight channel
ETPA	Straight channel
TPA	50:50
BTP	Sinusoidal channel
P5TP3	Sinusoidal channel

This channel preference can be explained by the size of the channel pore openings. Replacement of the SDA from TPA to a smaller alkyl chain leads to a preference of the alkyl pointing towards the straight channel. This has a smaller pore opening allowing two of the larger propyl chains to point towards the larger sinusoidal channel. This is reversed by the replacement of the SDA with a larger alkyl substituent and therefore a preference of pointing towards the larger sinusoidal channel, indicating the ability of the SDA to orientate to steric preference.

A change in the effect of the size of the structure directing agent on crystal size has been observed using the hydroxide route whereas a change in crystal size and shape has been observed

for the fluoride route synthesis using the n-alkyltributylammonium silicalite-1 series. Upon increasing structure directing agent size, the crystal size interestingly increases using the hydroxide route and decreases using the fluoride route, which will both affect the zeolite surface area and catalytic properties of the aluminosilicate form.

4.1.4. N-alkyltributylammonium Silicalite-1 Series

In order to determine if the previous silicalite-1 trends could be replicated for another series, or if the size of the SDA affects the zeolite channel preference, silicalite-1 was studied using increasing n-alkyltributylammonium silicalite-1 from methyl to pentyl. Despite excessive synthetic attempts, it was not possible to successfully synthesise P3TPA (n-propyltributylammonium) silicalite-1. Additionally, TBA (tetrabutylammonium) was not used to attempt to synthesise silicalite-1 due to it being well known for synthesising another zeolite silicalite-2 with MEL framework.^{29,30}

4.1.4.1. MTBA Silicalite-1

Silicalite-1 was successfully synthesised using n-methyltributylammonium (Figure 4.21). The ^{13}C $\{^1\text{H}\}$ spectrum obtained of silicalite-1 synthesised yielded 13 chemical resonances from phenomenal spectral resolution. This is demonstrated by the splitting of peaks around 58 - 67 ppm (butyl C_α) appearing as three peaks separated by 657 Hz (Figure 4.22).

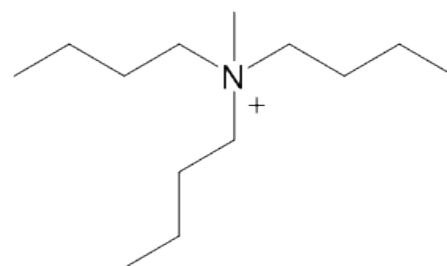


Figure 4.21 – Structure of MTBA (n-methyltributylammonium cations) SDA

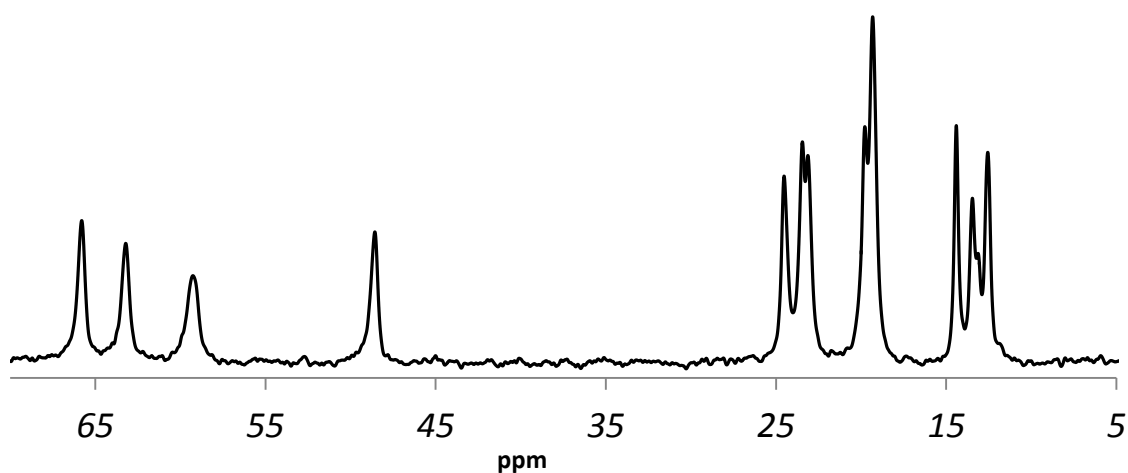


Figure 4.22 - $^{13}\text{C} \{^1\text{H}\}$ CP MAS NMR of silicalite-1 synthesised with n-methyltributylammonium using the fluoride route synthesis

The exceptional spectral resolution displayed by MTBA silicalite-1 allowed for the assignment of these peaks in the straight and sinusoidal channels whereby downfield chemical shift peaks represent alkyl chains in the smaller straight channels and upfield peaks represent alkyl chains in the larger sinusoidal channel. This assignment confirms an orientation whereby the methyl chain and one butyl chain preferentially sit directed towards the smaller straight channel and two butyl substituent's sit directed towards and extended into the sinusoidal channels.

This represents the first occurrence of identifying channel assignments in silicalite-1 sample outside the n-alkyltripropylammonium series.

Table 4.7 - Table of chemical shift values for fluoride route MTB silicalite-1 sample using solid state NMR

MTBA Assignment (δ)	N-methyl ppm	Tributyl / ppm			
		C2 (α)	C3 (γ)	C4 (δ)	C5 (ϵ)
$^1\text{H} \{^{13}\text{C}\}$ CP MAS SS NMR	Straight - 48.65	Straight-	Straight-	Straight -	Straight -
		65.85	24.54	19.83	14.45
		Sinusoidal -	Sinusoidal -	Sinusoidal	Sinusoidal -
		63.26/ 59.25	23.52 / 23.13	-19.36	13.47/ 12.60

Each of the butyl chain straight and sinusoidal assignments represents a 1:2 peak area ratio, indicating preference of the methyl facing the straight chain, as demonstrated in Figure 4.23:

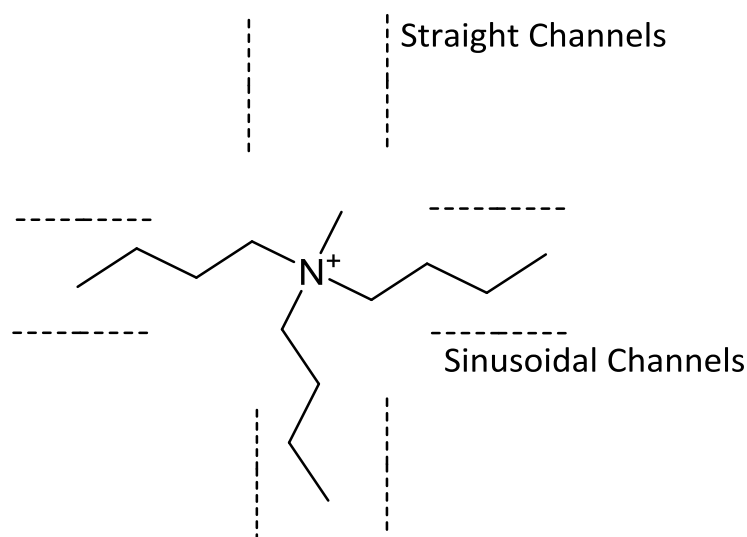


Figure 4.23 - Schematic representation of MTBA silicalite-1 within the zeolite framework and the orientation of MTBA within straight and sinusoidal channels (not to scale)

4.1.4.2. ETB Silicalite-1

Upon increasing the alkyl chain to n-ethyltributylammonium (Figure 4.24) silicalite-1, a spectrum with good spectral resolution is also obtained, successfully yielding 11 carbon resonances shown (Figure 4.25) and characterised (Table 4.8).

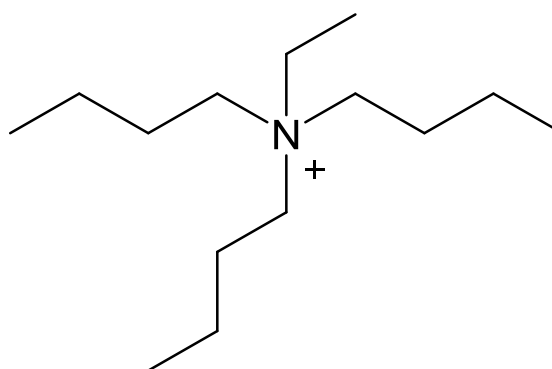


Figure 4.24 - Structure of ETB (n-ethyl-triisopropylammonium) cation SDA

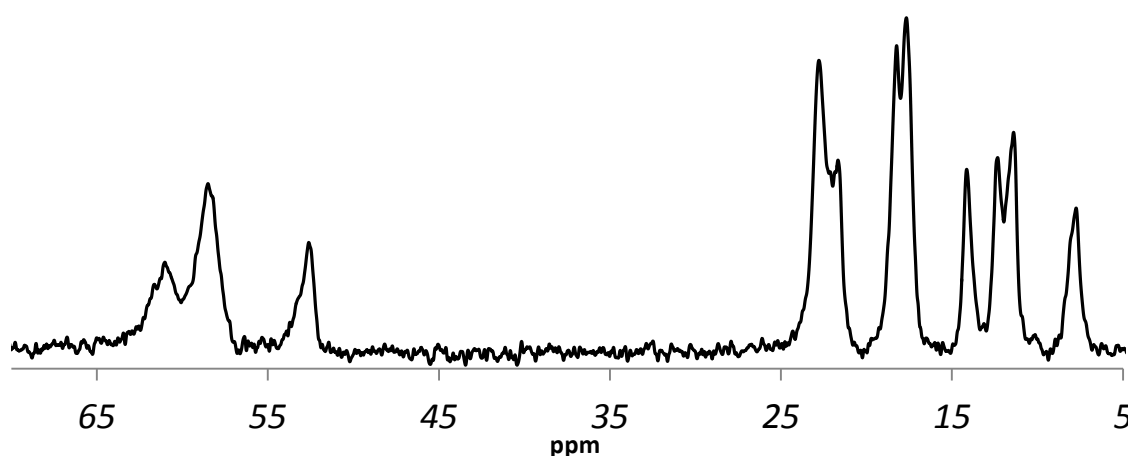


Figure 4.25 - $^{13}\text{C} \{^1\text{H}\}$ CP MAS NMR of silicalite-1 synthesised with n-ethyltributylammonium using the fluoride route synthesis

Table 4.8 - Table of chemical shift values for fluoride route ETB silicalite-1 sample using solid state NMR

ETBA Assignment (δ)	N-ethyl / ppm		Tributyl / ppm			
	C1 (α)	C2 (β)	C3 (α)	C4 (β)	C5 (γ)	C6 (β)
$^1\text{H}\{^{13}\text{C}\}$ CP MAS SS NMR	52.63	7.73	Straight - 62.06 Sinusoidal - 59.59	Straight - 22.78 Sinusoidal - 21.67	Straight - 18.24 Sinusoidal - 17.66	Straight - 14.14 Sinusoidal - 12.33 / 11.40

The 2:1 peak area ratio of the butyl substituent's sitting in the sinusoidal and straight channels respectively is retained upon increasing the alkyl chain to ethyl. Again this represents the SDA preference of sitting within the zeolite pore with the ethyl chain pointing towards the smaller straight channel.

4.4.4.3. P5TBA Silicalite-1

Upon increasing the alkyl chain to pentyl in the n-alkyltributylammonium silicalite-1 series, a decrease in chemical resolution is observed. The $^{13}\text{C}\{^1\text{H}\}$ CP MAS NMR spectrum obtained is shown below (Figure 4.27), and characterised as follows (Table 4.9).

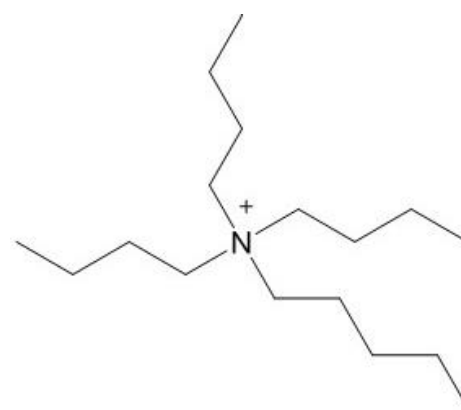


Figure 4.26 - Structure of P5TBA (pentyltributylammonium) cation SDA

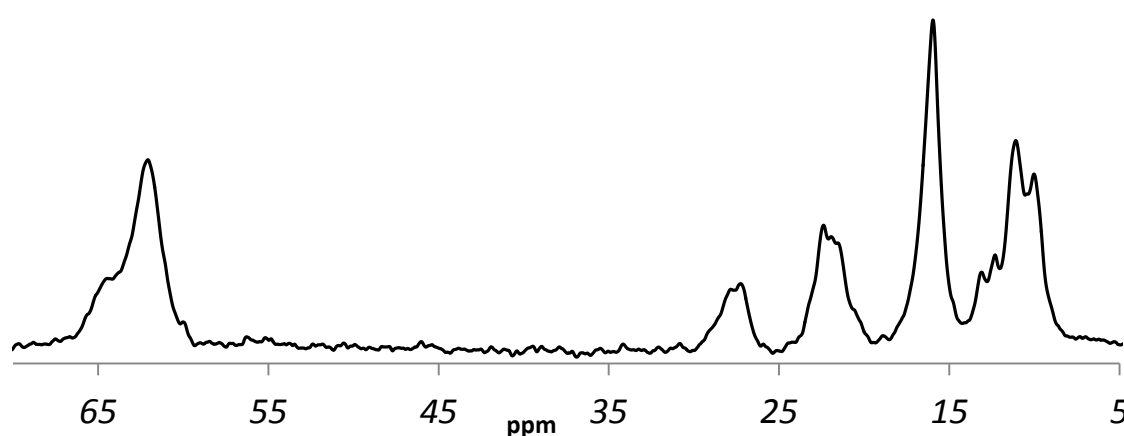


Figure 4.27 - $^{13}\text{C}\{^1\text{H}\}$ CP MAS NMR of silicalite-1 synthesised with n-pentyltributylammonium using the fluoride route synthesis

Table 4.9 - Table of chemical shift values for fluoride route P5TBA silicalite-1 sample using solid state NMR

P5TBA Assignment (δ)	N-pentyl / ppm					Tributyl / ppm			
	C1 (α)	C2 (β)	C3 (γ)	C4 (δ)	C5 (ϵ)	C3 (α)	C4 (β)	C5 (γ)	C6 (δ)
$^1H \{^{13}C\}$ CP MAS SS NMR	64.52	27.57	21.54	16.72	13.14 12.30	62.10	22.38	16.0	11.71 10.05

Due to the significant number of resonances and decreased resolution observed, the only peak splitting observed are the butyl and pentyl terminal carbons. The peak splitting observed for the butyl substituent's exhibit a reduced peak area in the sinusoidal channel indicating the pentyl preference in the sinusoidal channel. The pentyl peak also exhibits a 1:1 peak splitting which is attributed to effects either from angular distortion of the butyl locations in the straight and sinusoidal channels or due to the fluoride motion observed in P5TBA (discussed in chapter 5).

The reduced chemical resolution observed in silicalite-1 when using n-pentyltributylammonium as an SDA is thought to be due to crystallisation of the material suffering as a consequence of the size and high C:N ratio of the SDA. This increased C:N consequently increases the hydrophobicity of the SDA and reduces the attractive forces to Si-O⁻ species during synthesis. For these reasons larger SDA zeolites have been known to require a longer time to synthesise or require a higher heat to crystallise.

4.1.5. N-alkyltributylammonium Silicalite-1 Summary

In the n-alkyltributylammonium silicalite-1 series, increasing the alkyl chain length impacts the location of the varied alkyl chain from the straight channel to sinusoidal channel in the same trend that was observed for the n-alkyltriethylammonium silicalite-1 series (Table 4.10):

Table 4.10 - Table showing change in channel preference upon ascending the n-alkyltributylammonium silicalite-1 series

Silicalite-1 SDA	N-alkyl channel preference
MTBA	Straight
ETBA	Straight
P3TBA	-
TBA	-
P5TBA	Sinusoidal

Despite the lack of ^{13}C spectra for P3TBA and TBA silicalite-1, it is possible to theorize exactly where the change in channel preference should be observed. In theory, increasing the alkyl chain length within the n-alkyltributylammonium silicalite-1 series to propyl, would orientate the SDA with the n-alkyl chain in the smaller straight channel. A butyl alkyl chain would orientate with alkyl chains in a 50:50 mixture of straight and sinusoidal channels, and replacing the alkyl chain with a larger one would lead to the a location in the sinusoidal channel, if this series follows steric preference like the n-alkyltripropylammonium series.

4.1.6. N-alkyltriethylammonium Silicalite-1 Series

The n-alkyltriethylammonium silicalite-1 series was also studied by ^{13}C solid state NMR, ranging from propyl to hexyl (Figure 4.28);

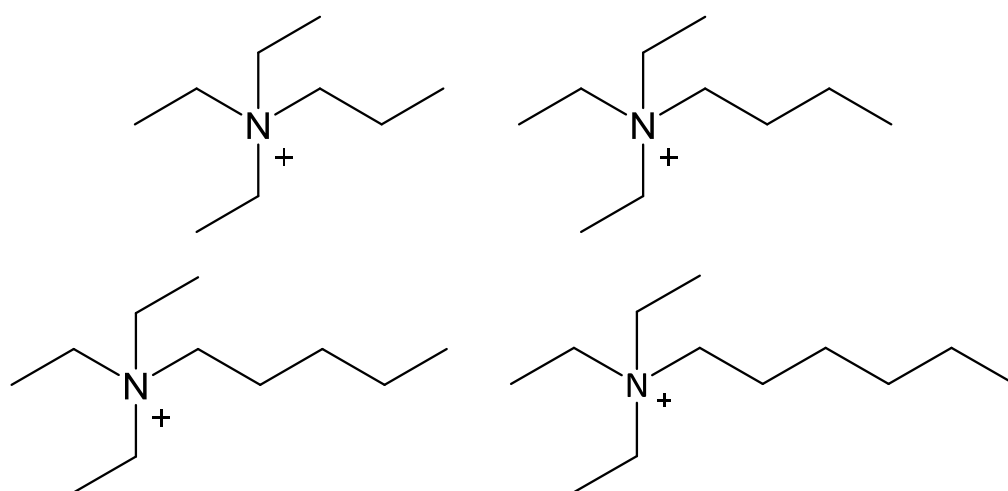


Figure 4.28 – Schematic Diagram of n-alkyltriethylammonium cation series where the alkyl chain ranges from propyl to hexyl

The range of solid state NMR results for the n-alkyltriethylammonium series are shown below (Figure 4.29) and characterised (Table 4.11) as follows:

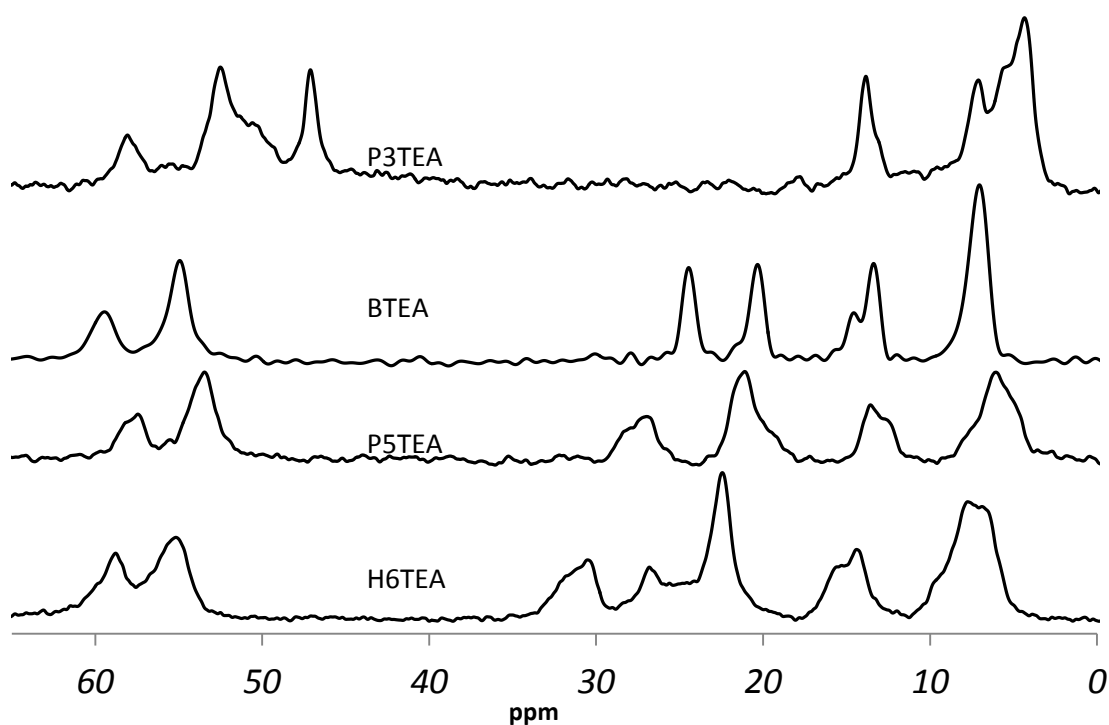


Figure 4.29 - $^{13}\text{C} \{^1\text{H}\}$ CP MAS NMR of silicalite-1 synthesised with n-alkyltriethylammonium silicalite-1 series

Table 4.11 – Table of ^{13}C chemical shift assignments for the n-alkyltriethylammonium silicalite-1 series studied

SDA Silicalite-1	Triethyl / ppm		N-alkyl / ppm				
	C1 (α)	C2 (β)	C3 (α)	C4 (β)	C5 (γ)		
<i>P3TEA</i>	Straight - 54.35 Sinusoidal - 48.90	Straight - 8.69 Sinusoidal - 7.55	59.87	17.02	10.36		
<i>BTEA</i>	C1 (α)	C2 (β)	C3 (α)	C4 (β)	C5 (γ)	C6 (δ)	
	54.94	7.47	59.45	24.46	20.34	Straight - 14.57 Sinusoidal - 13.39	
<i>P5TEA</i>	C1 (α)	C2 (β)	C3 (α)	C4 (β)	C5 (γ)	C6 (δ)	C7 (ϵ)
	54.76	22.57	59.54 58.91	29.56 28.42	21.43	14.94 13.96	8.56 7.37 6.34
<i>H6TEA</i>	C1 (α)	C2 (β)	C3 (α)	C4 (β)	C5 (γ)		
	55.82 55.03	21.42	58.71	32.16 30.44	26.85		
			C6 (δ)	C7 (ϵ)	C8 (ζ)		
			15.50 14.33	9.46 7.74	6.61 5.87		

Throughout the n-alkyltriethylammonium silicalite-1 series, the combination of reduced spectral resolution and growing number of overlapping peaks made distinguishing the orientation very difficult. There was not sufficient peak splitting observed in the ethyl peaks in order to determine the alkyl substituent orientations. It is possible this is the case for the whole n-alkyltriethylammonium silicalite-1 series because the ends of the ethyl chains do not reach the openings of the pores.

Within the n-alkyltriethylammonium silicalite-1 series, it is possible to consider another comparative method whereby the alkyl chain could yield orientation information. This series of SDA silicalite-1 species all possess a peak that does not suffer from peak overlapping, and has sufficient chemical resolution to observe splitting patterns (Figure 4.30).

These peaks all represent an n-alkyl peak but indicate some form of splitting. This splitting could be due to a number of features. It could arise from the existence of this alkyl chain in both channels as we have previously observed. For example, the BTEA splitting occurs in a peak area ratio of 1:2 indicating the butyl could exist in the straight channel in 1/3rd of pores and the sinusoidal in 2/3rd of pores.

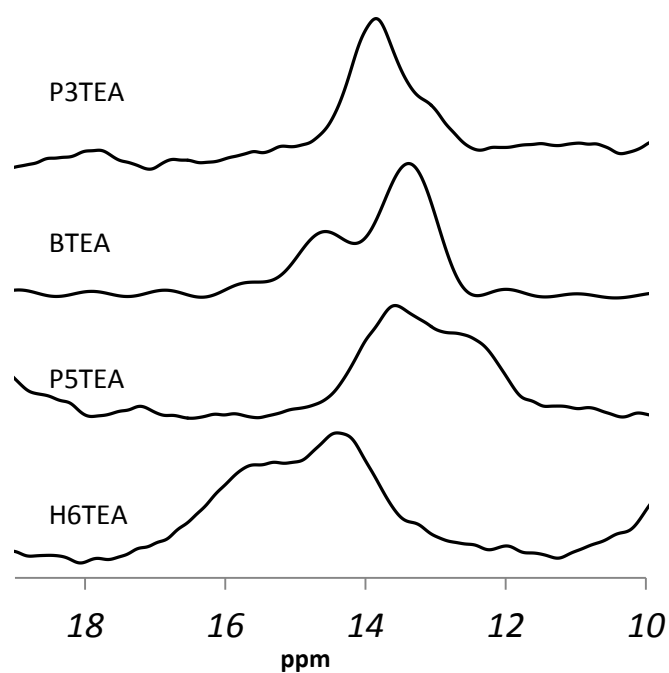


Figure 4.30 - Comparison of $^{13}\text{C} \{^1\text{H}\}$ NMR spectra for propyl to hexyl n-alkyltriethylammonium silicalite-1 from 11-18 ppm

However this peak area ratio seems to change throughout the series with no obvious trend. The fact that the triethyl substituent is so small and does not reach into the pores may mean that within this series other effects are enhanced, such as fluoride motion (discussed in chapter 5) or SDA motion for the particular sample leaving this series open for further investigation.

4.2. ^{14}N Solid State NMR

Nitrogen solid state NMR can be used to study zeolite materials as a sensitive probe into the occluded structure directing agent within zeolite pores.³¹ There are two NMR active isotopes of nitrogen, ^{14}N and ^{15}N which both present unfavourable qualities as well as possible assets.³² For the simpler study of chemical shift resonances, ^{15}N would be considered the best choice. Despite low sensitivity from a low natural abundance (0.37 %), ^{15}N possesses a spin $\frac{1}{2}$ nuclei and isotopic labelling is possible, though expensive. ^{14}N on the other hand, has an exceptionally high natural abundance of 99.6 % but suffers from low sensitivity due to a lower gyromagnetic ratio than ^{15}N .³³ The crucial difference between these isotopes is the spin difference, whereby ^{14}N has a spin 1 nucleus, inferring it has a quadrupolar moment.

A quadrupolar moment (eQ) is characteristic for each individual nucleus in the periodic table and can be positive or negative. It couples with the electric field gradient (EFG) via an electric interaction called quadrupolar coupling,³⁴ discussed in Chapter 2. The EFG originates from surrounding electrons and is affected by two properties of the nucleus; anisotropy (C_Q) and asymmetry (η_Q). This means that the observation of a nucleus with cubic or almost cubic electron symmetry will reduce the EFG to zero, having no effects on the Zeeman Interaction. The non-spherical asymmetry and large quadrupolar coupling constant observed for ^{14}N means that the EFG tensor and therefore quadrupolar coupling tensor will perturb the energy of the Zeeman Interactions by observation of second order effects³⁴ (Figure 4.31):

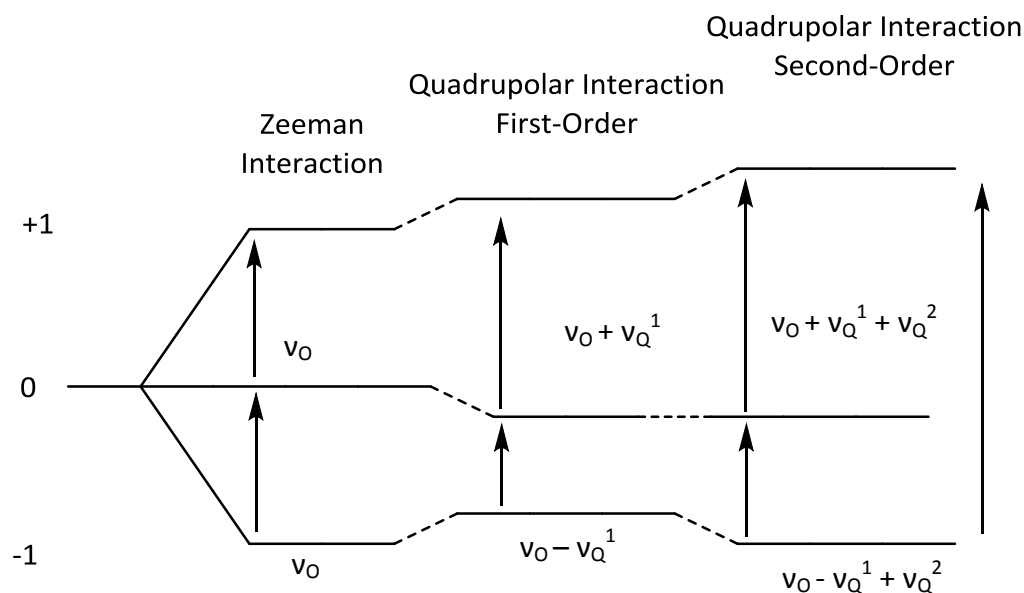


Figure 4.31 – Schematic diagram of the first and second order quadrupolar effects on the Zeeman interaction of a spin= 1 nuclei³⁵

The spin = 1 nucleus splits into three energy levels using the $2n+1$ rule, whereby the two single transitions are possible. These transition separations can be described by Equation 4.1;

$$\omega_0 = \frac{\gamma_N B_0}{2\pi} \quad \text{Equation 4.1.}$$

Where, ω_0 = NMR frequency, γ_N = gyromagnetic ratio of nucleus, B_0 = applied magnetic field

These single transitions are easy to detect however they are affected by the quadrupolar interaction in the first order.³⁵ The use of magic angle spinning (MAS) effectively reduces θ , and therefore the orientation dependence $(3 \cos^2\theta - 1)$ to zero. The second order effects however, brought about by ^{14}N 's large quadrupolar coupling constant cannot be entirely removed by MAS.³⁶ These quadrupolar coupling parameters can therefore be studied and extracted to identify differences in the local environment, which is the reason for the use of ^{14}N experiments within this work.

^{14}N solid state NMR experiments display a central transition peak, and if spun sufficiently slowly ($\sim 2\text{-}5$ kHz for these materials) also display spinning sidebands separated by the spinning rate. The spinning sideband (SSB) pattern displays numerous equidistant peaks upfield and downfield of the

central transition and are called satellite transitions. Analysis of these peaks allows us to identify information about the local environment of the ^{14}N nucleus providing a platform which allows the simple comparison of similar and dissimilar samples.

This work aims to study the local environment of silicalite-1 using a variety of different shape and size structure directing agents to identify the effect on the local order of the ^{14}N .

4.2.1. ^{14}N MAS NMR Results

Since the early 1990's, ^{14}N studies have slowly developed in the literature for zeolites, ZSM-5 materials, silicalite-1³⁷ and precursors. The majority of early studies identified ^{14}N experimental results for quaternary ammonium cations.^{31,33,38} These samples studied have successfully identified the ^{14}N quadrupolar interactions under MAS³⁸ and static conditions^{39,40} however they do not represent the structure of the organics within the zeolite framework. As such, the relationship between the structure directing agents, lattice symmetries and ^{14}N quadrupolar coupling parameters have not been fully deduced.

Despite prior use of ^{14}N to study the silicalite-1 structure,⁴¹ only recently have these experiments been used to extract quadrupolar coupling parameters for TPA silicalite-1 using both hydroxide and fluoride route syntheses.^{22,42} ^{14}N has been used in a recent study of fluoride route silicalite-1 samples synthesised using a short range of n-alkyltripropylammonium silicalite-1 samples whereby the quadrupolar coupling parameters were also determined.²⁵ The extraction of quadrupolar coupling parameters can provide very useful information due to the high sensitivity of ^{14}N to the geometries of structure directing agents.^{31,40}

Initial attempts of this work to study ^{14}N solid state NMR were conducted at University of St Andrews and Keele University. Many difficulties were incurred whereby low signal:noise and rolling baselines made the correct fitting of chemical shift anisotropy (CSA) parameters unobtainable, even after phasing and baseline correction. A grant was then obtained to run the samples on the 850 MHz spectrometer at Warwick University.

The following results investigate the effects of altering alkyl chain lengths on the n-alkyltripropylammonium and n-alkyltributylammonium silicalite-1 series, in order to elucidate local effects and to contribute to the developing literature on these zeolite materials.

4.2.1.1. TPA Silicalite-1

The ^{14}N spectrum obtained of TPA silicalite-1 (Figure 4.32) displays a phased and baseline spinal corrected spectrum overlaid with fitting spectrum Bruker Topspin 3.2 SOLA⁴³ (Solids Lineshape Analysis), as shown;

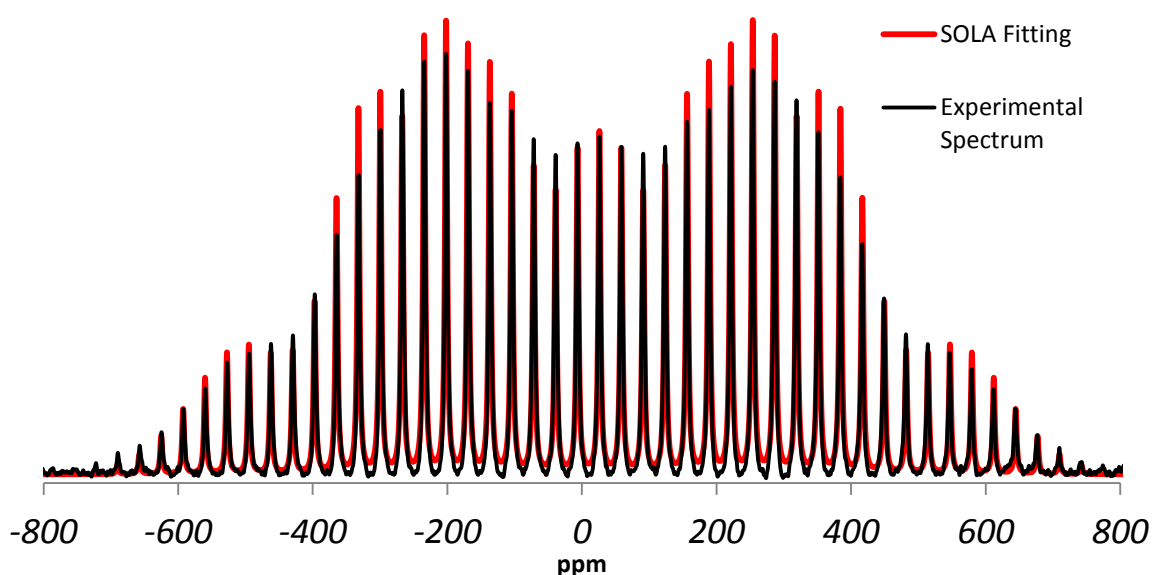


Figure 4.32 - ^{14}N MAS NMR spectrum of TPA silicalite-1 and SOLA fitting profile ($\nu\text{MAS} = 2 \text{ kHz}$)

Unlike satellite transitions, the central transition (δ_{ISO}) remains unaffected by changing the strength of the external magnetic field. The isotropic peak at 26.48 ppm was therefore easily obtained by comparison to previous ^{14}N spectra. These isotropic chemical shifts are also in accordance with previously observed ^{14}N of $\delta_{\text{ISO}} 25.5 \text{ ppm}$.²²

The spectrum obtained presents a SBB pattern full of discontinuities, with clearly distinguished ‘horns’ and ‘wings’. Extraction of the quadrupolar coupling parameters from the fitted spectrum using SOLA determined the following quadrupolar coupling parameters:

$$\delta_{\text{ISO}} 26.48 \text{ ppm } (C_Q = 54 \text{ kHz}, \eta_Q = 0.315)$$

These results are in very good agreement with previously observed parameters ($C_Q=53$ kHz and $\eta_Q = 0.3^{25}$) for TPA silicalite-1. Notably the ^{14}N quadrupolar coupling parameters are very different from parameters obtained for TPAI ($C_Q = 31.7$ kHz, $\eta_Q = 0.00$),⁴⁴ TPACl ($C_Q = 17$ kHz, $\eta_Q = 0.0$)⁴⁰ and TPABr ($C_Q = 47.78$ kHz, $\eta_Q = 0.0$)³⁹ molecules that are not incorporated into the zeolite structure. This observation confirms the impact of the zeolite framework structure on the local environment of the structure directing agent, and more specifically the effect the framework structure has on SDA bond angles and ^{14}N charge distributions, previously observed by Alonso and co-workers.³¹ The remainder of the n-alkyltripropylammonium silicalite-1 series was investigated to observe the effects the ^{14}N environment from altering the alkyl chain from methyl to pentyl.

4.2.1.2. MTPA Silicalite-1

The ^{14}N spectrum obtained for MTPA silicalite-1 is baseline spinal corrected and overlaid with a SOLA fitted spectrum.

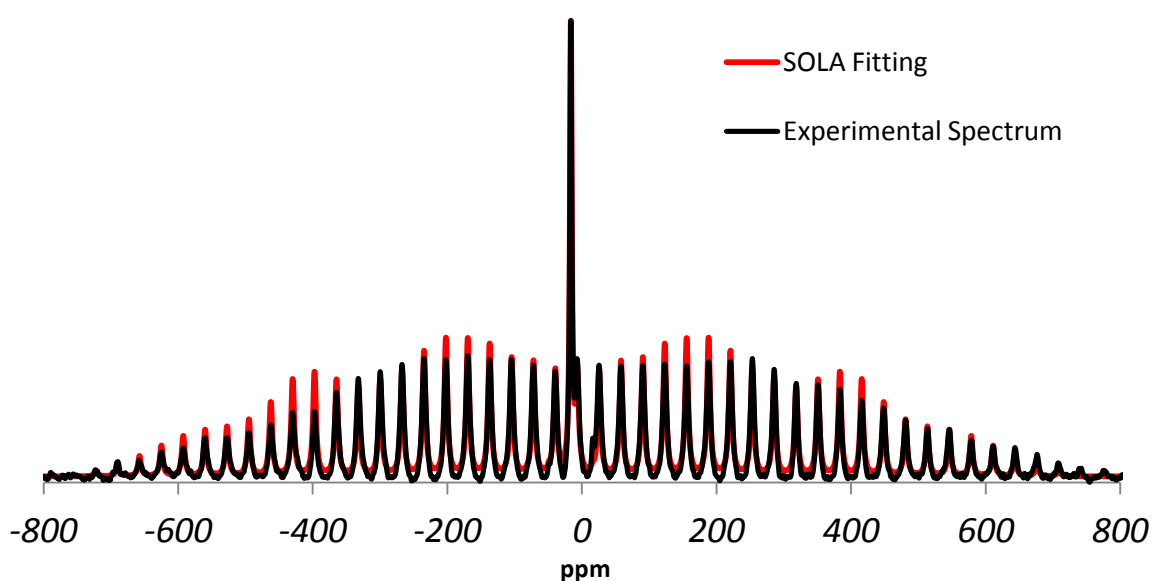


Figure 4.33 - ^{14}N MAS NMR spectrum of MTPA silicalite-1 and SOLA fitting profile ($\nu\text{MAS} = 2$ kHz)

The spectrum obtained was fitted and characterised as follows:

$$\delta_{\text{ISO}} 27.6 \text{ ppm } (C_Q = 57 \text{ kHz}, \eta_Q = 0.469)$$

An additional peak occurs at $\delta_{\text{ISO}} -16.71$ ppm ($C_Q = 1$ kHz, $\eta_Q = 0.2$) which does not occur for TPA silicalite-1 but does occur in varying intensity throughout some of the remainder of the NMR samples studied. Due to the high symmetry value, similarity in chemical shift for all additional peaks observed and the proximity of the peak to NH_4Cl .³¹ This additional peak is assigned to residual ammonium cations in the sample.

4.2.1.3. ETPA Silicalite-1

Upon increasing the alkyl chain length to n-ethyltripropylammonium in silicalite-1, a ^{14}N spectrum is obtained which displays good agreement to the SOLA fitted pattern as well as an additional ammonium peak (Figure 4.34);

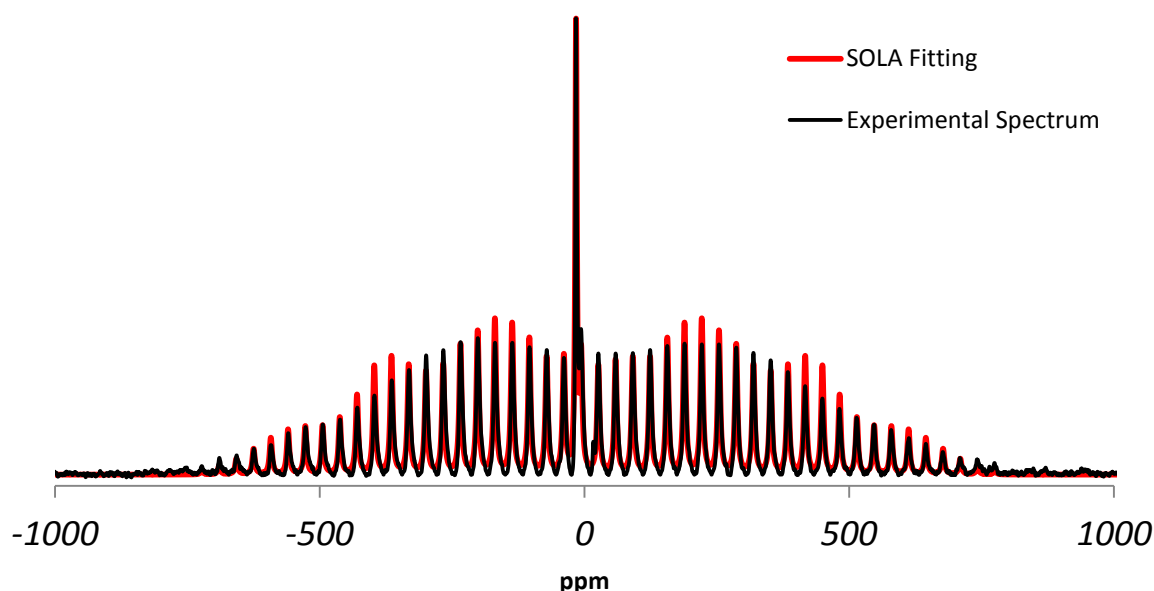


Figure 4.34 - ^{14}N MAS NMR spectrum of ETPA silicalite-1 and SOLA fitting profile ($\nu\text{MAS} = 2$ kHz)

The spectrum contains slightly less discontinuities than observed in TPA silicalite-1 however was characterised as follows;

$$\delta_{\text{ISO}} 27.4 \text{ ppm } (C_Q = 57 \text{ kHz}, \eta_Q = 0.427)$$

$$\delta_{\text{ISO}} -16.77 \text{ ppm } (C_Q = 1 \text{ kHz}, \eta_Q = 0.2)$$

Increasing the alkyl chain length in the n-alkyltripropylammonium silicalite-1 series from methyl to propyl has decreased the anisotropy and the asymmetry parameters observed. This trend is not observed by Dib and co-workers²⁵ ($C_Q = 58.0$ kHz, $\eta_Q = 0.4$) for the same chemical system however it is a logical trend in light of these results on the whole.

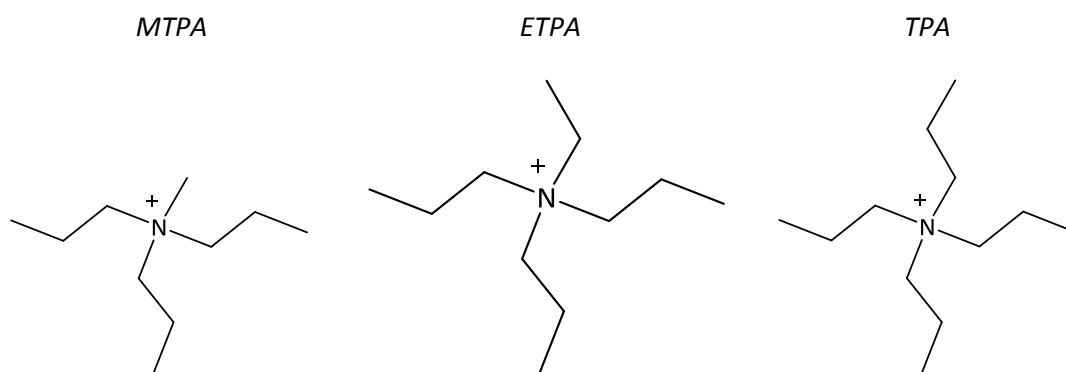


Figure 4.35 – Schematic diagram of increasing alkyl chain n-alkyltripropylammonium silicalite-1 series

The reduction in asymmetry parameter observed upon increasing the alkyl chain from methyl to propyl is a logical observation due to the symmetry of the molecular shape increasing towards the more symmetrical SDA of TPA.

4.2.1.4. BTPA Silicalite-1

The ^{14}N NMR spectrum was obtained for the further increase of the alkyl chain to BTPA silicalite-1, as shown in Figure 4.36;

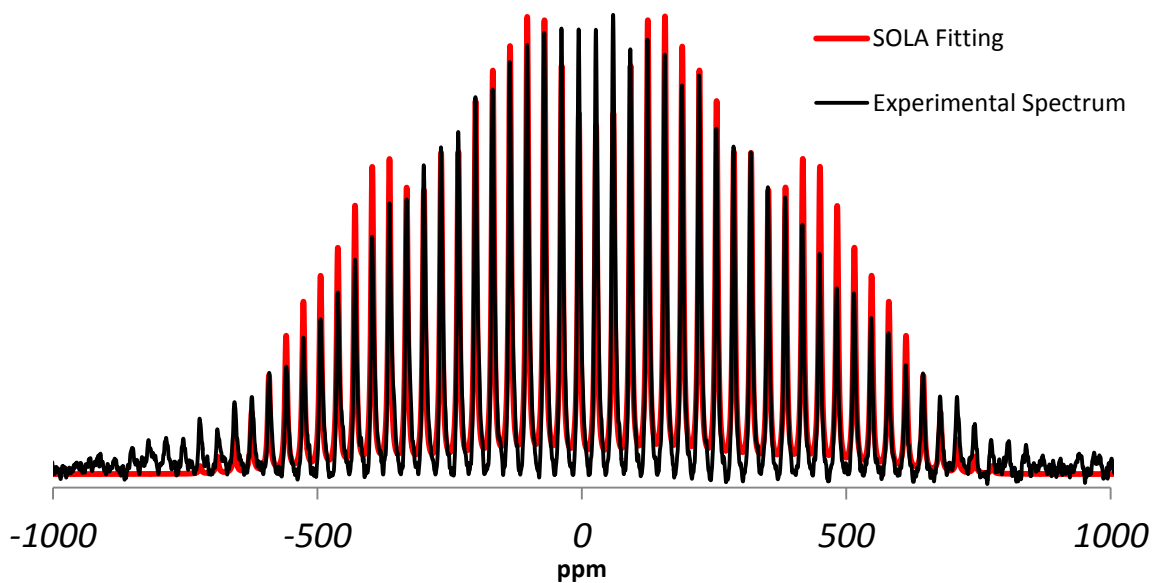


Figure 4.36 - ^{14}N MAS NMR spectrum of BTPA silicalite-1 and SOLA fitting profile ($\nu_{\text{MAS}} = 2 \text{ kHz}$)

The spectrum displays less discontinuities than have previously been observed from MTPA, ETPA and TPA and more closely resembles a TPA-OH ^{14}N NMR spectrum.²² However, this SSB shape is also observed by Dib and co-workers whose quadrupolar parameters ($C_Q = 54.0 \text{ kHz}$, $\eta_Q = 0.6$) resemble the results obtained confirming that the lack of shape is due to the function of structure directing agent;

$$\delta_{\text{iso}} 25.98 \text{ ppm } (C_Q = 56 \text{ kHz}, \eta_Q = 0.579)$$

4.2.1.5. P5TP3A Silicalite-1

The decreased SSB shape continues while ascending the n-alkyltripropylammonium series whereby a reduction in the quality of the fitted spectrum is observed;

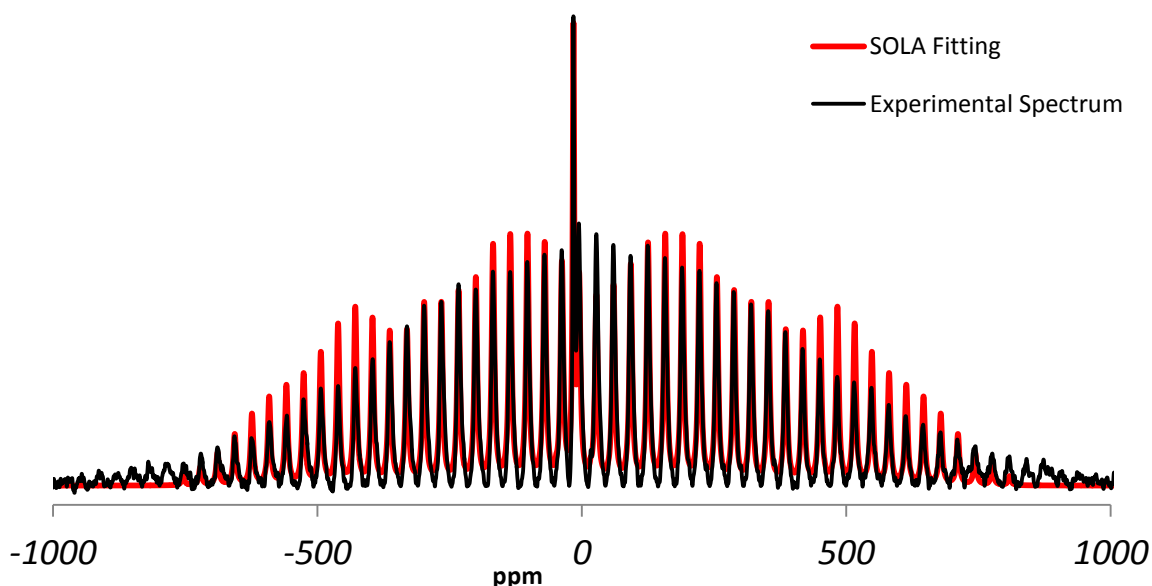


Figure 4.37 - ^{14}N MAS NMR spectrum of P5TP3A silicalite-1 and SOLA fitting profile ($\nu\text{MAS} = 2 \text{ kHz}$)

This fitted spectrum however returns quadrupolar coupling parameters of the P5TP3A silicalite-1 sample and ammonium fluoride as follows;

$$\delta_{\text{iso}} 27.0 \text{ ppm } (C_Q = 61 \text{ kHz}, \eta_Q = 0.575)$$

$$\delta_{\text{iso}} -16.3 \text{ ppm } (C_Q = 1 \text{ kHz}, \eta_Q = 0.2)$$

Increasing the alkyl chain from TPA, to BTPA and P5TPA indicates the opposite effect than was observed from the initial alkyl chain increase of MTPA, ETPA and TPA. Instead of the continued decrease of anisotropy and asymmetry parameters, the values pivot at TPA and both subsequently increase.

4.2.1.6. ^{14}N NMR n-alkyltripropylammonium Silicalite-1 Conclusion

The general trends of ^{14}N quadrupolar parameters in the n-alkyltripropylammonium silicalite-1 series are graphically demonstrated in Figure 4.38 and Figure 4.39.

As can be clearly observed from the graphs, the lowest anisotropy and asymmetry parameters in the n-alkyltripropylammonium series are for TPA silicalite-1.

This indicates that even within the structural confinements of the zeolite pore, the more symmetrical structure directing agent holds the most symmetry and anisotropy.

Anisotropy parameters have been determined to depend mostly the following components: the spatial distribution of counter-ions, the distortion required on the C-N-C angles to conform to the zeolite size³⁵ and the variations in nitrogen to anion distances.

Upon increasing the alkyl chain length in the n-alkyltripropylammonium silicalite-1 series, an increase in fluoride motion occurs (discussed in chapter 5) and a change from n-alkyl channel location from straight, to 50:50, to sinusoidal channel. These results therefore identify a simultaneous change. As the trend of decreasing quadrupolar coupling parameters also pivots at TPA, a change in n-alkyl channel preference from straight to sinusoidal channel is observed.

The n-alkyltributylammonium silicalite-1 series was also investigated to identify the effects of changing the size of the structure directing agent from methyl to pentyl. Propyl and butyl were not used in this series due to reasons previously discussed.

4.2.1.7. MTBA Silicalite-1

The smallest of the tributyl series, MTBA was studied using ¹⁴N NMR and returned a comparatively wide chemical shift range extensive spinning sidebands (Figure 4.40);

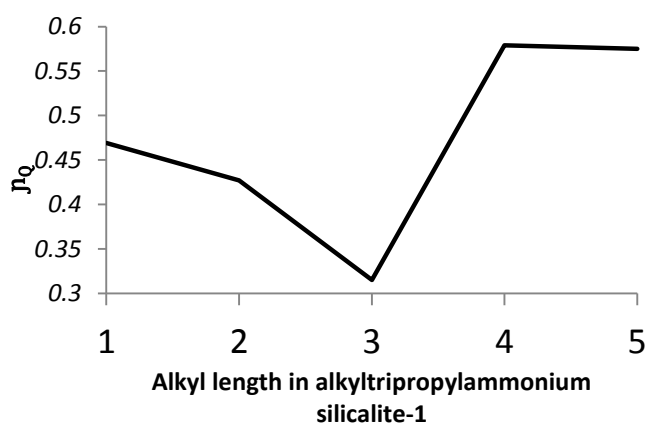


Figure 4.38 - Graph representing the asymmetry (η_Q) parameters obtained for the n-alkyltripropylammonium silicalite-1 series

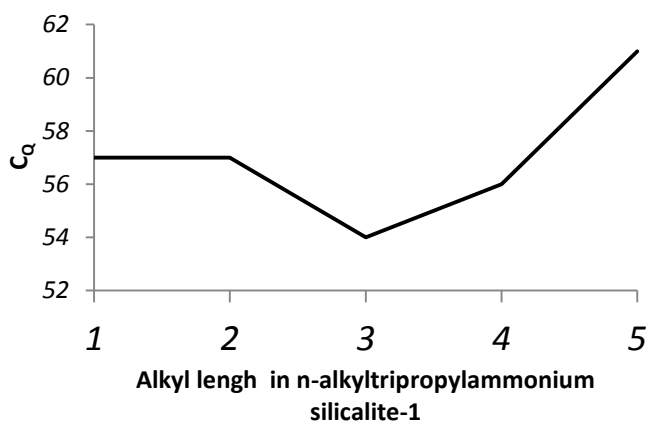


Figure 4.39 – Graph representing the anisotropy (C_Q) parameters obtained for the n-alkyltripropylammonium silicalite-1 series

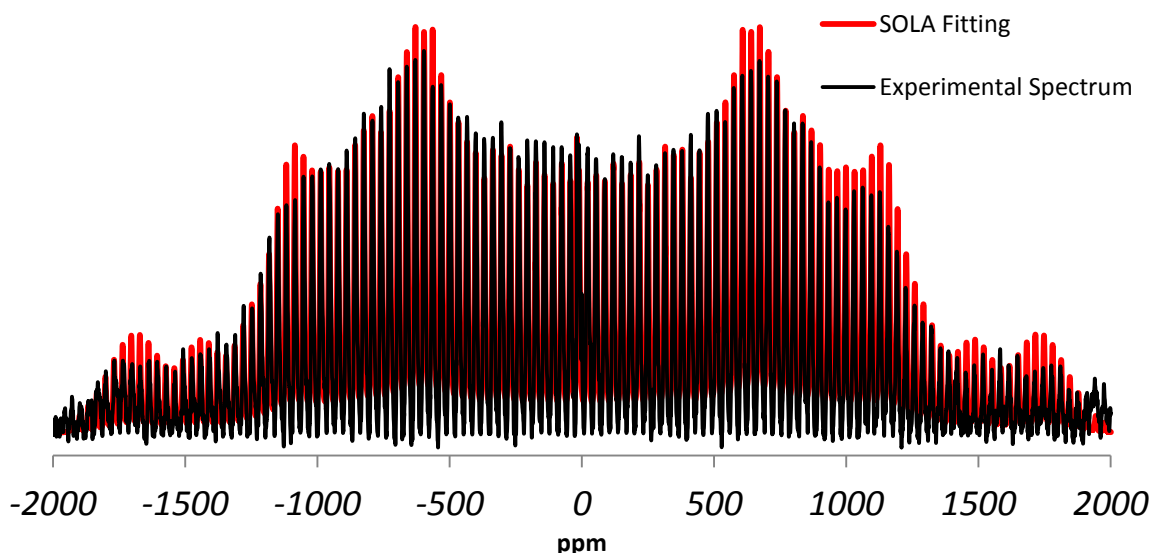


Figure 4.40 - ^{14}N MAS NMR spectrum of MTBA silicalite-1 and SOLA fitting profile ($\nu_{\text{MAS}} = 2 \text{ kHz}$)

The ^{14}N NMR spectrum obtained shows a vast amount of SBB discontinuities with defined ‘horns’ and ‘wings’ and was fitted in very good agreement using SOLA fitting software as follows;

$$\delta_{\text{ISO}} 23.3 \text{ ppm} (C_Q = 57 \text{ kHz}, \eta_Q = 0.490)$$

$$\delta_{\text{ISO}} -16.3 \text{ ppm} (C_Q = 1 \text{ kHz}, \eta_Q = 0.2)$$

This series of samples appear to have very similar quadrupolar coupling parameters, at a slightly different chemical shift and with an additional ammonium cation peak present as a very small impurity.

Comparison of the ^{14}N quadrupolar coupling parameters in silicalite-1 synthesised using MTPA and MTBA allows identification of the effects of SDA size on quadrupolar coupling parameters and shows very little difference in anisotropy or asymmetry parameters. This indicates that the exchange of tripropyl and tributylammonium cations has very little effect on the ^{14}N quadrupolar coupling constants. In each case, the methyl chain has been determined to have a straight channel preference meaning the only other difference between these SDAs is the increase in fluoride motion observed in MTPA. These results would indicate that the fluoride mobility does not have a significant effect on the ^{14}N quadrupolar parameters.

4.2.1.8. ETBA Silicalite-1

Upon increasing the alkyl chain in the n-alkyltributylammonium silicalite-1 series, the following spectrum and characterisations were obtained;

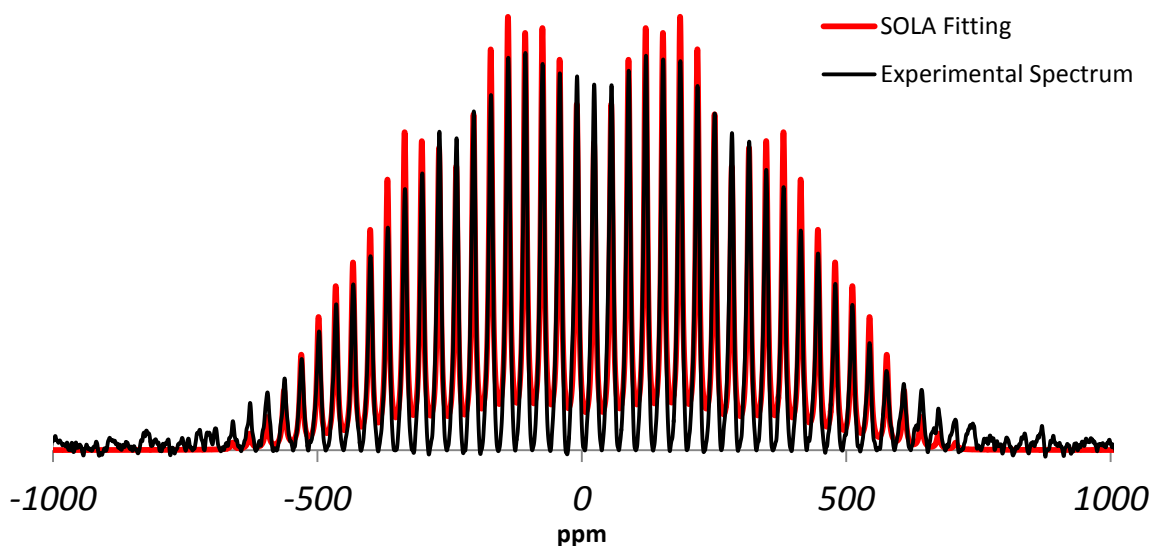


Figure 4.41 - ^{14}N MAS NMR spectrum of ETBA silicalite-1 and SOLA fitting profile ($\nu_{\text{MAS}} = 2 \text{ kHz}$)

The spectrum observed displays reduced discontinuities in a shorter range and SOLA fitting returned the following quadrupolar coupling parameters;

$$\delta_{\text{iso}} 22.87 \text{ ppm } (C_Q = 51 \text{ kHz}, \eta_Q = 0.522)$$

Comparison of silicalite-1 synthesised using ETBA and ETBA indicates a very different complex story to that observed in the MTPA/MTBA. The differences are summarised in Table 4.12.

Table 4.12- Table of ETBA and ETBA differences in parameters and determined structural qualities

SDA Silicalite-1	ETPA	ETBA
$\delta_{\text{iso}}/ \text{ppm}$	22.87	27.4
C_Q/ kHz	57	51
η_Q	0.427	0.522
Fluoride Motion	Dynamic	Static
Alkyl Channel Preference	Straight	Straight

The MTPA and MTBA observations that a change in fluoride mobility has little or no effect on quadrupolar coupling parameters indicates that within the ETPA and ETBA there is only one other difference observed that would lead to such different chemical shift and quadrupolar coupling parameters. That is the preference and location of the methyl alkyl chain in the straight channel in ETPA and the sinusoidal channel in ETBA. It would appear the combination of ETBA's ethyl in the straight channel and 2:1 butyl arms in the sinusoidal and straight channel put sufficient angular distortion on the ^{14}N in order to decrease the symmetry, reduce anisotropy parameters and increase the chemical shift of the isotropic peak.

4.2.1.9. P5TBA Silicalite-1

Overtaking the P3TBA and TBA silicalite-1 samples within the n-alkyltributylammonium silicalite-1 series allows observation of P5TBA with a large ammonium peak in the spectrum;

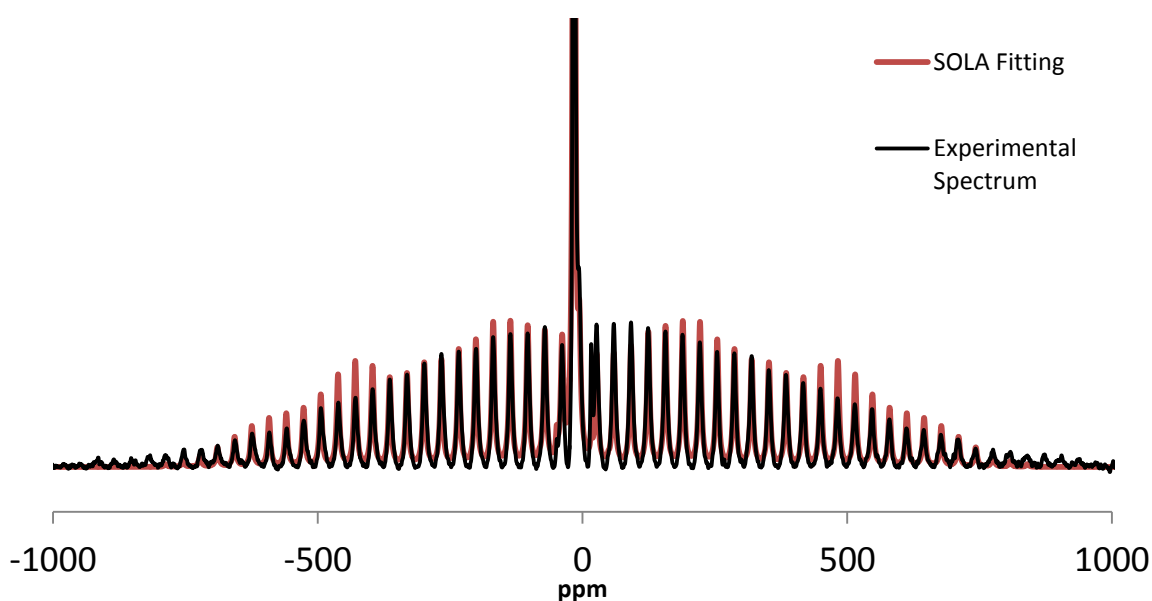


Figure 4.42 - ^{14}N MAS NMR spectrum of P5TBA silicalite-1 and SOLA fitting profile ($\nu\text{MAS} = 2 \text{ kHz}$)

The spectrum lacked discontinuities but was fitted using SOLA to obtain the following quadrupolar coupling parameters;

$$\delta_{\text{ISO}} 26.40 \text{ ppm} (C_Q = 61 \text{ kHz}, \eta_Q = 0.535)$$

$$\delta_{\text{ISO}} 16.53 \text{ ppm} (C_Q = 1 \text{ kHz}, \eta_Q = 0.2)$$

Comparison of the effects of SDA size in P5TP3A and P5TBA yields the same observation as the MTPA and MTBA comparison whereby little to no difference in anisotropy or asymmetry were obtained. It can therefore clearly be seen that increasing the size of the tributyl substituents have little to no effect on the quadrupolar coupling parameters when the fluoride motion remains unchanged and alkyl chains maintain the same channel preference.

4.2.2. ^{13}C and ^{14}N Solid State NMR Conclusions

The complementary use of ^{13}C and ^{14}N solid state NMR experiments allows the study of the effects of SDAs within a rigid zeolite framework. The results obtained using both ^{13}C and ^{14}N experiments go hand in hand in order to structurally define the orientation of structure directing agents within the zeolite pores, over a large range of quaternary ammonium structure directing agents.

^{13}C solid state NMR results demonstrate a preference throughout the varying shape and size SDA's studied of the larger alkyl chains preferentially orientating towards the larger sinusoidal channels throughout the zeolite. This leaves the remaining smaller alkyl chains to extend towards the smaller straight channels. In the event however that the majority of the SDA alkyl chains are short and sit within the zeolite pore without reaching the channels, it is found that the longer of the alkyl chains can be found in either straight or sinusoidal channels. This indicates the strong effect of the shape and size on the ordering of the SDA within zeolite frameworks which is closely linked to fluoride motion, discussed in Chapter 5.

^{14}N solid state NMR results allowed for the determination of quadrupolar coupling parameters. Prior to this work ^{14}N NMR studies have only been obtained for a small handful of silicalite-1 samples. The larger range of silicalite-1 materials studied within this work allowed determination of the chemical shift, asymmetry parameters and quadrupolar coupling constants. These values are dependent on the local order of the SDA's and as such can be used to determine the influence of the framework structure. The quadrupolar coupling parameters vary dependent on the distortion of the SDA bond angles within the zeolite pores. The results obtained indicate the most

symmetrical SDA, TPA returns the lowest asymmetry and quadrupolar coupling constant inside the silicalite-1 framework structure. Altering any alkyl chains from this TPA SDA therefore gives a method of monitoring the effects of the SDA bond distortions and therefore of the quadrupolar coupling values obtained.

4.3. References

- 1 S. A. Axon and J. Klinowski, *J. Chem. Soc., Faraday Trans.*, 1993, **89**, 4245–4248.
- 2 S. L. Burkett and M. E. Davis, *J. Phys. Chem.*, 1994, **98**, 4647–4653.
- 3 S. L. Burkett and M. E. Davis, *Chem. Mater.*, 1995, 920–928.
- 4 R. Gougeon, L. Delmotte, P. Reinheimer, B. Meurer and J. M. Che, *Magn. Reson. Chem.*, 1998, **36**, 415–421.
- 5 H. Van Koningsveld, H. Van Bekkum and J. C. Jansen, *Acta Crystallogr. Sect. B*, 1987, **43**, 127–132.
- 6 D. Olsen, G. Kokotailo, S. Lawton and W. Meier, *J. Phys. Chem.*, 1981, **85**, 2238–2243.
- 7 H. Koller, A. Wölker, L. A. Villaescusa, M. J. Díaz-Cabañas, S. Valencia and M. A. Cambor, *J. Am. Chem. Soc.*, 1999, **121**, 3368–3376.
- 8 P. Voogd, H. Van Bekkum, D. Shavit and H. W. Kouwenhoven, *J. Chem. Soc. Faraday Trans.*, 1991, **87**, 3575–3580.
- 9 E. Dib, A. Gimenez, T. Mineva and B. Alonso, *Dalt. Trans.*, 2015, **44**, 16680–16683.
- 10 C. A. Fyfe, R. J. Darton, H. Mowatt and Z. S. Lin, *Microporous Mesoporous Mater.*, 2011, **144**, 57–66.
- 11 C. A. Fyfe, D. H. Brouwer, A. R. Lewis and J. Chezeau, *J. Am. Chem. Soc.*, 2001, **123**, 6882–6891.
- 12 S. L. Brace, P. Wormald and R. J. Darton, *Phys. Chem. Chem. Phys.*, 2015, **17**, 11950–11953.
- 13 J. Patarin, M. Soulard, H. Kessler, J. L. Guth and J. Baron, *Zeolites*, 1989, **9**, 397–404.
- 14 S. A. Axon and J. Klinowski, *J. Phys. Chem.*, 1994, **98**, 1929–1932.
- 15 J. B. Nagy, Z. Gabelica and E. G. Derouane, *Zeolites*, 1983, **3**, 43–49.
- 16 M. Kovalakova, B. H. Wouters and P. J. Grobet, *Microporous Mesoporous Mater.*, 1998, **22**, 193–201.
- 17 G. Boxhoorn, R. Vansaten, W. Vanerp, G. Hays, R. Huis and D. Clague, *J. Chem. Soc. - Chem. Commun.*, 1982, 264–265.
- 18 J. Nagy, Z. Gabelica and E. Derouane, *ZEOLITES*, 1983, **3**, 43–49.
- 19 S. L. Burkett and M. E. Davis, *Chem. Mater.*, 1995, **7**, 920–928.
- 20 A. Abraham, R. Prins, J. A. van Bokhoven, E. R. H. van Eck and A. P. M. Kentgens, *Solid State Nucl. Magn. Reson.*, 2009, **35**, 61–6.
- 21 N. A. Davies, R. K. Harris and A. C. Olivieri, *Mol. Phys.*, 1996, **87**, 669–677.
- 22 E. Dib, T. Mineva, P. Gaveau and B. Alonso, *Phys. Chem. Chem. Phys.*, 2013, **15**, 18349–18352.
- 23 J. Chezeau, L. Delmotte, J. Guth and M. Soulard, *Zeolites*, 1989, **9**, 78–80.
- 24 S. M. Alipour, R. Halladj and S. Askari, *Rev. Chem. Eng.*, 2014, **30**, 289–322.

- 25 E. Dib, A. Gimenez, T. Mineva and B. Alonso, *Dalt. Trans.*, 2015, **44**, 16680–16683.
- 26 E. Flanigen and R. Patton, US Patent, 4073865, 1978.
- 27 M. A. Cambor, L. A. Villaescusa and M. J. Diaz-Cabanas, *Top. Catal.*, 1999, **9**, 59–76.
- 28 M. A. Cambor, P. A. Barrett, M. J. Diaz-Cabanas, L. A. Villaescusa, M. Puche, T. Boix, E. Perez and H. Koller, *Microporous Mesoporous Mater.*, 2001, **48**, 11–22.
- 29 E. D. Burchart, H. Van Koningsveld and B. Van de Graaf, *Microporous Mater.*, 1997, **8**, 215–222.
- 30 C. A. Fyfe, Z. S. Lin, C. Tong and R. J. Darton, *Microporous Mesoporous Mater.*, 2012, **150**, 7–13.
- 31 B. Alonso, D. Massiot, P. Florian, H. H. Paradies, P. Gaveau and T. Mineva, *J. Phys. Chem. B*, 2009, **113**, 11906–20.
- 32 L. a O'Dell, *Prog. Nucl. Magn. Reson. Spectrosc.*, 2011, **59**, 295–318.
- 33 T. Mineva, P. Gaveau, A. Galarneau, D. Massiot and B. Alonso, 2011, 19293–19302.
- 34 D. Apperley, R. Harris and P. Hodgkinson, *Solid-state NMR: basic principles & practice*, Momentum Press, 2012.
- 35 E. Dib, T. Mineva and B. Alonso, in *Annual Reports on NMR Spectroscopy*, 2016, pp. 175–227.
- 36 M. Edgar, *Annu. Reports Sect. B Org. Chem.*, 2012, **108**, 292.
- 37 A. Thangaraj, P. R. Rajamohanan, P. M. Suryavanshi and S. Ganapathy, *J. Chem. Soc. - Chem. Commun.*, 1991, 493–494.
- 38 E. Dib, B. Alonso and T. Mineva, *J. Phys. Chem. A*, 2014, **118**, 3525–3533.
- 39 T. Giavani, K. Johannsen, C. J. H. Jacobsen, N. Blom, H. Bildsøe, J. Skibsted and H. J. Jakobsen, *Solid State Nucl. Magn. Reson.*, 2003, **24**, 218–235.
- 40 T. Pratum and M. Klein, *J. Magn. Reson.*, 1983, **53**, 473–485.
- 41 C. A. Fyfe, R. J. Darton, C. Schneider and F. Scheffler, *J. Phys. Chem. C*, 2008, **112**, 80–88.
- 42 E. Dib, T. Mineva, P. Gaveau and B. Alonso, *Eur. Phys. Journal-Special Top.*, 2015, **224**, 1769–1773.
- 43 SOLA Topspin 3.2, Bruker, 2016.
- 44 H. J. Jakobsen, A. R. Hove, R. G. Hazell, H. Bildsøe and J. Skibsted, *Magn. Reson. Chem.*, 2006, **44**, 348–356.

5.0. The Effect of Structure Directing Agent Fluoride Ordering in Pure Silica MFI Zeolites

A typical zeolite synthesis traditionally includes a silicon (or aluminium source), mineralising agent, structure directing agent and solvent system in order to crystallise the specific multi-dimensional pore and channel architecture of a zeolite.¹ Until the 1980's, the most common mineralising agent used for zeolite syntheses was a hydroxide based species of the composition X^+OH^- , whereby X is any number of cations including H^+ , Na^+ , NH_3^+ , K^+ .^{2,3,4} The introduction of fluoride as the mineralising agent anion by Flanigan and Patton⁵ and Guth and co-workers⁶ in 1978 however had a profound effect on zeolite science and is capable of fundamentally changing the zeolite properties obtained.⁷ The fluoride route involves the replacement of traditional anion species OH^- with F^- ions inferring considerable implications.

The main problem encountered with the use of hydroxide ions as a mineralising agent is their use to charge compensate the structure directing agent (SDA), thereby incorporating the hydroxide ions into the framework,⁸ creating silanol nests and zeolite defects.⁹ The use of fluoride replaces this charge compensation role¹⁰ and removes the large majority of OH defects,¹¹ thereby allowing for the synthesis of near perfect silicite-1 crystals.⁸

Other benefits of the fluoride route include the synthesis of new zeolite types (ITQ-3¹², ITQ-4⁷) with larger pores,^{7,13} relative to fluoride content.¹⁴ The role of the mineralising agent is to dissolve the silica species⁴ however it is also thought to act as a catalyst to condense species into Si-O-Si bonds¹⁵ thereby forming the zeolite framework with a significant reduction in crystallisation time of a given zeolite, and with increased crystal surface size, relative to the F:Si content.¹⁶ The introduction of fluoride as a mineralising agent with the aforementioned desirable qualities lead to an influx of studies which attempted to determine the effect of fluoride on the zeolite crystallisation¹⁷ and properties of MFI zeolite¹⁶ and other zeolites.^{18,19} Throughout these studies, an additional role of the fluoride anion was discovered: not only does the fluoride interact

strongly with the zeolite framework but it covalently bonds to the zeolite framework structure.^{10,20}

Koller and co-workers^{21,22} studied the fluoride silicalite-1 system (and others: Zeolite Beta, SSZ-23, ITQ-3, ITQ-4, ZSM-12) and in 1997 proved by solid state NMR that the fluoride was covalently bound to framework silicon creating a pentacoordinated silicon unit (Figure 5.1).

Prior to this work most zeolite characterisation was performed using X-ray diffraction, the go-to tool for materials characterisation however many difficulties have been experienced when studying zeolites and F-MFI. This includes X-ray diffraction being unable to structurally determine between isoelectronic fluoride in the sample and OH⁻ ions in defects.²³ X-ray diffraction is therefore not a reliable

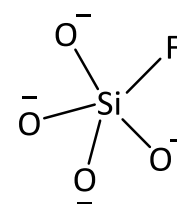


Figure 5.1 - Schematic diagram displaying pentacoordinated silicon species

technique in which to determine the location of fluoride in MFI framework cages. Additional difficulties are found in finding good single crystals for single crystal diffraction, such as crystals of sufficient size^{24,25} or that are not twinned²¹ and crystallographic techniques also struggle to accurately determine bond lengths of zeolites synthesised using the fluoride route. Diffraction techniques also affected by fluoride motion. This phenomenon will be discussed throughout this chapter and is the reason for years of incorrectly reported, averaged values for pentacoordinated species.^{11,26} The complementary use of solid state NMR with X-ray crystallographic techniques²⁷ is an excellent combination allowing for the study of the long range order of materials as well as identifying local order to <1 nm range by solid state NMR.¹⁷

The pentacoordinated silicon unit observed in fluoride based zeolite materials would seem an odd idea due to the fact that silicon is primarily a four-coordinate element. Koller and co-workers²² were not however the first to identify a non four-coordinated silicon. Six-coordinated silica exists in the crystalline silicate mineral thaumasite²⁸ and Van de Goor and co-workers²⁹ identified a five-coordinated silicon species in fluoride synthesized NON zeolite in 1995. This entertains the Aubert and co-workers suggestion that “in pure silica as-made crystalline microporous materials

synthesized in fluoride media, pentacoordinated silicon atoms seem to be a rule, as opposed to an exception".²⁰

By identification of chemical shift resonances in CP MAS NMR, Koller and co-workers²² observed a pentacoordinated silicon unit in the five-coordinate silicon range. This peak was observed at -145 ppm, far outside the normal $\text{SiO}_{4/2}$ region of -106 to 120 ppm³⁰ and proved the existence of the pentacoordinated silicon unit in the form of $\text{SiO}_{4/2}\text{F}^-$ using ^{19}F - ^{29}Si CP MAS NMR. Later work by Koller and co-workers²¹ elucidated a distinction between these pentacoordinated silicon units which have since been proved to be placed in the $[4^15^26^2]$ cage,^{7,31} on the Si-9³² mirror plane sites where an averaged peak at -125 ppm for F-TPA Si-MFI is observed. The broad chemical shift and a low chemical shift peak represent a dynamic fluoride movement between mirror plane silicon sites that can be frozen out at 140 K (-133 °C) (Figure 5.2):

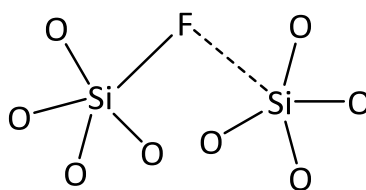


Figure 5.2 – Schematic diagram displaying pentacoordinated silicon species whereby the additional fluoride is covalently bonded to one si-9 site at any time

It is well known that the shape and size of the structure directing agent used in zeolite syntheses has an effect on the size of the zeolite pores and channels,^{16,33,34} a quality that subsequently has an effect on the zeolites important absorption capabilities.^{9,35} Despite being known that changing the size and shapes of these structure directing agents also has an effect on the ordering of the covalently bound fluoride, very little work has been focused on fluoride disorder effects in any other systems than TPA for F-silicalite-1. One such paper that does, is a 2015 paper investigating the fluoride disorder in a short series of n-alkyltripropylammonium silicalite-1 samples.³²

The aim of this chapter is to identify the effect on the fluoride motion that exists in silicalite-1 synthesized using a variety of different shape and size structure directing agents in order to contribute to the on-going literary developments of silicalite-1 structure and crystallisation.

5.1. ^{29}Si Solid State NMR Results

5.1.1. TPA F-silicalite-1

Silicalite-1 was synthesised using tetrapropylammonium iodide, confirmed by X-ray diffraction and subsequently studied by a variety of solid state NMR experiments. The ^{29}Si solid state NMR results shown below (Figure 5.3), display an NMR spectrum that can be deconvoluted using MestReNova³⁶ into 12 peaks, representative of the 12 silicon environments. These silicon environments have previously been assigned and classified as orthorhombic *Pmna* space-group within the TPA silicalite-1 system.³²

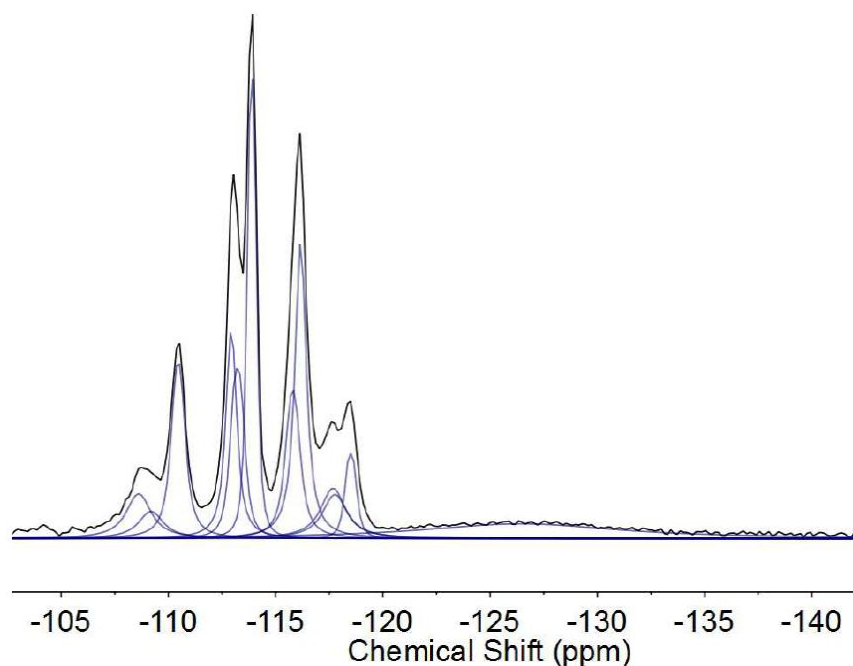


Figure 5.3 – Spectrum (black) and deconvolution (blue) of $^1\text{H}\{^{29}\text{Si}\}$ CP MAS NMR spectrum of [TPA]-F MFI (6 kHz rotation speed, 7 ms contact time and 3 s recycle delay)

The chemical shift of these silicon sites and FWHM (full width at half maximum) as follows.

$^1\text{H}\{-^{29}\text{Si}\}$ CP MAS NMR [400 MHz, ppm, FWHM in Hz]; - 108.60 (110), - 109.19 (110), - 110.46 (60), - 112.93 (48), - 113.22 (61), - 113.89 (40), - 115.80 (63), - 116.16 (49), - 117.68 (110), - 117.77 (110), - 118.50 (49), - 126.42 (882).

Also in line with the previously observed SS-NMR results from Koller and co-workers²¹ and Fyfe and co-workers, is the appearance of a pentacoordinated silicon peak at -125 ppm. This was reported as a dynamically disordered fluoride (at RT), covalently bonded to a silicon in the $[4^15^26^2]$ cage. The broad resonance can be more clearly viewed in the enlargement displayed below (Figure 5.4):

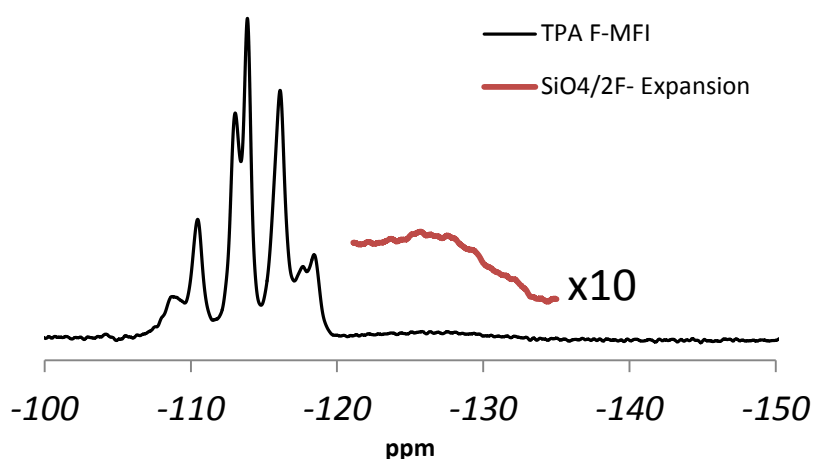


Figure 5.4 – $^{29}\text{Si}\{^1\text{H}\}$ CP MAS SS-NMR spectra of TPA F-MFI at 6 kHz rotation speed with a 7 ms contact time and 3 s recycle delay

The peak observed at -125 ppm (enlarged in red) is assigned to the silicon covalently bonded to the mineralising agent fluoride. This peak is observed as a broad peak due to motion of the fluorine between mirror plane silicon sites in the $[4^15^26^2]$ cage.^{22,32} The broadness of the peak observed, as opposed to two distinct peaks for the two silicon sites, is thought to be due to the fluoride motion being fast compared to the NMR timescale.

No reason for this motion has been previously suggested, however one theory is that the fluoride motion is related to and dependant on the structure directing agent. More specifically, related to the distance to the positively charged nitrogen species within the SDA, as the major role of the

fluoride is to charge balance the SDA. Theoretically, the closer the fluoride to the positively charged nitrogen cation, the larger the coulombic interaction between them and the stronger the attractive force keeping the fluoride statically bound to one silicon site.

This theory was tested by studying silicalite-1 synthesised using a variety of differently shaped and sized structure directing agents, in order to determine the effect on the fluoride ordering.

5.1.2. ^{29}Si SS-NMR N-alkyltributylammonium Silicalite-1 Series

The first series of structure directing agents used to test the theory was an increasing fourth alkyl chain on quaternary tributylammonium cations as shown in Figure 5.5:

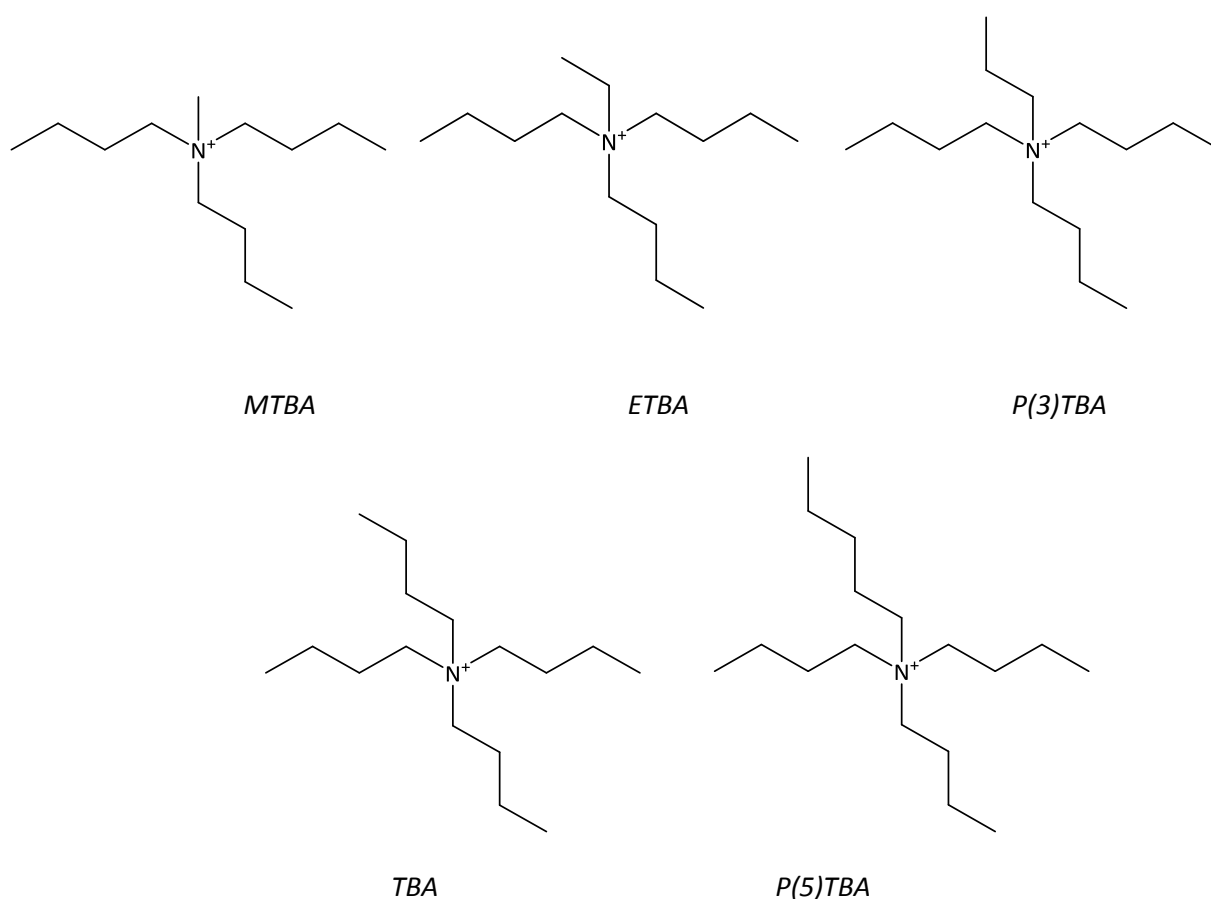


Figure 5.5 – Schematic diagram of structures of varied alkyl n-alkyltributylammonium cations in the tributylammonium silicalite-1 series

Methyl and ethyl alkyl chains were first investigated however despite numerous attempts at synthesising silicalite-1 zeolite using n-propyltributylammonium, no crystalline samples could be obtained using the hydrothermal route in autoclaves or polypropylene bottles at 100 °C or 180 °C.

N-butyltributylammonium was the next logical chain in this series however it was not used to attempt to synthesise silicalite-1 zeolite due to it being the primary structure directing agent used for synthesis of a different zeolite, silicalite-2³⁷ (MEL³⁸).

5.1.2.1. MTBA F-silicalite-1

Silicalite-1 was synthesised using n-methyltributylammonium and studied by X-ray diffraction and solid state NMR. Comparison of the XRD powder pattern with International Center for Diffraction Data (ICDD), a match was found to MFI with orthorhombic³⁹ crystal symmetry and *Pmna*⁴⁰ space group. This symmetry would indicate that there are 12 silicon environments present in the sample however solid state NMR results returned the following spectrum;

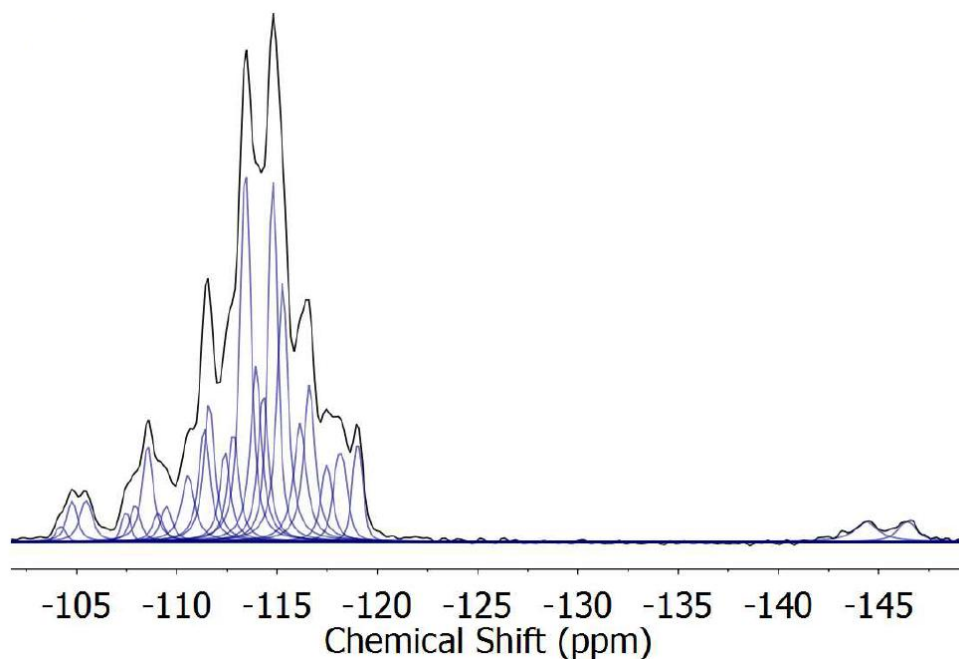


Figure 5.6 – Spectrum (black) and deconvolution (blue) of $^1\text{H}\{^{29}\text{Si}\}$ CP MAS NMR spectrum of [MTBA] F-MFI (6 kHz rotation speed with 7 ms contact time and 10 s recycle time)

Instead of the traditional 12 peaks observed for orthorhombic *Pmna* symmetry, deconvolution of the $^1\text{H}\text{-}^{29}\text{Si}$ CP MAS solid state NMR spectrum revealed 24 individual resonances, which represents monoclinic symmetry;

$^1\text{H}\text{-}\{^{29}\text{Si}\}$ CP MAS NMR [400 MHz, ppm, FWHM in Hz]; - 104.21 (48), - 104.77 (50), - 105.47 (60), - 107.46 (43), - 107.92 (50), - 108.54 (51), - 109.06 (50), - 109.48 (54), - 110.55 (61), - 111.37 (53), -

111.61 (50), - 112.40 (49), - 112.81 (51), - 113.42 (51), - 113.94 (51), - 114.31 (50), - 114.79 (46), - 115.28 (51), - 116.14 (59), - 116.61 (53), - 117.48 (54), - 118.15 (64), - 119.02 (49), [- 144.38 (110) 146.43 (90)].

Monoclinic symmetry has previously been observed for aluminium containing ZSM-5 zeolite dependant on temperature,⁴¹ crystal size,^{35,42} and and if the SDA has been removed from the pore. It can be viewed by miniscule differences in the X-ray diffraction powder pattern, highlighted in Figure 5.7:

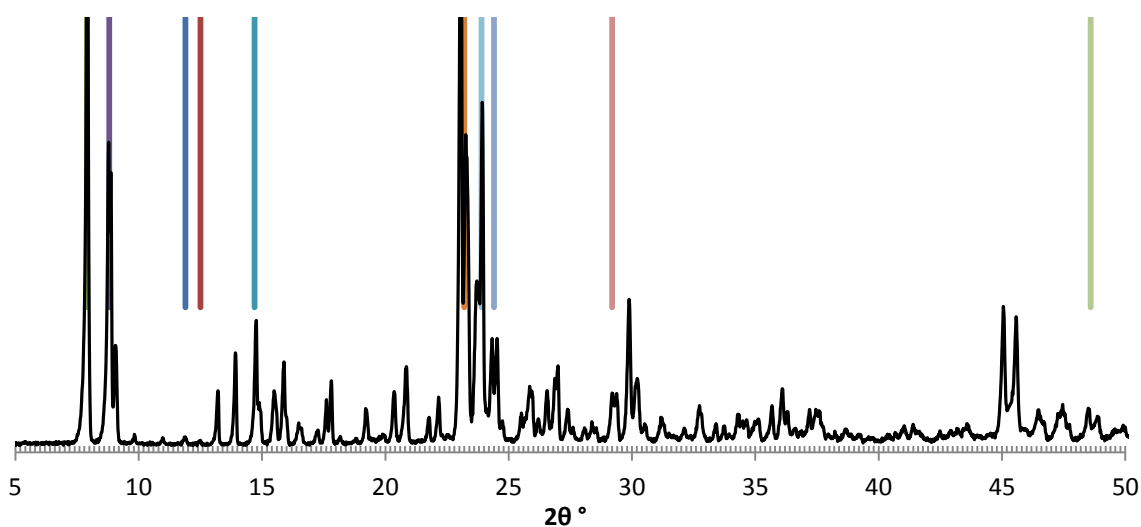


Figure 5.7 – X-ray diffraction pattern of ETBA F-MFI from 5 to 50 2θ ° for identification of monoclinic peaks

The X-ray diffraction pattern for a sample that contains >12 silicon resonances has therefore been studied and compared to observations of Dose and co-workers³⁵ who identify monoclinic behaviour outlined in the following Table 5.1:

Table 5.1 – Table to summarise the changes observed in a monoclinic morphology of silicalite-1 as opposed to orthorhombic

XRD Peak	2θ °	Expected Change for Orthorhombic to Monoclinic	Change observed
	7.9	Line intensity greatly increased	No
	8.8	Line intensity greatly increased	Yes
	11.9	Line intensity greatly reduced	Yes
	12.5	Line intensity greatly reduced	No
	14.7	Doublet merges to singlet	Some convergence
	23.3	Doublet becomes more apparent	Yes
	23.9	Doublet becomes less apparent	No
	24.4	Doublet replaces singlet	No
	29.2	Doublet replaces singlet	No
	48.6	Doublet replaces singlet	Insufficient resolution

Despite using a highly crystalline sample, identification of the peaks that show monoclinic symmetry is not possible for all comparable peaks within the XRD pattern. As such, the results of this comparison are not sufficiently conclusive to discern monoclinic behaviour in the X-ray diffraction pattern of silicalite-1 samples.

This long range order characterisation can however be complemented by the local order determined by solid state NMR. It is believed that the observation of an additional 12 peaks in the deconvolution can be explained by consideration of the effect of the fluoride motion on the local structure, as opposed to the long range order that may remain unaffected by X-ray diffraction study. With the fluoride bonded to only one silicon site at any one time in the $[4^{15}26^2]$ cage, the 12 sites and *Pmna* symmetry observed by X-ray diffraction becomes 24^{43} tetrahedral sites in NMR when mirror plane sites are observed on the local order.

The fluoride peak observed in this silicalite-1 CP SS-NMR spectrum synthesised using n-methyltributylammonium as a structure directing agent clearly shows a doublet at – 145.43 ppm (Figure 5.8):

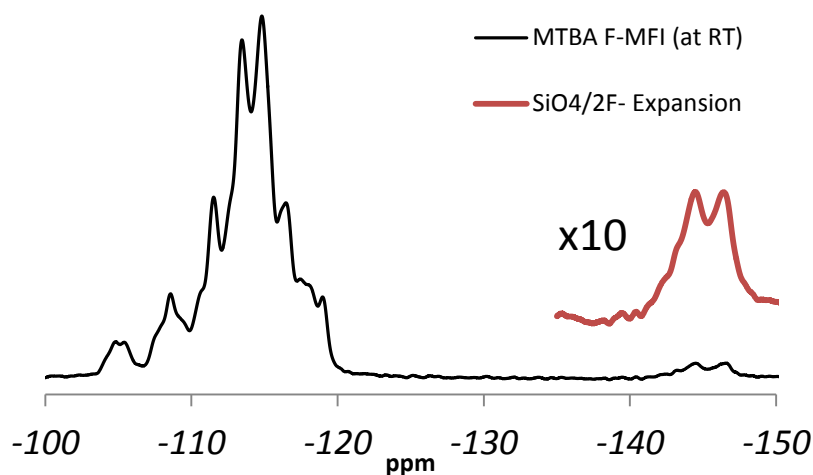


Figure 5.8 - $^1\text{H} \{^{29}\text{Si}\}$ CP MAS SS-NMR spectra of MTB F-MFI at room temperature at 6 kHz rotation, with a 7 ms contact time and 3 s recycle delay

This double peak is J coupled whereby $J_{\text{Si-F}} = 165$ Hz demonstrating a strong incorporation of the fluoride to the silicon framework. This peak is representative of a statically bound pentacoordinated Si-F which mimics the behaviour observed in Koller and Co-workers⁴⁴ TPA silicalite-1 (IFR and SSZ-23) spectra whereby the fluoride motion is ‘frozen out’ at -40 °C.

It would appear that the short alkyl chain length of methyl in the n-methyltributylammonium structure directing agent is small enough to allow sufficient coulombic interaction between the positively charged nitrogen and fluoride ion to restrict the fluoride to 1 silicon site. Alternatively, it is able to affect the frequency of the motion relative to the NMR timescale. This restriction to statically disordered fluoride was investigated at different temperatures to determine whether temperature could affect the motion.

5.1.2.2. MTBA F-silicalite-1 at +50 °C

Upon increasing the temperature of the MTBA F-MFI spectra collected, a very slight increase in the fluoride motion was observed. The chemical shift of the averaged pentacoordinated silicon peaks shift slightly (0.18 ppm) downfield towards the chemical shift region that we observe for dynamic disorder of pentacoordinated silicon species. This is complemented by the slight

movement of the two peaks closer together from 1.95 ppm apart at room temperature to 1.48 ppm apart at 50 °C.

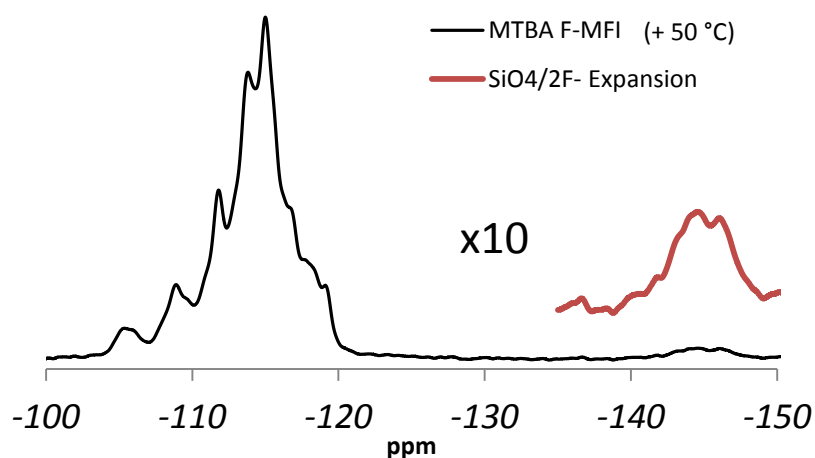


Figure 5.9 - $^1\text{H} \{^{29}\text{Si}\}$ CP MAS SS-NMR spectra of MTB F-MFI at 50 °C, 6 kHz rotation speed, a 7 ms contact time and 3 s recycle delay

5.1.2.3. MTBA F-silicalite-1 at -40 °C

Upon decreasing the temperature of the MTBA silicalite-1 sample from room temperature the opposite effect is observed. The chemical shift of the pentacoordinated silicon peaks shift slightly (0.87 ppm) upfield towards the region observed for static disorder giving an averaged chemical shift of the peaks at -146.30 ppm. This is complemented by the slight movement of the two peaks further apart from 1.95 ppm apart at room temperature to 2.11 ppm apart at -40 °C.

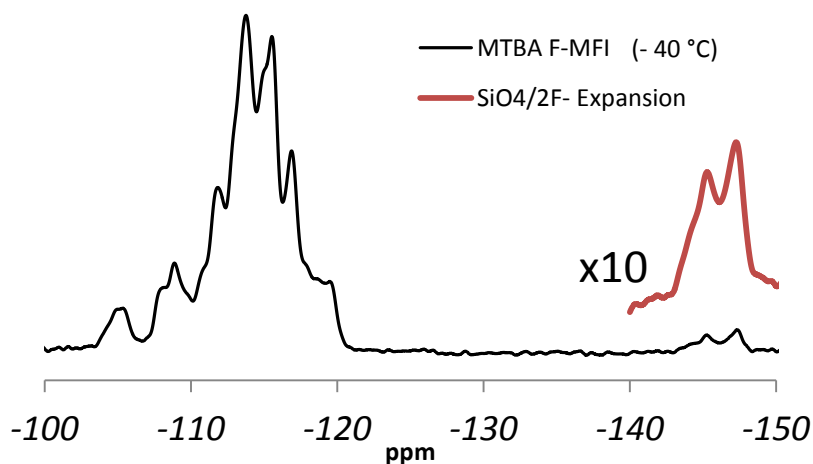


Figure 5.10 - $^1\text{H} \{^{29}\text{Si}\}$ CP MAS SS-NMR spectra of MTB F-MFI at -40 °C, 6 kHz rotation speed, a 7 ms contact time and 3 s recycle delay

The peak shape of the static pentacoordinated silicon peaks shown above (Figure 5.10) shows that of an unequal doublet. This has been observed previously by Koller and co-workers^{2,4} for ITQ-3 zeolite, Darton and co-workers¹¹ for zeolite SSZ-42 and also Haubenrisser and co-workers¹⁹ ¹⁹F spectra of fluorophosphates.⁴⁵ The inequality of this doublet is reported to be due to interactions being dominated by heteronuclear dipole interactions and chemical shift anisotropy's as well as j-couplings. They also suggest that these effects are the reason that doublets are not observed for all zeolites; however this theory is unlikely due to the more recent developments of the different types of fluoride disorder.

5.1.2.4. ETBA F-silicalite-1

Upon increasing the alkyl chain from methyl to ethyl (tributylammonium) silicalite-1, a similar 24 peak spectra is observed:

¹H-²⁹Si} CP MAS NMR [400 MHz, ppm, FWHM in Hz]; - 107.82 (50), - 107.24 (68), - 108.93 (46), - 108.36 (54), - 109.52 (57), - 110.13 (47), - 110.50 (68), - 111.47 (64), - 111.92 (65), - 111.92 (47), - 112.16 (53), - 113.80 (58), - 114.11 (50), - 114.17 (51), - 114.78 (51), - 115.38 (56), - 115.54 (49), - 116.38 (50), - 117.00 (46), - 117.38 (53), - 118.00 (54), - 119.28 (59), - 119.28 (63), - 141.50 (110).

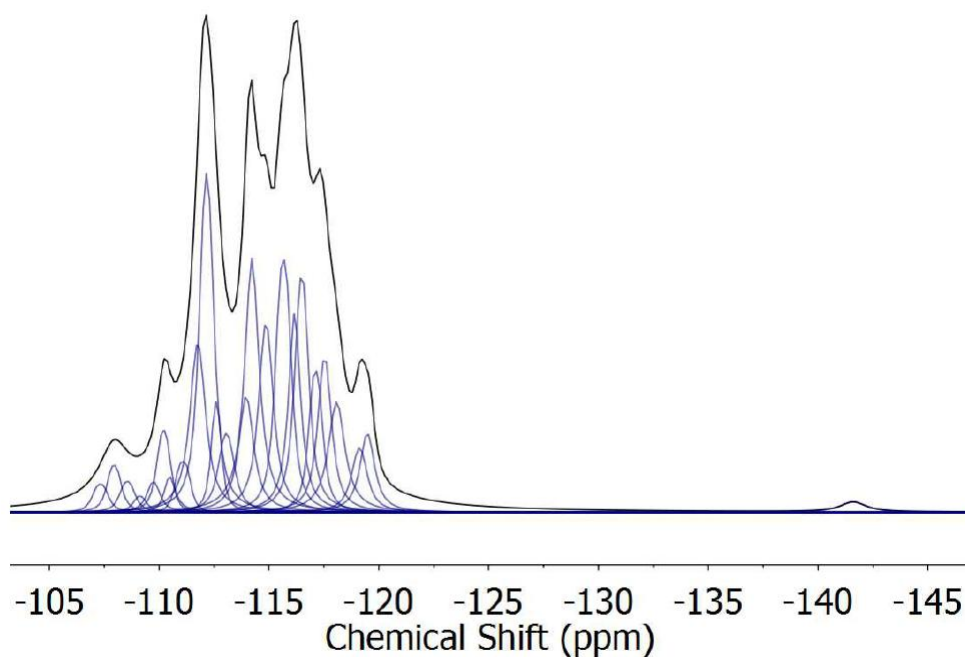


Figure 5.11 – MestReNova deconvolution of ¹H {²⁹Si} CP MAS NMR spectrum of ETB F-MFI (6 kHz rotation speed with 7 ms contact time and 10 s recycle time)

The increase in alkyl chain length by one carbon removes the statically bound J-coupled Si-F doublet observed at -146 ppm for MTBA and instead displays a small averaged peak at -141.46 ppm which resembles somewhere inbetween the static MTBA sample and dynamic TPA sample (Figure 5.12):

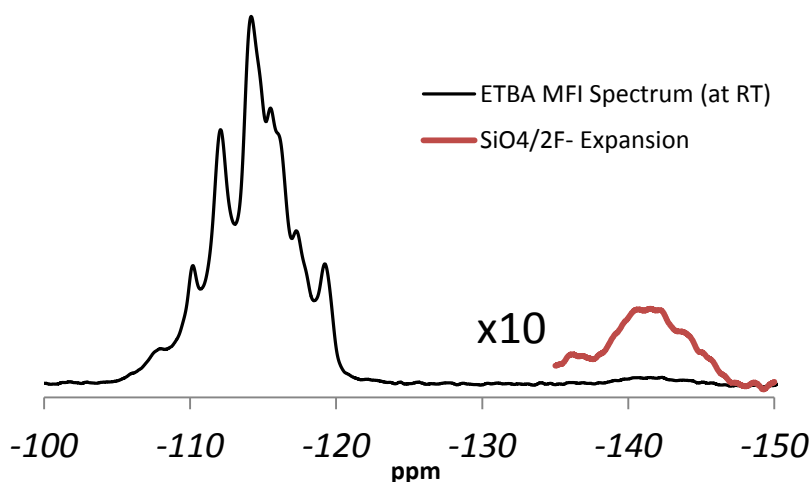


Figure 5.12 - $^1\text{H}\{^{29}\text{Si}\}$ CP MAS SS-NMR spectra of MTB F-MFI at room temperature, 6 kHz rotation speed, a 7 ms contact time and 3 s recycle delay

Based on the theory suggested, this change in fluoride mobility detected is a direct response to the increase in alkyl chain length. Increasing the alkyl length would decrease the coulombic interaction between the structure directing agents positively charged nitrogen and the fluoride allowing for a change from static to dynamic disorder of the fluoride. Though the peak observed is an averaged peak with no J-coupled doublet it has not shifted as much as would be expected towards the chemical shift region for dynamic disorder. It is most likely that this peak observes fluoride motion but at a considerably slower rate than that of the TPA silicalite-1 fluoride. To determine whether this slow motion dynamic disorder could be removed the spectrum was also observed at $-10\text{ }^\circ\text{C}$ (Figure 5.13):

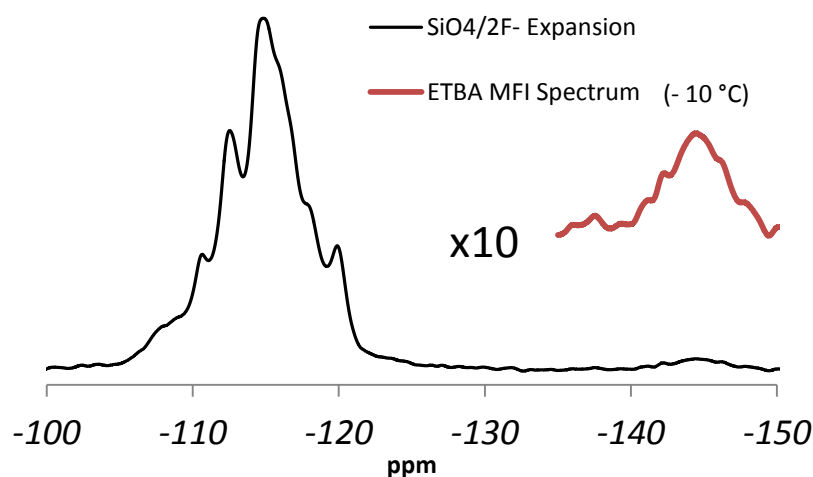


Figure 5.13 - $^1\text{H}\{^{29}\text{Si}\}$ CP MAS SS-NMR spectra of ETB F-MFI at $-10\text{ }^\circ\text{C}$, 6 kHz rotation speed, a 7 ms contact time and 3 s recycle delay

The reduction in temperature exhibits a movement towards the statically disordered region of the spectrum at -144.43 ppm . This movement from static to dynamic disorder leads to a change from a wide to narrow peak at increased chemical shift towards the Q4 range in the spectral results. Thus the theory would follow that continued increase in the alkyl chain on the tributylammonium to propyl, butyl and pentyl would increase the disorder and chemical shift observed.

5.1.2.5. P5TBA F-silicalite-1

Due to the reduced chemical resolution it was not possible to distinguish the silicon sites present in silicalite-1 synthesised using P5TBA. As such, this sample could not be deconvoluted and the number of silicon sites in the spectrum could not be determined.

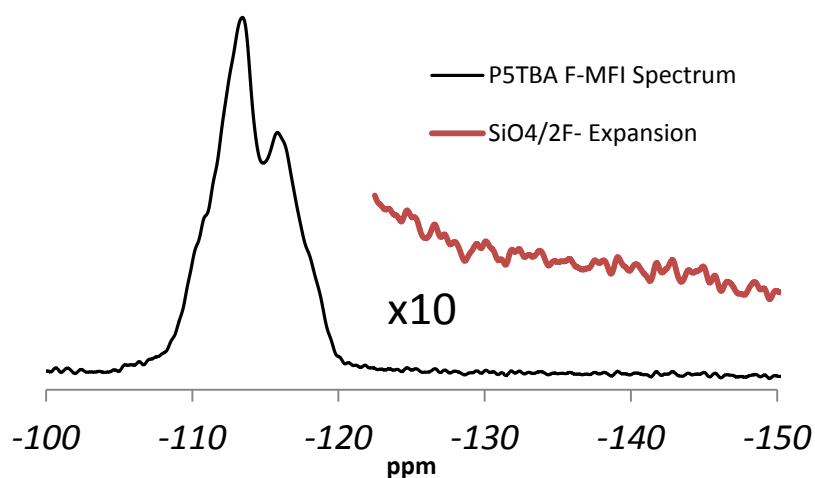


Figure 5.14 - $^1\text{H}\{^{29}\text{Si}\}$ CP MAS SS-NMR spectra of P5TBA F-MFI at room temperature, 6 kHz rotation speed, a 7 ms contact time and 3 s recycle delay

The above spectrum (Figure 5.14) observed for silicalite-1 synthesised using n-pentyltributylammonium lacks an obvious statically disordered fluoride however upon zooming into the baseline within the dynamic disorder region, a very broad peak can clearly be seen. It is thought that in line with the trend of increasing n-alkyl chain leading to a movement from static to dynamic disorder, that this broad silicon peak is due to a dynamically disordered fluoride at around the center of the silicon intensity at – 133 ppm.

5.1.2.6. ²⁹Si SS-NMR N-alkyltributylammonium Silicalite-1 Summary

Upon increasing the alkyl chain length in the n-alkyltributylammonium silicalite-1 series synthesised using the fluoride route, a clear movement from statically disordered to dynamically disordered fluoride motion is observed. This is accompanied with the corresponding downfield chemical shift and convergence of the double peak observed for statically bound fluoride to a single peak for dynamic fluoride motion: summarised in Table 5.2.

Table 5.2 – Table of experimental properties obtained from increasing alkyl chain length of n-alkyltributylammonium at varied temperatures

SDA /Silicalite-1	Disorder	Average δ_{ISO} (ppm)
-40 °C	Static	- 146.30
MTBA RT	Static	-145.43
50 °C	Static	- 145.31
ETBA RT	Dynamic	-141.43
- 10 °C	Dynamic	-144.43
P5TBA	Dynamic	~ -133

This effect can however be influenced by temperature whereby increased temperature contributes to the dynamic motion of fluoride and decreased temperature contributes to reducing the fluoride dynamic motion.

5.1.3. ²⁹Si SS-NMR N-alkyltripropylammonium Silicalite-1 Series

The n-alkyltripropylammonium silicalite-1 (Figure 5.15) series was investigated to determine whether changing the size of the trialkyl groups would have an effect on the fluoride motion observed.

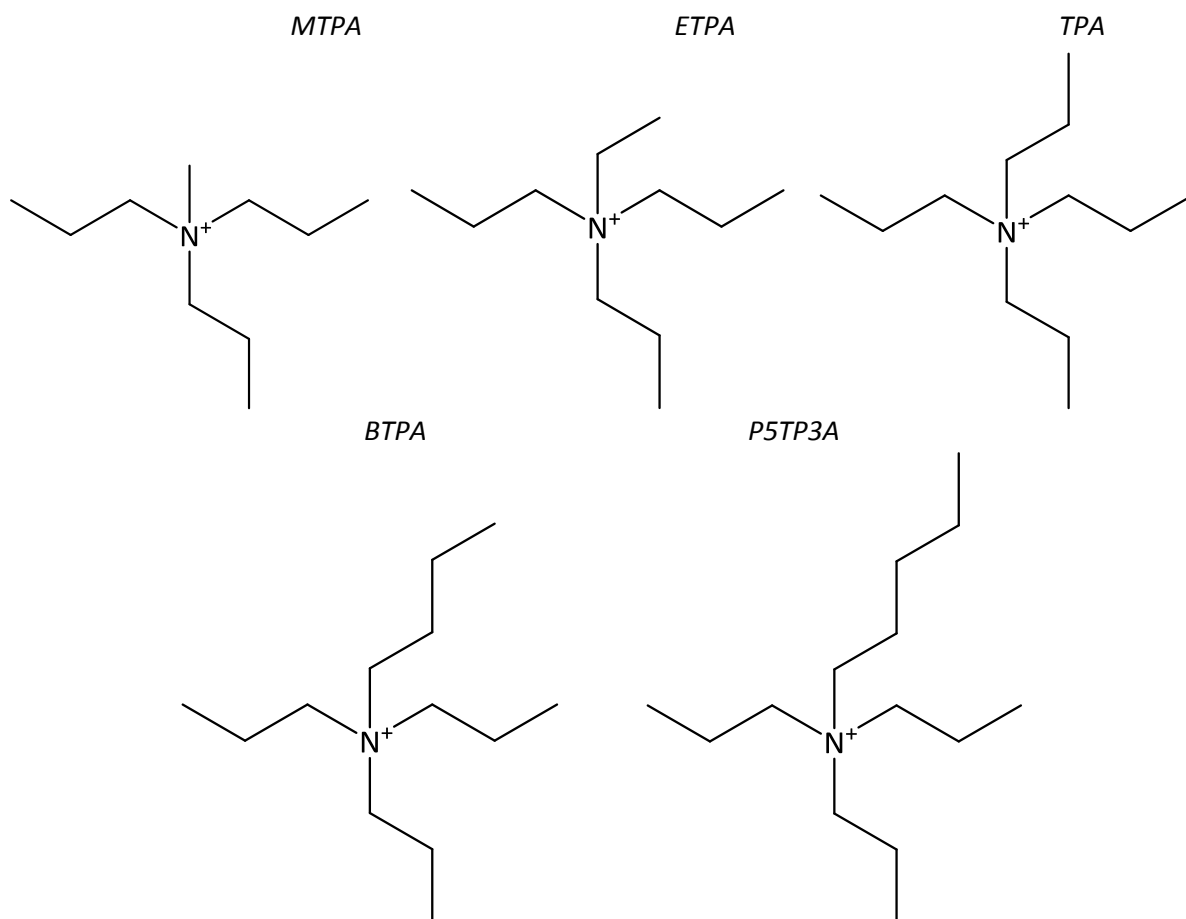


Figure 5.15 - 2D structures of varied length n-alkyltripropylammonium cations

In line with the concurrent theory, we should also observe a movement from static to dynamic disorder when increasing this alkyl chain length.

The only literature study in which these materials can be compared is the previously mentioned study by Dib and co-workers⁴⁶ who determined the effects of a 3-structure directing agent range within this series from ethyl to to butyl tripropylammonium silicalite-1.

5.1.3.1. MTPA F-silicalite-1

Silicalite-1 was synthesised using n-methyltripropylammonium studied by solid state NMR to determine 24 silicon sites representative of monoclinic crystal symmetry (Figure 5.16);

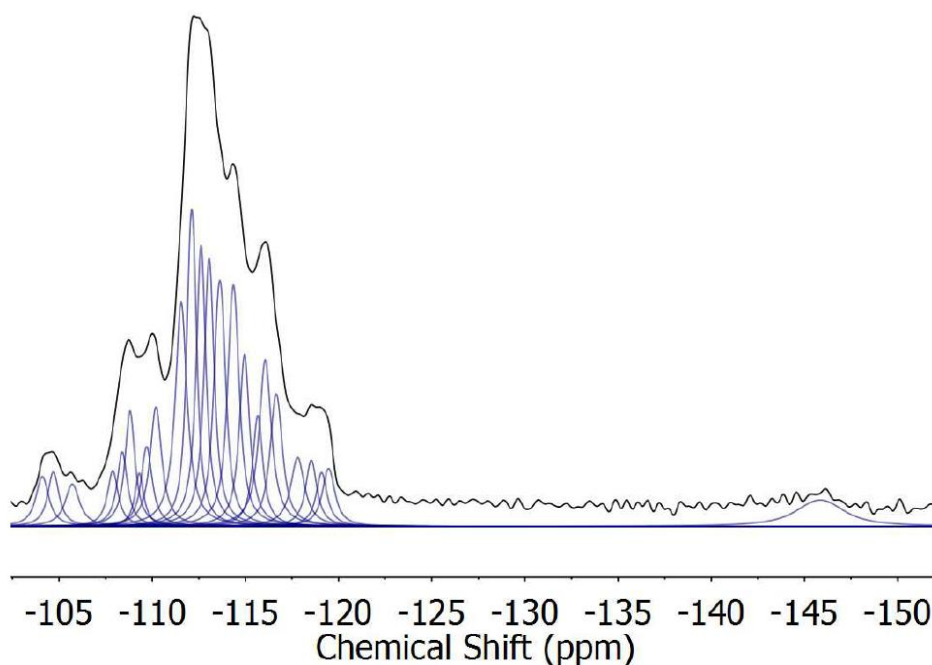


Figure 5.16 - MestReNova deconvolution of $^1\text{H}\{^{29}\text{Si}\}$ CP MAS NMR spectrum of MTP F-MFI (Room temperature, 6 kHz rotation speed with 7 ms contact time and 10 s recycle time)

$^1\text{H}\{^{29}\text{Si}\}$ CP MAS NMR [400 MHz, ppm, FWHM in Hz]; - 104.10 (66), - 104.69 (58), - 105.71 (74), - 107.88 (56), - 108.80 (51), - 108.39 (53), - 109.31 (47), - 109.70 (57), - 110.19 (60), - 111.55 (60), - 112.11 (49), - 112.61 (49), - 113.05 (51), - 113.62 (59), - 114.35 (59), - 114.95 (52), - 115.66 (52), - 116.06 (63), - 116.65 (62), - 117.80 (72), - 118.53 (58), - 119.09 (58), - 119.46 (65), - 145.84 (243).

The resulting spectrum obtained shows a significant decrease in chemical shift resolution compared to similar silicalite-1 samples synthesised using n-methyltributylammonium and tetrapropylammonium, so much so that a 10 times expansion is required in order to observe any increase in silicon intensity:

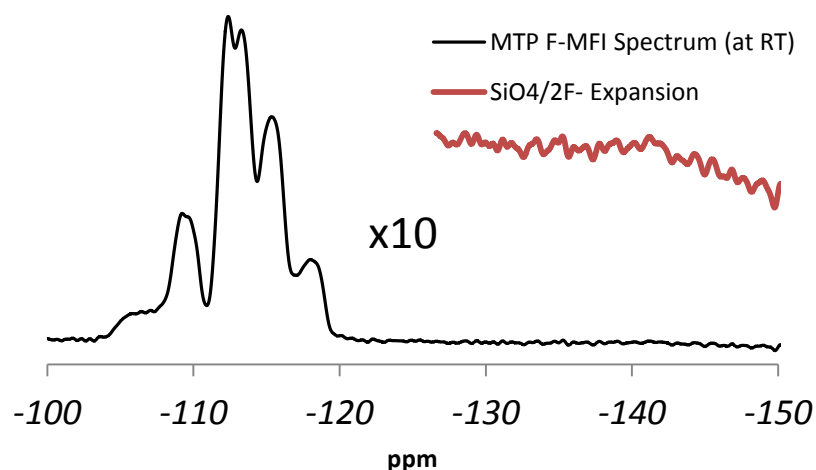


Figure 5.17 - $^1\text{H} \{^{29}\text{Si}\}$ CP MAS SS-NMR spectra of MTP F-MFI at room temperature, 6 kHz rotation speed, a 7 ms contact time and 3 s recycle delay

The expansion allows the identification of a broad spectral peak at roughly -135 ppm. In order to fully elucidate the peak, the sample was collected again at a reduced temperature of $-40\text{ }^\circ\text{C}$ in order to freeze the peak out (Figure 5.18):

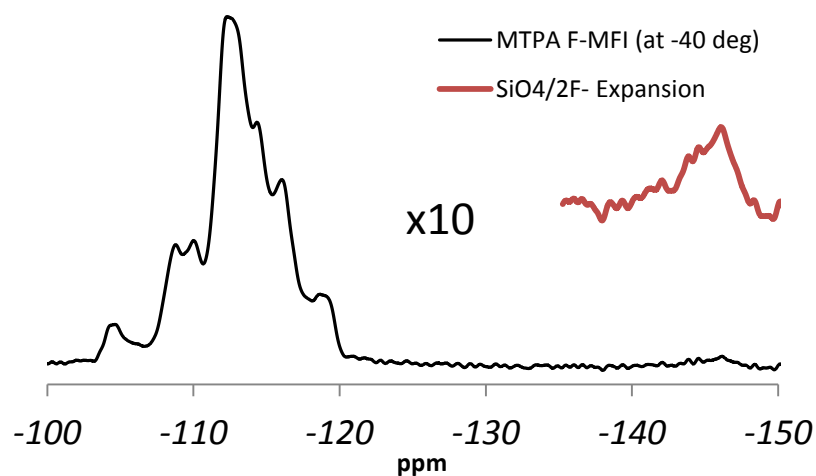


Figure 5.18 - $^1\text{H} \{^{29}\text{Si}\}$ CP MAS SS-NMR spectra of MTPA F-MFI at $-40\text{ }^\circ\text{C}$, 6 kHz rotation speed, a 7 ms contact time and 3 s recycle delay

Significant chemical shift resolution enhancements are possible by reducing the sample to $-40\text{ }^\circ\text{C}$ indicating that the reduced resolution at room temperature was due to the fluorides dynamic disorder. A J-coupled doublet can thereby be observed centred at -145.34 ppm where the fluorides are statically bound to silicon when the motion is 'frozen' out.

5.1.3.2. ETPA F-silicalite-1

Due to the diminishing resolution for all the following structure directing agents in the n-alkyltripropylammonium MFI series no deconvolutions and direct determination of the number of silicon sites from the by NMR spectra could be obtained.

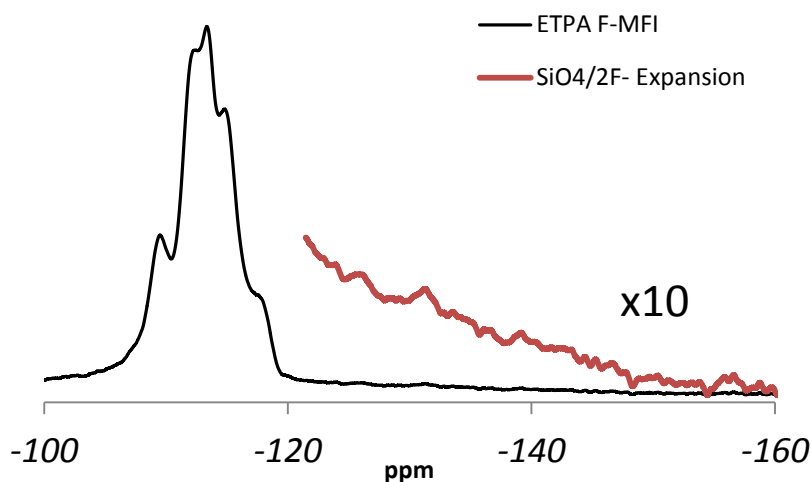


Figure 5.19 - $^1\text{H} \{^{29}\text{Si}\}$ CP MAS SS-NMR spectra of ETPA F-MFI at room temperature, 6 kHz rotation speed, a 7 ms contact time and 3 s recycle delay

In addition to the reduced chemical shift resolution within this series, we also observe interesting pentacoordinated silicon peak intensity from ~ -148 ppm to -120 ppm in silicalite-1 synthesised using both ethyl (Figure 5.19) and butyl (Figure 5.20) in the n-alkyltripropylammonium series.

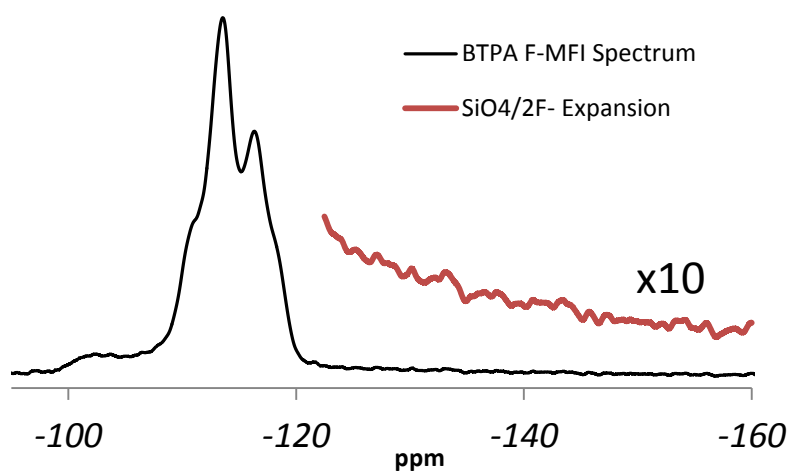


Figure 5.20 - $^1\text{H} \{^{29}\text{Si}\}$ CP MAS SS-NMR spectra of BTPA F-MFI at room temperature, 6 kHz rotation speed, a 7 ms contact time and 3 s recycle delay

Upon studying the baseline within this range, we identify a gradual increasing silicon peak that is calculated to be centred at -133.03 ppm for ETP and -133.80 ppm BTP representative of dynamic disorder. This silicon peaks observed in these spectra are slightly dissimilar from the broad dynamic peak observed in Dib and co-workers spectrum of the same material⁴⁶ at -127 ppm.

5.1.3.3. P5TP3A F-silicalite-1

The P5TP3A F-MFI NMR spectrum displayed above (Figure 5.21) displays the same gradual increase in silicon intensity observed for the previous two alkyl chain lengths in this series of n-alkyltripropylammonium MFI species.

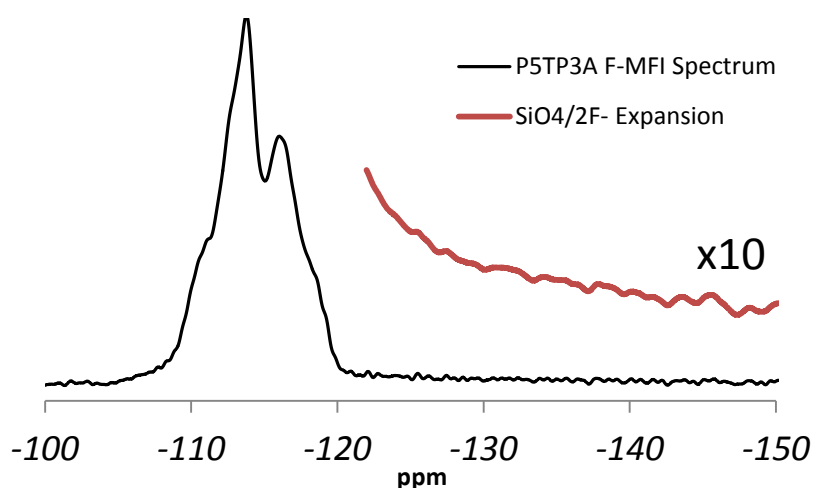


Figure 5.21 - $^1\text{H} \{^{29}\text{Si}\}$ CP MAS SS-NMR spectra of P5TP3A F-MFI at -40°C , 6 kHz rotation speed, a 7 ms contact time and 3 s recycle delay

Due to the dissimilarities in silicon peaks observed in this work compared to Dib and co-workers it is considered that this feature is representative of the materials made here which may have slight chemical differences due to small changes in the synthetic procedures to that compared to Dib and co-workers materials whereby their synthetic procedure uses roughly 1/3rd more structure directing and water, amongst other differences.

5.1.3.4. ²⁹Si SS-NMR N-alkyltripropylammonium Silicalite-1 Summary

Upon increasing the alkyl chain in the n-alkyltripropylammonium silicalite-1 series from methyl to pentyl we observe the same increase in fluoride motion as was observed in the n-alkyltributylammonium silicalite-1 series. This is summarised in Table 5.3.

Table 5.3 – Table of chemical shift resonances observed for silicalite-1 synthesised using varied structure directing agents

SDA/Silicalite-1	Disorder Observed	D ISO/ ppm
- 40 °C MTP	Frozen to static at – 40 °C	-145.34 (-144.58+ -146.09)
MTP	Dynamic	-130
ETP	Dynamic	-133 (broad)
TPA	Dynamic	-125 (broad)
BTP	Dynamic	-134 (broad)
P5TP3A	Dynamic	-134 (broad)

These results support the theory of increased fluoride mobility upon increasing the fourth alkyl chain, potentially due to the reduction in coulombic interaction between the fluoride and positively charged nitrogen in the SDA.

5.2. ¹⁹F Solid State NMR of Silicalite-1 Species

¹⁹F solid state NMR can also be used to study the pentacoordinated silicon species in question and has successfully done so in a variety of different zeolite systems herein. This is possible due to the high sensitivity of ¹⁹F, as a spin half nuclei with 100 % abundance and high resonance frequency.⁴⁷

Previous observations of fluoride chemical shift in these pentacoordinated silicon units have not been entirely consistent. This is likely due to the small changes in synthetic methods which lead to slightly different framework sizes and confirmations, which are local order traits that can be differentiated by solid state NMR. The pentacoordinated silicon peak can occur anywhere in the range of -64 ppm to -80 ppm for small cage species whereby downfield chemical shift ranges are observed from smaller cage species.⁴

Founding work by Koller and co-workers²¹ report a TPA F-MFI ¹⁹F chemical shift at -64 ppm, compared to Dib and co-workers⁴⁶ TPA F-MFI 62.8 ppm chemical shift and Fyfe and co-workers⁴⁸

at -64.9 ppm. This chemical shift can be changed even more by Rojas and co-workers⁴⁹ synthesis of MFI zeolite using 4-bis-imizadole to report a chemical shift of -68 ppm, allowing an apparently wide ¹⁹F range for the same MFI zeolite.⁵⁰ It is possible that these differences in chemical shift reporting's are due to differences in the NMR experiments used, such as whether proton decoupling was used and a high spectrum obtained. It is also possible these different chemical shifts are observed due a difference in the temperature in which they were collected as it has been previously deduced that the temperature of the sample has an effect on the fluoride motion. This has also been observed by Koller and co-workers²¹ whereby a difference of 6 ppm is observed in the sample TPA F-MFI at room temperature where the fluoride motion is dynamic and at 140 K where the fluoride motion is static.

¹⁹F solid state NMR experiments have been investigated on two series of SDA silicalite-1 samples, n-alkyltributylammonium and n-alkyltripropylammonium, to determine whether the difference in ¹⁹F chemical shift of the fluoride supports the difference in motion of the fluoride observed by ²⁹Si solid state NMR.

5.2.1. ¹⁹F Solid State NMR Results

5.2.1.1. MTBA F-silicalite-1

A chemical shift resonance of -67.68 ppm is observed for the statically disordered silicalite-1 zeolite which is in line with fluorides contained in the [4¹5²6²] cage (Figure 5.22).

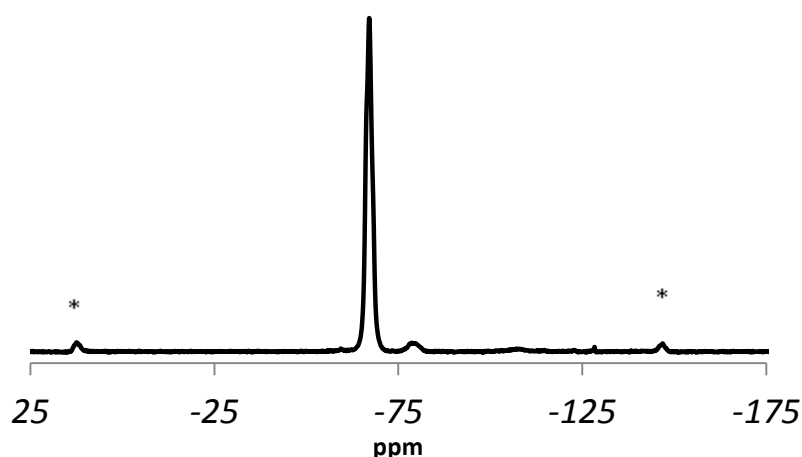


Figure 5.22 - ¹⁹F MAS NMR of MTBA F-MFI at 30 kHz rotation speed and 280 K (spinning sidebands are asterisked*)

An additional small peak at -79.68 ppm is also observed which has previously been observed^{48,49,51} and is reportedly due to an additional fluoride resonance in low temperature synthesised NH₄F samples only.

5.2.1.2. ETBA F-silicalite-1

Upon increasing the length of the alkyl chain to n-ethyltributylammonium silicalite-1, the chemical shift of the dynamic fluoride is reduced to -63.61 ppm, a lower value than is experienced in the literature for TPA silicalite-1 and slightly below the -64 to -80 ppm range discussed.

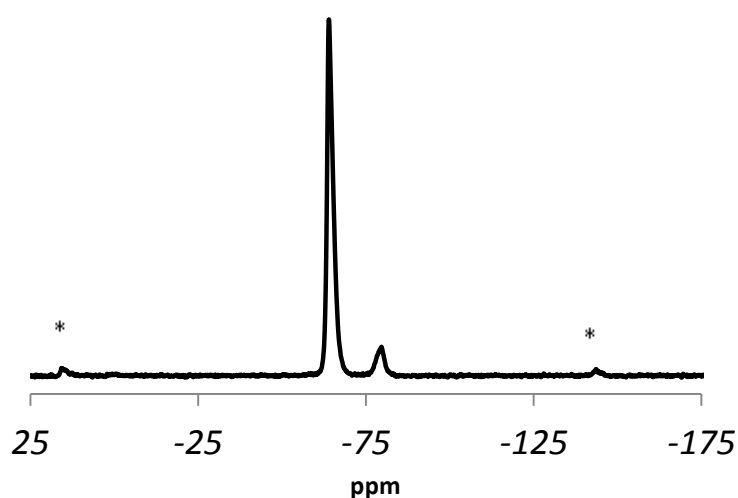


Figure 5.23 - ¹⁹F MAS NMR of ETBA F-MFI at 30 kHz rotation speed - and 280 K (spinning sidebands are asterisked*)

This result is in line with the increased motion of the fluoride from static to dynamic observed in ²⁹Si SS NMR. The asterisked peaks are simply spinning sidebands of the isotropic fluoride peak and the addition structural defect peak at -78.91 ppm.⁴⁹

5.2.1.3. MTPA F-silicalite-1

The ¹⁹F MTPA silicalite-1 spectrum studied displays the fluoride peak at -65.10 ppm for the dynamically disordered material. It very interesting to observe the lack of significant peak at -77.96 ppm that is observed in all other zeolites studied and is reported to be a common structural defect in MFI zeolites.⁴⁹

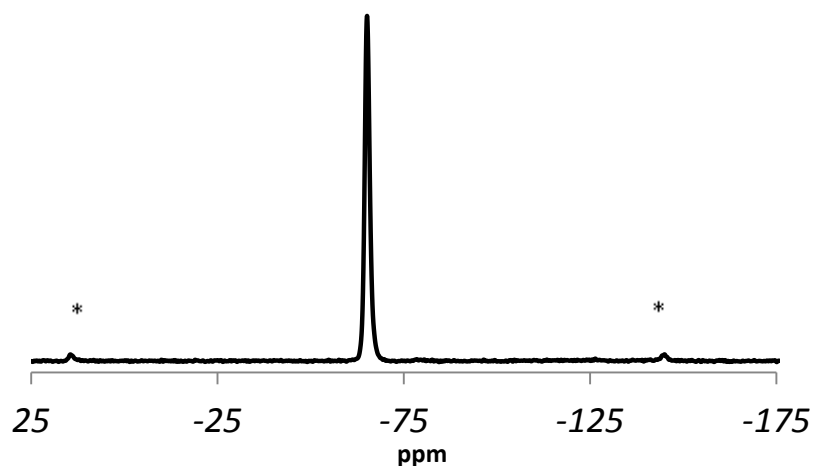


Figure 2.24 - ^{19}F MAS NMR of MTPA F-MFI at 30 kHz rotation speed and 280 K (spinning sidebands are asterisked*)

5.2.1.4. ETPA F-silicalite-1

Upon increasing alkyl chain length in the n-alkyltripropylammonium silicalite-1 series, a small chemical shift difference of the fluoride peak from -65.10 ppm for MTPA to -65.02 ppm in ETPA is observed. The latter sample has also been reported by Dib and co-workers to have a fluoride peak at -63.9 ppm indicating a possible difference in the local environments of the two fluorides, or temperature of the samples obtained. In addition to the -78.76 ppm peak, there are two extra peaks at \sim -127.2 ppm and a broad resonance at -106 to -110 ppm. The first of these peaks has been observed previously in SSZ-44 by Darton and co-workers¹¹ and is determined to be due to absorbed fluoride that can be removed by washing. The later peak is very small in intensity, is not apparent in the ETPA silicalite-1 spectrum by Dib and co-workers⁴⁶ however would be overlapped by a spinning sideband and is likely due to a small % structural defect.

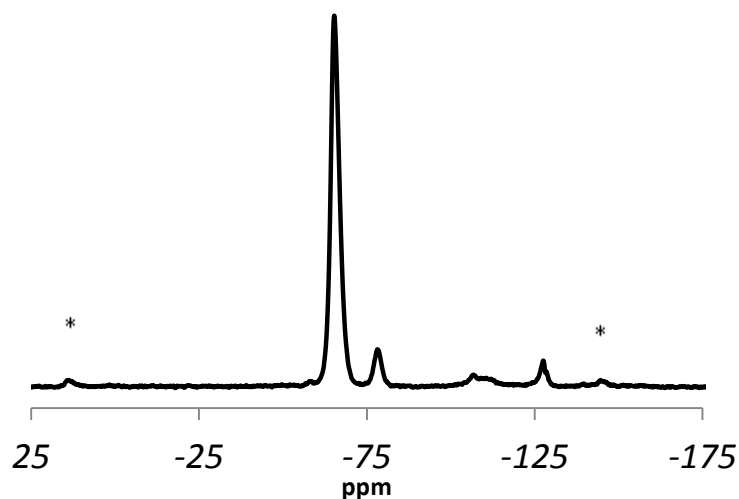


Figure 2.25 - ^{19}F MAS NMR of ETPA F-MFI at 30 kHz rotation speed and 280 K (spinning sidebands are asterisked*)

5.2.1.5. BTPA F-silicalite-1

Further increase of the alkyl chain reports a fluoride peak at -63.98 ppm. This is in line with the trend of the upfield shift previously observed for two smaller n-alkyltributylammonium silicalite-1 samples obtained and that is also observed within the Dib and co-workers trend.

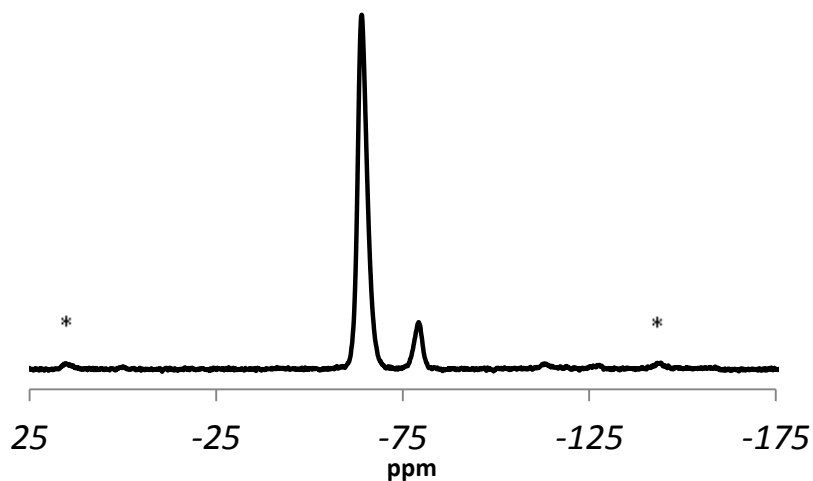


Figure 5.26 - ^{19}F MAS NMR of BTPA F-MFI at 30 kHz rotation speed and 280 K (spinning sidebands are asterisked*)

This trend also conforms to the theory of reduced chemical shift of the ^{19}F peak upon increased movement of the fluoride ion observed in the n-alkyltributylammonium silicalite-1 series.

5.2.1.6. ¹⁹F Silicalite-1 Summary

Upon increasing the alkyl chain in both the n-alkyltripropylammonium and n-alkyltributylammonium silicalite-1 series, we observe an increase in ¹⁹F chemical shift of structure directing agents have that proved to have larger fluoride motion in the ²⁹Si results above. This is summarised as follows:

Table 5.4 – Table of isotropic chemical shifts of silicalite-1 fluoride

SDA/MFI	Isotropic peak (small peak)/ δ ppm	Literature / δ ppm
MTPA	- 65.10	-
ETPA	- 65.02 (- 78.76)	- 63.9 (65.6) ⁴⁶
TPA	-	- 62.8 (63.4) ⁴⁶ - 64 ²¹ - 65.9 ⁴⁸
BTPA	- 63.98 (-79.25)	- 62.60 (63.0) ⁴⁶
MTBA	- 67.68(-79.68)	-
ETBA	- 63.61 (-78.91)	-

5.3. Conclusions

The use of ²⁹Si and ¹⁹F solid state NMR experiments allow for the study of silicalite-1 framework materials. The results obtained can be used in collaboration with the ¹⁴N and ¹³C NMR experiments in order to give an overall picture of silicalite-1 materials and how they vary upon the use of different size and shape structure directing agents.

²⁹Si SS NMR results show the existence of fluoride, covalently bonded to the framework structure in all silicalite-1 zeolites studied, using a wide variety of shape and size SDA's. The fluoride becomes bonded to the framework creating a pentacoordinated silicon unit which exists outside the usual Q4 region in ²⁹Si SS NMR. This allows it to be studied easily, without overlapping with other framework silicon environments. The results indicate a change in motion of the fluoride from static to dynamic disorder, coinciding with the SDA used in silicalite-1 whereby an increase in the n-alkyl chain in n-alkyltrialkylammonium leads to a change from static to dynamic disorder of the fluoride. This trend holds throughout the n-alkyltripropylammonium and n-alkyltributylammonium SDA series. It is consistent with the theory that the fluoride is statically bound when the n-alkyl substituent is small enough to maintain a sufficiently strong coulombic

interaction between the fluoride and positively charged nitrogen. Upon increasing this n-alkyl substituent, it is thought the coulombic interaction decreases, allowing increased fluoride motion.

In order to further substantiate this theory, further work would have to be done. This could include ^{13}C labelling the end carbon on the n-alkyl substituent, for example within the n-alkyltripropylammonium series and conducting triple resonance experiments to detect the strength of the interaction. One of the major complications that would require consideration for these experiments would be the change in orientation of the SDA upon increasing n-alkyl substituent from straight to sinusoidal channels, as described in Chapter 4.

This is the first known occurrence of both static and dynamic disorder being observed at room temperature in zeolite materials by adapting the shape and size of the structure directing agent. Its importance lies in the well known role of the structure directing agent in the crystallisation, growth and properties of zeolites. Continued work in determining information about the orientation of structure directing agent within a zeolite framework may contribute to a more comprehensive understanding about the nucleation and crystallisation of zeolites and further the driving force towards synthesising custom made zeolites.

^{19}F SS NMR has also been used to study some silicalite-1 zeolite materials and contribute to knowledge surrounding the pentacoordinated silicon unit. The results of two series studied predominantly show a single ^{19}F chemical environment. The chemical shift of the fluoride is observed to decrease consistently upon increased fluoride motion.

Not only could this work be used to study other SDA's for these pure silica zeolite materials, it could also be adapted to study other kinds of inorganic materials.

5.4. References

- 1 T. J. Daou, J. Dhainaut, A. Chappaz, N. Bats, B. Harbuzaru, H. Chaumeil, A. Defoin, L. Rouleau and J. Patarin, *Oil Gas Sci. Technol.*, 2014, **70**, 447–454.
- 2 R. Aiello, F. Crea, E. Nigro, F. Testa, R. Mostowicz, a. Fonseca and J. B. Nagy, *Microporous Mesoporous Mater.*, 1999, **28**, 241–259.
- 3 Z. Lethbridge, J. Williams, R. Walton, K. Evans and C. Smith, *Microporous Mesoporous Mater.*, 2005, **79**, 339–352.
- 4 L. Mafra, J. A. Vidal-Moya and T. Blasco, *Structural Characterization of Zeolites by Advanced Solid State NMR Spectroscopic Methods*, Elsevier Ltd, Burlington, Volume 77., 2012, vol. 77.
- 5 E. Flanigen and R. Patton, US Patent, 4073865, 1978.
- 6 H. Kessler, J. M. Chezeau, J. L. Guth, H. Strub and G. Coudurier, *Zeolites*, 1987, **7**, 360–366.
- 7 P. A. Barrett, M. A. Cambor, A. Corma, R. H. Jones and L. A. Villaescusa, *J. Phys. Chem. B*, 1998, **102**, 4147–4155.
- 8 M. Cambor, L. Villaescusa and M. Diaz-Cabanas, *Top. Catal.*, 1999, **9**, 59–76.
- 9 J. M. Chezeau, L. Delmotte, J. L. Guth and Z. Gabelica, *Zeolites*, 1991, **11**, 598–606.
- 10 S. I. Zones, R. J. Darton, R. Morris and S.-J. Hwang, *J. Phys. Chem. B*, 2005, **109**, 652–61.
- 11 R. J. Darton, D. H. Brouwer, C. A. Fyfe, L. A. Villaescusa and R. E. Morris, *Chem. Mater.*, 2004, **16**, 600–603.
- 12 M. A. Cambor, A. Corma, P. Lightfoot, L. A. Villaescusa and P. A. Wright, *Angew. Chemie - Int. Ed.*, 1997, **36**, 2659–2661.
- 13 M. A. Cambor, P. A. Barrett, M. J. Diaz-Cabanas, L. A. Villaescusa, M. Puche, T. Boix, E. Perez and H. Koller, *Microporous Mesoporous Mater.*, 2001, **48**, 11–22.
- 14 S. Auerbach, K. Carrado and P. Dutta, *Handbook of zeolite science and technology*, CRC Press, New York, 2003.
- 15 M. A. Cambor, L. A. Villaescusa and M. J. Diaz-Cabanas, *Top. Catal.*, 1999, **9**, 59–76.
- 16 B. Louis and L. Kiwi-Minsker, *Microporous Mesoporous Mater.*, 2004, **74**, 171–178.
- 17 R. M. Shayib, N. C. George, R. Seshadri, A. W. Burton, S. I. Zones and B. F. Chmelka, *J. Am. Chem. Soc.*, 2011, **133**, 18728–18741.
- 18 J. C. Jansen, *Advanced zeolite science and applications*, Elsevier, 1994.
- 19 L. A. Villaescusa, I. Bull, P. S. Wheatley, P. Lightfoot and R. E. Morris, *J. Mater. Chem.*, 2003, **13**, 1978–1982.
- 20 E. Aubert, F. Porcher, M. Souhassou, V. Petříček and C. Lecomte, *J. Phys. Chem. B*, 2002, **106**, 1110–1117.
- 21 H. Koller, A. Wölker, L. A. Villaescusa, M. J. Díaz-Cabañas, S. Valencia and M. A. Cambor, *J.*

- Am. Chem. Soc.*, 1999, **121**, 3368–3376.
- 22 H. Koller, A. Wolker, H. Eckert, C. Panz and P. Behrens, *Angew. Chemie - Int. Ed.*, 1997, **36**, 2823–2825.
- 23 D. Corradini, D. Dambournet and M. Salanne, *Sci. Rep.*, 2015, **5**, 11553.
- 24 H. van Koningsveld and J. M. Bennett, Springer Berlin Heidelberg, 1999, pp. 1–29.
- 25 T. Willhammer and X. Zou, in *Zeolites in Sustainable Chemistry: Synthesis, Characterization and Catalytic Applications*, eds. X. Feng-Shou and M. Xiangju, Springer, 2015, pp. 151–187.
- 26 M. P. Atfield, C. R. A. Catlow and A. A. Sokol, *Chem. Mater.*, 2001, **13**, 4708–4713.
- 27 R. Morris, *Kristallography*, 2007, **1**, 33–38.
- 28 R. K. Iler, *The chemistry of silica : solubility, polymerization, colloid and surface properties, and biochemistry*, Wiley, 1979.
- 29 G. Van De Goor, C. C. Freyhardt and P. Behrens, *Zeitschrift Fur Anorg. Und Allegemenie Chemie*, 1995, **621**, 311–322.
- 30 C. A. Fyfe, A. R. Lewis, J. M. Chezeau and H. Grondey, *J. Am. Chem. Soc.*, 1997, **119**, 12210–12222.
- 31 E. Aubert, F. Porcher, M. Souhassou, C. Lecomte and H. Poincare, *J. Phys. Chem. B*, 2002, **106**, 1110–1117.
- 32 C. A. Fyfe, D. H. Brouwer, A. R. Lewis and J. Chezeau, *J. Am. Chem. Soc.*, 2001, **123**, 6882–6891.
- 33 E. M. Flanigen, R. L. Patton and S. T. Wilson, *Stud. Surf. Sci. Catal.*, 1988, **37**, 13.
- 34 R. F. Lobo, S. I. Zones and M. E. Davis, *J. Incl. Phenom. Mol. Recognit. Chem.*, 1995, **21**, 47–78.
- 35 M. E. Dose, K. Zhang, J. A. Thompson, J. Leisen, R. R. Chance, W. J. Koros, B. A. Mccool and R. P. Lively, *Chem. Mater.*, 2014, **26**, 4368–4376.
- 36 Mestrelab Research, 2014.
- 37 A. Lita, Y. Tao, X. Ma, L. Van De Burgt and A. E. Stiegman, *Inorg. Chem.*, 2011, **2**, 4–11.
- 38 C. A. Fyfe, Z. S. Lin, C. Tong and R. J. Darton, *Microporous Mesoporous Mater.*, 2012, **150**, 7–13.
- 39 G. D. Price, J. J. Pluth, J. V. Smith, J. M. Bennett and R. L. Patton, *J. Am. Chem. Soc.*, 1982, **104**, 5971–5977.
- 40 H. Van Koningsveld, H. Van Bekkum and J. C. Jansen, *Acta Crystallogr. Sect. B*, 1987, **43**, 127–132.
- 41 H. Van Koningsveld, J. C. Jansen and H. Vanbekkum, *Zeolites*, 1987, **7**, 564–568.
- 42 E. E. Mallon, M. Y. Jeon, M. Navarro, A. Bhan and M. Tsapatsis, *Langmuir*, 2013, **29**, 6546–6555.
- 43 M. Trzpit, M. Souldard, J. Patarin, N. Desbiens, F. Cailliez, A. Boutin, I. Demachy and A. H.

- Fuchs, *Langmuir*, 2007, **23**, 10131–10139.
- 44 H. Koller, A. Wolker, L. A. Villaescusa, M. J. Diaz-Cabanas, S. Valencia and M. A. Camblor, *J. Am. Chem. Soc.*, 1999, **121**, 3368–3376.
- 45 U. Haubenreisser, U. Sternberg and A. Grimmer, *Mol. Phys.*, 1987, **60**, 151–163.
- 46 E. Dib, A. Gimenez, T. Mineva and B. Alonso, *Dalt. Trans.*, 2015, **44**, 16680–16683.
- 47 S. Ando, R. K. Harris, U. Scheler, D. M. Grant and J. Wiley, *Encycl. Nucl. Magn. Reson.*, 2002, **9**, 531–550.
- 48 C. A. Fyfe, R. J. Darton, H. Mowatt and Z. S. Lin, *Microporous Mesoporous Mater.*, 2011, **144**, 57–66.
- 49 A. Rojas, L. Gomez-Hortigueela and M. A. Camblor, *J. Am. Chem. Soc.*, 2012, **134**, 3845–3856.
- 50 S. A. Axon and J. Klinowski, *J. Chem. Soc., Faraday Trans.*, 1993, **89**, 4245–4248.
- 51 L. Delmotte, M. Soulard, F. Guth, A. Seive, A. Lopez and J. L. Guth, *Zeolites*, 1990, **10**, 778–783.

6.0. Determination of SDA to Framework Distance in Silicalite-1 by Solid State NMR

2D solid state NMR, like its solution state counterpart allows further investigation into chemical systems that cannot be deduced by simpler 1D experiments. 2D experiments are defined by two frequency axes rather than the usual one in order to determine further structural information about a chemical species. Solid state NMR experiments used in this work include DCP (double cross polarisation) and REDOR (rotational echo double resonance) NMR experiments, in order to identify and exploit internuclear interactions in zeolites.

Structural determination of MFI and other porous framework materials has been attempted for decades, primarily using x-ray diffraction methods.^{1,2} Many difficulties can occur in using this technique, such as finding any single zeolite crystal of sufficient size to study by single crystal X-ray diffraction,^{1,3} or finding zeolite crystals that are not twinned.⁴ Additional problems incur due to the particular qualities of MFI synthesised via the fluoride route.^{4,5} As discussed in Chapter 5, use of the fluoride route creates an additional Si-F bond as a pentacoordinated silicon species at one silicon-9 site per mirror plane at any given time.^{4,6,7} Two different geometries are therefore observed for $[\text{SiO}_{4/2}]$ and $[\text{SiO}_{4/2}\text{F}]$ ⁸ whereby the long range structure reflects an average between the two species⁹ (Figure 6.1).

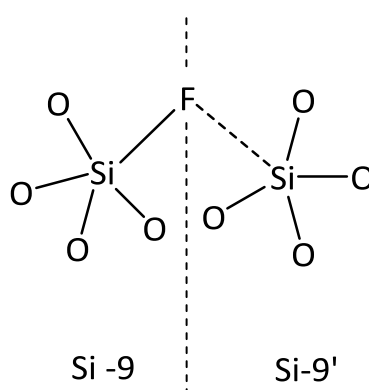


Figure 6.1 – Schematic diagram displaying pentacoordinated silicon species whereby the additional fluoride is covalently attached to one silicon-9 site at any one time

As a result of this incomplete occupancy and the averaging of species, an inaccurate and enlarged distance has often been reported for the interesting pentacoordinated Si-F bond in ZSM-5^{10,11} and other zeolites (STF⁹, silicalite-1¹², Si-FER¹³, Octadecasil¹⁴).

Due to the development of these distance averaging issues, other techniques have been sought out to use alongside X-ray diffraction as collaborative techniques.^{13,15,16} The use of solid-state NMR alongside XRD allows characterisation of species on both long and short range order for a more accurate characterisation.^{5,17,18}

Fyfe and co-workers⁷ have previously successfully elucidated the Si-F bond location and distances in silicalite-1 by the use of DCP and REDOR experiments. The experiments are used in a different capacity within this work: to determine the distance between the structure directing agent (SDA) methyl group and the framework species in MTBA fluoride silicalite-1. Successful determination of the location of asymmetric MTBA within the pore of zeolite MFI will contribute to the ever growing attempts to solve zeolite chemist's questions such as: How exactly are zeolites crystallised? How do we synthesise custom made zeolites?

6.1. Cross Polarisation Theory

Cross polarisation¹⁹ is a technique used to overcome difficulties experienced with single pulse experiments on dilute spin nuclei.²⁰ Dilute spins can either be isotopically dilute whereby the spin has low abundance (e.g. ¹³C), or chemically dilute (e.g. ³¹P) whereby spins can have a high abundance but are treated as a dilute spin due to being a single atom in a large molecule. The difficulty in observation is increased when both of these occasions are combined, such as attempting to study ¹⁵N single excitation of TPA F-MFI zeolite.

Nuclei that have low abundance, such as ²⁹Si tend to have particularly long inter-pulse delays and therefore suffer from long experimental times and low signal:noise resolution. In this situation, cross polarisation magic angle spinning (CP MAS), discovered in 1975 by Schaefer and co-workers²¹ is used, often in combination with high power proton decoupling (HPPD) to utilise these

dilute spins and gain information about chemical systems that have not been able to previously able to obtain.²²

6.1.1. Cross Polarisation: The Experiment

The cross polarisation experiment occurs via the transfer of magnetisation from a dipolar coupled ¹H or ¹⁹F abundant spin to a dilute nuclear spin.²³ This is possible by writing the following cross polarisation pulse program:

1. Application of a 90_x ° pulse to ¹H (B₁^H) to rotate the magnetisation to y-axis
2. Magnetisation maintained at y-axis by application of an on resonance field along y-axis to spin lock.
3. The application of a pulse on the dilute spin resonance frequency (B₁^X) simultaneously with spin-lock for a certain length contact time.
4. Magnetisation transfer during this contact time from ¹H highly abundant nuclei to low abundance nuclei, such as ¹³C.
5. Simultaneous collection of low abundance spins during acquisition time occurs while ¹H or another high abundance nuclei is decoupled, as necessary.
6. The magnetisation transfer will only occur whereby the Hartman-Hahn²⁴ condition is matched, and both spins energy and nutation frequencies are equal (Equation 6.1.):

$$\gamma^H B_1^H = \gamma^X B_1^X \quad \text{Equation 6.1.}$$

Where $\gamma^{H/X}$ = the nuclei's magnetogyric ratio ($\text{rads}^{-1}\text{T}^{-1}$) and $B_1^{H/X}$ = applied magnetisation to on resonance abundant (H) and dilute spins (X)

One way of considering the Hartmann-Hahn²⁴ condition is via the transfer of heat from abundant spins to dilute spins, and dilute spins to abundant spins. Due to the larger heat capacity of abundant spins, the overall effect of this process reduces the heat of dilute spins, and therefore increases magnetisation factor to γ_H/γ_X . This increased sensitivity²⁵ can have a significant impact on the spectrum obtained, for example a 100 % magnetisation transfer of ¹H to ¹³C gives a signal

enhancement of $\gamma^H / \gamma^C = 4$, and a $(\gamma^H / \gamma^C)^2 = a$ 16 fold reduction in experimental time. This significant enhancement is utilised even further when other nuclei systems are studied, such as ^{15}N .²⁰

The inter-pulse recycle delay is reduced from the length of the dilute spin's recycle delay (T_1^X) in a single excitation experiment to the time of ^1H 's recovery of magnetisation (T_1^H)²⁶. This significantly increases the number of scans in a given time, increasing the signal:noise ratio of the spectrum obtained.

6.2. Synthesis

6.2.1. ^{13}C labelled n-methyltriphenylsilane

The following reagents were required for setting up for ^1H - ^{13}C - ^{29}Si double CP MAS NMR: labelled ^{15}N , ^{13}C glycine and labelled ^{13}C n-methyltriphenylsilane, shown below (Figure 6.2).

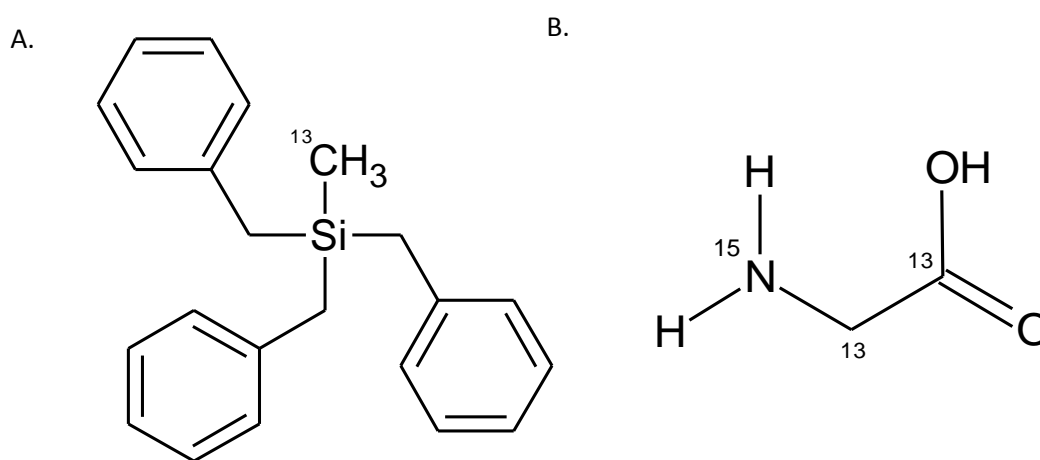


Figure 6.2 – Structure of reference samples used for A. ^{13}C N-methyltriphenylsilane(MTPS) and B. $^{13}\text{C}_2$ (99 %), ^{15}N (99%) Glycine

The particular double labelled glycine required, (Figure 6.2), was available for purchase from Cambridge Isotope Laboratories Inc. as follows: $^{13}\text{C}_2$ (99 %) ^{15}N (99 %) glycine.

Due to the specific requirements of the ^{13}C n-methyltriphenylsilane reference sample, it was not readily available to purchase and as such, required synthesising.

¹³C-MTPS Synthesis: Due to the high cost of labelled materials, all of this work was attempted with non-labelled reagents until proven successful. This took multiple reaction attempts and different synthetic methods but finally proved successful under the following conditions of Aberhart and Lin²⁷ for the methyl lithium synthesis (step 1 below), and methylation of triphenylsilane from Gilman and Melvin²⁸ (Step 2 below).

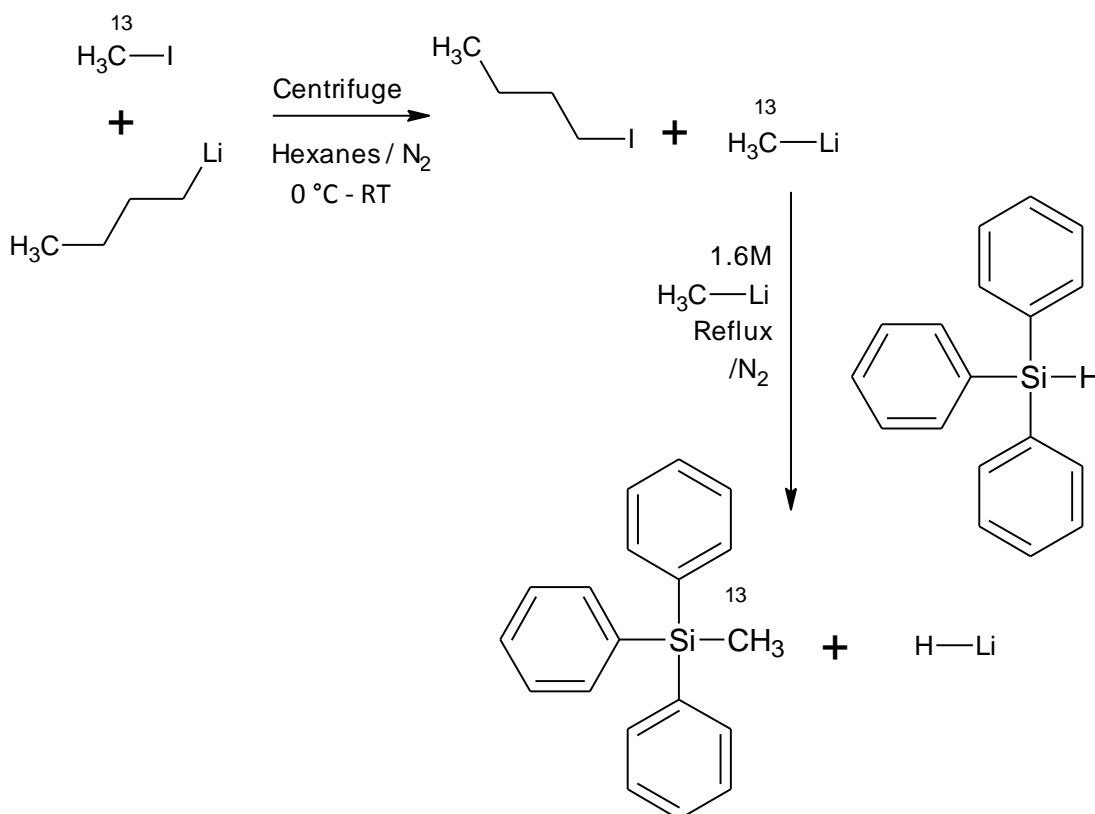


Figure 6.3 - Reaction scheme for the synthesis of labelled ¹³C n-methyltriphenylsilane: Initial ¹³C n-methyl lithium synthesis at 0 °C in Hexanes/N₂ and secondary step for product synthesis under reflux/N₂

Step 1: Methyl Lithium Synthesis

Synthesis: A 50 ml glass centrifuge tube was set-up and sealed with a disposable crimp septum and placed in an ice bath. The tube was flushed with nitrogen and 8.75 ml 1.6 M butyllithium and 1.0 g of ¹³C labelled iodomethane were injected into the centrifuge tube. The reagents were stirred and warmed to room temperature over a 30 minute time period and subsequently stirred for 20 minutes. The tube was centrifuged (30 minutes, 2500 rpm) and a solid precipitate was observed. The centrifuge tube then underwent a nitrogen-flush and the removal and replacement

of 6 ml clean dry hexanes by injection. This process was repeated 3 times to ensure any soluble impurities were removed and lastly replaced with 6 ml ether (pre-dried over sodium wire). The product was titrated against 0.1 M HCl 3 times to obtain a molar concentration of 1.375 M.

Step 2: N-methyltriphenylsilane (MTPS) Synthesis

0.49 g triphenylsilane was added to a 50 ml N₂ flushed flask and sealed. 0.75 ml 1.375 M ¹³C methyl lithium in diethyl ether was injected and stirred before 0.64 ml ¹²C methyl lithium in diethyl ether was also added and stirred for 1 day.

Step 3: MTPS Work-up

1.0 ml of the MTPS solution was extracted into ether, washed with distilled water and dried with magnesium sulphate. The drying agent was filtered and the solvent removed under reduced pressure leaving crystals for characterisation.

Step 4: MTPS Characterisation

The crystals obtained for MTPS (Figure 6.4) were characterised as follows: ¹H NMR (300 MHz, CDCl₃, ppm); δ 0.01 (3H, A), 7.38 (3H, E), 7.52 (6H, D), 7.60 (C, 6H); ¹³C NMR (300MHz, CDCl₃, ppm); δ 136.30 – 135.96 (B), 135.45 (C), 129.96 – 129.53 (D), 128.20 – 127.99 (E), -3.23 (A). They were deemed fit for use for setting up as a reference sample for the following CP-REDOR experiment.

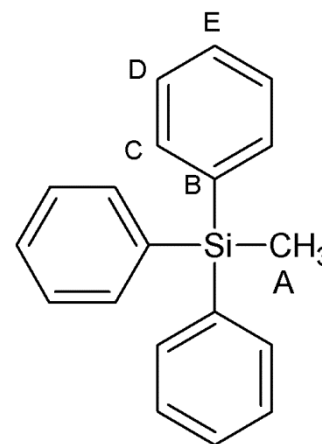


Figure 6.4 - Labelled molecular structure of MTPS for NMR assignment

6.2.2. Labelled ¹³C N-methyltributylammonium Iodide

Silicalite-1 zeolite was synthesised using ¹³C labelled n-methyltributylammonium iodide as follows:

SDA Synthesis: Tributylamine (2.26g, 15.45mmol), methanol (5 ml) and ¹³C labelled Iodomethane (1.0 g, 7.0 mmol) purchased from Sigma Aldrich (99.0% ¹³C with copper stabilizer) were refluxed

for 20 minutes. After this period, non-labelled ^{12}C Iodomethane (4.0 g, 28.18 mmol) was added and left for another 20 minutes. Finally, additional Iodomethane (2.28 g, 16.06 mmol) was added in excess and left to reflux for 24 hours.

After reflux, methanol was removed under reduced pressure and the product was recrystallised from a mixture of ethyl acetate and ethanol. White crystals were obtained (4.27 g, 88.78 %) and characterised as follows: ^1H NMR (300 MHz, CDCl_3 , ppm); δ 3.43 (6H, m, N-CH_2), 3.25 (3H, s, N-CH_3), 1.68 (6H, m, $\text{CH}_2\text{-CH}_2\text{-CH}_2$), 1.42 (6H, m, $\text{CH}_2\text{-CH}_2\text{-CH}_3$), 0.97 (9H, s, $\text{CH}_2\text{-CH}_3$); ^{13}C NMR (300MHz, CDCl_3 , ppm); δ 61.70 ($\text{N-CH}_2\text{-CH}_2$), 49.24 (N-CH_3), 24.44 ($\text{N-CH}_2\text{-CH}_2$), 19.66 ($\text{CH}_2\text{-CH}_2\text{-CH}_3$), 13.79 ($\text{CH}_2\text{-CH}_2\text{-CH}_3$).

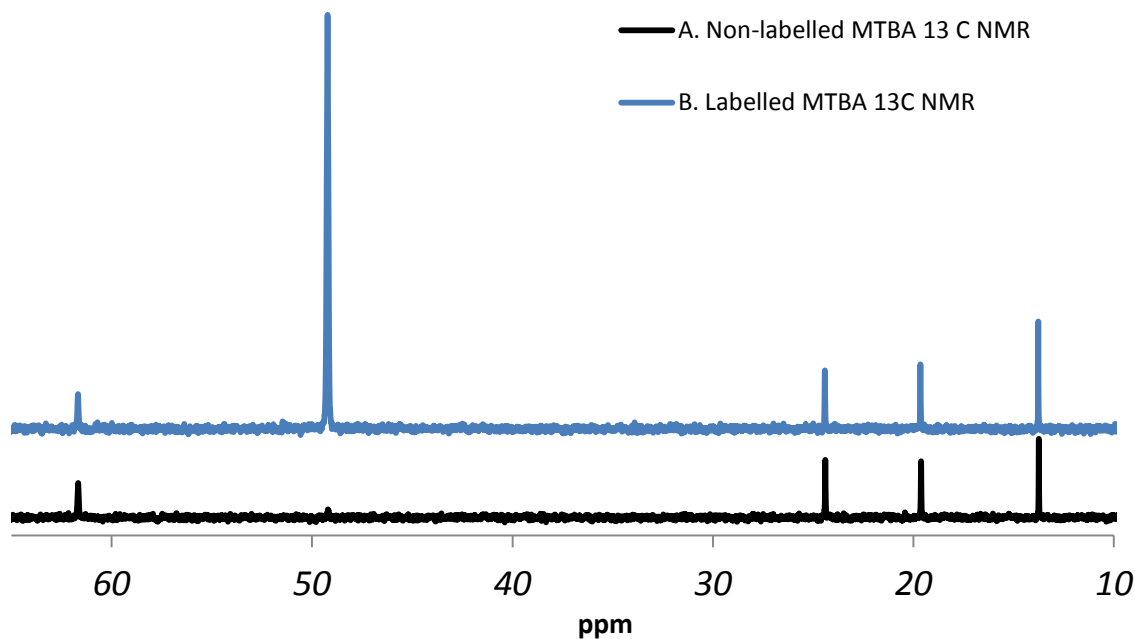


Figure 6.5 - Comparative spectra of ^{13}C NMR spectra for A. labelled ^{13}C MTBA and B. ^{12}C MTBA

The degree of labelling observed can be clearly seen (roughly 30 x the natural amount) in Figure 6.5 above comparing a non-labelled ^{13}C NMR of MTBA (Figure 6.5a), with the labelled sample (Figure 6.5b), whereby the labelled ^{13}C peak occurs at ~ 49 ppm.

Zeolite Synthesis: Silicalite-1 was synthesised using ^{13}C MTBA as structure directing agent as follows: 0.39 g of ^{13}C labelled MTBA, and 0.62 g of ammonium fluoride were added to a 46 ml autoclave liner. 6.0 ml of distilled water and 1.0 g of silicon dioxide were added and stirred

thoroughly creating a thick viscous gel. This was placed in a 180 °C oven for 6 days in a stainless steel autoclave.

Work-up: After removing the autoclave from the oven and allowing the contents to cool to room temperature and pressure, the liner contents were emptied and rinsed into a 50 ml centrifuge tube. The sample was centrifuged (15 minute, 2500 rpm) three times, dried at 60 °C overnight, and confirmed as zeolite MFI by comparison of the XRD diffraction pattern obtained (Figure 6.6), to that published by the International Zeolite Association.²⁹

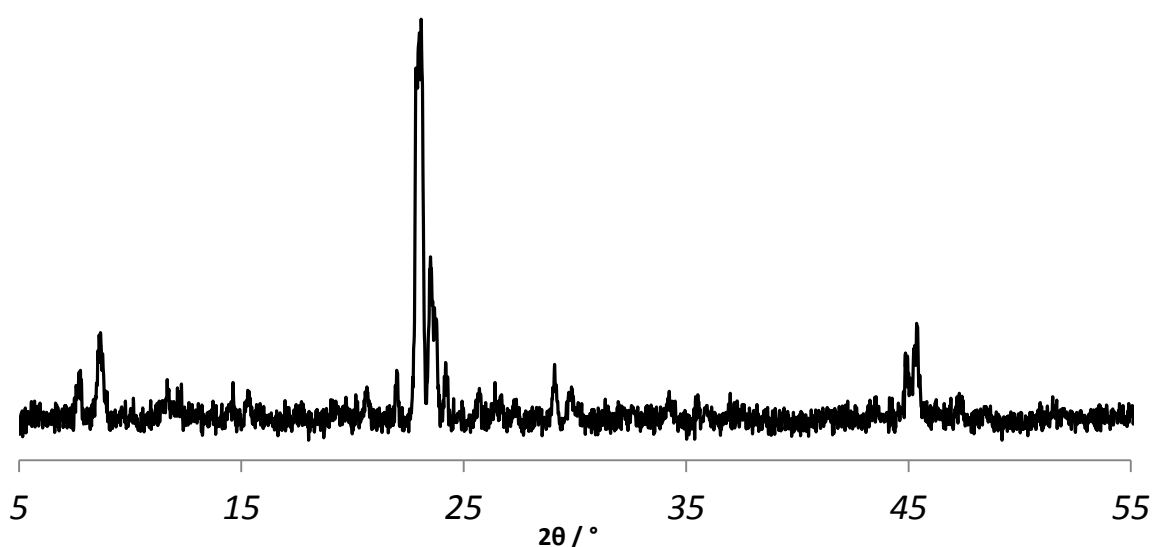


Figure 6.6 - XRD powder pattern of ¹³C labelled MTBA/MFI on a Bruker Advance diffractometer with Cu K α source

6.3. Double Cross Polarisation

The use of cross polarisation CP was first used in a double cross polarisation (DCP) experiment by Skejskal and Schaefer in 1977.²¹ It involves the use of the single-step transfer cross polarisation experiment in a triple resonance set up as a two-step process.³⁰ It surrounds the concept of the simultaneous irradiation and magnetisation transfer of three nuclei to allow determination of weak heteronuclear interactions through space and through bonds.

The first step in a DCP experiment is a single CP between ¹H nuclei and a X dilute spin such as ¹³C to build up magnetisation and increase sensitivity. The second step transfers the built up magnetisation on the X dilute nuclei to the Y dilute nuclei, such as ²⁹Si, which is the step that

allows the dipolar coupling to be studied between these nuclei under ^1H decoupling conditions. This decoupling is essential due to the difficulty in matching the Hartmann-Hahn²⁴ condition in DCP. The second step magnetisation transfer is dependent on the dipolar coupling strength allowing a relative identification of the closest nuclei within that transfer.

Initial DCP experiments created a pathway for more recent work that can be utilised and catered towards determining information about zeolites. For example the ^1H - ^{15}N - $\{^{13}\text{C}\}$ system studied by Schaefer and co-workers,^{31,32} the ^1H - ^{13}C - $\{^{29}\text{Si}\}$ system studied by Wisser and co-workers and the ^1H - ^{13}C - $\{^{19}\text{F}\}$ of zeolite MFI studied by Fyfe and co-workers.⁷

The latter work by Fyfe et al⁷ studied the TPA MFI-F system and was able to assign the 12 ^{29}Si peaks of zeolite MFI and conduct a successful ^1H - ^{19}F - ^{29}Si DCP experiment to confirm the location of the Si-F bond within the $[4^15^26^2]$ cage. In addition to the cage determination, Fyfe and co-workers were also able to use a DCP experiment to place the covalent silicon fluoride bond on silicon-9, and determine the bond distance using the REDOR experiment.

Since its discovery, the use of the DCP experiment has been used to probe a variety of different systems including proteins,³³ zeolites,⁷ biomolecules.³⁴ Despite this, the use of the DCP experiment in zeolite systems has been relatively sparse and information about only a few different zeolite systems have been determined using the enlightening technique. These include STF⁵ and TPA-MFI.

The closest literature study that bears any resemblance to the experiments on zeolites conducted within this work are Fyfe and co-workers,⁷ discussed above whereby no information about the organic structure directing agent (SDA) was investigated. Also, Wisser and co-workers³⁴ used DCP to investigate silica and organic molecule interactions but do not cover any zeolite materials.

6.3.1. Double Cross Polarisation: Experimental Information

Tetrapropylammonium iodide has been the most commonly used structure directing agent for ZSM-5 synthesis for decades.³⁵ Despite this, multiple other structure directing agents have proven

capable of successfully synthesising silicate-1 in this work.³⁶ N-methyltributylammonium iodide has been shown to be a more efficient structure directing agent for silicalite-1 synthesis and will be the SDA species used for the high silica MFI sample synthesised for this work.

The synthesis of silicalite-1 (MFI) using ^{13}C labelled n-methyltributylammonium iodide was studied by double cross polarisation to determine the distance of SDA within the zeolite pore to the zeolite framework. Double cross polarisation experiments have very sharp Hartmann-Hahn matching conditions and as such require sensitive set-up. Double labelled glycine (99 % ^{15}N , and 99 % ^{13}C) was used as an initial reference sample in order to set up the DCP experiment.

Due to the strict Hartmann Hahn matching condition, a second reference sample was also required for the DCP experiment set-up. The sample was required to be on the order of magnitude in distance and dipolar coupling between silicon and carbon and therefore hopefully detect dipolar couplings between labelled n-methyltributylammonium iodide and framework silicon. There were no known commercially available products that could satisfy this requirement so this product was synthesised in the laboratory. The sample chosen was n-methyltriphenylsilane due to it being a solid at room temperature, easily synthesised by reflux and therefore allowing for the labelled reagent to be as small chain as possible and most affordable: ^{13}C labelled iodomethane. The n-methyltriphenylsilane was however primarily used due to the short distance between the framework silicon and labelled methyl SDA.

The ^1H - ^{13}C - ^{29}Si DCP experiment is not a commonly used experiment due to the low natural abundance of ^{13}C and ^{29}Si .³⁴ This low abundance leads to a low signal:noise ratio so any ^{29}Si spectrum eventually obtained would not contain sufficient resolution to distinguish silicon T sites. The use of isotropic labelling is used in this situation to facilitate the successful experiment.

The aim of this work was to successfully set-up a solid state NMR experiment to determine the dipolar coupling constant between n-methyltributylammonium and the zeolite framework. Furthermore, to construct dipolar coupling curves and extract the distances determined from SDA to close silicon sites.

6.3.2. Double Cross Polarisation Experimental Set-up

The DCP experiment was set up on glycine and the synthesised ^{13}C n-methyltriphenylsilane before the ^{13}C n-methyltributylammonium silicalite-1 sample could be investigated.

6.3.2.1. Reference 1: Glycine Set-up

A ^{13}C (99 %), ^{15}N (99 %) glycine sample was packed into a 2.5 mm rotor and set at 11 kHz rotation at the magic angle. Three routing radiofrequency channels were set up whereby:

- Channel 1 – ^{15}N – 500 W amplifier
- Channel 2 – ^1H
- Channel 3 – ^{13}C – 500 W amplifier

The NMR was tuned and optimised on all channels and a standard ^1H – ^{13}C CP MAS²¹ NMR experiment was run. The CP condition and decoupling parameters were optimized for the set-up of the double CP experiment and a short scan single CP for glycine was run (Figure 6.7):

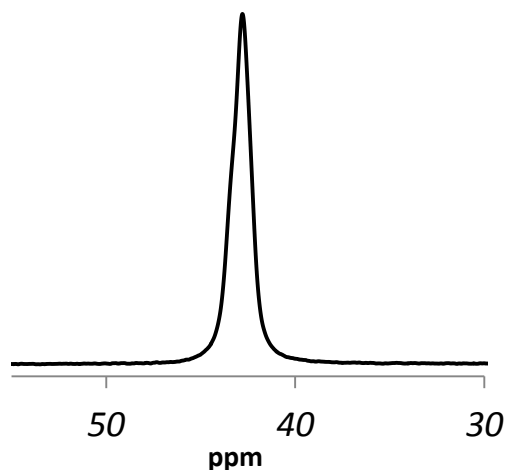


Figure 6.7 - ^1H – ^{13}C Solid state MAS CP experiment on reference glycine for double CP experiment set-up

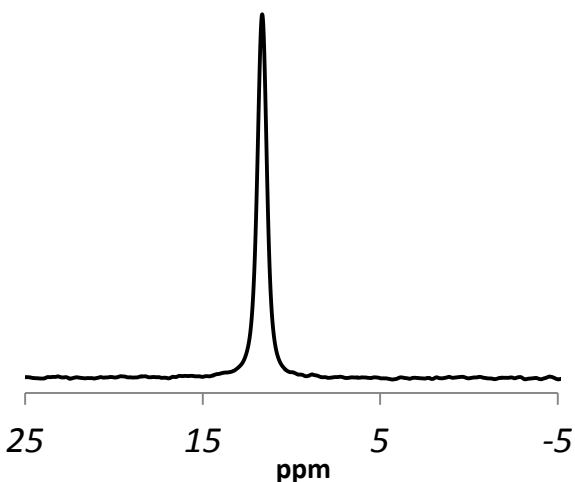


Figure 6.8 - ^1H – ^{15}N Solid state MAS CP experiment on reference glycine for double CP experiment set-up

A single CP experiment for ^1H – ^{15}N was subsequently set up and run to optimise the CP condition and decoupling parameters for the second step in the double CP experiment (Figure 6.8).

The double CP experiment was adapted from the $^1\text{H} - ^{13}\text{C}$ CP experiment and set up based mostly on the parameters determined from single CP experiments. The experiment was adapted to include a ramped pulse on the ^{15}N channel and calculating the attenuation at the new pulse length using the pulse length and calibrated pulse length. The DCP condition and decoupling parameters were optimised for both cross polarisation magnetisation transfers in the current experiment, yielding the successful DCP experiment shown in Figure 6.9.

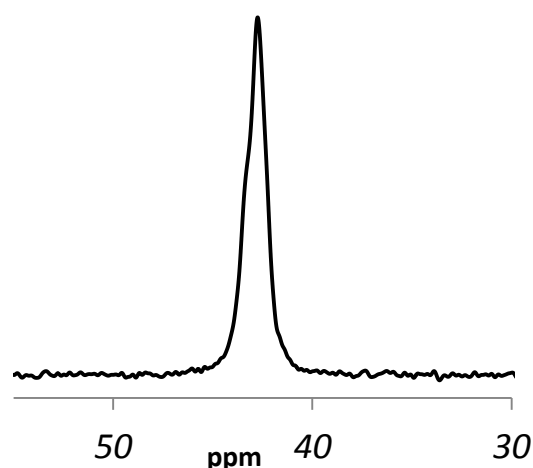


Figure 6.9 - $^1\text{H} - ^{15}\text{N} - ^{13}\text{C}$ Solid state NMR double CP experiment on reference glycine

6.3.2.2. Reference 2: MTPS Set-up

Successful set-up and observation of glycine allowed for progression to the second reference sample set-up: $^{13}\text{C} - ^1\text{H} - ^{29}\text{Si}$ double CP on the synthesised ^{13}C labelled n-methyltriphenylsilane.

The NMR was tuned and optimised on all channels and a standard $^1\text{H} - ^{13}\text{C}$ CP MAS²¹ NMR experiment was run. The CP condition and decoupling parameters were optimized and a short scan single CP for MTPS was run (Figure 6.10):

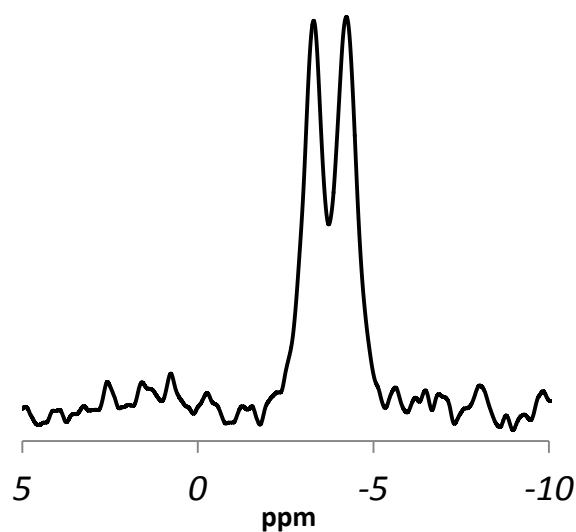


Figure 6.10 - $^1\text{H} - ^{13}\text{C}$ Solid state MAS CP experiment on MTPS for double CP experiment set-up

Additionally, a single CP experiment for $^1\text{H} - ^{29}\text{Si}$ was set up and run to optimise the CP condition and decoupling parameters for the other half of the double CP experiment (Figure 6.11).

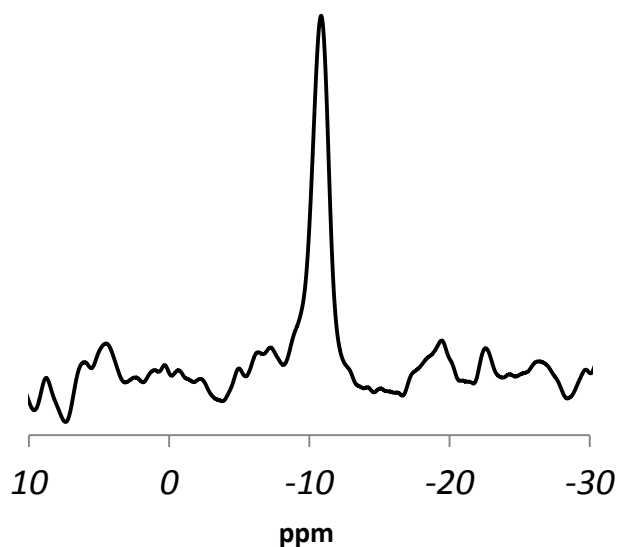


Figure 6.11 - $^1\text{H} - ^{29}\text{Si}$ Solid state MAS CP experiment on reference MTPS for double CP experiment set-up

The double CP experiment was adapted from the $^1\text{H} - ^{29}\text{Si}$ CP experiment and set up based mostly on the parameters determined from single CP experiments. The double CP conditions and decoupling parameters optimised for the both cross polarisation magnetisation transfers in the current experiment, yielding the following short-scan successful spectrum (Figure 6.12).

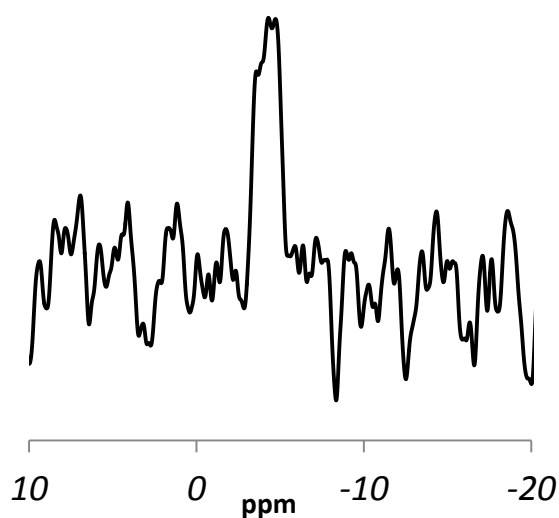


Figure 6.12 - $^{13}\text{C} - ^1\text{H} - ^{29}\text{Si}$ -Solid state double CP MAS NMR experiment on reference MTPS

6.3.2.3. Double Cross Polarisation Conclusions

Despite the successful set-up of purchased labelled glycine and synthesised labelled n-methyltriphenylsilane, the double cross polarisation DCP experiment conducted on labelled n-methyltributylammonium iodide was unsuccessful. Many difficulties were encountered in attempting to find the CP matching conditions for the double cross polarisation experiment despite being set-up from parameters of two successful single CP experiments (^1H - ^{13}C and ^1H - ^{29}Si). This could be due to a combination of two issues. It is possible the SDA to framework distance is too far inferring the magnetisation transfer would be reduced and therefore difficult to observe. It may also be due to the known difficulties in finding the extremely sharp Hartmann-Hahn²⁴ matching conditions for DCP experiments. Instead a Rotational-Echo, Double-Resonance (REDOR) experiment was chosen that was thought to have a higher chance of success in the allocated NMR time due to not possessing the extremely sharp Hartmann Hahn condition.

6.4. Rotational-Echo, Double Resonance (REDOR) Results

The REDOR experiment is a 'recoupling' technique developed initially by Gullion³⁷ in 1989 and works by perturbation of the spinning process of a sample. Rotor synchronised pulses are applied at a certain time which prevents dipolar coupling and forms a reduced intensity dipolar echo then allows dipolar induced dephasing to build.³⁸ The 'recoupling' is so named for the ability to recover the lost dipolar couplings under MAS.³⁹

Most solid state NMR experiments are designed to reduce dipolar coupling to zero by observing at 1 full rotation under MAS. The selective re-introduction of dipolar coupling parameters is therefore possible by changing the observation to less than full rotations. Due to the pulses being applied in synchronicity with rotation however, the spinning speed must be kept very steady (within $\pm 0.1\%$ of the MAS rate) in order for the pulse application to stay in time with rotation.

The REDOR experiment is used to determine dipolar couplings between spins that are close in proximity, as they have a $1/r^3$ relation to distance between spins. The use of this experiment as compared to the failed DCP experiment is summarised below (Table 6.1):

Table 6.1 – Table of comparison of REDOR and DCP experimental requirements

	REDOR	DCP
Experiment	Dephasing of transverse carbon magnetisation by Y dilute spin (^{15}N , ^{29}Si) π pulses on rotor schedule whilst ^1H decoupling Can suffer signal loss due to recovering of lost dipolar information.	Double cross polarisation transfer whereby CP 1 occurs for sensitivity enhancement and CP 2 to study the dipolar coupling
Spin Sensitivity	Yes to roughly 0.1 % of spin rate ⁴⁰	Yes to roughly 0.1 % of spin rate ⁴⁰
Analysis Difficulty	Due to the dephasing and acquisition start point being rotation dependent Yes So long as limited to dipolar coupling ³⁷	Dilute spin magnetisation transfer is dependent on spin rate Complicated ⁴¹ Due to additional couplings such as proton couplings being considered and stringent Hartmann-Hahn ²⁴ matching conditions
Isotope labelling required	Yes	Yes
Special experiment requirements	Site Specific ⁴²	Essential due to lack of sensitivity Strict Hartmann Hahn conditions to be met
Data Sensitivity	Significantly higher ⁴³	Significantly lower ⁴⁰ However this comparison can be evened out under different coupling interactions, e.g. labelled strong homonuclear interactions
Additional reference sample required	No	Yes

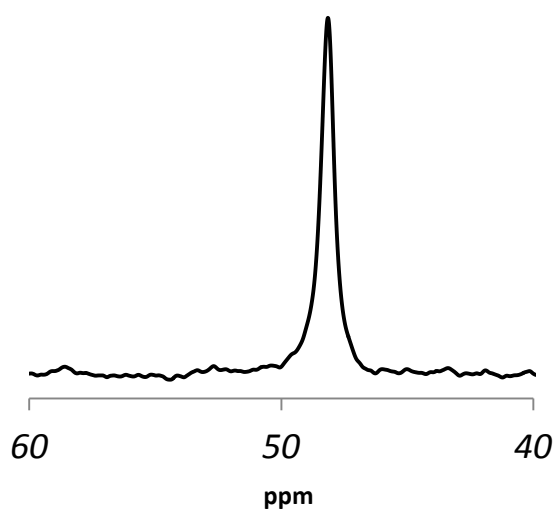
The REDOR experiment relies on comparisons of the difference obtained when no pulse applied and a pulse is applied to a sample to obtain a reference (S_0) and echo signal (S'), respectively. These can be compared by identifying the normalised dipolar dephased signal ($\Delta S/S_0$).⁴⁴ A 2D spectrum is built up from multiple rotor cycles (NT_r) of these normalised signals to create a REDOR curve which can be fitted to determine dipolar coupling between spins as well as determine internuclear distances.

This REDOR experiment has already been successfully conducted by Fyfe and co-workers⁷ in TPA silicalite-1⁷ and octadecasil⁴⁵ zeolites in a different capacity to identify the pentacoordinated fluoride location in the zeolite structure. This bond however is a silicon fluoride covalent bond, unlike the interaction observed within this work. Due to the low abundance of ¹³C (1.11 %) and ²⁹Si (4.69 %) in this chemical system, isotropic labelling is required. It is also essential due to the high resolution required in the ²⁹Si spectrum in order to distinguish silicon T sites around -110 ppm for Q4 Si and to determine the dipolar coupling to these silicon sites.

6.4.1. REDOR Set-up

The synthesised sample of silicalite-1 using labelled ¹³C n-methyltributylammonium iodide was packed into a 2.5 mm rotor and set at 10 kHz rotation at the magic angle. A second reference sample was not required for this set-up as with the double CP experiment due to less stringent match conditions so all optimisations were performed on the sample itself. Three routing radiofrequency channels were set up whereby:

- Channel 1 – ¹³C – 500 W amplifier
- Channel 2 – ¹H
- Channel 3 – ²⁹Si – 500 W amplifier



The NMR was tuned on all channels and a standard ¹H – ¹³C CP MAS NMR experiment was run. The CP condition and decoupling parameters were optimized and a short scan CP was run on ¹³C MTBA (Figure 6.13).

Figure 6.13 - ¹H – ¹³C Solid state MAS CP experiment on ¹³C MTBA/MFI for REDOR experiment

Additionally, a single CP experiment for $^1\text{H} - ^{29}\text{Si}$ was set up and run to optimise the CP condition and decoupling parameters for the second step of the double CP experiment on ^{13}C MTBA (Figure 6.14):

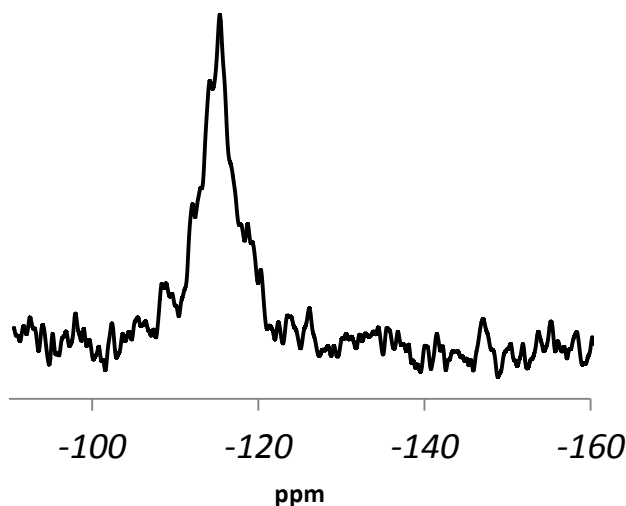


Figure 6.14 $^1\text{H} - ^{29}\text{Si}$ Solid state MAS CP experiment on ^{13}C MTBA/MFI for REDOR experiment

The 2D REDOR experiment was subsequently set up from the CP experiments with optimised match conditions and the successful 2D REDOR experiment was completed.

6.4.2. REDOR Results

The REDOR experiment was successful exhibiting a 2D NMR correlation of 256 1D NMR experiments. These 256 spectra are made up of 128 reference and echo NMR spectra.

The ^{29}Si NMR spectrum has already been resolved for silicalite-1 zeolite by Fyfe et al⁷ identifying the specific chemical shift for all 12 silicon sites in MFI-F/TPA and classifying it as orthorhombic with *Pmna* symmetry at room temperature. As previously discussed in Chapter 4, silicalite-1 has *Pmna* symmetry whereby we observe 12 silicon sites in MFI/TPA but 24 in MFI/MTBA.³⁶ This is due to the presence of the additional silicon fluoride bond and pentacoordinated silicon observed in only 1 side of the mirror plane of silicalite-1.⁸ Due to the symmetry it is still however possible to assign the 24 NMR peaks observed in MFI/MTBA to the 12 silicon sites observed in the MFI/TPA.³⁶

In order to analyse the 2D REDOR spectra, all observable peaks were identified and set a region (Figure 6.15):

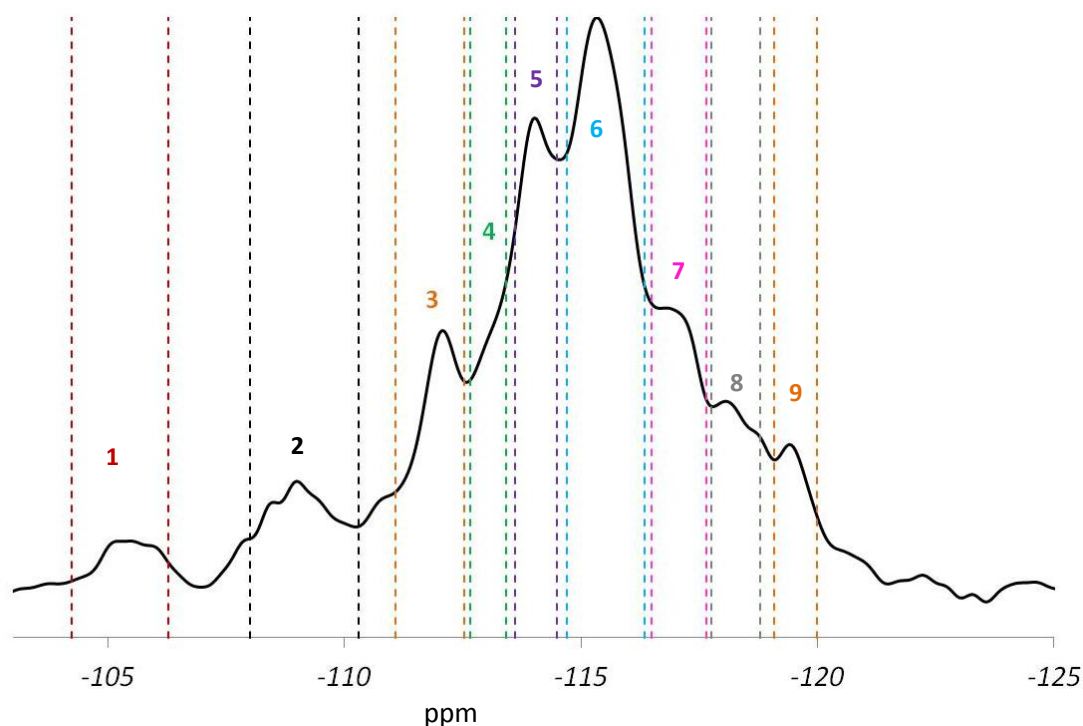


Figure 6.15 - Regions of 1D spectrum from 2D REDOR experiment for most silicon environments with exception of the low intensity pentacoordinated peak 10 at -144 ppm

This 1D NMR row of the 2D REDOR experiment shows 9 of the 12 regions we are looking to assign. The 10th region (not shown) exists considerably further outside the Q4 silicon NMR range displayed as it is the peak that corresponds to the pentacoordinated silicon fluoride site.⁸ The two additional regions cannot be observed as they are hidden under another peak. Silicon 7 is hidden under region 3 and silicon 3 is hidden under region 6. It was not possible to increase the signal:noise sufficiently in order to distinguish these peaks. This is due to the fact that the number of scans would have had to quadrupled in order to observe double the signal:ratio.

The regions analysed are summarised below in Table 6.2.

Table 6.2 – ²⁹Si regions observed for known silicon peaks in ¹H-¹³C {²⁹Si} NMR spectrum

Region/ Silicon Peak	Start of Region (ppm)	End of Region (ppm)
Region 1	104.246	106.276
Region 2	108.139	110.308
Region 3	111.087	112.532
Region 4	112.574	113.466
Region 5	113.488	114.669
Region 6	114.680	116.436
Region 7	116.436	117.650
Region 8	117.650	118.795
Region 9	119.177	119.883
Region 10	143.304	145.147

These regions were investigated individually and compared in order to determine the amount of dephasing observed and therefore the proximity of the SDA's ¹³C labelled methyl group to the silicon framework. Each ²⁹Si region was investigated by plotting the normalised difference (S/S_0) between the reference and echo spectra per rotor cycle to calculate the dipolar coupling constant. The results of this comparison are presented below (Table 6.3) in order of largest to smallest relative dephasing.

Table 6.3- Table comparing peak regions to reference framework silicon's and relative amount of dephasing observed

Silicon Peak	Dephasing Observed	Reference Silicon Number	Relative Dephasing
4	Yes	6	100.0 %
5	Yes	5	90.0 %
8	Yes	8	80.0 %
3	Yes	12	80.0 %
	Overlapped	7	-
6	Yes	2	73.3 %
	Overlapped	3	-
1	Yes	10	73.3 %
7	Yes	11	73.3 %
2	Yes	1	40.0 %
9	No	4	26.6 %
10	No	9	8.3 %

The silicon regions observed in the 2D NMR spectra are assigned to known reference silicon assignments (Table 6.3) and shown below in Figure 6.16.

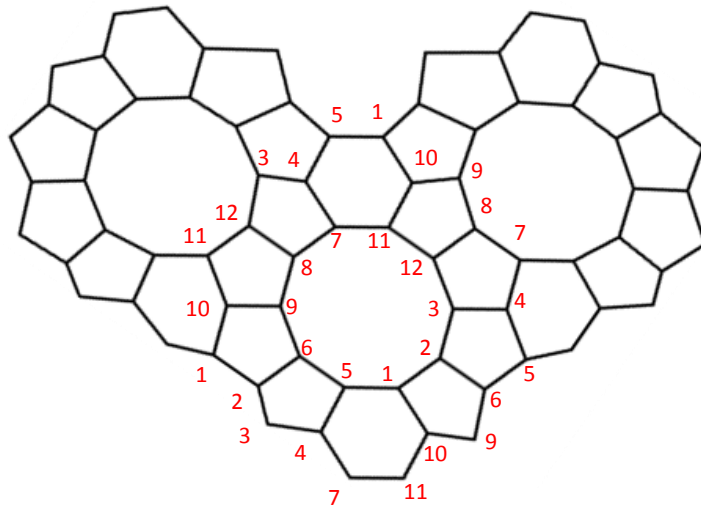


Figure 6.16- Schematic diagram of silicalite-1 zeolite and silicon assignments

Dipolar coupling plots have been constructed from the normalised difference in dephased and echo spectra ($S' - S_0/S_0$) following general REDOR studies by Gullion^{37,46} and Bertmer and Eckert⁴⁴ and a more applicable recent study by Wisser et al.³⁴ These plots generated display a REDOR curve from which the dipolar coupling constant can be extracted.⁴⁷ Solver Statistics was used in Microsoft Excel to fit a curve and value of the dipolar coupling constant to the experimental data for all silicon regions using the following equations and a least squares method:

Dipolar Coupling Constant
$$\frac{\Delta S}{S_0} = \frac{16}{15} N^2 T_r^2 \sum D^2$$
 Equation 6.2.

Where, S' = Dephased spectra, S_0 = Echo spectra, N = Number of rotor cycles, T_r = rotor period and D = dipolar coupling constant.

Distance Equation
$$D = \frac{\gamma_I \gamma_S h \mu_0}{4\pi^2 r^3 4\pi}$$
 Equation 6.3.

Where, D = dipolar coupling constant,, γ_I magnetogyric ratio of I coupled nuclei ($\text{rads}^{-1}\text{T}^{-1}$), γ_S = magnetogyric ratio of S coupled nuclei ($\text{rads}^{-1}\text{T}^{-1}$), h = Plancks constant ($\text{m}^2\text{kg s}^{-1}$), μ_0 = permeability constant (Hz)

6.4.2.1. ²⁹Si Regions Exhibiting the Maximum Dephasing

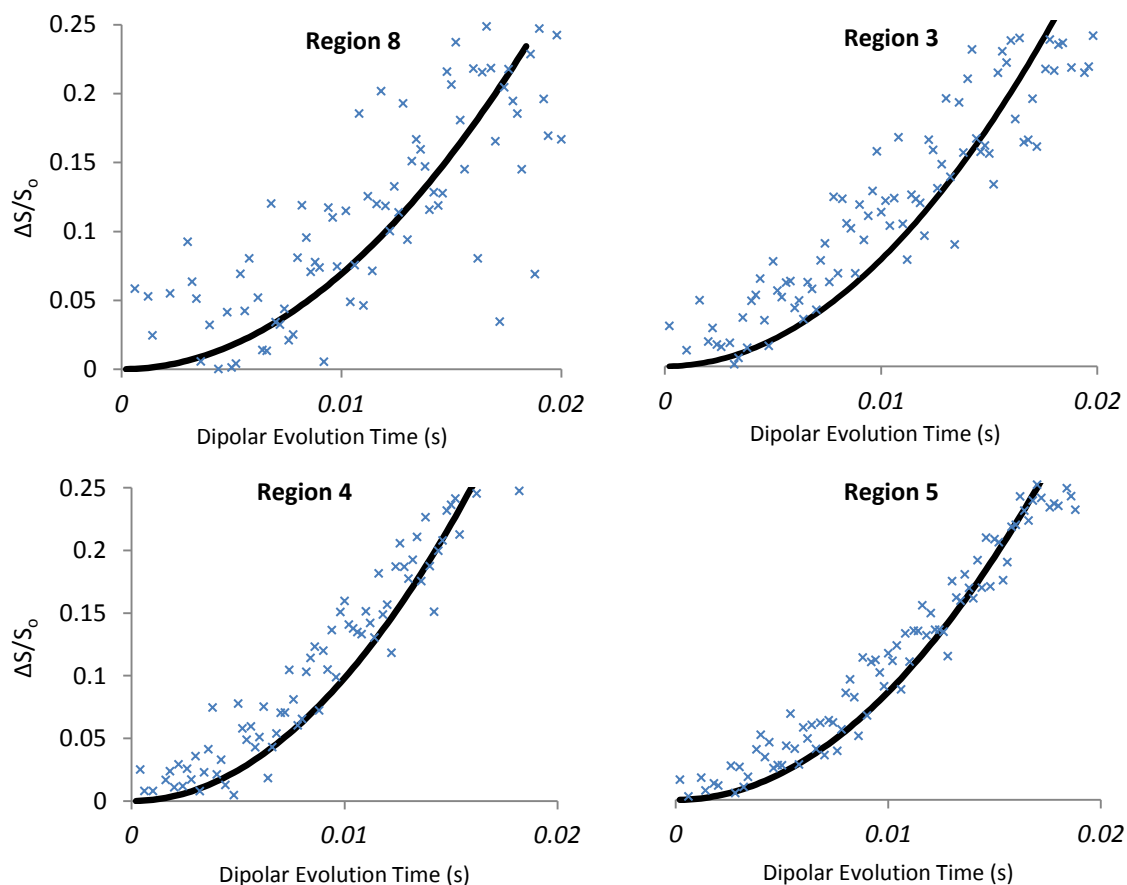


Figure 6.17 - REDOR curves (blue data) of dephasing observed in regions exhibiting maximum dephasing with Solver Statistics parabolic approximation curve (black line) fitted up to 0.025 $\Delta S/S_0$ for regions 4, 5 8 and 3

By limiting the REDOR curve to 0.25 $\Delta S'/S_0$, the heteronuclear dipolar moment can simply be calculated from Equation 6.2. Below this region, the $\Delta S'/S_0$ ratio has a relation to the second moment of dipolar coupling constant.⁴⁴

Table 6.4 - Table of dipolar coupling constants and distances calculated for largest dephasing silicon peaks

Silicon Region	4	5	3	8
Silicon Site	6	5	12 + 7	8
Dipolar Coupling Constant / kHz	85.28	79.49	75.68	71.60
Error Margin	+0.03	+0.02	+0.03	+0.05
R ²	0.93	0.95	0.84	0.70
Distance Si- ¹³ C	4.13 Å	4.23 Å	4.29 Å	4.38 Å

The positive continuous dephasing observed in REDOR NMR plots are expected and directly representative of the distance between the labelled ¹³C SDA to the respective silicon framework peak. These dephasing curves suggest the SDA methyl arm is pointing towards the 5-membered

ring of silicon sites 2-6 shown in Figure 6.18, and is capable of moving around within the zeolite pore. The large dephasing observed for region 3 is potentially due to the contributions from Si-7 and Si-12, whereas the methyl is not likely to reach far enough into the 2-6 ring to cause the observed level of dephasing.

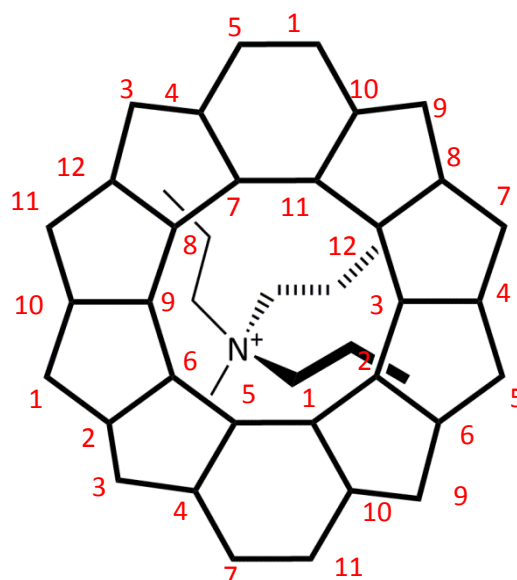


Figure 6.18 - Schematic Diagram of a MTBA SDA in zeolite Silicalite-1

6.4.2.2. ²⁹Si Regions Exhibiting Medium Dephasing

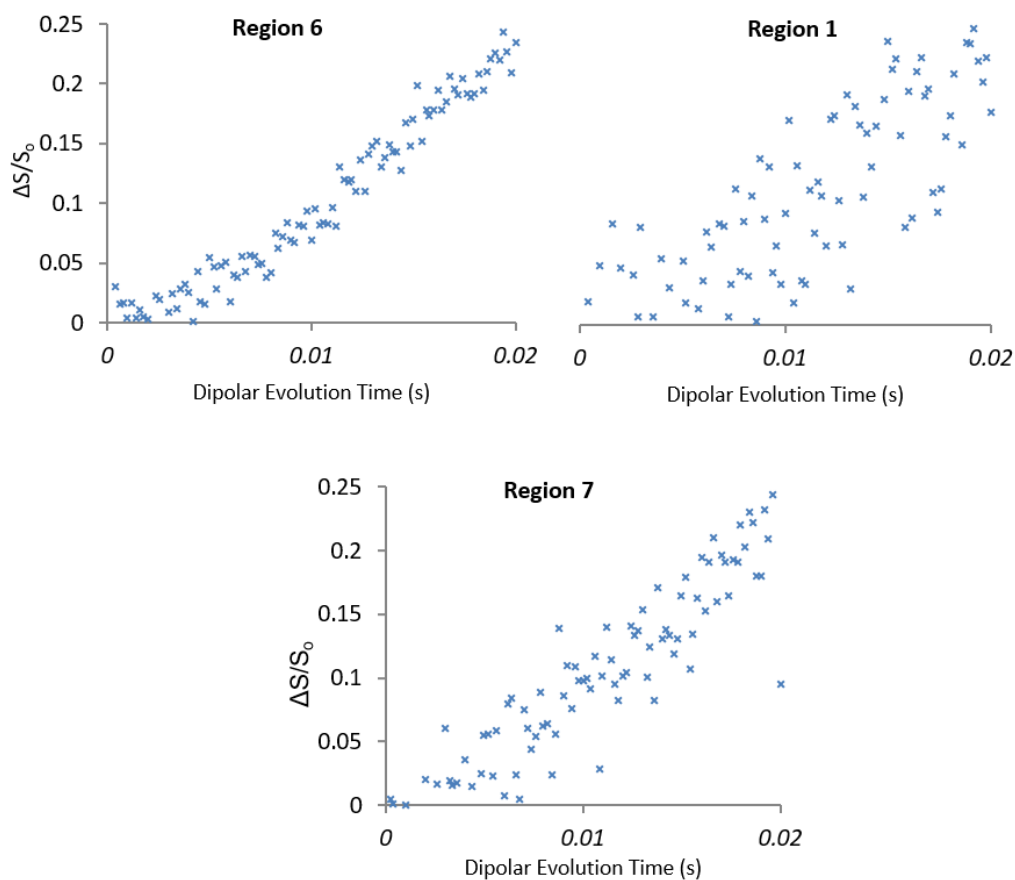


Figure 6.19 - REDOR curves (blue data) of dephasing observed in regions exhibiting medium dephasing with Solver Statistics parabolic approximation curve (black line) fitted up to 0.025 $\Delta S/S_0$ for regions 6, 1 and 7

The silicon's experiencing medium levels of dephasing are 6, 1 and 7, shown above (Figure 6.19). The results are in accordance with the theoretical position of the MTBA SDA in the MFI pore schematic above (Figure 6.18). The silicon 10 (region 1) dephasing graph above has limited data points because the dephasing data is not as conducive to the curve as previous good dephasing graphs. This is corroborated by the limited low signal:noise for that peak on the REDOR NMR spectrum which hosts the pentacoordinated silicon fluoride in 1 silicon per mirror plane.

Table 6.5- Table of dipolar coupling constants and distances calculated for medium dephased silicon peaks

Silicon Region	6	1	7
Silicon Site	2 + 3	10	11
Dipolar Coupling Constant / kHz	70.46	69.85	67.86
Error Margin	+/-0.02	0.05	+/-0.03
R ²	0.95	0.63	0.84
Distance Si- ¹³ C	4.40 Å	4.41 Å	4.45 Å

6.4.2.3. ²⁹Si Exhibiting Minimal Dephasing

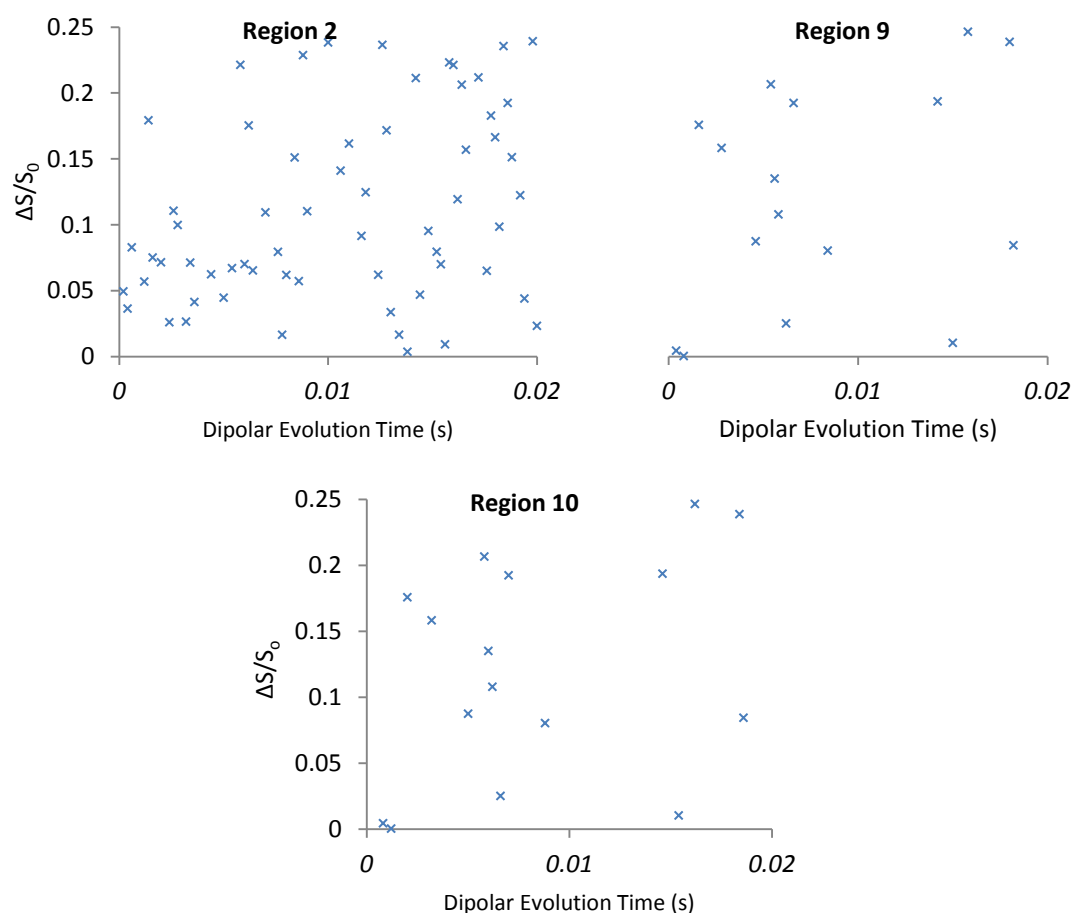


Figure 6.20 - REDOR curves (blue data) of dephasing observed in regions exhibiting maximum dephasing with Solver Statistics parabolic approximation curve (black line) fitted up to 0.025 $\Delta S'/S_0$ for regions 2, 9 and 10.

The three graphs displayed above for region 2 (Si-1), region 9 (Si-4) and region 10 (Si-9) show little to no ideal dephasing. This is displayed in their significantly reduced R^2 values and also corroborates the above schematic (Figure 6.18) which would expect these silicon's to be the furthest away from the labelled ^{13}C methyl SDA. The silicon site fittings are not of sufficient accuracy in order to report the dipolar coupling constant indicating these distances are larger than 4.5 Å.

6.5. Conclusions

The use of 2D solid state NMR has been used in order to determine the orientation of the N-methyltributylammonium SDA within a silicalite-1 framework structure. This was possible by utilising the cross polarisation technique and REDOR NMR experiments. The results demonstrate the use of solid state NMR as a complementary technique to X-ray diffraction in order to discover new information about chemical systems that remain previously undiscovered. It also allows bond distance determination of Si-F, a task that X-ray diffraction struggles to accurately accomplish.

The REDOR NMR experiment used was able to determine the dipolar couplings between ^{13}C labelled N-methyltributylammonium and surrounding framework silicon's. From this, the internuclear distances were calculated which enabled the exact location and orientation of the SDA within the framework to be determined.

Due to the novelty of this work no there is no literature information or single crystal structure to compare these distances and the location of the SDA in silicalite-1 to however the distances determined (4.13 Å) are certainly possible considering the known silicalite-1 pore size and SDA size and shape. It is possible that computer modelling could be used in order to support the orientation and bond distances that have been determined within this work. This may also spread some light on the exact location of the other trialkylammonium substituents within the SDA, without the need for expensive chemical labelling.

Successful use of the failed DCP experiment could be improved in future work by using labelled ^{29}Si during zeolite synthesis. Additionally, the REDOR experiment has the potential to be repeated for multiple other structure directing agents used both in this work to synthesise silicalite-1 and other zeolites systems, given enough NMR spectrometer time.

6.6. References

- 1 H. van Koningsveld and J. M. Bennett, Springer Berlin Heidelberg, 1999, pp. 1–29.
- 2 S. Auerbach, K. Carrado and P. Dutta, *Handbook of zeolite science and technology*, CRC Press, New York, 2003.
- 3 T. Willhammer and X. Zou, in *Zeolites in Sustainable Chemistry: Synthesis, Characterization and Catalytic Applications*, eds. X. Feng-Shou and M. Xiangju, Springer, 2015, pp. 151–187.
- 4 H. Koller, A. Wolker, L. A. Villaescusa, M. J. Diaz-Cabanas, S. Valencia and M. A. Camblor, *J. Am. Chem. Soc.*, 1999, **121**, 3368–3376.
- 5 C. A. Fyfe, D. H. Brouwer, A. R. Lewis, L. A. Villaescusa and R. E. Morris, *J. Am. Chem. Soc.*, 2002, **124**, 7770–7778.
- 6 S. L. Brace, P. Wormald and R. J. Darton, *Phys. Chem. Chem. Phys.*, 2015, **17**, 11950–11953.
- 7 C. A. Fyfe, D. H. Brouwer, A. R. Lewis and J. Chezeau, *J. Am. Chem. Soc.*, 2001, **123**, 6882–6891.
- 8 H. Koller, A. Wölker, L. A. Villaescusa, M. J. Díaz-Cabañas, S. Valencia and M. A. Camblor, *J. Am. Chem. Soc.*, 1999, **121**, 3368–3376.
- 9 C. A. Fyfe, D. H. Brouwer, A. R. Lewis, L. A. Villaescusa and R. E. Morris, *J. Am. Chem. Soc.*, 2002, **214**, 7770–7778.
- 10 G. D. Price, J. J. Pluth, J. V. Smith, J. M. Bennett and R. L. Patton, *J. Am. Chem. Soc.*, 1982, **104**, 5971–5977.
- 11 K. Chao, J. Lin, Y. Wang and G. Lee, *Zeolites*, 1986, **6**, 35–38.
- 12 E. Aubert, F. Porcher, M. Souhassou, C. Lecomte and H. Poincare, *J. Phys. Chem. B*, 2002, **106**, 1110–1117.
- 13 L. A. Villaescusa, I. Bull, P. S. Wheatley, P. Lightfoot and R. E. Morris, *J. Mater. Chem.*, 2003, **13**, 1978–1982.
- 14 N. C. Nielsen, L. A. Strassø and A. B. Nielsen, in *Solid-State NMR*, ed. J. Chan, Springer Berlin Heidelberg, 2011, pp. 1–45.
- 15 R. Morris, *Kristallography*, 2007, **1**, 33–38.
- 16 D. H. Brouwer, R. J. Darton, R. E. Morris and M. H. Levitt, *J. Am. Chem. Soc.*, 2005, **127**, 10365–10370.
- 17 H. Morell, K. Angermund, A. R. Lewis, D. H. Brouwer, C. A. Fyfe and H. Gies, *Chem. Mater.*, 2002, **14**, 2192–2198.
- 18 S. Cadars, D. H. Brouwer and B. F. Chmelka, *Phys. Chem. Chem. Phys.*, 2009, **11**, 1825–1837.
- 19 A. Pines, M. Gabby and J. Waugh, *J. Chem. Phys.*, 1973, **59**, 569.
- 20 D. Apperley, R. Harris and P. Hodgkinson, *Solid-state NMR: basic principles & practice*, Momentum Press, 2012.

- 21 E. Stejskal, J. Schaefer and J. Waugh, *J. Magn. Reson.*, 1977, **28**, 105–112.
- 22 V. McBrierty and K. Packer, *Nuclear Magnetic Resonance in Solid Polymers*, Cambridge University Press, 1993.
- 23 H. Chon, S. Woo and S. Park, *Int. Zeolite Conf.*, 1996, 468.
- 24 S. Hartmann and H. E, *Phys. Rev.*, 1962, **128**, 2042.
- 25 A. Bax, B. L. Hawkins and G. E. Maciel, *J. Magn. Reson.*, 1984, **59**, 530–535.
- 26 J. C. Jansen, *Advanced zeolite science and applications*, Elsevier, 1994.
- 27 D. J. Aberhart and L. J. Lin, *J. Chem. Soc. Perkin Trans. 1*, 1974, **1**, 2320–2326.
- 28 H. Gilman and H. W. Melvin, *J. Am. Chem. Soc.*, 1948, **71**, 4050.
- 29 G. T. Kokotailo, S. L. Lawton, D. H. Olsen and W. M. Meier, *Nature*, 1978, **272**, 437–438.
- 30 L. Sperling, in *Interfacial Aspects of Multicomponent Polymer Materials*, eds. D. Lohse, T. Russell and L. Sperling, Springer US, Boston, MA, 1997, pp. 1–16.
- 31 J. Schaefer, E. Stejskal, J. Garbow and R. McKay, *J. Magn. Reson.*, 1984, **59**, 150–156.
- 32 S. C. Christiansen, N. Hedin, J. D. Epping, M. T. Janicke, Y. Del Amo, M. Demarest, M. Brzezinski and B. F. Chmelka, *Solid State Nucl. Magn. Reson.*, 2006, **29**, 170–182.
- 33 E. Stejskal, J. Schaefer and R. McKay, *J. Mag*, 1984, **57**, 471–485.
- 34 D. Wissler, S. I. Bruckner, F. M. Wissler, G. Althoff-Ospelt, J. Getzschmann, S. Kaskel and E. Brunner, *Solid State Nucl. Magn. Reson.*, 2015, **66**, 33–39.
- 35 S. M. Alipour, R. Halladj and S. Askari, *Rev. Chem. Eng.*, 2014, **30**, 289–322.
- 36 S. L. Brace, P. Wormald and R. J. Darton, *Phys. Chem. Chem. Phys.*, 2015, **17**, 11950–11953.
- 37 T. Gullion and J. Schaefer, *J. Magn. Reson.*, 1989, **81**, 196–200.
- 38 A. Hing, N. Tjandra, P. Cottam, J. Schaefer and C. Ho, *Biochemistry*, 1994, **33**, 8651–61.
- 39 J. Leppert, B. Heise, M. Görlach and R. Ramachandran, *J. Biomol. NMR*, 2002, **23**, 227–238.
- 40 A. M. Christensen, J. Schaefer and K. J. Kramer, *Magn. Reson. Chem.*, 1991, **29**, 418–421.
- 41 J. Schaefer, E. Stejskal, J. Garbow and R. McKay, *J. Magn. Reson.*, 1984, **59**, 150–156.
- 42 R. Verardi, N. J. Traaseth, L. R. Masterson, V. V Vostrikov and G. Veglia, *Adv. Exp. Med. Biol.*, 2012, **992**, 35–62.
- 43 S. Christiansen, N. Hedin, J. Epping, M. Janicke, Y. Amo, M. Demarest, M. Brzezinski and B. Chmelka, *Solid State Nucl. Magn. Reson.*, 2006, **29**, 170–182.
- 44 M. Bertmer and H. Eckert, *Solid State Nucl. Magn. Reson.*, 1999, **15**, 139–152.
- 45 C. A. Fyfe, A. R. Lewis, J. M. Chezeau and H. Grondey, *J. Am. Chem. Soc.*, 1997, **119**, 12210–12222.
- 46 T. Gullion, *Concepts Magn. Reson.*, 1998, **10**, 277–289.
- 47 H. Foerster, J. Struppe, S. Steuernagel, F. Aussenacc, F. Benevelli, P. Gierth and S. Wegner, in *Solid State NMR AVANCE Solids User Manual*, Stanley J Niles, Rheinstetten, Germany, 2009.

7.0. Conclusions

Silicalite-1 zeolite has been synthesised using a wide variety of different shape and size structure directing agents. The purpose of this was to define the specific effects of the structure directing agent on the zeolite formed, due to its well-known role in the crystallisation and growth of the zeolite.

The complementary use of solid state NMR and X-ray diffraction has allowed both the long range order of silicalite-1 zeolites to be studied whilst also determining local information about the structure directing agent occluded within the zeolite framework. Determination of Si-F bond distances within the framework structure of pure silica zeolites by X-ray diffraction has previously experienced difficulties. Solid state NMR has therefore been used in order to investigate the local structure of silicalite-1 and structure directing agents using ^{13}C , ^{19}F , ^{14}N and ^{29}Si CP MAS experiments. These experiments elucidated trends in chemical shift, fluoride motion and location and orientation of the structure directing agent within the zeolite pore giving information about the structures and orientation of species.

The main results of these comprehensive studies indicate that upon replacing one alkyl chain in a quaternary ammonium structure directing agent with a smaller alkyl chain leads to a structure directing agent orientation with the smaller n-alkyl chain directed towards the smaller straight channel. Correspondingly, replacing it with a larger n-alkyl chain orientates the larger n-alkyl chain towards the larger sinusoidal channel.

The use of a fluoride based mineralising agent allowed the fluoride to become covalently bonded to the silicon framework structure in all silicalite-1 materials studied; as has previously been observed in the literature for TPA-silicalite-1 and other pure silica zeolites. This created an additional Si-F bond and pentacoordinated silicon unit which could be studied by solid state $^{29}\text{Si}\{^1\text{H}\}$ CP MAS NMR. This fluoride was found to exist with static disorder where an SDA was used with one small n-alkyl chain such as MTBA or MTPA. Increasing the length of the n-alkyl chain

however demonstrated increased mobility of the fluoride motion to dynamic disorder. This was thought to be due to the reduction in coulombic interaction between the fluoride and positively charged nitrogen however further study is required in order to support the theory.

The synthesis of an isotopically labelled sample of MTBA silicalite-1 has allowed the use of a CP REDOR experiment. The dipolar coupling interaction was studied between labelled ^{13}C N-methyltributylammonium structure directing agent and the surrounding framework silicon species. These dipolar couplings were used in order to calculate the bond distances and therefore deduce the exact orientation of the structure directing agent within the zeolite pore.

Additional work could be carried out by labelling and determining the distance between the MTBA butyl groups and zeolite silicon species. This would not only further confirm the orientation of the SDA, but determine the exact location of the entire SDA within the zeolite pores and channels. This could be also replicated for a variety of the different SDA silicalite-1 samples studied within this work, as well as for other zeolite systems. Not only would the cost of the isotropic labelling of these samples have to be considered but also there would have to be a sufficient dipolar coupling interaction between the desired pair, and therefore a sufficiently short distance between them in order for the REDOR NMR experiment to be able to detect.

The REDOR NMR experiment could be used to follow the crystallisation of silicalite-1 and other zeolites in order to determine how the framework forms around the SDA, achievable via systematic studies as functions of crystallisation time. This could be expanded by conducting the study *in-situ* within an NMR rotor, as zeolites like silicalite-1 can be synthesised under relatively mild conditions, for example reaction temperatures below 100 °C where there are very low autogenous pressures.

The novel work carried out within this project supplies a thorough and informative systematic study of zeolite materials using a wide variety of structure directing agents which is lacking in the zeolite community. It additionally delves deeper into studying one zeolite and SDA in particular by the use of a complex 2D solid state NMR experiment. This latter work is able to study zeolite

materials in an atypical manor, in order to gain very useful structural information and has the potential to be repeated for a wide variety of other zeolite and inorganic materials.

"But I don't want to go among mad people,"

*"Oh, you can't help that,
we're all mad here.
I'm mad.
You're mad."*

"How do you know I'm mad?"

*"You must be,"
"or you wouldn't have come here."*

Lewis Carroll